On the Origin and Growth of Cosmic Magnetic Fields

Ph.D. Thesis in Astronomy

Alexander Maximilian Beck

Munich, October 2013

On the Origin and Growth of Cosmic Magnetic Fields

Ph.D. Thesis in Astronomy

at the Faculty of Physics
of the Ludwig-Maximilians-Universität München

submitted by

Alexander Maximilian Beck

from Munich, Germany

Munich, October 2013

First evaluator: Prof. Dr. Harald Lesch
Second evaluator: Prof. Dr. Jochen Weller

Date of the oral exam: December 4th, 2013

Zusammenfassung

Diese Doktorarbeit versucht einen Beitrag zum Verständnis des kosmischen Magnetismus zu leisten. Insbesondere versucht sie zur Ergründung des Rätsels des Ursprungs der beobachteten Magnetfelder in unserem Universum beizutragen. Diese Fragestellung wird durch analytische Rechnungen und kosmologische magnetohydrodynamische Simulationen der Struktur- und Galaxienbildung bearbeitet. Wir schlagen vor, modellieren und simulieren zum ersten Mal ein selbst-konsistentes Szenario für die Entstehung von Magnetfeldern aus Supernovaexplosionen und anschließender Verstärkung und Verteilung innerhalb eines sich entwickelnden und expandierenden Universums. Die Stärke unseres Szenarios besteht darin, dass ein primordialer Ursprung des magnetischen Feldes nicht erforderlich ist. Die magnetischen Saatfelder sind eine natürliche Konsequenz der Strukturbildung.

In Kapitel 0 **('Einleitung')** geben wir einen kurzen Überblick über die aktuellsten Beobachtungen von Magnetfeldern innerhalb kosmischer Strukturen, insbesondere innerhalb von Galaxien. Außerdem sammeln wir unser aktuelles Wissen über die Strukturbildung im Universum und stellen die wichtigsten physikalischen Prozesse, die zur Entstehung von Sternen und Galaxien führen, dar. Insbesondere diskutieren wir die Entstehung und Entwicklung der ersten Objekte bei sehr hoher Rotverschiebung. Anschließend stellen wir die Grundlagen der Plasmaphysik und Magnetohydrodynamik dar. Diese Theorien bilden das Fundament für die Entwicklung von Magnetfeldern. Am Ende der Einleitung fassen wir die wichtigsten offenen Fragen des kosmischen Magnetismus zusammen, welche mit dem Dreiklang aus 'säen', 'verstärken' und 'verteilen' gut beschrieben werden könnten.

In Kapitel 1 **('Artikel I')** untersuchen wir die Entwicklung primordialer magnetischer Saatfelder während des Zusammenbaues eines Milchstraßen-typischen galaktischen Haloes. Zunächst entwickeln wir ein analytisches Modell zur Berechnung der Wachstumsraten und Wachstumszeiten der mittleren Magnetfeldamplitude innerhalb des diffusen Halogases mit der Zeit. Danach führen wir kosmologische Simulationen der Milchstraßen-typischen galaktischen Halobildung durch und zeigen, dass während des Zusammenbaus magnetische Saatfelder auf μG-Beträge verstärkt werden. Wir glauben, dass das Magnetfeld durch Kompression und zufällige Bewegungen, welche natürlicherweise während der Bildung des Haloes auftreten, verstärkt wird. Zuletzt vergleichen wir das analytische Modell und die Simulationen und finden sehr gute Übereinstimmung bezüglich des Wachstums des Halomagnetfeldes.

In Kapitel 2 **('Artikel II')** entwickeln wir ein Modell für die Entstehung magnetischer Saatfelder aus Supernovaexplosionen. Supernovae sind ein wesentlicher Bestandteil der Strukturbildung und es ist bekannt, dass Supernovaüberreste starke Magnetfelder besitzen. Wir implementieren unser Modell in GADGET und führen wieder kosmologische Simulationen der Milchstraßen-typischen galaktischen Halobildung durch. Wir zeigen, dass durch die Entstehung von magnetischen Saatfeldern durch Supernovae und anschließender Verstärkung Magnetfelder von μG-Stärke innerhalb des Haloes erzeugt werden können. Zusätzlich analysieren wir die Verteilung der intrinsischen Rotationsmaße des sich bildenden Haloes mit Rotverschiebung. Wir finden eine räumlich ausgedehnte Verteilung der Rotationsmaße innerhalb des Haloes mit Werten zwischen 100-1000 rad m^{-2} bei hoher Rotverschiebung. Zusammenfassend ist zu sagen, dass mit der Beschreibung der Saatfeldentstehung durch Supernovae ein freier Parameter aus der Entwicklung kosmischer und galaktischer Magnetfelder entfernt wird.

In Kapitel 3 **('Artikel III')** schlagen wir ein Szenario für die Magnetisierung kosmischer Leerräume vor. Die Leerräume sind die größten bekannten Objekte und sie füllen den größten Teil unseres Universums. In den Leerräumen wurden kürzlich sogar Magnetfelder mit einer Minimalstärke von mindestens 10^{-15} G abgeschätzt. Die Herkunft dieser Magnetfelder ist weitgehend unbekannt, jedoch wurde innerhalb der Leerräume auch eine kleine Anzahl von schwach leuchtenden Galaxien entdeckt. Diese Galaxien könnten mit den Magnetfeldern in Verbindung stehen und deshalb verbinden wir in diesem Artikel die Beobachtungen von Galaxien in den Leerräumen mit den Beobachtungen von

Magnetfeldern in den Leerräumen. Wir schlagen einen Mechanismus vor, durch den während der Entwicklung des Universums Magnetfelder aus den Galaxien in die Leerräume transportiert worden sind. Ohne ein primordiales Saatfeld voraussetzen zu müssen, reproduziert unser Szenario den beobachteten Magnetfeldwert.

In Kapitel 4 und 5 **('Artikel IV und V')** untersuchen wir die Entwicklung von Magnetfeldern in wechselwirkenden Systemen von Galaxien. Als Erstes untersuchen wir die Magnetfeldentwicklung und -verstärkung in wohldefinierten und kontrollierbaren Szenarien der Verschmelzung von kleinen Galaxien. Diese Studie ist insbesondere interessant, weil die Verschmelzung von Galaxien ein wesentlicher Teil der hierarchischen Strukturbildung ist und somit einen großen Einfluss auf die Entwicklung der kosmischen Magnetfelder hat. Wir zeigen, dass jede Wechselwirkung kleiner Galaxien eine Verstärkung des Magnetfeldes innerhalb der Galaxien als auch außerhalb (im intergalaktischen Medium) durch Kompression, turbulente Bewegungen und Stöße verursacht. Als Zweites zeigen wir synthetische Beobachtungen der kompakten galaktischen Gruppe 'Stephan's Quintett'. Aufgrund der Komplexität und der unbekannten Verschmelzungsgeschichte ist die Modellierung des Quintetts sehr schwierig, jedoch gibt es N-Körper-Simulationen, welche die wesentliche Morphologie einigermaßen reproduzieren. Wir resimulieren die bestehenden Modelle mit Magnetfeldern und berechnen synthetische Röntgen- und Synchrotronkarten und finden grundsätzlich gute Übereinstimmung, aber auch wesentliche Ungenauigkeiten beim Vergleich von Detailstrukturen.

In Kapitel 6 **('Artikel VI')** betrachten wir den numerischen Divergenzfehler. In unseren kosmologischen Simulationen ist es besonders wichtig, die Bedingung $\nabla \cdot \mathbf{B} = 0$ zu erfüllen. Wir adaptieren das Dedner-Divergenzbereinigungsschema auf unsere numerische Methode und implementieren den Algorithmus in GADGET. Wir führen die üblichen MHD Standard-Tests durch und finden, dass unser Bereinigungsschema in der Lage ist, das Magnetfeld zu regularisieren und das, ohne zu zuviel magnetische Energie zu dissipieren. Zusätzlich führen wir eine Langzeitsimulation des Orszag-Tang-Tests durch und finden, dass zu dissipative MHD-Implementationen große Schwierigkeiten haben, eine stabile Lösung zu reproduzieren.

In Kapitel 7 **('Ausblick')** geben wir einen Ausblick auf zukünftige Entwicklungen. Wir entwickeln weitere Modelle für zusätzliche physikalische Prozesse (z.B. der Transport von magnetischer Energie durch kosmische Strahlung). Dies wird uns erlauben, unsere Simulationen von isolierten galaktischen Halos auf großskalige kosmologische Strukturen zu erweitern. Dann können wir die Magnetisierung kosmischer Leerräume simulieren und untersuchen.

In dieser Arbeit zeigen wir, dass während der Strukturbildung im Universum magnetische Saatfelder entstehen, welche anschließend in Übereinstimmung mit Beobachtungen verstärkt und verteilt werden. Bisher sind die meisten Modelle für die Entwicklung galaktischer Magnetfelder von primordialen Saatfeldern und statischen Gravitationspotentialen in sich ruhig entwickelnden Galaxien ausgegangen. Allerdings ist die Strukturbildung hochgradig nichtlinear und umfasst außerdem eine große Menge weiterer hochkomplexer physikalischer Prozesse (z.B. sich schnell verändernde Gravitationspotentiale oder Strahlungsprozesse). Der Ursprung und die Entwicklung der kosmischen Magnetfelder ist mit all diesen Prozessen verbunden und außerdem, noch viel komplizierter, die kosmischen Magnetfelder könnten durch Rückkopplung die Strukturbildung selbst beeinflussen. Wir sind noch sehr weit davon entfernt, den kosmischen Magnetismus mit allen Details zu verstehen, jedoch ist es das Ziel dieser Arbeit, etwas Licht in das (noch dunkle) magnetische Universum zu bringen.

Summary

This Ph.D. thesis contributes to the understanding of cosmic magnetism. In particular, it intends to approach the mystery of the origin of the magnetic fields we observe in our Universe. This question is covered by analytical toy-modeling and cosmological magnetohydrodynamic (MHD) simulations of structure and galaxy formation. For the first time, we propose, model and simulate a fully self-consistent scenario for the creation of magnetic seed fields by supernovae (SN) and the subsequent amplification as well as distribution within the evolving Universe. The strength of this scenario lies in the fact that a primordial origin of the magnetic field is not required. The magnetic seed field is a natural consequence of the structure formation process.

In Chapter 0 **('Introduction')** we briefly review the latest observations of magnetic fields within cosmic structures and especially, within galaxies. Furthermore, we gather our current knowledge about structure formation within the Universe and also summarize the most important physical processes which lead to the creation of stars and galaxies. In particular, we discuss the formation and evolution of the very first objects at high redshifts. We then move on to lay out the basics of plasma physics and magnetohydrodynamics, which form the theoretical fundament of magnetic field evolution. The introduction closes by condensing the most important and open questions of cosmic magnetism, which, in particular, can be well described by the triad of 'seeding', 'amplification' and 'distribution'.

In Chapter 1 **('Paper I')** we study the evolution of primordially seeded magnetic fields during the formation of a Milky Way-like galactic halo. First, we present an analytical model predicting the growth rates and the absolute growth times for the mean magnetic field halo amplitude across cosmic time. Secondly, we perform cosmological simulations of Milky Way-like galactic halo formation and we find that magnetic seed fields of any strength are amplified up to μG values within the halo. We claim the amplification to be presumably driven by compression and random motions occuring naturally by the formation process of the halo itself. Last, we compare our analytical model and our numerical simulations and we find excellent agreement regarding the growth of the halo magnetic field.

In Chapter 2 **('Paper II')** we present a model for the creation of the magnetic seed fields by SN explosions. SN are an essential part of structure formation and SN remnants are known to host strong magnetic fields. We implement the model into GADGET and perform again cosmological simulations of Milky Way-like galactic halo formation. We find that the seeding by SN and subsequent amplification results in μG magnetic fields within the halo. Additionally, we analyse the intrinsic rotation measure (RM) distribution of the forming galactic halo with redshift. We find the halo to host a widespread distribution of RM values of several 100-1000 rad m^{-2} at high redshifts. Concluding, the seeding by SN allows to remove the magnetic seed field as a free and ambiguous input parameter from the evolution of cosmic and galactic magnetic fields.

In Chapter 3 **('Paper III')** we propose a magnetization scenario for cosmic voids. Voids are the largest and emptiest structures know in the Universe. However, recently, magnetic fields of at least 10^{-15} G have been detected within the voids. The origin of these magnetic fields is extremely mysterious, but an also observed faint galaxy population within the voids might hold the key to the magnetization of the voids. In this paper we link the latest observations of void galaxies to the observations of the void magnetic fields. We propose a mechanism by which the magnetic fields in the voids are originating from outflows of the assembling void galaxies during cosmic time. Our scenario is able to recover the observed lower limit of the magnetic fields in voids, again, importantly, without a primordial origin of the magnetic seed field.

In Chapters 4 and 5 **('Papers IV and V')** we study the evolution of magnetic fields within interacting and merging systems of galaxies. First, we present a study of the magnetic field amplification during well-defined and controlled simulations of galactic minor mergers. This study is in particular

interesting as minor mergers are believed to be an essential part of hierarchical structure formation and hence, are greatly affecting the evolution of the magnetic field. We find that every galactic minor interaction causes an amplification of the magnetic field within the galaxies as well as within an ambient intergalactic medium (IGM) by compression, random motions and shocks. Secondly, we present the first synthetic observations of the compact galactic group Stephan's Quintet (SQ). Due to its complexity and unknow merger history, modeling of SQ is still very challenging, however, existing N-body simulations can already reproduce the main morphology to some accuracy. We resimulate existing models to include MHD and calculate synthetic X-ray and radio emission maps and find good agreement in general, but some inaccuracies when comparing more detailed structures.

In Chapter 6 **('Paper VI')** we analyse the numerical divergence error. In particular, we are interested in maintaining the $\nabla \cdot \mathbf{B} = 0$ constrain within our simulations. We adapt the Dedner divergence cleaning method for our SPMHD scheme and implement the algorithm into GADGET. We perform a set of standard tests and find our cleaning scheme to work well in regularizing the magnetic field without being too dissipative. Furthermore, we study the Orszag-Tang vortex in long-time simulations and find major difficulties for MHD schemes which are too dissipative.

In Chapter 7 **('Final remarks')** we give an outlook into future developments. We will continue to develop modules for additional physics (i.e. transport of magnetic energy by CR). Furthermore, we will extend our simulations from the scales of isolated galactic haloes into large cosmological volumes. Then, in principle, we will be able to study in more detail the magnetization of a large galaxy population and of the voids.

The articles presented in this thesis contribute significantly to the understanding of cosmic magnetism. We show that during the formation of structures within the Universe, magnetic fields can be seeded, amplified and transported to the amplitudes and distribution we observe today. In the past, most models for the evolution of galactic magnetic fields assumed static gravitational potentials as well as quietly evolving galaxies. However, structure formation is a highly non-linear process and includes a wide range of physical processes (i.e. rapidly changing gravitational potentials, cooling or feedback). The origin and evolution of cosmic magnetic fields is directly coupled to all of these processes and even more complicated, the magnetic field might leave its imprint on structure formation itself. We are still very far from understanding cosmic magnetism in its full complexity, however, the scope of this thesis is to shed a small piece of light on some of its mysteries.

Contents

Developing an advanced numerical toolbox

Chapter 0

Introduction

An **elephant**[1] is among the biggest animals wandering on our Earth. Now consider an elephant standing in the middle of a small room full of people participating in lively discussions. Imagine that all the people stick to their own discussions and none of them seems to see the elephant. Why are they ignoring the obvious, the truth? Maybe the imprint of old habits is too strong or maybe too many difficulties would arise creating a feeling of inconvinience. If a guy far in the back asks the question 'What about the elephant?' his answer would be a wall of irritated faces of disbelief: 'How do you dare to bring up such a topic?' The elephant is something odd, beyond the lines of normalised thinking. For now, instead of analysing human behaviour, let us focus on something far more easy, such as cosmology and plasma physics, which are both rational and straight forward.

Currently, in physics we know four main forces: the strong interaction, the weak interaction, the gravitational interaction and the electromagnetic interaction. The strong and weak forces are most important on nuclear scales. However, the gravitational force as described by the theory of general relativity is of infinite range and thus is the dominant driver for large-scale dynamics in our Universe.

Over the last decades, the Lambda Cold Dark Matter (ΛCDM) model has emerged as the standard model of cosmology. Within this framework, our Universe is mainly made of 'dark' components such as 'Dark Energy', which could be associated with a cosmological constant Λ or an unknown scalar field, responsible for the accelerated cosmic expasion and 'Dark Matter' an additional invisible form of matter which is necessary to describe observed gravitational interactions properly. Only a very small component is made up of visible baryonic matter such as gas, stars and galaxies.

Most of this baryonic matter in our Universe is in an aggregate state which we call the Plasma state, in which the gas is ionized and consists of charged particles such as electrons and protons. Commonly, the theory of Magnetohydrodynamics is used for the description of ideally conducting fluids. However, as the treatment of electric and magnetic fields adds further levels of complexity to the astrophysical problems, the description is often resorted to simple hydrodynamics and the electromagnetic fields are simply ignored. Currently, the full laws of plasma physics and, in particular, the **magnetic field** are the **elephants in the astrophysical discussion room**.

Up to now, the theoretical or numerical descriptions of galaxy formation have mainly focused on gravitation and hydrodynamics. However, galaxies are known to host magnetic fields of an equipartition energy density. As galaxies form on nodes of the Cosmic web, the evolution of the galactic magnetic fields will be directly coupled to the formation and evolution of the galaxies. Thus we can ask: How do galaxy formation and galactic magnetic field evolution couple? In particular, can magnetic fields influence galaxy formation itself? The need for further investigations arises as we do not have satisfying answers yet. However, magnetic ignorance is our worst possible choice, because:

The larger our ignorance, the stronger the magnetic field.[2]

[1] This introduction was shamelessly inspired by the XXV Canary Island Winter School 'Cosmic Magnetic Fields'.
[2] Lodewijk Woltjer, Nordwijk Symposium, 1966

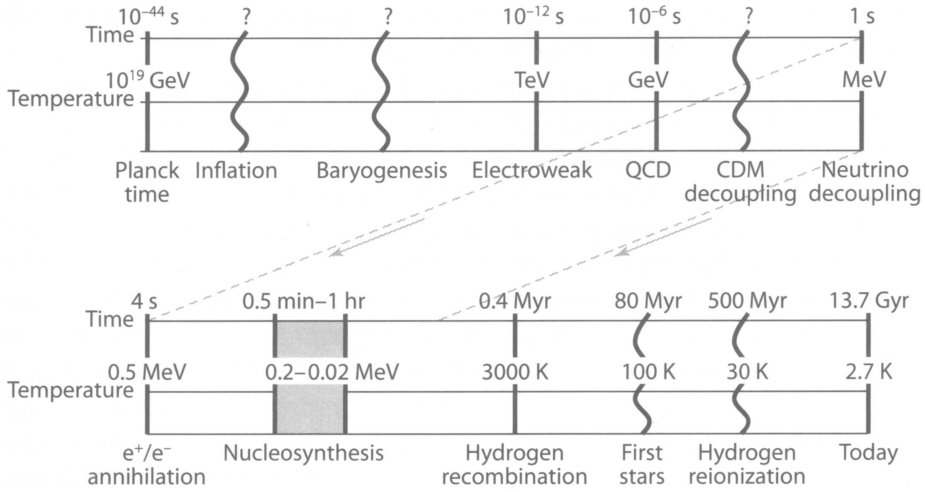

Figure 1: History of our Universe. Following inflation (a phase of rapid expansion), baryogenesis resulted in the observed asymmetry between matter and antimatter. Afterwards, the symmetry between electromagnetic and weak interactions was broken as well as protons and neutrons created during a quantum chromodynamic phase transition. Subsequently, dark matter and baryonic matter decoupled. Then, neutrinos escaped as well as electron-positron annihilation took place shortly before the first light elements were created during primordial nucleosynthesis. As hydrogen atoms later recombined and the radiation field decoupled, the cosmic microwave background was established. Last, with the formation of the first stars and galaxies the intergalactic medium got reionized. (Image taken from Loeb & Furlanetto (2012).)

Dark times and the first galaxies

This section is dedicated to overview the basic processes of dark structure formation in our Universe and, in particular, dark matter haloes. The modelling of the dark matter density field and the resulting gravitationally driven motions are an important cornerstone for a proper description of the evolution of cosmic and galactic magnetic fields. Over the past decades, thousands of textbooks and review articles have been written about the early Universe, the formation of structures and cosmology in general. In particular, the excellent and most recent textbooks of Binney & Tremaine (2008), Mo et al. (2010), Loeb (2010) and Loeb & Furlanetto (2012) greatly helped us to prepare this chapter. Unfortunately, within this thesis, we can only give a limited summary into the most interesting aspects.

The Universe is believed to have been created out of a singularity in spacetime, the Big Bang (see Fig. 1). At the beginning, the density and temperature were extraordinarily high and all four main forces as well as quantum mechanics and general relativity are expected to have been unified. However, on the most tiny scales, strong fluctuations in the energy E and time t according to the uncertainty principle of quantum mechanics must have been present

$$\Delta E \Delta t \geq \frac{\hbar}{2}. \tag{1}$$

Immediately afterwards, the Universe underwent a phase of rapid expansion called Inflation, during which the space expanded by several tens of e-foldings. The former energy perturbations then manifested into matter and radiation perturbations. As time passed and the Universe continued to expand

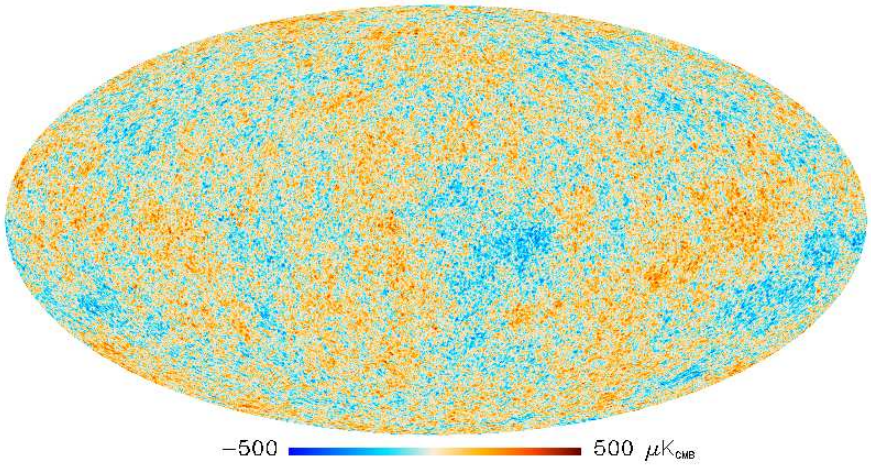

Figure 2: Combination temperature map of the cosmic microwave background. Shown are the temperature fluctuations after subtraction of the Milky Way's foreground emission. Although the distribution is almost homogenous, small-scale and large-scale fluctuations of the order of 10^{-5}, including both hot and cold spots can clearly be identified. Such observations contributed significantly in the establishment of the ΛCDM model as the present-day cosmological standard model. (Image taken from Planck Collaboration et al. (2013).)

and cool, the forces split and the first particles were created. Although the Universe became quickly dominated by matter, it was still very hot and fully ionized. Radiation and matter were coupled by electron-photon scattering. At a temperature of about $T \approx 3000$ K, the free electrons and protons recombined into hydrogen atoms and radiation and matter decoupled. At this point, the relic radiation, which we call the cosmic microwave background was established. The cosmic microwave background is nearly isotropic, however, small anisotropies give us one of the currently best pictures of the cosmological quantum fluctuations (see Fig. 2). These fluctuations formed the seed gravitational perturbations, which lead to todays structures. After the formation of the first stars and galaxies the Universe got reionized.

The homogenous Universe

The cosmological principle assumes the Universe to be homogenous and isotropic. Obviously, this principle cannot hold on small scales, but nevertheless, it is a good approximation on large scales. Then, for the Universe as a whole, we can describe space and time by the Robertson-Walker metric, which is given by

$$\mathrm{d}s^2 = c^2\mathrm{d}t^2 - a(t)^2\left[\frac{\mathrm{d}r^2}{1-kr^2} + r^2(\mathrm{d}\theta^2 + \sin^2\theta\mathrm{d}\phi^2)\right]. \tag{2}$$

Here, we use spherical spatial coordinates (r, θ, ϕ) and we assume the coordinates to be comoving with spacetime. The change of spatial scale with time is described by the dimensionless scalefactor $a(t)$. This cosmological scalefactor is usually constructed to range from $a(0) = 0$ at the time of the Big

Bang to $a(t_0) = 1$ at the present time t_0. The curvature parameter k determines the geometry of the Universe and can take values of $k < 0$ (open), $k = 0$ (flat) or $k > 0$ (closed).

Next, let us assume that the Universe can be described as an ideal fluid and its geometry is given by the Robertson-Walker metric. Then, Einstein's field equations of general relativity simplify into the Friedmann equations

$$\left(\frac{\dot{a}}{a}\right)^2 = \frac{8\pi G}{3}\rho - \frac{kc^2}{a^2} + \frac{\Lambda c^2}{3}, \tag{3}$$

and

$$\frac{\ddot{a}}{a} = -\frac{4\pi G}{3}\left(\rho + \frac{3p}{c^2}\right) + \frac{\Lambda c^2}{3}. \tag{4}$$

Here, G is the gravitational constant, c the speed of light, ρ the total density and Λ a cosmological constant. This cosmological constant acts like an energy density of the vacuum and leads to a negative pressure and a repulsive force acting opposite to gravity. The total pressure p is determined by an equation of state for the ideal fluid and might vary along cosmic time. We assume that the radiation field is no longer important. The contributions of matter, cosmological constant and curvature parameter can be described with the following set of standard cosmological parameters

$$\rho_c = \frac{3H_0^2}{8\pi G}, \qquad \Omega_M = \frac{\rho}{\rho_c}, \qquad \Omega_\Lambda = \frac{\Lambda c^2}{3H_0^2}, \qquad \Omega_k = -\frac{kc^2}{a_0^2 H_0^2}. \tag{5}$$

These parameters are assumed to be given at present time. Here, ρ_c is the critical density of the Universe and H_0 the present-day Hubble constant. The general Hubble function $H(a)$ gives the expansion rate of the space with cosmic scale or time and is given by

$$H(a) = \frac{\dot{a}}{a} = H_0\sqrt{\frac{\Omega_M}{a^3} + \Omega_\Lambda + \frac{\Omega_K}{a^2}}. \tag{6}$$

The age of the Universe can then be easily calculated to

$$\text{Age} = \int_0^1 \frac{da}{aH(a)}. \tag{7}$$

At the beginning of the 20th century, Edwin Hubble observed a systematic redshift in the emitted light of distant galaxies. The wavelength of light received on earth was redshifted by

$$z = \frac{\lambda_{\text{obs}} - \lambda_{\text{em}}}{\lambda_{em}}, \tag{8}$$

where λ_{obs} is the observed wavelength and λ_{em} the emitted restframe wavelength. He interpreted that distant galaxies must by systematically moving away from our Galaxy, because the space between the galaxies is expanding. The redshift z can be linked directly to the cosmological scalefactor $a(t)$ by

$$a(t) = \frac{1}{1 + z(t)} \tag{9}$$

and is of fundamental importance in modern astrophysics. The determination of the cosmological parameters and, in particular, of H_0, Ω_k, Ω_Λ and Ω_M, is the main goal of current high precision cosmology. Currently (see e.g. Komatsu et al., 2011; Planck Collaboration et al., 2013), the geometry of space is found to be flat ($\Omega_k = 0$) and the parameters are measured to be of the orders of $\Omega_M = 0.3$, $\Omega_\Lambda = 0.7$ and $H_0 = 70$ km s^{-1} Mpc^{-1}. If we ignore the radiation dominated phase, we see from equation (6) that at early times the Universe is dominated by matter and at late times by the cosmological constant (dark energy), which leads to an accelerated expansion of space. Furthermore, these

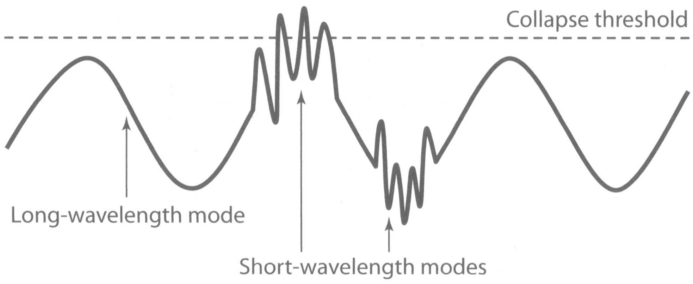

Figure 3: Simplistic model for halo formation and the evolving fluctuations within the primordial density field. The collapse threshold is shown as represented by the Press & Schechter (1974) model. Collapse takes place, where the superposition of long and short wavelength modes reaches the density threshold. This might also lead to dark matter halo clustering. (Image taken from Loeb & Furlanetto (2012).)

observations also indicate that the matter within the Universe is made up of a component of unknown nature, the dark matter, a special type of matter, which seems not to interact electromagnetically and which is assumed to be very cool. The Big Bang theory including dark energy, cold dark matter and inflation is the standard model of cosmology, the ΛCDM model.

The linear growth of density fluctuations

The small quantum fluctuations imprinted into the primordial matter density field do grow over time as they are subject to gravitational forces. The growth, which started as the Universe became dominated by matter, can be decomposed into a linear and a non-linear stage. To approximate the growth in the linear regime, let us consider a small perturbation of amplitude $|\delta| \ll 1$ in a Universe with an otherwise uniform matter density of $\bar{\rho}$. We can introduce comoving coordinates $\mathbf{x} = \mathbf{r}/a$ and also will use the assumption of an ideal fluid again. Furthermore, the fluid is moving with the Hubble flow $\mathbf{v} = H(t)\mathbf{r} = d\mathbf{r}/dt$ and the peculiar motions on top of the Hubble flow are expressed as $\mathbf{u} = \mathbf{v} - H\mathbf{r}$. If the actual matter density $\rho(\mathbf{r})$ varies from the mean density a local density perturbation results

$$\delta(\mathbf{r}) = \frac{\rho(\mathbf{r}) - \bar{\rho}}{\bar{\rho}}. \tag{10}$$

The continuity equation of the ideal comoving fluid is given by

$$\frac{\partial \delta}{\partial t} + \frac{1}{a}\nabla \cdot [(1+\delta)\mathbf{u}] = 0. \tag{11}$$

And the equation of motion (in this case the Euler equation) is given by

$$\frac{\partial \mathbf{u}}{\partial t} + H\mathbf{u} + \frac{1}{a}(\mathbf{u}\cdot\nabla)\mathbf{u} = -\frac{1}{a}\nabla\phi - \frac{1}{a\bar{\rho}}\nabla(\delta p), \tag{12}$$

with a pressure perturbation $\delta p = c_s^2 \delta\bar{\rho}$, which depends on the type of matter considered. For cold dark matter the pressure perturbation vanishes, but baryonic matter can very well carry a non-vanishing sound speed. The density perturbation also leads to a perturbated gravitational potential which can be described by the Newtonian Poisson equation

$$\nabla^2\phi = 4\pi G\bar{\rho}a^2\delta. \tag{13}$$

The linear approximation is valid as long as the perturbation is small. When the amplitude becomes large, i.e. $|\delta| \approx 1$, the linear theory breaks down. This can be associated with streams of matter crossing and colliding and thus triggering non-linear motions. By combining the preceeding equations we obtain an evolution equation for the perturbation δ with time of the form

$$\frac{\partial^2 \delta}{\partial t} + 2H\frac{\partial \delta}{\partial t} = 4\pi G\bar{\rho}\delta - \frac{c_s^2 k^2}{a^2}\delta. \tag{14}$$

In the case of cold dark matter (vanishing sound speed), this equation has only one growing solution with time, which is of the form

$$\delta(t) \sim D(t) \sim H(t)\int_0^t \frac{dt'}{a^2(t')H^2(t')}, \tag{15}$$

where $D(t)$ is the growth factor. This solution can be used all the way through the linear growth stage. From observations (see e.g. Loeb, 2010; Planck Collaboration et al., 2013) we know that the fluctuations in the CMB temperature are of the same order as the fluctuations in the gravitational potential of collapsed objects such as galaxy clusters. This can be understood if the fluctuations in the gravitational potential depth remained frozen into the matter since they were imprinted during inflation.

The nature of density fluctuations

Usually, the density field is expressed as a sum of periodic Fourier modes of wavenumber k, which can be written as

$$\delta_{\mathbf{k}} = \int d^3x \delta(x) e^{i\mathbf{k}\cdot\mathbf{x}}, \tag{16}$$

and

$$\delta(\mathbf{x}) = \int \frac{d^3k}{(2\pi)^3}\delta_{\mathbf{k}} e^{-i\mathbf{k}\cdot\mathbf{x}}. \tag{17}$$

In the linear regime, each mode will grow independently of each other with a factor of $D(t)$. However, the perturbation can vary across space and will be different on large and small scales. For a statistical analysis we define the correlation function

$$\xi(\mathbf{x}) = \langle \delta(\mathbf{x})\delta(0)\rangle, \tag{18}$$

and the power spectrum

$$P(\mathbf{k}) = \langle \delta_{\mathbf{k}}\delta^*_{\mathbf{k}'}\rangle = (2\pi)^3\delta^D(\mathbf{k}-\mathbf{k}')P(\mathbf{k}). \tag{19}$$

The correlation function and the power spectrum are intimately related by

$$\xi(\mathbf{x}) = \int \frac{d^3k}{(2\pi)^3} e^{i\mathbf{k}\cdot\mathbf{x}} P(\mathbf{k}). \tag{20}$$

From inflation theory it can be assumed that perturbations with different $\mathbf{k}$-modes are statistically independent. Then, the initial density field is a Gaussian random field described by the power spectrum $P(k)$, where $k = |\mathbf{k}|$ for an isotropic Universe. Furthermore, the initial power spectrum is assumed to be nearly scale-invariant, i.e. $P(k) \sim k$.

Last, we can normalize the power spectrum on a certain length or mass scale M. Firstly, we define a smoothing (or filter) function $W(\mathbf{r})$ such that $\int W(\mathbf{r})d^3r = 1$. Then, the variance $\langle \delta_M^2\rangle$ follows as

$$\sigma^2(M) = \int \frac{d^3k}{(2\pi)^3} P(k)\frac{|W_{\mathbf{k}}|^2}{V^2}. \tag{21}$$

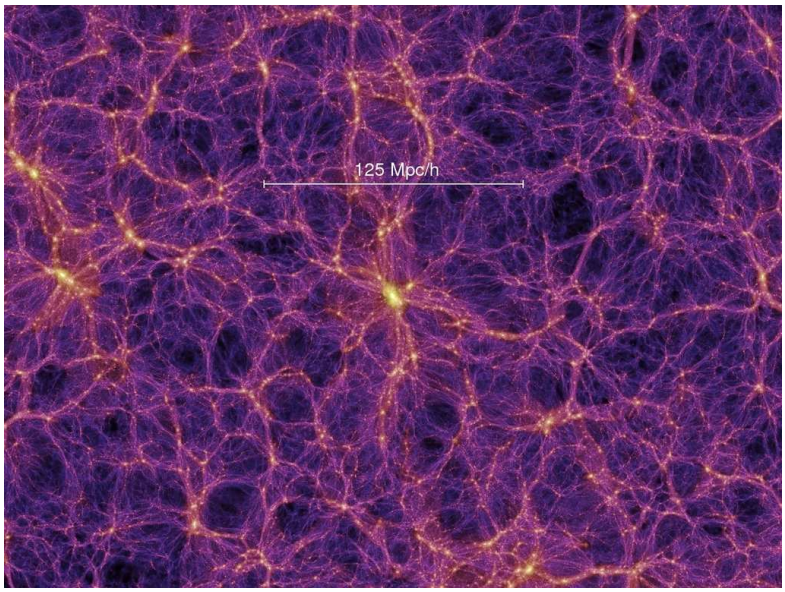

Figure 4: Millenium simulation at redshift zero. Shown is a 15 Mpc/h thick slice through the matter density field in one of the largest cosmological box simulations ever performed. Growth of the density and velocity perturbations from the cosmological initial conditions until today results in the formation of the Cosmic web. This simulations allows to follow the collapse into the non-linear regime and helps to study the formation of haloes, filaments, sheets and voids. (Image according to Springel et al. (2005c).)

The probability that different regions (with same size M) have a perturbation amplitude between δ and $\delta + d\delta$ is a Gaussian function with a zero mean and a variance $\sigma^2(M)$ of the form

$$p(\delta)d\delta = \frac{1}{\sqrt{2\pi\sigma^2}} e^{-\delta^2/2\sigma^2} d\delta. \tag{22}$$

A density perturbation will grow until it reaches the critical overdensity necessary for the collapse into a structure (see also Fig. 3). The density threshold for collapse depends on the collapse model and if linear or non-linear theory is considered. A popular choice is a spherical collapse model and a common density threshold is $\delta_{crit} = 18\pi^2$. If smoothed on a length scale of 8 Mpc, a typical value for the power spectrum normalisation is $\sigma \approx 0.8$ (see Komatsu et al., 2011; Planck Collaboration et al., 2013). However, as a Gaussian random perturbated density field has no symmetries in space, the collapse is rather ellipsoidal (see e.g. Sheth et al., 2001; Sheth & Tormen, 2002; Angrick & Bartelmann, 2010).

The Zel'dovich approximation and non-linear growth

The Zel'dovich approximation (Zel'dovich, 1970) is a good and basic concept to easily understand the formation of the present-day large-scale structure. Over the past decades, many all-sky surveys (see e.g. the Sloan Digital Sky Survey by Abazajian et al., 2003) have revealed the organization of the large-scale structure into a 'Cosmic web', which consists of pancakes, filaments and haloes of matter. Let us consider a particle at an initial position $\mathbf{q}$ in space and provided that the Universe was purely homogeneous its later position would be $\mathbf{r}(t) = a(t)\mathbf{q}$. However, small perturbations in the density

field are present, which we want to express with a displacement function $\mathbf{p}(\mathbf{q})$. In the linear or mildly non-linear regime we can assume the displacements to be given by the initial density field and thus the initial gravitational potential field. Then, the later position can be expressed as

$$\mathbf{r}(t) = a(t)\left[\mathbf{q} + b(t)\mathbf{p}(\mathbf{q})\right], \tag{23}$$

where b(t) is a function describing the growth of displacements with time. Strictly speaking, the displacements do not only grow with time, but also change their spatial direction with time. This spatial change is ignored in the Zel'dovich approximation. $\mathbf{q}$ are Lagrangian coordinates representing individual mass cells. Conservation of mass in the Lagrangian framework demands $\rho(\mathbf{r},t)d^3\mathbf{r} = \bar{\rho}d^3\mathbf{q}$. Then, the Jacobian transformation gives

$$\rho(\mathbf{r},t) = \bar{\rho}\det(\partial q^i/\partial r_j) = \frac{\bar{\rho}(t)}{\det\left[\delta_{ij} + b(t)(\partial p_j/\partial q_i)\right]}, \tag{24}$$

and to first order in $b(t)\mathbf{p}(\mathbf{q})$, the density perturbation δ is given by

$$\delta = -b(t)(\nabla_{\mathbf{q}} \cdot \mathbf{p}). \tag{25}$$

After transforming the density field into Fourier space and separating the time dependence equation (24) can be rewritten in the following form

$$\rho(\mathbf{r},t) = \frac{\bar{\rho}(t)}{\left[1 - b(t)\lambda_1(\mathbf{q})\right]\left[1 - b(t)\lambda_2(\mathbf{q})\right]\left[1 - b(t)\lambda_3(\mathbf{q})\right]}. \tag{26}$$

This result can be interpreted easily if $\lambda_{1,2,3}$ are understood to be the eigenvalues of some gravitational stress tensor, which defines the tidal stress at each location in space. These eigenvalues give the speed of deformation along the three principal axis. The sign of each of the eigenvalues determines whether collapse or expansion occurs along each axis. Firstly, collapse of matter will proceed along the axis with the largest eigenvalue and result in the formation of a pancake. Secondly, collapse will proceed along the axis with the second largest eigenvalue and result in the formation of a filament. Thirdly and last, collapse will proceed along the axis with the smallest eigenvalue and result in the formation of a halo. The strength of the Zel'dovich approximation lies in the fact that it can still be used in the mildly non-linear regime. However, when streams of matter are crossing, the approximation breaks down and the resulting non-linear structure formation is best studied by numerical simulations (see Fig. 4). The Zel'dovich approximation is a common method to follow the linear collapse from the earliest times until the starting time of the numerical simulations and is often used to create initial conditions.

The emergence of stars and galaxies

We continue with the basic processes of visible structure formation in our Universe and, in particular, within galaxies. The modelling of the baryonic matter density field and the associated processes of gas cooling and stellar feedback also are important cornerstones for a proper description of the evolution of cosmic and galactic magnetic fields. Fig. 5 presents a diagram visualizing the main paths of galaxy formation. The baryonic matter content of the Universe falls into the potential wells of the dark matter structures, where it forms gaseous clouds. The gas clouds contract by gravity on a timescale, which is well approximated by the free fall time

$$\tau_{\mathrm{ff}} = \frac{1}{4}\sqrt{\frac{3\pi}{2G\rho}}. \tag{27}$$

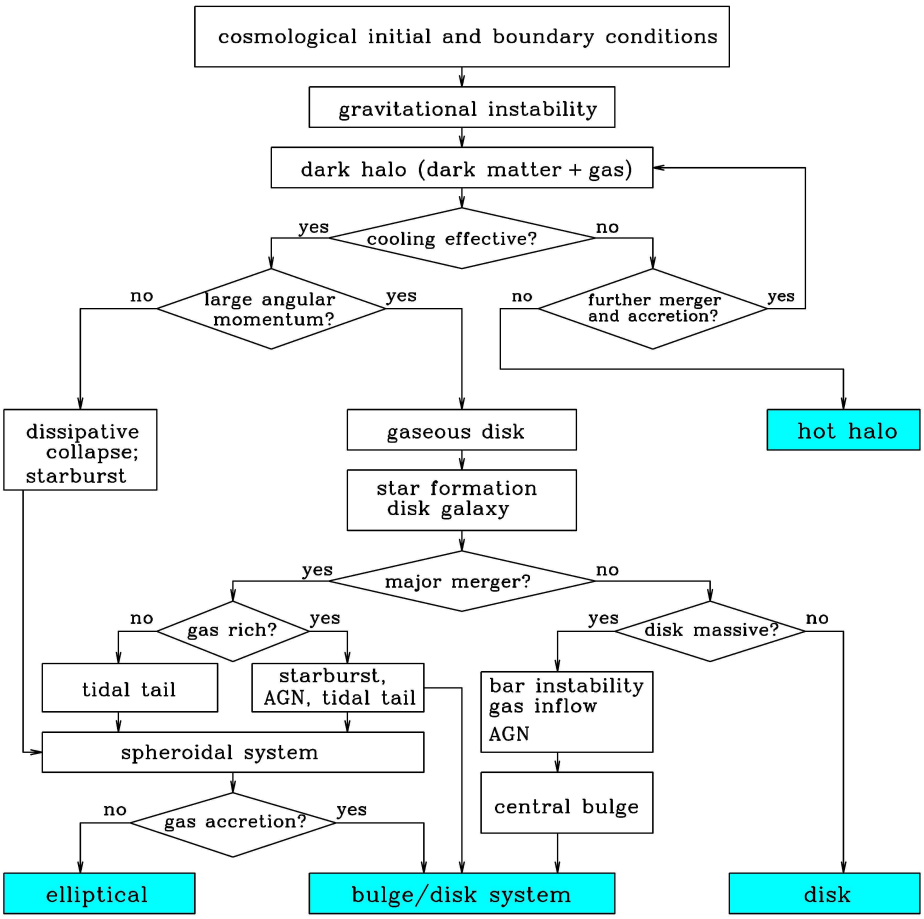

Figure 5: Flow chart for galaxy formation. Shown are the paths which lead from the cosmological initial conditions to the formation of galaxies. Several highly non-linear and coupled physical processes are responsible for the different galactic outcomes. (Image taken from Mo et al. (2010).)

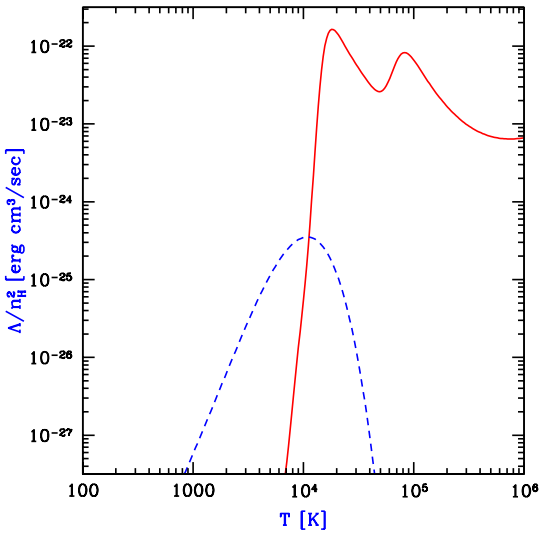

Figure 6: Volume cooling rates as a function of temperature. The solid line shows the cooling curve for a primordial atomic gas (76 per cent hydrogen and 24 per cent helium). The dashed line shows the cooling curve for H_2 , with an abundance of one per cent. The formation of H_2 is essential for high densities and the formation of the first stars. (Image taken from Barkana & Loeb (2001).) Additional molecules and metals make the cooling even more efficient at low and high temperatures (not shown).

However, the gas also carries non-vanishing thermal, turbulent and magnetic pressures, which counteract gravity and prevent collapse. The Jeans criterion

$$M_{\rm J} = \frac{\pi}{6} \frac{c_s^3}{G^{3/2}\rho^{1/2}} \tag{28}$$

is a common quantity to determine if a cloud with a stabilizing characteristic intrinsic speed c_s is able to collapse under its own gravity. If the cloud is not dense enough, or the pressures are too high, the collapse is prevented. However, within the (partly) ionized gas, protons and electrons are frequently interacting with each other and produce radiation. These radiative cooling processes allow the gas to loose energy, cool to low temperatures and reach high densities on a timescale of

$$\tau_{\rm cool} = \frac{3}{2} \frac{nkT}{n^2\Lambda}, \tag{29}$$

where Λ is the cooling function. The cooling function gives the energy loss with time and it depends on the gas composition, ionization degree, density and temperature (see also Fig. 6). The gas cools by either excitation, ionization or recombination of atoms or simply by free-free emission (thermal bremsstrahlung). A primordial gas can only cool to temperatures of about 10^4 K. Hence, for further collapse and the formation of stars it is necessary to have molecules or metals providing additional cooling channels. For the very first stars, it is essential to form molecular hydrogen (H_2) by

$$H + e^- \longrightarrow H^- + \gamma, \tag{30}$$

and

$$H^- + H \longrightarrow H_2 + e^-. \tag{31}$$

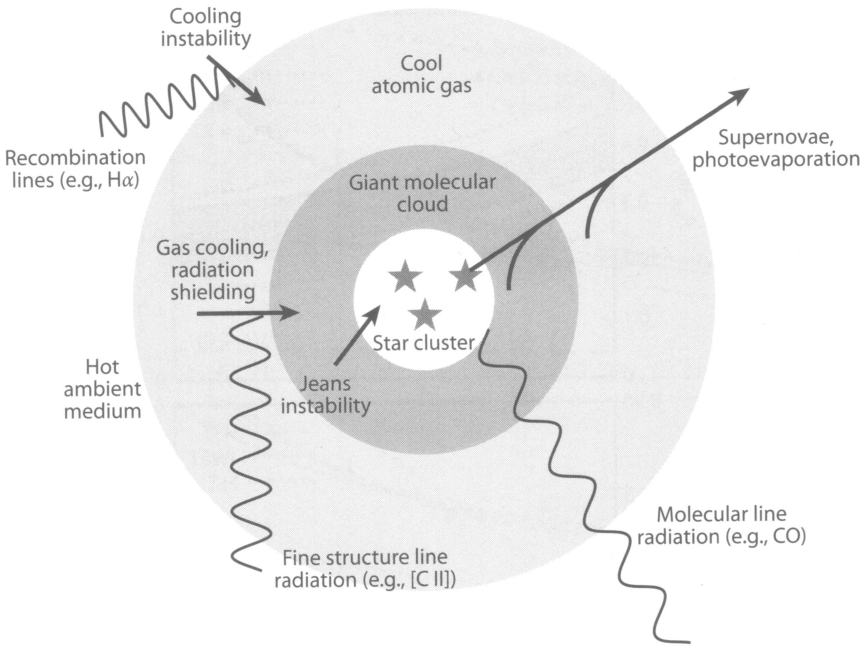

Figure 7: Baryon flows in the interstellar medium. The multiphase interstellar medium is a hot, ambient medium surrounding cold gas clouds, which form when thermal instabilities allow the gas to cool locally. The cooling depends on the gas composition and thus on the density and temperature and on the local amount of molecules and metals. Subsequently, gravitationally unstable regions will collapse and form stars, which then return gas and energy into the ambient medium by feedback processes. (Image taken from Loeb & Furlanetto (2012).)

This molecule can also loose energy via vibrations, allowing the gas to cool to very low temperatures and trigger the run-away collapse of the gas cloud. As stars are born, they give energy back into the surrounding gas by radiation, winds or SN. This leads to a baryonic cycle within the multi-phase interstellar medium (McKee & Ostriker, 1977) of cold, warm and hot gas (see Fig. 7). The baryonic structures are mainly located at intersections of the cosmic web. Dekel et al. (2009) find that streams of cold gas are penetrating to the center of dark matter haloes and are feeding the baryonic structures. With the formation of the first stars, the first protogalaxies appear. In a hierarchical bottom-up process of protogalactic merger events, the present-day galaxies have formed.

Cosmic and galactic magnetic fields

Cosmic magnetic fields are an interesting topic, because magnetic fields are observed in nearly all astrophysical environments. They are present within the smallest planetary moons as well as the largest cosmological voids (see Table 1). Within normal stars, magnetic fields of several hundreds of Gauss are generated by movements of charged particles and dynamo processes. As the stars turn into SN, the magnetic field is compressed into the stellar remnants leading to high field amplitudes within white dwarfs or neutron stars. On interplanetary, interstellar, intragalactic or intracluster scales the magnetic fields could be the result of a complex interplay of stellar or galactic winds, radiation

Observed Magnetic Fields				
Remnants	$10^3 - 10^4$	km	$< 10^{-6}$	G
Planets	$10^4 - 10^5$	km	$10^{-1} - 10^0$	G
Normal Stars	$10^6 - 10^7$	km	$10^1 - 10^3$	G
White Dwarfs	$\approx 10^3$	km	$10^5 - 10^7$	G
Neutron Stars	$\approx 10^1$	km	$10^9 - 10^{18}$	G
Interplanetary	$10^{-9} - 10^{-8}$	kpc	$10^1 - 10^2$	μG
Interstellar	$10^{-3} - 10^{-2}$	kpc	$10^0 - 10^3$	μG
Intragalactic	$10^{-1} - 10^1$	kpc	$10^0 - 10^3$	μG
Intracluster	$10^2 - 10^4$	kpc	$10^{-1} - 10^1$	μG
Extragalactic	$10^3 - 10^5$	kpc	$10^{-9} - 10^{-3}$	μG

Table 1: Observed magnetic field strengths for various astrophysical objects. The length scale ranges over more than 20 orders of magnitude from objects as small as neutron stars up to the largest voids. The associated magnetic field strengths even range over more than 30 orders of magnitude. (Data taken from Vallée (2011a) and Vallée (2011b).)

processes, SN, CR, shocks or turbulence. Most excitingly, up to now, the nature of the extragalactic magnetic fields is not known.

Observing magnetic fields within astrophysical environments is a difficult and dirty business. We do not want to go into details about the observational methods and, at this point, refer to the extensive literature (see e.g. Rybicki & Lightman, 1979; Zel'dovich et al., 1983; Rohlfs & Wilson, 2004; Grupen, 2005; Longair, 2010). The magnetic fields cannot be observed directly and, instead, their impact on radiation processes has to be considered in order to estimate the amplitudes and structures of the magnetic fields. The Zeeman-effect can be used to observe strong magnetic fields, as the energy levels of atoms split up in the presence of magnetic fields. The splitting of the energy levels leads to an associated splitting of the spectral emission or absorption lines. Unfortunately, the Zeeman-effect only works well for molecular clouds or stars, where very strong magnetic fields are present. It is not useful to determine magnetic fields within galaxies or beyond as the Zeeman shifts are small compared to Doppler broading of lines caused by thermal motions. Furthermore, magnetic fields could be detected via observations of polarized stellar light, when it scatters of elongated dust grains, which might be aligned along a magnetic field (Davis & Greenstein, 1951). However, the unknown properties of the dust grains and the effects of anisotropic scattering make this effect of little use for the determination of magnetic fields in space.

The most important source of information about magnetic fields in astrophysics is non-thermal power-law distributed polarized synchrotron radiation of relativistic electrons gyrating around magnetic field lines (see Fig. 8). Whenever snychrotron radiation is detected, magnetic fields must be present. The (see Shukurov, 2007) total I and polarized P synchrotron intensities and the Faraday rotation measure RM are weighted integrals of magnetic field along the line of sight L from the source to the observer

$$I = K_0 \int_L n_{\rm cr} B_\perp^2 \, dl, \tag{32}$$

$$P = K_0 \int_L n_{\rm cr} \overline{B}_\perp^2 \, dl, \tag{33}$$

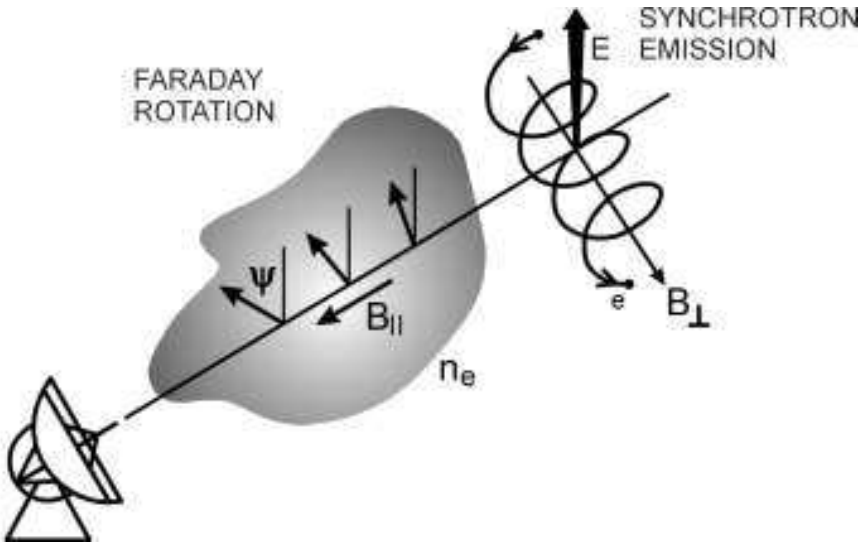

Figure 8: Synchrotron emission and Faraday rotation. Relativistic charged particles gyrating around magnetic fields lines emit polarized synchrotron radiation. The polarization of the radiation, when travelling towards an observer, can be rotated by intervening magnetized gas (Faraday-effect). These methods are commonly used to detect magnetic fields within astrophysical gas environments. (Image taken from Beck & Wielebinski (2013).)

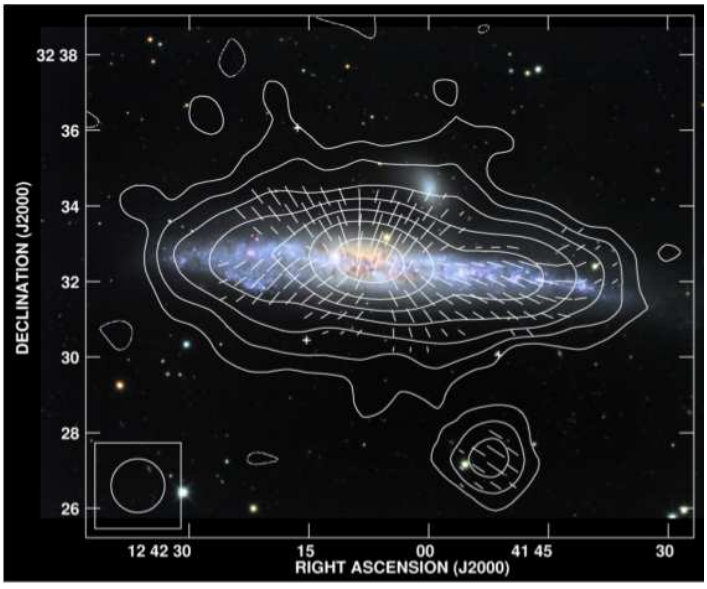

Figure 9: Radio continuum emission of NGC 4631 at 3.6 cm (8.35 GHz). The contours represent the total intensity and the arrows the magnetic field vectors. In the background is an optical image. The magnetic field extends far outside the galaxy into the galactic halo. (Image taken from Krause (2009).)

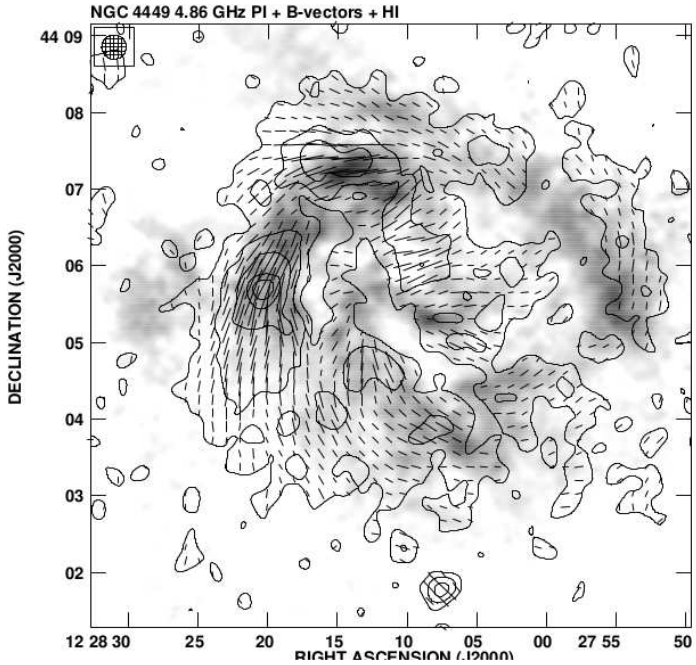

Figure 10: Radio continuum emission of NGC 4449 at 6.2 cm (4.86 GHz). The contour levels represent the polarized intensity and are (3, 10, 20, 30, 35) × 5.4 μJy. In the background is a HI column density map. Magnetic fields are an intrinsic property of astrophysical gas environments. (Image taken from Chyży et al. (2000).)

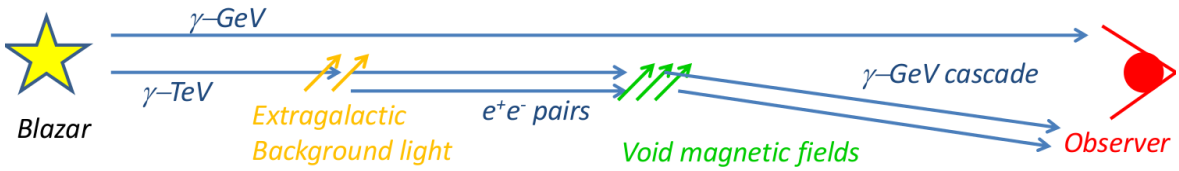

Figure 11: Method to indirectly constrain magnetic fields in voids. γ-TeV photons produced by distant Blazars create e^+/e^- pairs when interacting with the extragalactic background light. These pairs produce detectable GeV cascade emission, but if void magnetic fields are present, the pairs are deflected and the cascade emission is not detected. This indirect method allows to constrain magnetic fields in voids to be $\geq 10^{-15}$ G.

$$RM = K_1 \int_L n_\mathrm{e} B_\parallel dl, \tag{34}$$

where n_cr is the relativistic electron (CR) density, n_e the thermal electron density and $K_{0,1}$ are dimensional constants. These integrals provide an average measure of the magnetic field within the emitting or magneto-active volume. The total magnetic field $\mathbf{B} = \overline{\mathbf{B}} + \mathbf{b}$ is made up of a regular $\overline{\mathbf{B}}$ and random $\mathbf{b}$ component such that $\langle \mathbf{B} \rangle = \overline{\mathbf{B}}$, $\langle \mathbf{b} \rangle = 0$ and $\langle B^2 \rangle = B^2 + \langle b^2 \rangle$.

With the assumption of equipartition between the energy density of the magnetic field and the energy density of the CR, the magnetic field amplitude can be estimated by

$$\frac{B^2}{8\pi} \sim a \int EN(E)dE, \tag{35}$$

where a is the quotient of CR energy to electron energy. We have also assumed an isotropic power-law distribution of the electron energy of the form

$$N(E)dE \sim E^{-x}dE, \tag{36}$$

where $N(E)dE$ can be associated to the CR density n_cr. For an emitting gas in pressure equilibrium between turbulent, CR and magnetic pressure and if the only type of energy loss is the escape of particles, an exponent of $x = -2.5$ follows (Syrovatskii mechanism, see e.g. Longair, 2010). If the electron energy is given by a power-law, then the observed synchrotron intensity must be a power-law, too. The typical spectral index is $\alpha = (x-1)/2$. Furthermore, the value of the RM depends on the direction of the magnetic field lines and thus, can be used, if n_e is known, to obtain a three-dimensional picture of the magnetic field structure.

Observations (again, see the extensive literature and e.g. Hummel, 1986; Klein et al., 1988; Fitt & Alexander, 1993; Kronberg, 1994; Beck et al., 1996; Widrow, 2002; Chyży et al., 2003; Beck, 2007; Chyży et al., 2007; Kulsrud & Zweibel, 2008; Beck, 2009; Vallée, 2011a,b) of magnetic fields within the cosmic gas are usually performed in the radio frequency range (3 kHz to 300 GHz). Within typical galaxies (see Figs. 9 and 10), these observations reveal the existence of a regular magnetic field of the order of one μG and a total magnetic field of the order of ten μG. Synchrotron radiation is usually detected from regions where also optical emission is detected and the magnetic field structure usually follows the gas structure. However, for example, within spiral galaxies, magnetic spiral arms, which are displaced from the optical spiral arms, can sometimes be found. Furthermore, magnetic fields are also found outside the galaxies within the galactic haloes or within the gas of galaxy clusters.

Additionally, RM observations allow to constrain magnetic fields at high redshifts or within regions, where no intrinsic synchrotron emission originates. In particular, some galactic structures at $z > 2$ are found to host intrinsic RM values of several 1000 rad m^{-2}, which corresponds to very dense and highly magnetized gaseous regions (see e.g. Athreya et al., 1998). Furthermore, extragalactic magnetic fields can be indirectly constrained by observations of the TeV and GeV emission of distant blazars (for an illustration see Fig. 11). Using this method, Neronov & Vovk (2010) reported a lower limit of $\approx 10^{-15}$ G on extragalactic magnetic fields.

Summing up, magnetic fields seem to be everywhere within the Universe (see also Table 1). So far, we do not completely understand the origin and evolution of these fields. In particular, the evolution of the magnetic fields within galaxies is influenced by the evolution of the galaxies themselves. Thus, it is very interesting to study the evolution of magnetic fields during the formation of structure and galaxies by theoretical models and numerical simulations.

Theoretical magnetic field dynamics

This section is dedicated to overview the basic theoretical processes of magnetic field evolution. A plasma is a (partly) ionized gas and it is well described by a distribution function $f(\mathbf{x}, \mathbf{v}, t)$, which

is evolved in time by the Fokker-Planck equation. However, if the microscopic mean free path of the gaseous particles is small compared to the macroscopic dimensions of the gas, we can use the methods of continuum mechanics. Furthermore, the kinetic contribution of electrons is much smaller than the kinetic contribution of protons and we can describe the gas as a single-particle fluid. For a magnetized plasma we can combine hydrodynamics and electrodynamics into magnetohydrodynamics (MHD). The excellent textbooks and review articles of Alfven (1950), Spitzer (1965), Frank-Kamenezki (1967), Jackson (1975), Kippenhahn & Moellenhoff (1975), Parker (1979), Shu (1992), Brandenburg & Subramanian (2005) and Kulsrud (2005) greatly helped us to prepare this section.

Magnetohydrodynamics

In electrodynamics, the evolution of electric **E** fields and magnetic **B** fields is given by the four famous Maxwell equations

$$\nabla \times \mathbf{E} = -\frac{1}{c}\frac{\partial \mathbf{B}}{\partial t}, \tag{37}$$

$$\nabla \times \mathbf{B} = \frac{4\pi}{c}\mathbf{j} + \frac{1}{c}\frac{\partial \mathbf{E}}{\partial t}, \tag{38}$$

$$\nabla \cdot \mathbf{E} = 4\pi\rho_e, \tag{39}$$

$$\nabla \cdot \mathbf{B} = 0, \tag{40}$$

where c is the speed of light, $\mathbf{j}$ the electric current and ρ_e the electric charge density. Together with Ohm's laws (σ is the electric conductivity)

$$\mathbf{j} = \sigma\left[\mathbf{E} + \frac{1}{c}(\mathbf{v} \times \mathbf{B})\right], \tag{41}$$

they form a full set of equations for the evolution of electric and magnetic fields. If we assume that electric fields are weak compared to magnetic fields, i.e. $\mathbf{E} \ll \mathbf{B}$, we can neglect the electric displacement current and derive the induction equation of MHD easily

$$\frac{\partial \mathbf{B}}{\partial t} = \nabla \times \left[\mathbf{v} \times \mathbf{B} - \frac{c^2}{4\pi\sigma}(\nabla \times \mathbf{B})\right], \tag{42}$$

where the term $c^2/4\pi\sigma$ is also often called magnetic resistivity η. This resistivity is responsible for changes in the topology of the magnetic field, such as mergers of field lines. In the limit of infinite conductivity, the magnetic resistivity vanishes and the magnetic field is said to be perfectly frozen into the plasma. However, often a turbulent resistivity η_T is used to model topology changes by kinetic motions (on the physics of magnetic reconnection see e.g. Priest & Forbes, 2007). The induction equation is the fundamental evolution equation for cosmic magnetic fields and it is obvious that the correct evolution of the magnetic field depends on an accurate velocity field.

From the induction equation we see that if no magnetic field is initially present, no magnetic field will ever be generated or evolved in time given the preceeding limits of MHD. This seed field problem is usually adressed in two ways. The first solution is the assumption of an arbitrary global seed field function depending on the initial plasma properties of the form

$$\mathbf{B}_{\rm seed} = f\left[\mathbf{x}_0, \mathbf{v}_0, T_0, \rho_0, ...\right]. \tag{43}$$

The second solution is the addition of a time-dependent local magnetic seeding function to the induction equation of the form

$$\left.\frac{\partial \mathbf{B}}{\partial t}\right|_{\rm seed} = g\left[\mathbf{x}(t), \mathbf{v}(t), T(t), \rho(t), ...\right]. \tag{44}$$

In either case, the seed field must be constructed without divergence. If we consider a plasma containing both electrons and protons, the different mobilities of the electrons and of the protons lead to different distributions of the associated density and pressure fields. Then, when using a more general form of Ohm's law and if the electron density (n_e) gradient is not parallel to the electron pressure (p_e) gradient, a seeding term of the form

$$\frac{\partial \mathbf{B}}{\partial t} = -\frac{c}{e}\left(\nabla n_e \times \nabla p_e\right) \tag{45}$$

can be derived. This is often also called the Biermann battery and a common assumption of the magnetic seed field origin. Especially, within shocks, the density and pressure gradients might not be parallel, which results in battery effects and magnetic fields are generated. As Wiechen et al. (1998) show, the friction between ionized and neutral gas components can also generate magnetic seed fields. Furthermore, a large variety of global magnetic seeding mechanisms exists and at this point we refer to the extensive review literature (see e.g. Kronberg, 1994; Beck et al., 1996; Widrow, 2002; Kulsrud, 2005; Kulsrud & Zweibel, 2008; Widrow et al., 2012). Basically, the global magnetic seed fields could be the result of any evolutionary epoch of cosmic time and the local magnetic seed fields can be generated by structures such as stars or black holes and the corresponding feedback onto the gas.

The induction equation together with the continuity equation

$$\frac{\partial \rho}{\partial t} + \nabla \cdot (\rho \mathbf{v}) = 0, \tag{46}$$

an equation evolving the specific energy ϵ

$$\rho\left(\frac{\partial \epsilon}{\partial t} + (\mathbf{v}\cdot\nabla)\epsilon\right) = -p(\nabla\cdot\mathbf{v}) + \mathcal{H} - \mathcal{L}, \tag{47}$$

which includes heating ($\mathcal{H}$) and cooling ($\mathcal{L}$) functions modelling radiative processes within the gas and an equation of motion containing the pressure force, the gravitational force, the Lorentz force and in the absence of viscosity of the standard form

$$\rho\left(\frac{\partial \mathbf{v}}{\partial t} + (\mathbf{v}\cdot\nabla)\mathbf{v}\right) = -\nabla p - \rho\nabla\phi + \frac{c}{4\pi}(\nabla\times\mathbf{B})\times\mathbf{B}, \tag{48}$$

together with an equation of state $p = p(\rho, \epsilon)$, form the full set of standard MHD equations for the macroscopic plasma quantities $\mathbf{x}$, $\mathbf{v}$, $\mathbf{B}$, ρ and p.

We have ignored the redistribution of specific energy by anisotropic thermal conduction and the dissipation of kinetic or magnetic energy into heat by viscous or resistive processes. The importance of radiative heating and cooling is such that changes in the specific energy will result in pressure and hence velocity changes and then affect the magnetic field evolution. Furthermore, the velocity field is also affected by the gravitational interactions, which are dominated by the dark matter content of the Universe. Hence, modelling the dynamics of the dark matter density field and modelling the radiative processes of the baryonic density field are essential for a proper evolution of the magnetic field. Summing up, the evolution of the magnetic field is a non-linear interplay of many microscopic and macroscopic processes and highly coupled to the entire set of physics of structure and galaxy formation. Such complex systems can only be studied with numerical simulations.

Let us take a closer look at the form of the Lorentz force. We split the vector product and obtain

$$\mathbf{j}\times\mathbf{B} \sim (\nabla\times\mathbf{B})\times\mathbf{B} = (\mathbf{B}\cdot\nabla)\mathbf{B} - \nabla\left(\frac{\mathbf{B}^2}{2}\right). \tag{49}$$

The first term on the right hand side is called 'magnetic tension force', which corresponds to minimizing the length of magnetic field lines. The second term on the right hand side is called 'magnetic pressure

force', which corresponds to maximizing the distance between neighbouring field lines. The plasma parameter

$$\beta = \frac{p_{\rm thermal}}{p_{\rm magnetic}} \tag{50}$$

is commonly used to study the importance of magnetic fields in a plasma. In the case of a low β the plasma is dominated magnetically and in the case of a high β the plasma is dominated thermally. Waves within a plasma can be sonic, Alfvénic or even a combination of both and the most general form of the wave phase velocity (see e.g. Kulsrud, 2005) is given by

$$v_{ph}^2 = \frac{1}{2}\left(v_a^2 + c_s^2 \pm \sqrt{(v_a^2 + c_s^2)^2 + 4c_s^2 v_a^2 \sin(\theta)}\right). \tag{51}$$

Here, $c_s^2 = \gamma p/\rho$ is the sound speed for a gas with adiabatic index of γ and $v_a^2 = \mathbf{B}^2/4\pi\rho$ the Alfvén speed. These characteristic speeds are commonly used to derive typical timescales of plasma processes or model diffusion coefficients.

The evolution of the magnetic energy

The induction equation without resistivity and the continuity equation can be combined into a single equation evolving the magnetic field over density with time

$$\frac{d}{dt}\left(\frac{\mathbf{B}}{\rho}\right) = \frac{1}{\rho}\nabla(\mathbf{B}\cdot\mathbf{v}). \tag{52}$$

Obviously, changes in the density result in changes of the magnetic field. The precise evolution of the magnetic field with density depends on the geometry of the density changes (direction of the compression or expansion). The magnetic energy increases only when magnetic field lines are brought closer to each other and not when the length of the field lines is changed. Hence, three different cases can be distinguished. Firstly, when the density changes proceed perpendicular to the magnetic field lines, only the spacing between field lines is changed and from equation (52) we find $\mathbf{B}^2 \sim \rho^2$, with an effective adiabatic index for the magnetic pressure of $\gamma = 2$. Secondly, when the density changes proceed parallel to the magnetic field lines, only the length of the lines is changed and we expect no changes in the magnetic energy and from equation (52) we find $\mathbf{B}^2 \sim$ const, with an effective adiabatic index for the magnetic pressure of $\gamma = 0$. Thirdly, when the density changes are spherically symmetric and isotropic, we expect a mixed behaviour of the above other two cases and from equation (52) we find $\mathbf{B}^2 \sim \rho^{4/3}$, with an effective adiabatic index for the magnetic pressure of $\gamma = 4/3$. As the collapse of matter within our Universe, or the expansion of the Universe itself, can be approximated to be spherically symmetric, the isotropic case is the most important case. The amplification by compression is also commonly occuring during the cooling of gas or in shocks.

Furthermore, the process of structure formation causes rapid changes in the gravitational potential of the matter density field, which lead to fluctuations in the corresponding velocity field. Additionally, the baryonic physics of galaxy formation also cause fluctuations in the velocity field. These fluctuations are commonly called random motions. However, we can also call them turbulent motions, if their energy spectrum shows a characteristic decreasing power law between a large injection scale and a small viscous dissipation scale. Turbulence (see e.g. Kolmogorov, 1941; Landau & Lifshitz, 1959; Kraichnan, 1965) is also an intrinsic property of astrophysical environments. It can be understood in terms that, at first, one large turbulent eddy is present. This eddy then breaks up into smaller and smaller eddies, until the dissipation scale is reached. On the dissipation scale, the kinetic energy is transferred into thermal energy. Furthermore, the smallest turbulent eddies turn over the fastest.

The Reynolds number (Reynolds, 1895) is commonly used to characterize turbulence

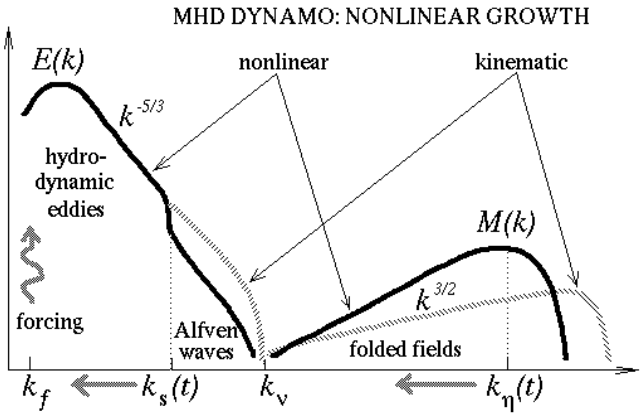

Figure 12: Kinetic and magnetic energy spectra in the non-linear MHD dynamo growth phase. Given a turbulent kinetic energy spectrum and a magnetic Prantl number larger than one, the turbulent eddies will turn over the fastest on the viscous scale and amplify the magnetic field. The growth of the magnetic energy occurs on the dissipation scale first. (Image taken from Schekochihin et al. (2004).)

$$\mathrm{Re} = \frac{\text{inertial forces}}{\text{viscous forces}} = \frac{v_T l_T}{\nu}, \tag{53}$$

where v_T and l_T are characteristic velocity and length scales and ν is the viscosity coefficient.

Now, imagine a magnetic field within a turbulent fluid and a resistivity scale smaller than the viscous scale (i.e. a magnetic Prantl number $\mathrm{Pr} = \nu/\eta \gg 1$). Furthermore, we assume a weak magnetic seed field and the magnetic pressure is lower than the turbulent pressure. Then, obviously, the turbulent motions affect the magnetic field evolution and, in particular, are able to increase the magnetic energy by conversion of kinetic energy (for pioneering work see Batchelor, 1950, 1953). The evolution of the magnetic field amplitude with time can be described by an exponential growth process

$$\frac{\partial}{\partial t}|\mathbf{B}| = \gamma|\mathbf{B}|, \tag{54}$$

where $\tau = 1/\gamma$ is a characteristic amplification timescale. For example, this timescale can correspond to the free fall time, the cooling time or the turnover time of the smallest turbulent eddies. As the turbulent eddies are turning over, the magnetic field lines are stretched, twisted and folded (see e.g. Zel'dovich et al., 1983). As the magnetic field lines are brought closer to each other, the magnetic energy increases. Astrophysical systems tend to evolve towards thermodynamical equilibrium. This implies the amplification to truncate when equipartition between the magnetic energy density and the turbulent energy density

$$\frac{B^2}{8\pi} = \frac{1}{2}\rho v_T \tag{55}$$

is reached and the dynamo saturates. Figs. 12 and 13 show the evolution of a magnetic energy spectrum in the presence of a given and driven turbulent energy spectrum. The amplification also truncates when the timescales of dissipative processes become smaller than the timescales of amplifying processes. Then, after saturation, the magnetic energy is transferred from small to large scales and also eventually decays. The small-scale or turbulent dynamo is the most important and fastest amplification process in the context of structure and galaxy formation.

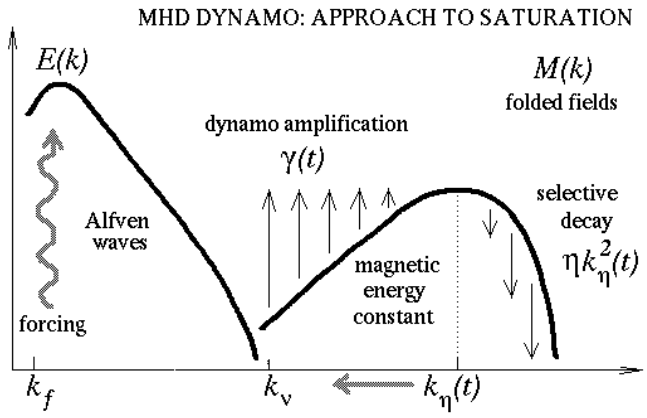

Figure 13: Kinetic and magnetic energy spectra in the non-linear MHD dynamo saturation phase. The magnetic energy has saturated and while it remains conserved, it is transported from small scales to large scales by dissipative processes, i.e. the wound-up magnetic field is unfolded and ordered. (Image taken from Schekochihin et al. (2004).)

Open questions of cosmic magnetism

At the end of this introduction we want to summarize the most important and open questions of cosmic magnetism (see also the reviews Kronberg, 1994; Beck et al., 1996; Widrow, 2002; Kulsrud & Zweibel, 2008; Vallée, 2011a,b). From observations we know that magnetic fields are present within all types of galaxies, within the gas between galaxies and even in the voids. In fact, at present, there is no null detection of magnetic fields within collapsing or virialized systems. Magnetic fields are an intrinsic property of astrophysical systems. The origin, time evolution and spatial evolution of these magnetic fields is speculative, however, the entire problem could be decomposed into three (each not less challenging) sub-problems.

- **The creation of magnetic seed fields:** In the limits of ideal MHD, no magnetic field will ever be evolved, where no magnetic field is initially present. Hence, magnetic seed fields need to be created, which will require the assumptions of MHD to break down. Firstly, the magnetic seed field could be a direct consequence of the BigBang, giving rise to a large zoo of very exotic, cosmological mechanisms of ranging popularity. Secondly, the magnetic seed fields could have been created primordially, i.e. after the BigBang, but before the first generation of stars and galaxies formed. Here, battery processes are most popular, which occur if charges are separated or if there is friction between neutral and (partly) ionized gas components. Thirdly, the magnetic seed fields could be generated locally by SN or AGN and then be later spilled into the surrounding gas. None of these mechanisms will be ever working alone, but at different epochs in time and regions of space, all of them are operating during structure formation increasing the theoretical complexity significantly. Within this thesis, Chapter 2 contributes to the seeding problem.

- **Amplification up to strong values:** The magnetic seed fields are commonly found to be too weak in strength compared to the observations of magnetic fields within virializing objects and hence, amplification of the magnetic seed fields is necessary. The magnetic energy increases if magnetic field lines are brought closer to each other. Firstly, magnetic fields can be amplified by simple compression of the field lines, which in the case of isotropic compression will lead to

$B \sim \rho^{2/3}$. Secondly, magnetic fields can be amplified by turbulent and random gas motions. These motions will stretch, twist and fold the field lines on whichever scales the motions are operating. In the presence of turbulence, the smallest turbulent eddies usually turn over the fastest and hence, the magnetic energy increases on the smallest scales first. This so-called small-scale or turbulent dynamo process will lead to $B \sim e^{t/\tau}$ with an amplification timescale τ. During hierarchical structure formation and the collapse and mergers of objects, the compression of gas as well as turbulent motions are naturally occuring. Thus, while cosmic structures are forming and virializing from high redshifts until today, magnetic seed fields are amplified to strong values. The amplification process is assumed to truncate when either the back-reaction of the magnetic field becomes dynamically important or the timescales of dissipating processes become smaller than the timescales of amplifying processes. Within this thesis, Chapters 1, 2, 4 and 5 contribute to the amplification problem.

- **Distribution onto large scales:** The observed magnetic fields often show regular patterns and appear ordered on scales larger than the small-scale amplification scale. It is commonly assumed that mean-field dynamo processes are ordering and structuring magnetic fields on galactic scales (e.g. create spiral patterns). However, magnetic fields are also observed within the large-scale structure of the Universe. There, if a cosmological or primordial origin of the magnetic seed fields is assumed, the origin of these fields might be explained. But, if the magnetic seed fields were created locally within collapsed objects, additional transport processes must have carried magnetic energy into vast regions of space. Merger-driven outflows, shocks, turbulence and associated diffusion can distribute magnetic energy onto larger scales and are found to work well for the close vicinity of galaxies (e.g. clusters of galaxies). However, the distribution into the furthest regions of the IGM or even into the voids is far from being understood. A possible magnetization scenario for those regions is given by AGN activity or the propagation of charged particles carrying or inducing magnetic fields. Within this thesis, Chapters 2 and 3 contribute to the distribution problem.

During structure formation, the seeding, amplification and distribution are **mutually cooperating**. Until now, numerical simulations focused mainly on the amplification problem and on studying dynamo processes in great detail. However, self-consistency of the simulations can only be obtained once all three sub-problems are modelled simultaneously. This thesis presents the first fully self-consistent cosmological simulations of the seeding, amplification and distribution of magnetic fields in the context of galaxy formation.

Chapter 1

Paper I: Origin of strong magnetic fields in Milky Way-like galactic haloes

A.M. Beck, H. Lesch, K. Dolag, H. Kotarba, A. Geng & F.A. Stasyszyn, 2012,
Monthly Notices of the Royal Astronomical Society, 422, 2152

ABSTRACT

An analytical model predicting the growth rates, the absolute growth times and the saturation values of the magnetic field strength within galactic haloes is presented. The analytical results are compared to cosmological MHD simulations of Milky Way-like galactic halo formation performed with the N-body/SPMHD code GADGET. The halo has a mass of $\approx 3 \cdot 10^{12}\ M_{\odot}$ and a virial radius of $\approx$ 270kpc. The simulations in a Λ cold dark matter (ΛCDM) cosmology also include radiative cooling, SF, SN feedback and the description of non-ideal MHD. A primordial magnetic seed field ranging from 10^{-10} to 10^{-34} G in strength agglomerates together with the gas within filaments and protohaloes. There, it is amplified within a couple of hundred million years up to equipartition with the corresponding turbulent energy. The magnetic field strength increases by turbulent small-scale dynamo action. The turbulence is generated by the gravitational collapse and by SN feedback. Subsequently, a series of halo mergers leads to shock waves and amplification processes magnetizing the surrounding gas within a few billion years. At first, the magnetic energy grows on small scales and then self-organizes to larger scales. Magnetic field strengths of $\approx 10^{-6}$G are reached in the centre of the halo and drop to $\approx 10^{-9}$G in the IGM. Analysing the saturation levels and growth rates, the model is able to describe the process of magnetic amplification notably well and confirms the results of the simulations.

Key words: methods: analytical, methods: numerical, galaxies: formation, galaxies: haloes, galaxies: magnetic fields, early Universe

This chapter is a complete presentation of Beck et al. (2012).

1.1 Introduction

The Λ Cold Dark Matter model (ΛCDM) is the standard tool describing the evolution of the universe (Komatsu et al., 2011). Quantum fluctuations in the primordial energy distribution develop into the condensing matter and trigger gravitational instabilities. Dark matter clumps in filaments and protohaloes and subsequently baryonic matter falls into the potential wells of the dark matter, thereby forming the first stars and galaxies. In a hierarchical process of merger events, larger structures grow (White & Rees, 1978; White & Frenk, 1991). Numerical simulations of structure formation within a ΛCDM universe show good agreement between the calculated and the observed distribution of matter and structures (Springel et al., 2005c, 2006). However, cosmic magnetic fields are still widely neglected in these kinds of simulations, although their presence can influence the dynamics of an astrophysical system significantly.

Observations reveal strong magnetic fields of μG strength in late-type galaxies (for reviews on cosmic magnetism, see e.g. Beck et al. (1996), Widrow (2002), Kulsrud & Zweibel (2008) and references therein). The energy density of these magnetic fields is comparable to other dynamically important energy densities, i.e. the magnetic field seems to be in equipartition with them. Neronov & Vovk (2010) also find strong magnetic fields permeating the IGM. The IGM magnetic fields are highly turbulent (Ryu et al., 2008) and their strength is estimated to the order of nG (Kronberg et al., 2008). Additionally, magnetic fields of μG strength can be found in high redshift galaxies (Bernet et al., 2008). Also, there is evidence of highly magnetized damped Lyman α systems at redshift ≈ 2, which act as building blocks for galactic systems (Wolfe et al., 2005).

The origin of these magnetic fields is still unclear. Global primordial magnetic fields can be seeded by battery processes in the early universe (Biermann, 1950; Mishustin & Ruzmaĭkin, 1972; Zel'dovich et al., 1983; Huba & Fedder, 1993). Alternatively, seed fields can be generated by phase transitions after the BigBang or various other mechanisms (see e.g. Widrow, 2002).

In a subsequent process, these weak seed fields of sometimes $\leq 10^{-20}$ G have to be amplified to the observed values. Lesch & Chiba (1995) demonstrate the possibility of strong magnetic fields at high redshifts through battery processes and protogalactic shear flow amplification. The presence of strong μG galactic magnetic fields is commonly explained by galactic dynamos converting angular momentum into magnetic energy in differentially rotating disks. The two main theories are the α-ω dynamo (Ruzmaikin et al., 1979) or the CR-driven dynamo (Lesch & Hanasz, 2003; Hanasz et al., 2009a). For reviews of dynamo theory, see Brandenburg & Subramanian (2005) or Shukurov (2007). However, these dynamos operate on time-scales (e-folding time, not absolute amplification time) of the order of 10^8 yr and require a differentially rotating galactic disk. Hence, irregular galaxies at high redshift have to be magnetized by another process. Another possible magnetization process is the 'cosmic dynamo' as given by Dubois & Teyssier (2010). Within their approach, the universe is magnetized by gravitational instabilies, galactic dynamos and wind-driven outflows of gas at times of violent SF activity.

Small-scale dynamos operate on time-scales of the order of 10^6 yrs through random and turbulent shear flow motions (Biermann & Schlüter, 1951). Magnetic energy increases exponentially on small scales first by stretching, twisting and folding the magnetic field lines by random motions and then organizing them on the largest turbulent eddy scale (Zel'dovich et al., 1983; Kulsrud & Anderson, 1992; Kulsrud et al., 1997; Malyshkin & Kulsrud, 2002; Schekochihin et al., 2002, 2004; Schleicher et al., 2010). Galaxy mergers are a natural part of the bottom-up picture of the growth of structures in the universe. Kotarba et al. (2010, 2011) and Geng et al. (2012b) show that turbulence induced during galactic major and minor mergers is able to amplify magnetic fields in galaxies and in the IGM up to equipartition between the magnetic and turbulent energy density, as expected from the

small-scale dynamo theory. This theory is a good method to describe the amplification processes and corresponding time-scales (e.g. Arshakian et al., 2009). However, galactic dynamos are still inevitable to explain the regularity of galactic magnetic fields and their spiral structure, which are revealed by observations.

Analytical calculations and cosmological simulations of structure formation including the evolution of magnetic fields can give new insights in the physical processes of creating, amplifying and saturating magnetic fields in the universe on all kind of scales.

In this work, an analytical model predicting the growth rates, the absolute growth times and the saturation values of the magnetic field strength within galactic haloes is presented. The analytical results are compared to cosmological MHD simulations of Milky Way-like galactic halo formation including SF and non-ideal MHD. It is shown that the analytical model and the cosmological simulations agree notably well for different initial, primordial magnetic seed fields spanning a range of 25 orders of magnitudes.

The paper is organized as follows. The analytical calculations are shown in section 1.2. Section 1.3 briefly describes the numerical method. In section 1.4 the cosmological inital conditions and the magnetic seed field are presented. A detailed analysis of the performed simulations and the magnetic field amplification is given in section 1.5. Section 1.6 compares the numerical results with the analytical description. The main results are summarized in section 1.7.

1.2 Analytical description

This section gives an analytical approach describing the behaviour of the magnetic field strength during halo formation. In order to derive an analytical model, expressions for the cosmological decay, the exponential amplification process, the saturation and the relaxing decay of the magnetic field strength are needed. For large hydrodynamical Reynolds numbers, a stationary flow transits from the laminar regime into the turbulent regime and becomes unstable. Hence, an overview of the characteristics of a non-stationary perturbated magnetic field in such an unstable flow in a cosmological context is given.

1.2.1 Local perturbation ansatz

The Reynolds number is a characteristic dimensionless quantity describing the ratio of inertial forces and viscous forces of a flow:

$$Re = \frac{\text{inertial forces}}{\text{viscous forces}} = \frac{VL}{\nu}, \tag{1.1}$$

with V and L being typical velocity and length scales of the flow and ν the kinematic viscosity. A stationary flow will become unstable if the Reynolds number Re exceeds a critical value Re_{crit}. In this case, any initial infinitesimal perturbation will be amplified through the flow. In the following calculations, the hydrodynamical flow is assumed to be unstable, since the inertial length scale is sufficiently larger than the viscous length scale. The magnetic Reynolds number Rm, which is defined as $Rm = VL/\eta$ (with the magnetic resistivity η), is also sufficiently large to allow for perturbations to grow. The induction equation of ideal MHD reads:

$$\frac{\partial \mathbf{B}(\mathbf{x},t)}{\partial t} = \nabla \times \left[\mathbf{v}(\mathbf{x},t) \times \mathbf{B}(\mathbf{x},t)\right]. \tag{1.2}$$

Within the small perturbation approximation, the velocity field $\mathbf{v}(\mathbf{x},t)$ and the magnetic field $\mathbf{B}(\mathbf{x},t)$, respectively, can be decomposed into the sum of a stationary component $\mathbf{v}_0(\mathbf{x},t)$ and $\mathbf{B}_0(\mathbf{x},t)$ and a perturbated component $\mathbf{v}_1(\mathbf{x},t)$ and $\mathbf{B}_1(\mathbf{x},t)$, respectively. For the induction equation (1.2), this procedure results in the following decomposition:

$$\frac{\partial \mathbf{B}_0}{\partial t} = \nabla \times [\mathbf{v}_0 \times \mathbf{B}_0], \tag{1.3}$$

$$\frac{\partial \mathbf{B}_1}{\partial t} = \nabla \times [\mathbf{v}_0 \times \mathbf{B}_1 + \mathbf{v}_1 \times \mathbf{B}_0]. \tag{1.4}$$

The right cross-product in equation (1.4) can be dropped, because only the growth of magnetic perturbations in a stationary flow is important and the growth of velocity perturbations in a weak stationary magnetic field can be neglected. The general solution of equation (1.4) is a sum of special solutions, whereby $\mathbf{B}_1$ includes a time-dependent factor $e^{-i\Omega t}$. The complex frequency Ω is given by $\Omega = \omega + i\Gamma$, with periodicity ω and growth rate Γ. For growing perturbations Γ will be positive. The perturbated component $\mathbf{B}_1$ can be further decomposed into

$$\mathbf{B}_1(\mathbf{x}, t) = B_t(t)\mathbf{s}(\mathbf{x}), \tag{1.5}$$

$$B_t(t) = B_t(t_0)e^{\Gamma t}e^{-i\omega t}, \tag{1.6}$$

with a spatially dependent complex vector function $\mathbf{s}(\mathbf{x})$ and a complex scalar amplitude $B_t(t)$. The time derivative of the square of the amplitude is:

$$\frac{\partial B_t^2(t)}{\partial t} = 2\Gamma B_t^2(t). \tag{1.7}$$

Equation (1.7) was also derived for a kinematic dynamo by Kulsrud & Anderson (1992) and for a turbulent magnetized dynamo by Malyshkin & Kulsrud (2002) using spectral analysis of the growth of the magnetic energy. In the weak-field approximation, the flow is able to amplify the frozen-in magnetic perturbations, since the magnetic field is frozen into the velocity field. Thereby, any information about the original orientation of the magnetic seed field is lost. As soon as equipartition is reached, the back-reaction of the magnetic field on the velocity field has to be considered and the weak-field approximation breaks. Then, one can either solve the full Navier-Stokes equations including magnetic pressure and tension forces or model the back-reaction by truncating the growth rate Γ. Belyanin et al. (1993) describe the latter 'Equipartition dynamo' approach by expanding Γ in a power series and considering second-order terms to truncate the growth rate. These non-linear effects force the maximum amplitude to an equipartition value and the dynamo process saturates. Generally, a 'supra-equipartition dynamo' should be expected, because compression of $B^2 \sim \rho^{\gamma_{\rm adi}}$ (e.g. the effective adiabatic index is $\gamma_{\rm adi} = 4/3$ for isotropic compression) can still occur. This would result in the magnetic energy density first to shoot over the turbulent energy density ($\gamma_{\rm adi} = 1$) and then decay towards the saturation level. However, this effect is too small to be significant. Now, to account for the saturation of the magnetic field at the equipartition level, Γ is amended (Belyanin et al., 1993) as follows:

$$\Gamma = \gamma \left[1 - \frac{B_t^2(t)}{B_{\rm sat}^2}\right], \tag{1.8}$$

and the equation for the growth of the magnetic field amplitude takes the form:

$$\frac{\partial B_t^2(t)}{\partial t} = 2\gamma \left[B_t^2(t) - \frac{B_t^4(t)}{B_{\rm sat}^2}\right]. \tag{1.9}$$

This growth of the magnetic perturbations is an iterative process: $\mathbf{B}_1$ can only grow to the order of magnitude of $\mathbf{B}_0$, then a new $\mathbf{B}_0$ and $\mathbf{B}_1$ have to be defined. Furthermore, since turbulence is the driver of the magnetic field amplification, equipartition between the magnetic and the turbulent

energy density is a good approximation for the saturation magnetic field (no further growth will occur, once the magnetic field has saturated):

$$\frac{B_{\rm sat}^2}{8\pi} = \frac{1}{2}\rho v_{\rm turb}^2, \tag{1.10}$$

with the density ρ and the turbulent velocity $v_{\rm turb}$ of the system. Together with the initial condition $B_t^2(t=0) = B_0^2$ equation (1.9) has the solution (Landau & Lifshitz, 1959):

$$B_t(t) = \frac{1}{\sqrt{(4\pi\rho v_{\rm turb}^2)^{-1} + B_0^{-2}e^{-2\gamma t}}}. \tag{1.11}$$

As a next step, the growth rate γ has to be determined. The kinetic energy of the turbulence can be assumed to follow a one-dimensional Kolmogorov spectrum of the form

$$I(k) \sim v_{\rm turb}^2 k^{-5/3}, \tag{1.12}$$

where $v_{\rm turb}^2$ is the mean-square turbulent velocity. From equation (1.7) Kulsrud et al. (1997) find for the growth rate γ

$$2\gamma \approx \int \frac{k^2 I(k)}{k v_k} dk \approx \int \sqrt{kI(k)} dk, \tag{1.13}$$

with an eddy turnover rate $kv_k \approx [kI(k)]^{1/2}$ and with v_k being the typical eddy velocity on k scale. Integrating equation (1.13) yields the growth rate γ. Performing additional calculations including resistivity, Kulsrud et al. (1997) find an advanced version of γ:

$$\gamma = 2.050 \frac{v_{\rm turb}^{3/2} k_{\rm turb}^{1/2}}{\eta_{\rm turb}^{1/2}}. \tag{1.14}$$

Equation (1.14) describes the turnover rate of the smallest turbulent eddy. Magnetic resistivity, which is essential for topological changes of the magnetic field lines through reconnection on small scales and transfer of magnetic energy into internal energy and which is effectively lowering the growth rate, is already included via $\eta_{\rm turb}$. The dynamo process increases the magnetic energy on the dissipation scale first with a rate of 2γ and saturates at a value comparable to the turbulent energy on small scales first. The magnetic energy is then transferred to larger scales with a rate of $3\gamma/4$ (Kulsrud et al., 1997) by Lorentz forces unwrapping the folded field lines on small scales in an inverse cascade process. Finally, the magnetic field reaches saturation at a value comparable to the turbulent energy in the largest eddy (Kulsrud & Anderson, 1992; Malyshkin & Kulsrud, 2002). The growth rate given by equation (1.14) is taken from the kinematic dynamo theory (Kulsrud et al., 1997), but Malyshkin & Kulsrud (2002) find that the calculation leading to equation (1.14) still holds for the magnetized turbulent dynamo in the weak-field approximation.

These small-scale dynamos operate whenever turbulent and random motions and shear flows are stretching, twisting and folding the magnetic fields lines (Zel'dovich et al., 1983; Schleicher et al., 2010). Field lines come close on small scales first and hence the magnetic energy increases at first on small scales. The amplification is dominated by the turbulent dynamo action and effects resulting from compression can be neglected within this model.

1.2.2 Cosmological evolution and decay

The next step towards an analytical model of the magnetic field amplification is to modify the growth equation (1.9) such that the scalefactor $a(t)$ describing the expansion of the universe during its evolution is accounted for. For an isotropic and stationary magnetic field, the magnetic flux has to be

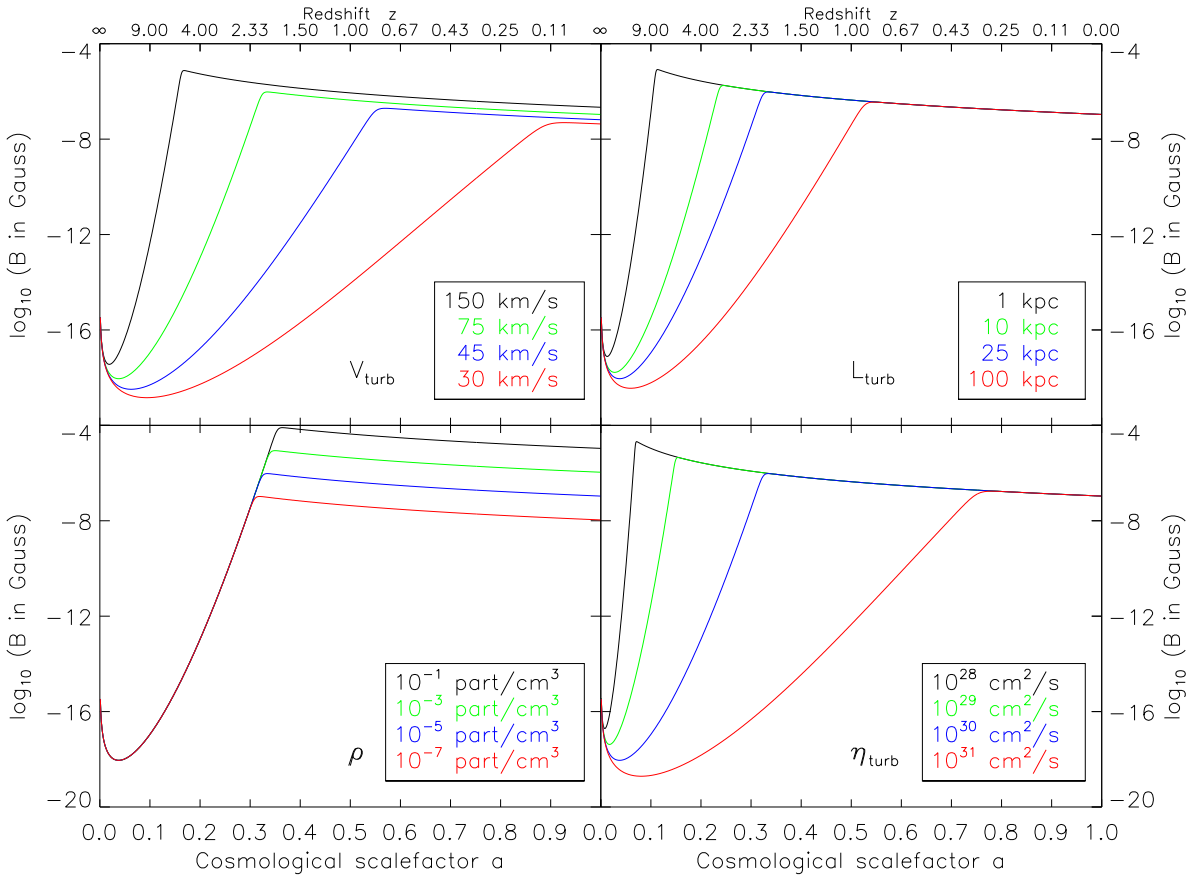

Figure 1.1: Analytical growth curves for the magnetic field amplitude as a function of redshift for different numerical parameters. In each panel, one parameter is varied, while the other parameters are held constant. Differences in the growth rates and saturation levels can be seen.

ΛCDM Cosmology Parameters		
Matter density	Ω_M	0.3
Dark energy density	Ω_Λ	0.7
Total density	Ω_0	1.0
Hubble constant	H_0	70 km s^{-1} Mpc^{-1}

Table 1.1: Parameters used for the ΛCDM cosmology.

conserved when space is expanding. From the first law of thermodynamics, the proportionality between the scalefactor a and the energy density of electromagnetic fields (or ultrarelativistic particles) $\varepsilon \sim B_t^2$, can be derived (Longair, 2008):

$$\varepsilon \sim a^{-4}. \tag{1.15}$$

Any cosmological equation for the evolution of the magnetic field amplitude has thus to account for the proportionality $B_t \sim a^{-2}$. In cosmological simulations, the scalefacor $a(t)$ instead of physical time t is the natural integration variable. Given a flat universe without any radiation pressure, the evolution equation for the scalefactor takes the form (e.g. Longair, 2008)

$$dtH_0 = da(\frac{\Omega_M}{a} + a^2\Omega_\Lambda)^{-\frac{1}{2}}, \tag{1.16}$$

with Ω_M and Ω_Λ being the density contributions of matter and the cosmological constant and H_0 the present-day Hubble constant. The employed parameters of this ΛCDM cosmology (Table 1.1) are close to the observed values (see Komatsu et al., 2011). With the initial condition $a(0) = 0$ equation (1.16) has the solution:

$$t(a) = \frac{2}{3H_0\sqrt{\Omega_\Lambda}} \cdot \mathrm{asinh}\left(\sqrt{\frac{\Omega_\Lambda}{\Omega_M}}a^{\frac{3}{2}}\right). \tag{1.17}$$

Combining equations (1.11), (1.14), (1.15) and (1.17) finally results in:

$$B_t(a) = \frac{1}{a^2}\left[(4\pi\rho v_\mathrm{turb}^2)^{-1} + B_0^{-2}e^{-2\gamma t(a)}\right]^{-\frac{1}{2}}. \tag{1.18}$$

Equation (1.18) is an approximation for the growth of the magnetic field strength during the matter-dominated and later phases of the Universe.

In the beginning, the term $a(t)^{-2}$ dominates and results in the cosmological dip at high redshifts. Then, the magnetic energy increases with $e^{2\gamma t(a)}$ during the gravitational collapse and due to SF-induced turbulence. This growth stops when equipartition is reached, since non-linear effects are truncating γ. Finally, when the system is relaxing and the turbulence is decaying, also the magnetic field will decay as $a(t)^{-2}$ corresponding to a power-law decay with $B_t \sim t^{-4/3}$. This decay is slightly stronger compared to the $B_t \sim t^{-5/4}$ decay given by Landau & Lifshitz (1959) or George (1992) for the final stages of decaying kinematic turbulence (assuming that the magnetic energy decays with the same power-law as the turbulent energy, which is an approximation). The final stage of decay is reached by the time, when the Reynolds number becomes sufficiently small. This happens when the back-reaction of the magnetic field on the velocity field suppresses turbulent motions and also magnetic amplification and the system relaxes. Subramanian et al. (2006) found the power-law decay to set in already for Reynolds numbers still as large as $Re \approx 100$ in galaxy clusters.

Analytical Model Parameters		
Turbulent length	$l_{\rm turb}$	25 kpc
Turbulent velocity	$v_{\rm turb}$	75 km s^{-1}
Turbulent dissipation	$\eta_{\rm turb}$	10^{30} cm^2 s^{-1}
Gas density	$n_{\rm gas}$	10^{-5} cm^{-3}

Table 1.2: Parameters used for the calculation of the analytical growth function (physical units).

1.2.3 Numerical parameters

Equation (1.18) contains four free parameters: $v_{\rm turb}$, $l_{\rm turb}$, $\eta_{\rm turb}$ and ρ. The numerical values for these parameters have to be taken from observations or extracted from numerical simulations. Table 1.2 shows the values used in this work. These values correspond to a time-scale (e-folding time) of $\tau = 1/\gamma \approx 90$ Myr and a saturation value of $B_{\rm sat} \approx 0.1\mu$G at redshift 0. Note that these numerical parameters are constant mean estimates and do not reflect the time and spatial details of the simulations, but nevertheless are a good approximation.

Estimating values for $v_{\rm turb}$ and $l_{\rm turb}$ is quite challenging, as the densities, velocities and length scales in galactic haloes range over many orders of magnitude. Therefore, such values can only be associated with typical values within galactic haloes.

Fig. 1.1 shows growth curves as a function of redshift for a wide range of values of these parameters. In each panel, three parameter are held constant (see Table 1.2), while the fourth parameter is varied. As indicated by the presented calculations, $v_{\rm turb}$, $l_{\rm turb}$ and $\eta_{\rm turb}$ affect the growth rate γ, while $v_{\rm turb}$ and ρ affect the saturation value $B_{\rm sat}$. Depending on the parameter configuration, the time-scale ranges from order of 10^6 yrs to 10^8 yrs and the saturation value for the magnetic field strength varies from 10^{-5} G to 10^{-8} G.

1.3 Numerical methods

The simulations in this work are performed with the N-body / SPMHD code GADGET (Springel et al., 2001b; Springel, 2005; Dolag & Stasyszyn, 2009). GADGET uses a formulation of SPH, in which both energy and entropy are conserved (Springel & Hernquist, 2002). For recent reviews on the SPH and SPMHD methods, see Springel (2010b) and Price (2012). Additionally, SUBFIND (Springel et al., 2001a; Dolag et al., 2009) is applied to identify haloes and subhaloes and to calculate their respective centre locations and virial radii.

A detailed description of the SPMHD implementation of MHD and its extension to non ideal MHD can be found in Dolag & Stasyszyn (2009) and Bonafede et al. (2011). Here, the standard (direct) SPMHD implementation is used, where the induction equation

$$\frac{\partial \mathbf{B}}{\partial t} = \nabla \times (\mathbf{v} \times \mathbf{B}) + \eta \Delta \mathbf{B} \tag{1.19}$$

is evolving the magnetic field and a spatially constant magnetic resistivity η is also applied. Following Bonafede et al. (2011), non-ideal resistivity is assumed to be driven by the turbulence within the gas and $\eta_{\rm turb}$ is of the order of $\approx 10^{30}$ cm^2 s^{-1}, which is consistent with models of the central regions of galaxy clusters (Schlickeiser et al., 1987; Rebusco et al., 2006). Therefore, the constant turbulent resistivity describes the magnetic field decay on sub-resolution scales and is many order of magnitudes larger compared to numerical or ohmic resistivity, which are hence not of interest for this work.

Multi-Phase Model Parameters		
Gas consumption time-scale	$t_{\rm SF}$	2.1 Gyr
Number density threshold	$n_{\rm th}$	0.13 cm^{-3}
Mass fraction of massive stars	β	10 per cent
Evaporation parameter	A	1000
Effective SN temperature	$T_{\rm SN}$	10^8 K
Temperature of cold clouds	$T_{\rm CC}$	1000 K

Table 1.3: Parameters for the SF model (Springel & Hernquist, 2003a) used in the simulations.

The magnetic field back-reacts on the velocity field via the Lorentz force. To account for the tensile instability (see e.g. Dolag & Stasyszyn, 2009; Price, 2012) in SPMHD, the unphysical numerical divergence force is substracted from the equation of motion following an approach by Børve et al. (2001). Similar to Kotarba et al. (2010), a limiter is applied to ensure that the correction force does not exceed the Lorentz force to avoid instabilities.

To ensure a proper evolution of the magnetic field in numerical simulations, it is of fundamental interest to maintain the $\nabla \cdot \mathbf{B}$ constraint. In particular, an erroreous calculation can lead to unphysical sources and sinks of magnetic energy. The MHD GADGET code keeps these numerical errors to a minimum. For a detailed discussion, see Dolag & Stasyszyn (2009).

The implementation of MHD in GADGET was successfully employed for the study of the magnetic field evolution during SF (Bürzle et al., 2011a,b), in isolated (Kotarba et al., 2009) and interacting galaxies (Kotarba et al., 2010, 2011; Geng et al., 2012a) and in galaxy clusters (Donnert et al., 2009).

Also, the Springel & Hernquist (2003a) SF model is applied. It describes radiative cooling, ultraviolet (UV) background heating and SN feedback in a consistent two-phase sub-resolution model for the ISM. Cold clouds with a fixed temperature of $T_{\rm CC}$ are embedded into a hot ambient medium at pressure equilibrium. These cold clouds are evaporating with an efficiency parameter of A and form stars on a time-scale of $t_{\rm SF}$, once they reach a density threshold of $\rho_{\rm th}$. A fraction β of these stars is expected to die instantly as SN, heating the gas with a temperature of $T_{\rm SN}$. Additionally, the hot phase is losing energy via cooling, which is modelled assuming a primordial gas composition (Hydrogen 76 per cent and Helium 24 per cent) with a temperature floor of 50 K (for details see Katz et al., 1996). The cooling only depends on density and temperature, but not on metallicity. This SF model leads to a self-regulated cycle of cooling, SF and feedback in the gas.

Table 1.3 shows the numerical values of these parameters used in the simulations, which are performed without galactic winds. These numbers are choosen to reproduce the Kennicutt-Schmidt law between surface density and surface SF rate (Schmidt, 1959; Kennicutt, 1998).

However, for simulations of the turbulent small-scale dynamo the precise details of the SF scheme are largely unimportant. Cooling is required to obtain higher gas densities and smaller spatial scales in order to start efficient dynamo action. Furthermore, feedback-driven turbulence will contribute to the gravitationally driven turbulence and raise the growth rates of the magnetic field strength.

1.4 Setup

1.4.1 Dark matter initial conditions

The presented simulations start from cosmological initial conditions introduced by Stoehr et al. (2002). Starting point is a large ΛCDM dark matter-only simulation box run with the GADGET code at different resolutions. The index of the power spectrum of the initial fluctuations is $n = 1$ and the

Simulation setup							
Scenario	SF	$N_{\rm Gas}$	$N_{\rm DM}$	$M_{\rm Gas}(\mathrm{M}_\odot)$	$M_{\rm DM}(\mathrm{M}_\odot)$	$B_{\rm start}^{\rm orientation}$	$B_{\rm start}^{\rm strength}$ (G)
ga0_bx0	yes	68323	68323	$2.6 \cdot 10^7$	$1.4 \cdot 10^8$	-	0
ga0_bx10	yes	68323	68323	$2.6 \cdot 10^7$	$1.4 \cdot 10^8$	x	10^{-10}
ga0_bx14	yes	68323	68323	$2.6 \cdot 10^7$	$1.4 \cdot 10^8$	x	10^{-14}
ga0_bx18	yes	68323	68323	$2.6 \cdot 10^7$	$1.4 \cdot 10^8$	x	10^{-18}
ga0_by18	yes	68323	68323	$2.6 \cdot 10^7$	$1.4 \cdot 10^8$	y	10^{-18}
ga0_bx22	yes	68323	68323	$2.6 \cdot 10^7$	$1.4 \cdot 10^8$	x	10^{-22}
ga0_bx26	yes	68323	68323	$2.6 \cdot 10^7$	$1.4 \cdot 10^8$	x	10^{-26}
ga0_bx30	yes	68323	68323	$2.6 \cdot 10^7$	$1.4 \cdot 10^8$	x	10^{-30}
ga0_bx34	yes	68323	68323	$2.6 \cdot 10^7$	$1.4 \cdot 10^8$	x	10^{-34}
ga1_bx0	yes	637966	637966	$2.8 \cdot 10^6$	$1.5 \cdot 10^7$	-	0
ga1_bx18	yes	637966	637966	$2.8 \cdot 10^6$	$1.5 \cdot 10^7$	x	10^{-18}
ga1_bx18_nosf	no	637966	637966	$2.8 \cdot 10^6$	$1.5 \cdot 10^7$	x	10^{-18}
ga2_bx0	yes	5953033	5953033	$3.0 \cdot 10^5$	$1.6 \cdot 10^6$	-	0
ga2_bx18	yes	5953033	5953033	$3.0 \cdot 10^5$	$1.6 \cdot 10^6$	x	10^{-18}

Table 1.4: Set-up of the different simulations: The table lists whether SF and cooling (SF/cool.) is applied, the number of gas ($N_{\rm Gas}$) and dark matter particles ($N_{\rm DM}$), the mass of the gas ($M_{\rm Gas}$) and dark matter particles ($M_{\rm DM}$), as well as the initial magnetic field orientation and strength for all simulated scenarios, respectively.

fluctuation amplitude is $\sigma_8 = 0.9$ (see e.g. Stoehr et al., 2002). In a 'typical' region of the universe, a Milky Way-like dark matter halo is identified. The resulting simulations (with increasing resolution) are labelled GA0, GA1 and GA2 and contain 13 603, 123 775 and 1 055 083 dark matter particles, respectively, inside R_{200}, which is the radius enclosing a mean density 200 times the critical density (virial radius).

The forming dark matter halo is comparable to the halo of the Milky Way in mass ($\approx 3 \times 10^{12} M_\odot$) and size ($\approx$ 270kpc). The halo was selected to have no major merger after a redshift of ≈ 1 and a subhalo population comparable to the satellite population of the Milky Way was also found. More details about the properties of this halo can be found in Stoehr et al. (2002), Stoehr et al. (2003) and Stoehr (2006). Hence, GA0, GA1 and GA2 provide ideal initial conditions to investigate the evolution of magnetic fields in a galactic halo, similar to the Milky Way.

1.4.2 Gas and magnetic field

To add a baryonic component, the high-resolution dark matter particles are split into an equal amount of gas and dark matter particles. The mass of the initial dark matter particle is splitted according to the cosmic baryon fraction, conserving the centre of mass and the momentum of the parent dark matter particle. The new particles are displaced by half the mean inter-particle distance.

The origin of cosmic magnetic fields is still unclear. During the early evolution of the universe, magnetic seed fields must have been generated by non-ideal mechanisms, which are independent of the magnetic field itself. It this work, primordial magnetic fields permeating the entire universe are assumed to be generated by battery processes (Biermann, 1950; Mishustin & Ruzmaĭkin, 1972; Zel'dovich et al., 1983; Huba & Fedder, 1993) in the early universe. When deriving the induction equation (1.19) of ideal MHD, the fluid is treated as a one particle-type plasma. Hence, in Ohm's law $\sigma \mathbf{E} = \mathbf{j}$ (with $\mathbf{E}$ the electric field and σ the conductivity of the plasma), the current density $\mathbf{j}$ is only described by the motion of the protons. Strictly, the plasma also contains electrons and the

current density $\mathbf{j}$ is a combination of the proton current density $\mathbf{j}_\mathrm{p}$ and an electron current density $\mathbf{j}_\mathrm{e}$. Then, electrons and protons are moving at different speeds in the plasma, reacting differently to perturbations. This results in currents and a non-ideal term in the induction equation of the form:

$$\left(\frac{\partial \mathbf{B}(\mathbf{x},t)}{\partial t}\right)_\mathrm{seed} = -c\frac{\nabla n_\mathrm{e} \times \nabla p_\mathrm{e}}{n_\mathrm{e}^2 e}, \tag{1.20}$$

with the speed of light c, the elementary charge e, the electron density n_e and the electron pressure p_e. In shocks or non-isotrop regions, the gradients of n_e and p_e may be non-parallel and a magnetic seed field of the strength $\approx 10^{-18}$ G may be generated (Biermann, 1950; Mishustin & Ruzmaikin, 1972; Zel'dovich et al., 1983; Huba & Fedder, 1993). To seed the magnetic field within the simulations, a magnetic field vector is given to every gas particle pointing into the same direction carrying the same amplitude (most used choice: 10^{-18} G in x-direction). This uniform set-up gives an initially divergence-free magnetic field inside the simulation volume.

Actually, the magnetic energy should be distributed to the different scales of the simulation, resulting in a magnetic spectrum. However, this spectral property of the magnetic field can be neglected for magnetic energy densites $\varepsilon_\mathrm{mag} = B^2/8\pi$ sufficiently smaller than the kinetic energy density $\varepsilon_\mathrm{kin} = \rho v^2/2$ (weak-field approximation). In this limit, the magnetic field $\mathbf{B}$ will be frozen into the velocity field $\mathbf{v}$ and follow its evolution. Hence, only the amplitude of the magnetic seed field is relevant, but not its direction.

Table 1.4 shows the simulations performed, which can be grouped into three sets. First, low-resolution simulations GA0 are used for a numerical study of different seed field strengths ranging from 10^{-10} G to 10^{-34} G and being uniform in x-direction. Additionally, a run of GA0 with a seed field in y-direction is shown to confirm the neglectability of the magnetic seed field direction. Secondly, for the seed field with the strength of 10^{-18} G, higher resolution runs GA1 and GA2 are added to analyze the influence of the numerical resolution on the evolution of the magnetic field. Furthermore, a special run of GA1 is performed to study the influence of the modelled SF on the evolution of the magnetic field. Finally, to study the influence of magnetic fields on the existing simulations, additional runs with only hydrodynamics are obtained.

1.5 Simulations

This section presents the results obtained from the numerical simulations introduced above. Contour images of different quantities are created by projecting the SPMHD data in a comoving $(1\ \mathrm{Mpc})^3$ cube on a 512^2 grid using the code P-SMAC2 (Donnert et al., in preparation).

1.5.1 Morphological and magnetic evolution

An overview of the different stages of structure formation and their implications on the magnetic field is shown in Fig. 1.2. First, dark matter protohaloes and filaments are formed at redshift $z \approx 30 - 10$ and baryonic matter falls into the potential wells. Within these structures, the frozen-in magnetic field gets compressed. For isotropic compression, this leads to $B \sim \rho^{2/3}$. Note that perpendicular compression of the magnetic field lines would lead to $B \sim \rho$. Due to the cosmological expansion, the magnetic field strength outside these protohaloes decreases with a^{-2}. Turbulence is mainly created by the gravitational collapse. Secondly, as the gas density increases in the first structures, the threshold density is reached and SF sets in at redshift ≈ 10, further enhancing the existing turbulence and consuming the available gas. In these dense regions, small-scale dynamo action starts, increasing the magnetic field strength exponentially, i.e. $B \sim e^{\gamma t}$ with the growth rate γ. Merger events will create shockwaves propagating into the IGM, possibly amplifying the magnetic field by compression and

Structure formation (ΛCDM)

Primordial universe	Energy fluctuations	Magnetic seeding	$B_{Seed} \sim 10^{-18}$ G
DM Potentials	Baryonic matter infall	Cosmological dip	$B \sim a(t)^{-2}$
Filaments Haloes	Compression	Isotrop compression	$B \sim \rho^{2/3}$
	Star formation	Turbulent dynamo Exponential amplification	$B \sim e^{\gamma \cdot t(a)}$
Haloes	Star formation Mergers		
IGM	Mergers Shocks Outflows		
Virialized systems	Equipartition	Power-law decay	$B_{Halo} \sim 10^{-7}$ G $B_{IGM} \sim 10^{-9}$ G
Galactic disks	Rotation	α-ω-dynamo CR-dynamo	$B_{Disk} \sim 10^{-5}$ G

Magnetic amplification

Figure 1.2: Overview of the different physical processes during structure formation. This table shows the stages of the evolution (column 1), during which an astrophysical process (column 2) triggers an MHD mechanism (column 3) operating on the magnetic field, resulting in the equations and magnetic field strength values given in column 4.

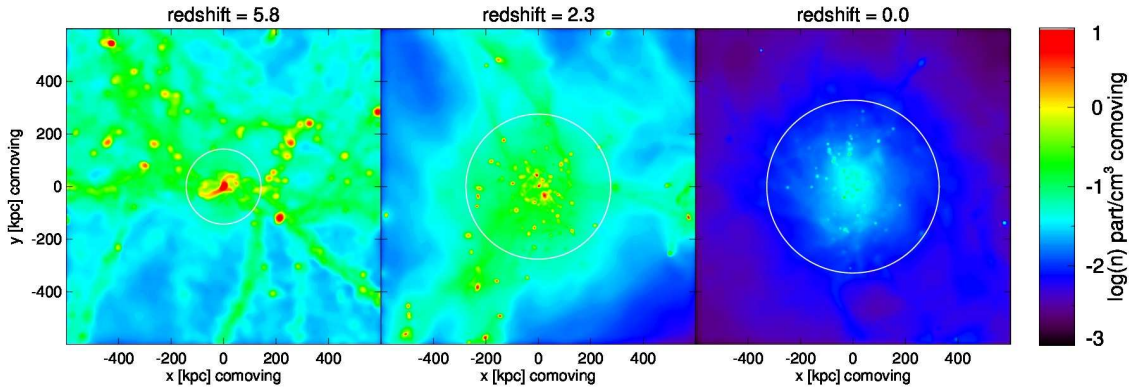

Figure 1.3: Projected number density n_{gas} in comoving units at different redshifts in the simulation ga2_bx18. The shown regions are cubes with 1-Mpc (comoving) edge length centred on the halo centre of mass. The white circles indicate the virial radius of the halo. The formation of filaments and protohaloes with subsequent merger events can be seen.

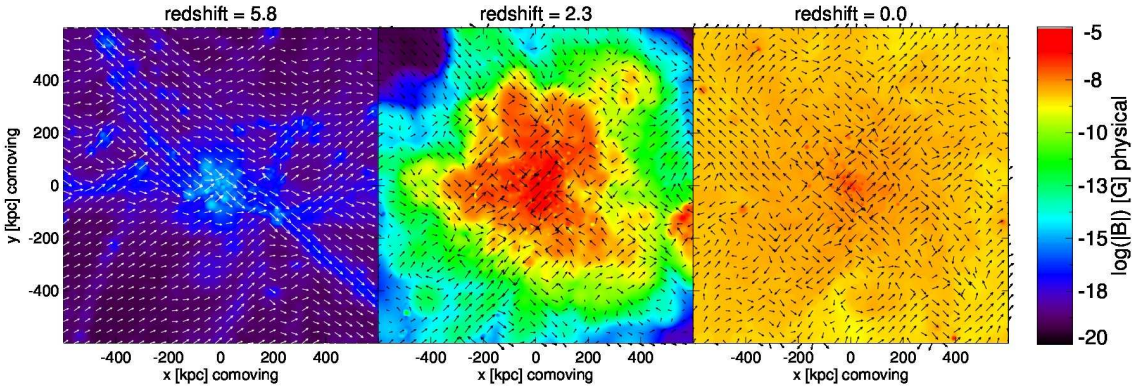

Figure 1.4: Projected total magnetic field strength and magnetic field vectors in physical units at different redshifts in the simulation ga2_bx18. The shown regions are cubes with 1-Mpc (comoving) edge length centred on the halo centre of mass. Clumping of the magnetic field together with the gas in filaments and amplification within protohaloes can be seen. Furthermore, shockwaves are driven into the IGM increasing the magnetic field strength, until it saturates on all scales.

small-scale dynamo action. As equipartition is reached, the system relaxes and turbulent motions will decay, with additionally the magnetic field decaying.

Fig. 1.3 shows the projected number density of the gas at three different redshifts in the simulation ga2_bx18, together with the corresponding virial radii of the forming galactic halo. Fig. 1.4 shows the corresponding projected total magnetic field strength, as well as arrows indicating the direction of the magnetic field. The different phases during the formation of the halo and the magnetic field amplification can clearly be seen. The magnetic field agglomerates together with the gas in filaments and protohaloes, where small-scale dynamo action is taking place. Furthermore, as merger events take place, shockwaves are propagating into the IGM creating turbulence. The IGM magnetic field is amplified in stages with several shockwaves propagating into it. Within each shockwave, the magnetic field is possibly amplified by compression within the shockfront and by small-scale dynamo action behind the shockfront (for an analysis of shockwaves and their effect on the magnetic field during merger events, see Kotarba et al., 2011). At redshift ≈ 1 the last major merger event takes place and the magnetic field saturates, i.e. it evolves into energy density equipartition. The magnetic field saturates inside the halo at a mean value of $\approx 10^{-7}$ G and within the IGM at $\approx 10^{-9}$ G, both at redshift 0.

Fig. 1.5 shows the rms magnetic field strength inside the galactic halo as a function of redshift for different seed field strengths. The amplification time-scale (i.e. the gradient of the $\mathbf{B}(a)$ function during the exponential amplification phase) is the same for all seed fields and only the total time until saturation varies. After saturation, the magnetic field strength decreases with a power-law slope of ≈ -1, as irregularities in the magnetic field are dissipated.

Fig. 1.6 shows radial profiles of the volume-weighted magnetic field strength inside the galactic halo for two different redshifts. At redshift 1 (after the last major merger), magnetic field strengths of several 10^{-5} G are reached in the centre of the halo and drop to $\approx 10^{-7}$ G at the virial radius with a slope of ≈ -1.1. At redshift 0 (virialized system with decaying turbulence), magnetic field strengths of several 10^{-6} G are reached in the centre of the halo and drop to $\approx 10^{-9}$ at the virial radius with a slope of ≈ -0.9. Since the gas density scales linearly with the distance from the galactic halo centre, this indicates a relation of the form $B \sim \rho$.

Summing up, within the presented simulations it is possible to amplify a weak primordial magnetic

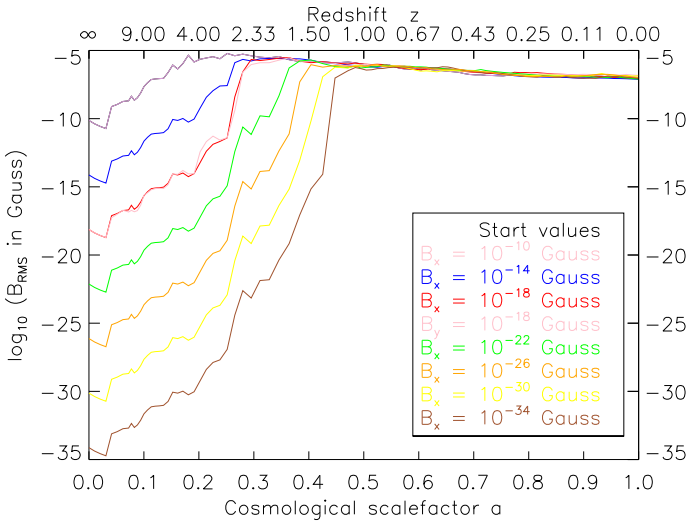

Figure 1.5: Growth curves of the volume-weighted rms magnetic field strength inside the halo in the simulations GA0 for different seed fields.

field up to the observed equipartition values.

1.5.2 Pressures and star formation

Fig. 1.7 summarizes the energy flow and its effect on the SF within the simulations. Via internal energy, SF provides a sink (cooling) and source (SN injection) of internal energy of the gas. Internal and kinetic energy are mutually exchanging via pressure forces and viscosity. Additionally, the gravitational collapse transforms potential energy into kinetic energy, which is converted partly back into potential energy through the fluid motions in the potential wells. Furthermore, kinetic motions create magnetic energy (induction equation). The Lorentz-force describes the back-reaction of the magnetic field on the velocity field. Non-ideal resistivity redistributes the magnetic energy and also converts it into internal energy. Internal, kinetic and magnetic energy densities contribute to a total pressure. The balance between the gravitational collapse and the total pressure support regulates the SF rate.

Fig. 1.8 shows the magnetic energy density $\varepsilon_{\rm mag} = B^2/8\pi$, the kinetic energy density $\varepsilon_{\rm kin} = \rho v^2/2$, the thermal energy density $\varepsilon_{\rm therm} = (\gamma - 1)\rho u$ and the turbulent energy density $\varepsilon_{\rm turb} = \rho v_{\rm turb}^2/2$ in the simulation ga2_bx18. The adiabatic index γ is 5/3 and u denotes the internal energy. Similar to Kotarba et al. (2010), $v_{\rm turb}$ is taken as an estimate of the turbulent velocity within the volume defined by an SPMHD particle. They find it to be a good SPMHD approximation of the turbulent velocity, although it overestimates the turbulence on small scales and ignores the turbulence on scales larger than the smoothing scale.

As shown in Fig. 1.8, the magnetic energy density increases from the seed value up to equipartition with the turbulent and thermal energy densities until a redshift of ≈ 3. The cosmological dip can be clearly seen at the start of the simulations. The magnetic energy density overshoots the turbulent energy density slightly in the beginning, which results from possible further compression after equipartition is reached. Afterwards, the virialized system relaxes and the turbulent and magnetic energies decline. The thermal energy density still rises, as the magnetic and turbulent energy are converted into thermal energy by resistivity and viscosity. With some delay, equipartition is also reached in the

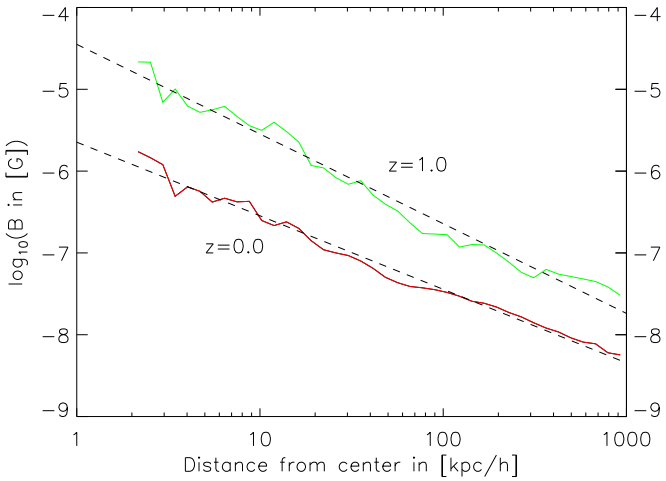

Figure 1.6: Radial profiles of the mean magnetic field strength inside the halo in the simulation ga2_bx18 for redshifts 1 and 0, respectively. For $z = 1$, which is just after the last major merger event, the field strength decreases with a slope of -1.1. For the relaxated system at $z = 0$ the slope is -0.9.

IGM by a stepwise amplification process: First, the magnetic field is amplified inside the most dense structures and subsequently the IGM magnetic field undergoes merger-driven shock amplification.

Fig. 1.9 shows the total SF rate as a function of the cosmological scalefactor for all GA0 simulations (see Table 1.4) with different seed field strengths. Before the formation of filaments and protohaloes, no SF takes place. At the time the first structures reach the necessary critical density ($z \approx 10$), SF begins. As more gas is accreted on to the main halo through gravitational infall or due to merger events, the SF rate rises. At a redshift of ≈ 3 it peaks and then starts to decline. For the simulations without any magnetic fields, SF is still constantly ongoing at a low rate by the end of the simulations. For the simulations including magnetic fields, the SF rate decreases earlier than in the non-magnetized comparison runs, as soon as equipartition is reached ($z \approx 3$) and is thus comperatively lower than in the comparison run or even stops completely by the end of the simulations. The magnetic configuration at equipartition provides additional support against further gas accretion, preventing the gas inside the halo from reaching the threshold density necessary to form stars.

Note that the details of SF depend on the resolution of the simulation. Springel & Hernquist (2003b) show that when increasing the resolution of the simulation, the time when the first stars form is pushed towards higher redshifts. Nevertheless, at low redshifts, the SF rate converges to a value independent of the resolution. Furthermore, the total stellar mass formed does not change with resolution. These details in the SF model also influence the turbulent dynamo action. The starting point of the dynamo action depends strongly on the time when the first gas has collapsed, cooled and reached small enough spatial scales. As soon as SF sets in, additional SN energy is injected into the system, leading to more turbulence and higher magnetic field growth rates. The saturation value of the magnetic field strength depends on the turbulent energy density, which in turn depends on the the total injected feedback and hence the total formed stellar mass.

The simulation ga1_bx18_nosf (not shown) is performed with the same set-up and methods, but with disabled SF module. Within this simulation, the magnetic energy density does not get amplified up to equipartition with the turbulent energy density, but only rises a few orders of magnitude. This

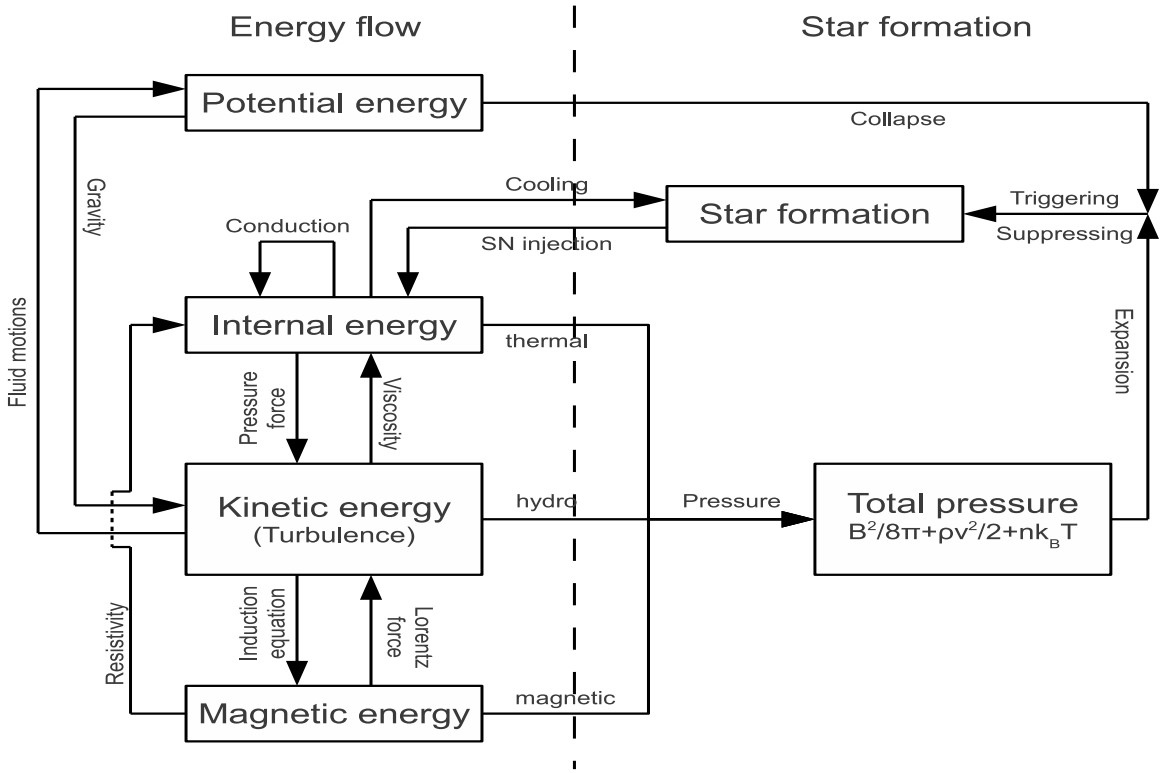

Figure 1.7: Diagram visualizing the flow of energy in the simulated MHD system. The SF model provides a source (SN injection) and a sink (cooling) of energy. On the other hand, the different pressure components (thermal, hydrodynamic and magnetic pressure) have an effect on the SF.

is clearly, because radiative cooling lowers the internal energy of the gas, thus allowing the gas to clump more heavily and reach higher densities. This results in smaller SPMHD smoothing lengths and hence the small-scale dynamo will also operate on smaller scales, thus leading to higher growth rates. Summing up, radiative cooling and SN feedback are important in MHD simulations of galactic halo formation.

1.5.3 Numerical reliability

The numerical magnetic divergence $\langle h\,|\nabla\cdot\mathbf{B}|\,/|\mathbf{B}|\rangle$ is a common measure regarding the reliability of SPMHD simulations (e.g. Price, 2012). It is calculated for every particle i inside its kernel, which is a sphere with radius equal to the smoothing length h_i. Even for simulations employing the Euler potentials, which are free of physical divergence by construction, this measure can reach values of the order of unity (Kotarba et al., 2009). The numerical divergence can be regarded as a measure for quality of the numerical calculations and the irregularity of the magnetic field inside each kernel and is not related to possible physical divergence (Kotarba et al., 2010; Bürzle et al., 2011a). Here, an estimator for the numerical divergence of the form

$$\mathrm{NumDivB}_i = \sum_j \frac{h_i + h_j}{|\mathbf{B}_i| + |\mathbf{B}_j|}\frac{m_j}{\rho_i}\,(\mathbf{B}_i - \mathbf{B}_j)\cdot\nabla W(r_{ij}, h_i) \tag{1.21}$$

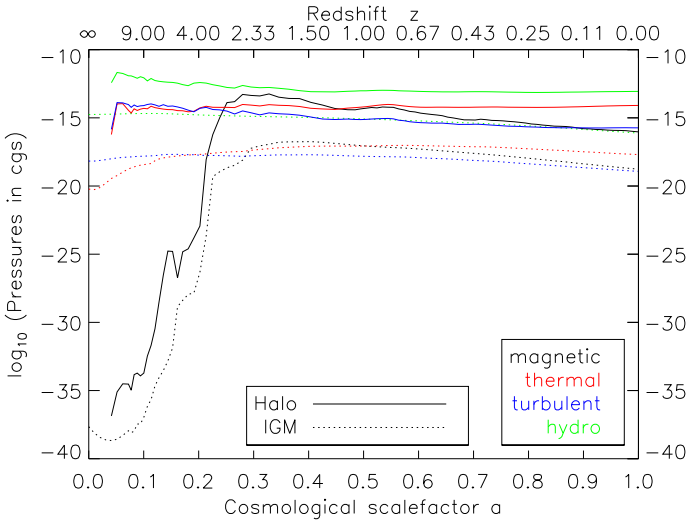

Figure 1.8: Volume-weighted energy densities as a function of redshift in the simulation ga2_bx18 inside the halo and within the IGM. The magnetic energy density (black line) gets amplified during the phase of halo formation until it reaches equipartition with the other energy densities, particularly the turbulent energy density (blue line).

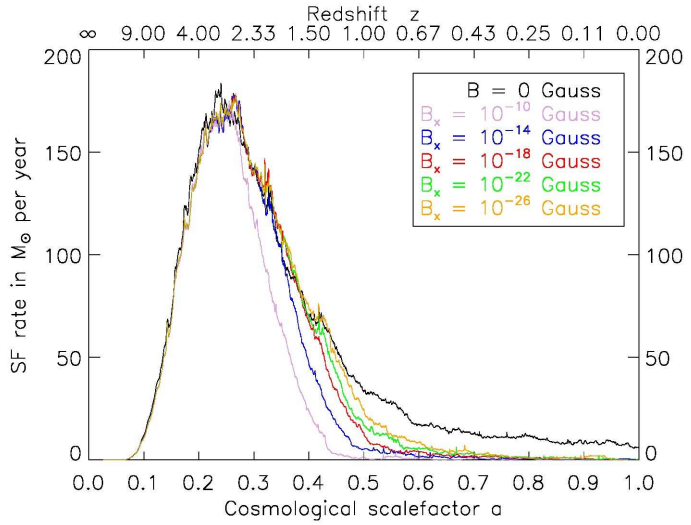

Figure 1.9: Total SF rate as a function of redshift in the simulations GA0 with different magnetic seed fields. For simulations with magnetic fields, the SF rate decreases when equipartition is reached and the additional magnetic pressure prevents the gas from reaching the density threshold required for SF.

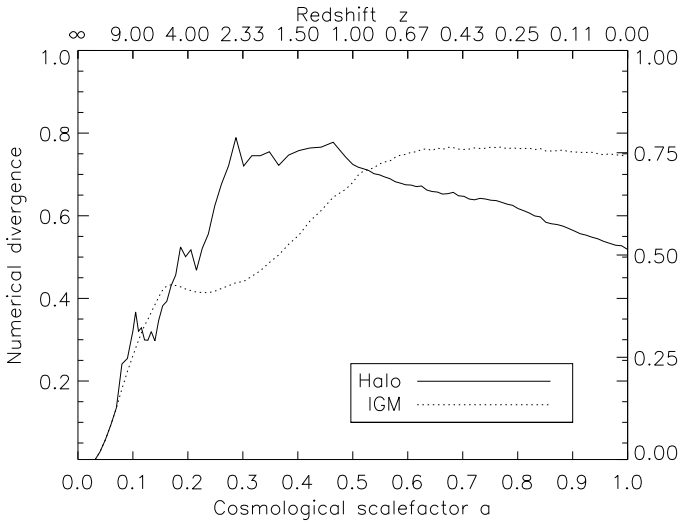

Figure 1.10: Mean numerical magnetic divergence measure $\langle h \left|\nabla \cdot \mathbf{B}\right| / \left|\mathbf{B}\right| \rangle$ in ga2_bx18 inside the halo and within the IGM.

is used, where W is the SPMHD kernel function between the particle i and its neighbours j.

Fig. 1.10 shows the mean numerical divergence within the halo (solid line) and within the IGM (dashed line) as a function of scalefactor for the simulation ga2_bx18. Throughout the entire simulation, the numerical divergence remains below unity. The numerical divergence is zero in the beginning of the simulations, as expected for a uniform magnetic seed field. During the phases of merger events and magnetic field amplification, the error estimator rises. The turbulent dynamo tangles the magnetic field lines and also creates irregularities below smoothing scales, resulting in a non-vanishing numerical divergence. During the phase of relaxation of the halo, NumDivB decreases, as the field lines are unfolded and ordered and the magnetic energy is dissipated or transferred to larger scales. Within the IGM, the numerical divergence remains constant. This is because within the IGM the NumDivB-decreasing process of magnetic field reordering is balanced by NumDivB-increasing processes. These are the accretion of gas onto the halo and the expansion of space, both resulting in an increasing smoothing length and thus an increasing NumDivB.

1.6 Agreement of model and simulations

Since the simulations start at a finite redshift and not at $z = \infty$, a simple shift of $B_0^2 = a_{\rm start}^{-4} B_{\rm start}^2$ for the initial magnetic field strength in equation (1.18) is used. The characteristic turbulent quantities in equation (1.14) are assumed to be constant in space and time. This approximation is good for the phase of strong SF between redshift 10 and redshift 1, where also the majority of the magnetic amplification is taking place, while later the growth rate is truncated and the form of the turbulent quantities is negligible.

In Fig. 1.11 simulated growth curves of the magnetic field strength are shown (dashed lines). These curves match notably well with the calculated curves (solid lines). Table 1.2 shows the numerical values used for the calculations, which are resulting in a time-scale (e-folding time) of ≈ 90 Myr for the growth of the large-scale magnetic field. Extracting such values directly from the simulations

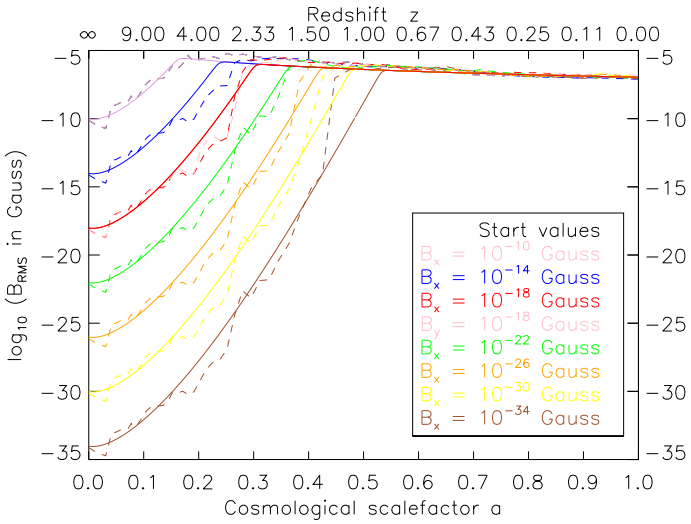

Figure 1.11: Analytical growth functions (solid lines) as given by equation (1.18) using the parameters listed in Table 1.2 for different magnetic seed field strengths. After an initial cosmological dip, the magnetic field grows exponentially until it reaches equipartition with the turbulent energy density. Additionally, the simulated growth cruves from Fig. 1.5 are shown (dashed lines).

is quite challenging, as the density, velocity and length scales within the simulated galactic haloes range over many orders of magnitude. However, the length scale $l_{\rm turb}$ on which the magnetic energy density increases first within the main halo is determined by the size of SF regions, which (within the main halo) can be associated to substructures. Such substructures (clumps of gas, stars and dark matter) can be identified using SUBFIND (Springel et al., 2001a; Dolag et al., 2009). Only the largest substructures still contain gas and form stars within the main halo, having masses of $\approx (10^8 - 10^{10}) {\rm M}_\odot$ and thereby diameters of a few 10 kpc. They are orbiting with typical velocities of a few 100 km s^{-1}, inducing gas rms velocities within the main halo between 50 and 100 km s^{-1} during the time of rapid growth of the halo, where the magnetic amplification is also taking place (between $z \approx 10$ and $z \approx 1$). Such values strongly motivate the choice of $l_{\rm turb} \approx 25$ kpc and $v_{\rm turb} \approx 75$ km s^{-1}, leading to the good agreement between the simulations and the analytical model.

Fig. 1.12 shows a comparison of the analytical growth function (red line) as calculated according to equation 1.18 using the values given in Table 1.2 together with the halo rms magnetic field strength in the simulations ga0_bx18, ga1_bx18 and ga2_bx18, respectively. All curves start with the same magnetic seed field of $B_{\rm start} = 10^{-18}$ G. The resolution of the simulations increases by each a factor of roughly 10 from ga0 to ga1 and from ga1 to ga2, respectively. Compared to the simulation with the standard resolution (brown line), the analytical growth function fits the simulated magnetic field evolution very well. Also, for higher resolutions (black and green lines), the fit is convincing. Note that for higher resolutions, SF sets in at higher redshifts leading to an earlier rise of collapsed, cooled gas and feedback and hence an earlier starting point for the turbulent dynamo. Nevertheless, the saturation value of the magnetic field strength is indistinguishable.

For the calculation of the hydrodynamic and magnetic Reynolds numbers, the typical velocity V and length scale L are determined by the physical properties of the system, i.e. the sound speed $c_{\rm s}^2 = \gamma(\gamma-1)u$ and the Alfvén speed $v_{\rm a}^2 = \mathbf{B}^2/4\pi\rho$ and the size of the halo, respectively, which do not depend on resolution. Within all the simulations, a constant turbulent resistivity $\eta_{\rm turb}$ is used and

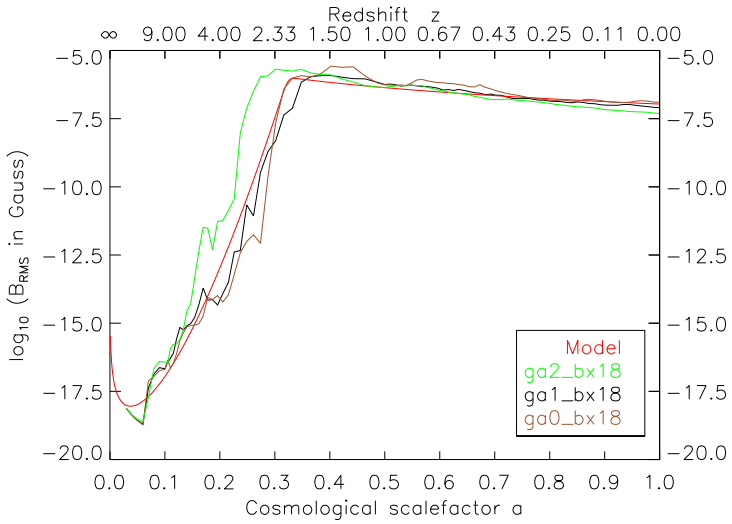

Figure 1.12: Volume-weighted rms magnetic field strength inside the halo as a function of redshift for three simulations with the same magnetic seed field of 10^{-18} G but different resolution, together with the analytical growth function (see equation (1.18) and Table 1.2). The analytical function fits the simulated evolution of the halo magnetic field very well.

hence, Rm stays constant. Additionally, artificial viscosity as given by Price (2012) is applied, where ν depends on particle properties and spacings. A higher resolution thus leads to smaller ν and thus (given the constant V and L) to higher Re numbers and hence more turbulence. A higher (or, better resolved) turbulence in turn results in a higher growth rate of the magnetic field.

The cosmological turbulent dynamo as described by equation (1.18) reproduces the main features of the simulated non-ideal magnetic field amplification very well.

1.7 Summary

In this paper, the evolution of magnetic fields during galactic halo formation is discussed. The main focus is placed on the investigation of the processes responsible for the amplification of magnetic fields from seed field levels to observed values. An analytical model for the evolution of the magnetic field driven by a turbulent dynamo is presented and the predictions of this model are compared with numerical, cosmological simulations of Milky Way-like galactic halo formation including the evolution of magnetic fields, radiative cooling and SF. The most important results are summarized as follows.

- A primordial magnetic seed field of low strength can be amplified up to equipartition with other energy densities during the formation and virialization of a galactic halo in a ΛCDM universe. The final magnetic field strength decreases with a slope of ≈ -1.0 from ≈ 10^{-6} G in the centre to ≈ 10^{-9} G behind the virial radius (IGM) of the halo and also reaches ≈ 10^{-5} G in interacting systems. These values are in notably good agreement with observations (Beck et al., 1996; Kronberg et al., 2008).

- The magnetic field amplification in filaments and protohaloes is dominated by turbulent dynamo action. Radiative cooling of the primordial gas is needed in order to reach spatial scales

small enough for the turbulent dynamo to operate efficiently. Equipartition is reached on small scales first and later on larger scales, consistent with theoretical expectations (Brandenburg & Subramanian, 2005; Shukurov, 2007; Arshakian et al., 2009). The turbulence is driven by the gravitational collaps, by SN activity and by mergers of protohaloes into the main galactic halo. After equipartition is reached, the magnetic energy decays with a power-law dependance of $B_t \sim t^{-4/3}$. The IGM magnetic field is amplified by outflows of magnetized gas from the centre of the haloes and by merger-driven shock amplification outside the main halo.

- The amplification time-scale (e-folding time) of the order of 10^7 yr is small enough to describe the generation of strong magnetic fields in irregular galaxies at high redshifts as observed (e.g. Bernet et al., 2008).
- The structure of the resulting magnetic field is random and turbulent. Additional dynamo processes, e.g. the α-ω dynamo (Ruzmaikin et al., 1979; Shukurov, 2007) or the CR-driven dynamo (Lesch & Hanasz, 2003; Hanasz et al., 2009a), are needed to produce regularity in the magnetic field topology.
- Last, but not least, a basic analytical model is able to reconstruct the numerical results very accurately. Weak magnetic perturbations grow in a non-stationary turbulent hydrodynamical flow. This amplification is slightly modified by the ΛCDM cosmology, particularly in the early universe. Non-ideal truncation of the growth rate finally yields equipartition. These processes result in an analytical growth function which fits the simulations astonishingly well.

In the current picture of galaxy formation – together with cooling and SF – magnetic fields are efficiently amplified from seed field levels up to the observed values. However, their detailed influence on the dynamics of the gas and the underlying seeding mechanisms still remains unclear and needs to be investigated further.

1.8 Acknowledgments

We thank the anonymous referee for the comments, which helped to improve many parts of this paper. Special thanks to Felix Stoehr for providing the original initial conditions. Rendered graphics are created with P-SMAC2 (Donnert et al., in preparation). FAS is supported by the DFG Research Unit 1254. KD is supported by the DFG Priority Programme 1177 and by the DFG Cluster of Excellence 'Origin and Structure of the Universe'.

Chapter 2

Paper II: Strong magnetic fields in protogalaxies from supernova seeding

A.M. Beck, K. Dolag, H. Lesch & P.P. Kronberg, 2013,
Monthly Notices of the Royal Astronomical Society, 435, 3575

ABSTRACT

We present a model for the seeding and evolution of magnetic fields in protogalaxies. Supernova (SN) explosions during the assembly of a protogalaxy self-consistently provide magnetic seed fields, which are subsequently amplified by compression, shear flows and random motions. Our model explains the origin of strong magnetic fields of μG amplitude within the first SF protogalactic structures shortly after the first stars have formed. We implement the model into the MHD version of the cosmological N-body / SPH simulation code GADGET and we couple the magnetic seeding directly to the underlying multi-phase description of SF. We perform simulations of Milky Way-like galactic halo formation using a standard ΛCDM cosmology and analyse the strength and distribution of the subsequent evolving magnetic field. Within SF regions and given typical dimensions and magnetic field strengths in canonical SN remnants, we inject a dipole-shape magnetic field at a rate of $\approx 10^{-9}$ G Gyr^{-1}. Subsequently, the magnetic field strength increases exponentially on timescales of a few tens of millions of years within the innermost regions of the halo. Furthermore, turbulent diffusion, shocks and gas motions transport the magnetic field towards the halo outskirts. At redshift $z \approx 0$, the entire galactic halo is magnetized and the field amplitude is of the order of a few μG in the center of the halo and $\approx 10^{-9}$ G at the virial radius. Additionally, we analyse the intrinsic rotation measure (RM) of the forming galactic halo over redshift. The mean halo intrinsic RM peaks between redshifts $z \approx 4$ and $z \approx 2$ and reaches absolute values around 1000 rad m^{-2}. While the halo virializes towards redshift $z \approx 0$, the intrinsic RM values decline to a mean value below 10 rad m^{-2}. At high redshifts, the distribution of individual SF and thus magnetized regions is widespread. This leads to a widespread distribution of large intrinsic RM values. In our model for the evolution of galactic magnetic fields, the seed magnetic field amplitude and distribution are no longer a free parameters, but determined self-consistently by the SF process occuring during the formation of cosmic structures. Thus, this model provides a solution to the seed field problem.

Key words: methods: analytical, methods: numerical, galaxies: formation, galaxies: haloes, galaxies: magnetic fields, early Universe

This chapter is a complete presentation of Beck et al. (2013a).

2.1 Introduction

Radio observations reveal magnetic fields on all scales in the Universe, ranging from small planets to large clusters of galaxies (for reviews on cosmic magnetism see e.g. Kronberg, 1994; Beck et al., 1996; Widrow, 2002; Kulsrud & Zweibel, 2008; Vallée, 2011a,b) and even the largest voids (see e.g. Neronov & Vovk, 2010). However, the origin and evolution of the magnetized Universe is still not well understood. At first, magnetic seed fields must have been created during structure formation. Afterwards, the seeds were amplified to the observed present-day values and transported to the present-day distribution by a complex interplay of MHD processes.

In the standard cosmological model, structures are believed to have assembled in a hierarchical process, with the smallest objects forming first and subsequently merging (on structure formation see e.g. the book of Mo et al., 2010). This bottom-up scenario is supported by numerical simulations, showing good agreement between the observed and calculated distribution of large structures. The process of structure formation can already lead to the creation of magnetic seed fields.

Faraday rotation is a powerful method to measure extragalactic magnetic fields. It occurs when the plane of polarization of a wave travelling towards the observer is rotated by an intervening magnetic field. The strength of the effect is described by the rotation measure (RM). Observations show that galaxies or galactic haloes at redshifts $z \gtrsim 2$ typically have a widespread distribution of absolute RM values of several 1000 rad m^{-2}. In contrast, RM values caused by the halo of our Galaxy are around 10 rad m^{-2} (see e.g. Simard-Normandin et al., 1981; Kronberg & Perry, 1982; Welter et al., 1984; Carilli et al., 1994; Oren & Wolfe, 1995; Carilli et al., 1997; Athreya et al., 1998; Pentericci et al., 2000; Broderick et al., 2007; Kronberg et al., 2008; Mao et al., 2010; Gopal-Krishna et al., 2012; Hammond et al., 2012; Mao et al., 2012). However, as the RM is the integrated line-of-sight product of electron density and magnetic field strength, difficulties arise in determining the origin of such large RM. It is not yet clear whether the observed large RM at high redshifts are caused directly by the sources or by intervening gas clouds with unknown impact parameters along the line of sight. In any case, the origin and evolution of those RM must be coupled to the formation and evolution of cosmic structures.

Stars are among the earliest objects in the Universe (see e.g. Abel et al., 2002; Bromm et al., 2009). Within protogalactic gas clouds, battery effects can generate very weak magnetic seed fields. These small fields are then carried into the newly forming stars, at which point they are enhanced by gravitational compression. Subsequently, highly turbulent and fast rotating (proto)stars amplify the seeds by small-scale and $\alpha\omega$-Dynamo action (on dynamos see e.g. Shukurov, 2007). When the stars explode as supernovae (SN), their magnetic fields are infused together with the gas into the surrounding interstellar medium. The magnetic field strength within SN remnants is observed to be between 10^{-6} and 10^{-3} G on scales of order a couple pc (Reynolds et al., 2012).

Focusing now on galactic scales, where μG interstellar magnetic fields are common, a variety of processes can be responsible for amplification of seed fields. Amplification is assumed to occur mainly by gravitational compression, turbulence and dynamo action. The most prominent dynamo theory is the mean-field dynamo (Krause & Raedler, 1980). However, this dynamo mechanism is challenged by the observations of strong magnetic fields in irregular objects or at very high redshift (see e.g. Bernet et al., 2008; Kronberg et al., 2008). In contrast, fast turbulent dynamos operate on time-scales of a few tens of millions of years and lead to exponential growth of the magnetic energy, first on small scales and then later transported to larger scales (see e.g. Zel'dovich et al., 1983; Kulsrud & Anderson, 1992; Kulsrud et al., 1997; Mathews & Brighenti, 1997; Malyshkin & Kulsrud, 2002; Brandenburg & Subramanian, 2005; Arshakian et al., 2009; Schleicher et al., 2010).

Random motions created by gravitational collapse or injected during structure formation (e.g. by feedback) can drive a small-scale dynamo. Using analytical calculations and numerical simulations,

Beck et al. (2012) showed that the process of galactic halo formation and virialization (see also Wise & Abel, 2007) is sufficient to enhance primordial magnetic fields up to the observed μG values. In their model, magnetic perturbations are amplified by turbulent motions until the point where equipartition is reached between the magnetic and turbulent energy density. Additionally, Kotarba et al. (2011) and Geng et al. (2012b,a) show the amplification of magnetic fields in major and minor galactic mergers. Both accompany structure formation, especially at high redshifts (Somerville et al., 2000). Recently, the first simulations of galaxy formation have been carried out that include the evolution of magnetic fields (see e.g. Wang & Abel, 2009; Beck et al., 2012; Pakmor & Springel, 2013; Latif et al., 2013). However, these simulations assumed the magnetic field to be of primordial origin and did not seed them within the simulations.

A more consistent description of the origin of galactic magnetic fields needs to incorporate SN-created seed fields. Their existence is independently verified and the resulting amplification, diffusion and gas motions have been calculated and discussed in several articles (see e.g. Bisnovatyi-Kogan et al., 1973; Rees, 1987; Pudritz & Silk, 1989; Kronberg et al., 1999; Rees, 1994, 2006; Chyży et al., 2011). A schematic overview of this magnetic build-up scenario during galaxy formation is shown in Fig. 2.1.

In principle, a similar scenario can be constructed with active galactic nuclei (AGN). Within the highly conducting accretion discs surrounding supermassive black holes, magnetic fields can be easily seeded by battery processes and amplified on very short dynamical time-scales. As indicated by observations of radio galaxies, the magnetized material is transported into the intergalactic medium (IGM) along powerful jets. This magnetized material can then mix with the galactic gas content and provide a magnetic seed field within the galaxies (see e.g. Willis & Strom, 1978; Strom & Willis, 1980; Kronberg, 1994; Furlanetto & Loeb, 2001; Kronberg et al., 2001; Rees, 2006; Kronberg, 2009; Colgate et al., 2011). The magnetic energy provided by an AGN can, if compressed into the volume of a galaxy, lead to μG magnetic field amplitudes (see Daly & Loeb, 1990; Kronberg et al., 2001). So far, simulations with AGN seeding and subsequent evolution have been mostly applied to the magnetization of the IGM of galaxy clusters (see e.g. Xu et al., 2008, 2010, 2012). However, within galaxies, the first generation of stars can provide magnetic seed fields earlier than the first generation of AGN.

In this work, we present a numerical model for the seeding of magnetic fields by SN explosions. We repeat previous cosmological simulations of Milky Way-like galactic halo formation (Beck et al., 2012), by incorporating our new SN seeding model. We analyse the distribution and amplitude of the resulting halo magnetic field. We also study the redshift evolution of the intrinsic RM of the galactic halo.

The article is organized as follows. The numerical method and initial conditions are briefly described in Section 2.2. Section 2.3 introduces the new seeding model. An analysis of our simulations, including the magnetic field evolution and the resulting intrinsic RM is given in Section 2.4. The main results are summarized in Section 2.5.

2.2 Numerics

2.2.1 Numerical method

We apply the same numerical method as already used in Beck et al. (2012). The simulations are performed with the N-body / SPMHD code GADGET (Springel et al., 2001b; Springel, 2005; Dolag & Stasyszyn, 2009). This code uses a formulation of SPH which conserves both energy and entropy (Springel & Hernquist, 2002). For a recent review on the SPH and SPMHD method see Price (2012). On-the-fly calculation of centre positions and virial radii of bound structures (haloes and subhaloes) is performed with SUBFIND (Springel et al., 2001a; Dolag et al., 2009).

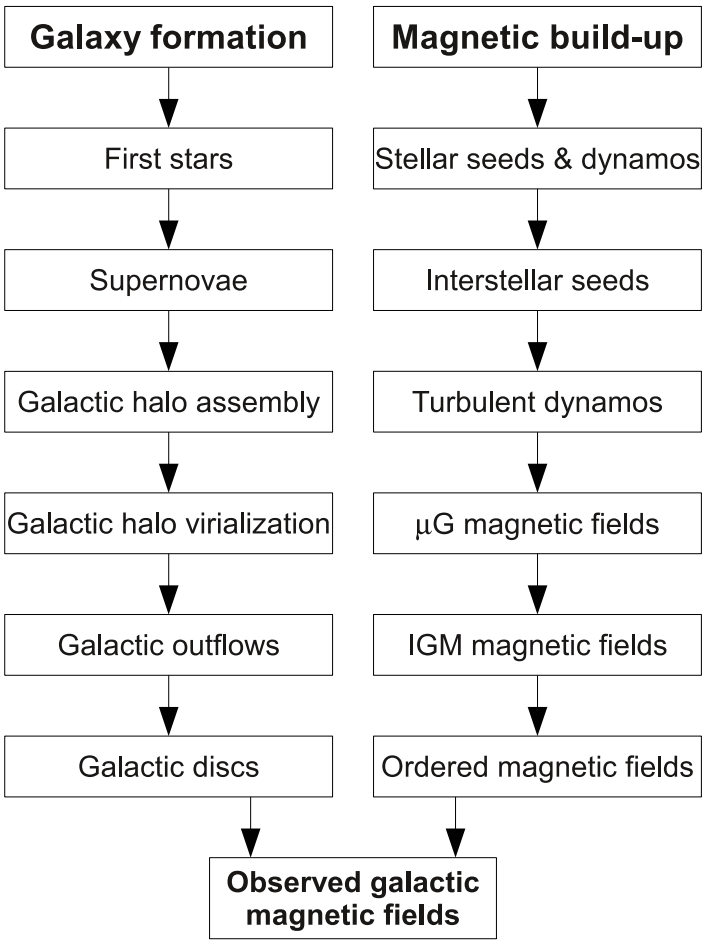

Figure 2.1: Schematic overview of the process of SN magnetic seeding, amplification and ordering during structure formation. Note that various other seeding mechanisms can mutually cooperate and provide local (e.g. AGN) or global (e.g. primordial) magnetic seed fields.

Multi-phase Model Parameters		
Gas consumption time-scale	$t_{\rm SF}$	2.1 Gyr
Gas density threshold	$n_{\rm th}$	0.13 cm^{-3}
SN mass fraction	β	0.1
SN per solar mass formed	α	0.008 $M_{\odot}^{-1}$
Evaporation parameter	A	1000
Effective SN temperature	$T_{\rm SN}$	10^8 K
Temperature of cold clouds	$T_{\rm CC}$	1000 K

Table 2.1: Parameters of the SF model (Springel & Hernquist, 2003a) used in the simulations.

Furthermore, we apply the Springel & Hernquist (2003a) SF model without the implementation of galactic winds. It describes radiative cooling, UV background heating and SN feedback in a consistent two-phase sub-resolution model for the interstellar medium. Cold clouds with a fixed temperature of $T_{\rm CC}$ are embedded into a hot ambient medium at pressure equilibrium. These cold clouds will evaporate with an efficiency parameter of A and form stars on a time-scale of $t_{\rm SF}$ at a density threshold of $\rho_{\rm th}$. A fraction β of these stars are expected to die instantly as SN, thereby heating the gas with a temperature component of $T_{\rm SN}$. Additionally, the gas is loosing energy via radiative cooling, modeled by assuming a primordial gas composition and a temperature floor of 50 K. The cooling depends only on density and temperature and not on metallicity. This leads to a self-regulated cycle of cooling, SF and feedback within the gas. The numerical values for the SF model in our simulations are given in Table 1.

Ideal MHD is implemented into GADGET following Dolag & Stasyszyn (2009) using the standard (direct) method, where the magnetic field is evolved by the induction equation and reacts back on the gas with the Lorentz force. Additionally, we need to model the diffusion of the magnetic field from the SF regions into the surrounding medium in a physically plausible way. Our approach is based on the implementation of magnetic resistivity in GADGET as described in Bonafede et al. (2011) using the diffusion coefficient η at an assumed constant value of $10^{27}{\rm cm}^2$ s^{-1}. This value is reasonable for galactic scales (Longair, 2010). Expect for the magnetic resistivity, we do not use an explict scheme to control the magnetic divergence (such as Dedner cleaning (Dedner et al., 2002; Stasyszyn et al., 2013), or any Euler potential method). The resistivity is represented by an effective subgrid model for the turbulent magnetic field decay and its value is larger than those of numerical or ohmic resistivity. However, as in our case the initial magnetic fields are very localized within SF regions and we need to handle carefully those cases in which magnetic fields are diffused outside the SF regions. This can happen in an implausible and unphysical way. Hence, we limit the distance over which the magnetic field is transported in each time-step, depending on the local diffusion velocity, diffusion length and time-step. Within our cosmological simulations we employ the transport of the magnetic field at each time-step in the following way.

Each SPMHD particle has an unique time-step Δt and smoothing length h (i.e. resolution length). First, we estimate the local diffusion speed

$$V_{\rm D} = \sqrt{\frac{1}{2}\left(c_{\rm s}^2 + v_{\rm a}^2\right)} \tag{2.1}$$

as the square-root mean of the local sound speed and Alfvén speed. Secondly, we estimate the distance $L_{\rm D}$ over which diffusion is taking place,

$$L_{\rm D} = V_{\rm D}\Delta t \tag{2.2}$$

as the product of local diffusion speed and time-step. If the local diffusion distance $L_{\rm D}$ is larger than our spatial resolution element (given by the smoothing length h), the normal diffusion coefficient η is used. If $L_{\rm D}$ is smaller than our spatial resolution element, we follow a stochastic approach in modelling the magnetic diffusion. In analogy to the stochastic SF algorithm, we draw a random number from the interval $[0, 1[$ and compare it to the quotient $L_{\rm D}/h$ of diffusion distance and smoothing length. If the random number exceeds the quotient $L_{\rm D}/h$ normal diffusion is performed. Otherwise, we switch off the diffusion by setting the diffusion coefficient η to zero for this time-step. Furthermore, we employ a minimum value of 5 km s^{-1} for the diffusion velocity. This new diffusion model allows us to mimic the transport of magnetic energy outside the SF regions in a conservative way and successfully suppresses numerical diffusion of the magnetic field into low-density regions.

2.2.2 Initial conditions

We use the same initial conditions as in Beck et al. (2012), which are originally introduced in Stoehr et al. (2002). Out of a large cosmological box, with a power spectrum index for the initial fluctuations

of $n = 1$ and an amplitude of $\sigma_8 = 0.9$ a Milky Way-like dark matter halo is identified. Simulations with different resolutions of this halo are created and labelled GA0, GA1 and GA2, containing 13 603, 123 775 and 1 055 083 dark matter particles inside the virial radius. The forming dark matter halo is comparable to the halo of the Milky Way in mass ($\approx 3 \times 10^{12} M_{\odot}$) and in virial size ($\approx 270$ kpc). The halo does not undergo any major merger after a redshift of z≈2 and also hosts a subhalo population comparable to the satellite population of the Milky Way. In order to add a baryonic component, the high-resolution dark matter particles are split into an equal amount of gas and DM particles. The mass of the initial DM particle is split according to the cosmic baryon fraction, conserving the centre of mass and the momentum of the parent DM particle. The new particles are displaced by half the mean interparticle distance.

2.3 Magnetic Seeding model

In this section we present the SN seeding model. We describe the numerical model for the amplitude of the magnetic energy injection, as well as the corresponding dipole structure. Starting with the induction equation of non-ideal MHD we include a time-dependent seeding term on the right-hand side of the induction equation in addition to the convective and (spatially constant) resistive term, resulting in

$$\frac{\partial \mathbf{B}}{\partial t} = \nabla \times (\mathbf{v} \times \mathbf{B}) + \eta \Delta \mathbf{B} + \left. \frac{\partial \mathbf{B}}{\partial t} \right|_{\mathrm{Seed}} . \tag{2.3}$$

The magnetic seeding amplitude per time-step Δt is given by

$$\left. \frac{\partial \mathbf{B}}{\partial t} \right|_{\mathrm{Seed}} = \sqrt{N_{\mathrm{SN}}^{\mathrm{eff}}} \frac{B_{\mathrm{Inj}}}{\Delta t} \mathbf{e}_{\mathrm{B}}, \tag{2.4}$$

where $\mathbf{e}_{\mathrm{B}}$ is a unity vector, B_{Inj} defines the injected magnetic field amplitude and $N_{\mathrm{SN}}^{\mathrm{eff}}$ is a normalization constant, which specifies the effective number of SN explosions. The number of SN explosions is not a free input parameter into our model but is calculated directly from the subgrid model for SF. Our simulations include SF via the Springel & Hernquist (2003a) model; however, we note that our seeding model can easily be coupled to any other SF model. The mass of cold gas turning into stars, per time-step, is

$$m_* = \frac{\Delta t}{t_*} m_{\mathrm{c}}, \tag{2.5}$$

with m_{c} the mass of cold gas available for SF. Within the adapted SF model, a total gas consumption time-scale t_{SF} is scaled by the gas density and a density threshold to yield the local SF time-scale

$$t_* = t_{\mathrm{SF}} \left(\frac{\rho_{\mathrm{th}}}{\rho} \right)^{\frac{1}{2}} . \tag{2.6}$$

The effective number of SN explosions is given by

$$N_{\mathrm{SN}}^{\mathrm{eff}} = \alpha m_*, \tag{2.7}$$

where the number of SN events per formed solar mass in stars is specified by α. Its numerical value can be calculated from the initial mass function (see Hernquist & Springel, 2003) and the corresponding value can be found in Table 2.1. We calculate the total injected magnetic field amplitude for all SN events to be

$$B_{\rm Inj}^{\rm all} = \sqrt{N_{\rm SN}^{\rm eff}} B_{\rm SN} \left(\frac{r_{\rm SN}}{r_{\rm SB}}\right)^2 \left(\frac{r_{\rm SB}}{r_{\rm Inj}}\right)^3. \tag{2.8}$$

Here, $B_{\rm SN}$ is the mean magnetic field strength within one SN remnant of radius $r_{\rm SN}$. We assume a spherical geometry for the remnant and isotropically expand the remnant's magnetic field from the initial radius into a bubble with radius $r_{\rm SB}$. The bubbles are then randomly placed and mixed within a sphere of radius $r_{\rm Inj}$ (for a similar scaling see Hogan, 1983). The size of the injection sphere is determined by the size of the numerical resolution elements (i.e. the SPMHD the smoothing length).

The magnetic field seeding rate that results from this model can be extrapolated from

$$\dot{B}_{\rm seed} \approx B_{\rm SN} \left(\frac{r_{\rm SN}}{r_{\rm SB}}\right)^2 \left(\frac{r_{\rm SB}}{r_{\rm Inj}}\right)^3 \frac{\sqrt{\dot{N}_{\rm SN}\Delta t}}{\Delta t}, \tag{2.9}$$

where $\dot{N}_{\rm SN}$ is the SN occurance rate. From Reynolds et al. (2012) we take for a canonical SN remnant a radius of $r_{\rm SN} = 5$ pc and a mean field strength of $B_{\rm SN} = 10^{-4}$ G, which we assume is afterwards blown into bubbles of $r_{\rm SB} = 25$ pc. Using equation 2.9, we can derive a quick estimate of the mean seeding rate of the Milky Way (volume rougly 300 kpc^3) during its lifetime of presumably 10 Gyr. If about 10^8 SN occured within our Galaxy, we find a magnetic seeding rate of $\approx 10^{-26}$ G s^{-1} or $\approx 10^{-9}$ G Gyr^{-1} (i.e. see also Rees, 1994). This estimate only takes into account the mixing of the past SN seed events; however, it neglects the subsequent evolution of the magnetic field. This can lead to amplification, distribution or dilution.

The magnetic field injected by the seeding term must be divergence-free. Hence, it is natural to choose a dipole structure with a dipole moment $\mathbf{m}$ and then the seeding term takes the form:

$$\left.\frac{\partial \mathbf{B}}{\partial t}\right|_{\rm Seed} = \frac{1}{|\mathbf{r}|^3}\left[3\left(\frac{\partial \mathbf{m}}{\partial t}\cdot \mathbf{e}_r\right)\mathbf{e}_r - \frac{\partial \mathbf{m}}{\partial t}\right], \tag{2.10}$$

with $\mathbf{e}_r$ the unity vector in $\mathbf{r}$ direction. Each SF region will create a magnetic dipole around itself. The time derivative of each dipole moment is then given by

$$\frac{\partial \mathbf{m}}{\partial t} = \sigma \frac{B_{\rm Inj}^{\rm all}}{\Delta t}\mathbf{e}_{\rm B}, \tag{2.11}$$

where σ is a numerical normalization constant and $\mathbf{e}_{\rm B} = \mathbf{a}/|\mathbf{a}|$ a unit vector defining the direction of the dipole moment. In the weak-field approximation we can choose the direction of the acceleration field $\mathbf{a}$.

In our numerical model, the magnetic dipoles do not extend to infinity. They are softened at the centre and truncated at the injection scale and the energy of the numerical dipoles has to be renormalized. Softening of the dipole is necessary in order to avoid discontinuities for $|\mathbf{r}| \to 0$. By integration over the modified volume, we follow Donnert et al. (2009) and find for the normalization constant

$$\sigma = r_{\rm Inj}^3 \sqrt{\frac{1}{2} f^3 (1 + f^3)}, \tag{2.12}$$

where $f = r_{\rm soft}/r_{\rm Inj}$ is the ratio between dipole softening length and truncation length (i.e. in SPMHD the smoothing length). In our implementation in the code, the truncation length is also the injection length $r_{\rm Inj}$. During the simulations, a magnetic field is injected on to its neighbour particles in a dipole shape for each SF gas particle. Overlapping dipoles are added linearly.

Simulation setup								
Scenario	N_{Gas}	N_{DM}	M_{Gas} $M_\odot$	M_{DM} $M_\odot$	$B^{SN}_{Strength}$	R^{SN}_{Radius}	R^{Bubble}_{Radius}	f^{SN}_{Soft}
ga0_seed_all	68323	68323	$2.6 \cdot 10^7$	$1.4 \cdot 10^8$	10^{-4} G	5 pc	25 pc	$0.25h$
ga1_seed_all	637966	637966	$2.8 \cdot 10^6$	$1.5 \cdot 10^7$	10^{-4} G	5 pc	25 pc	$0.25h$
ga2_seed_all	5953033	5953033	$3.0 \cdot 10^5$	$1.6 \cdot 10^6$	10^{-4} G	5 pc	25 pc	$0.25h$
ga2_seed_low	5953033	5953033	$3.0 \cdot 10^5$	$1.6 \cdot 10^6$	10^{-5} G	5 pc	25 pc	$0.25h$
ga2_seed_high	5953033	5953033	$3.0 \cdot 10^5$	$1.6 \cdot 10^6$	10^{-3} G	5 pc	25 pc	$0.25h$
ga2_prim	5953033	5953033	$3.0 \cdot 10^5$	$1.6 \cdot 10^6$	$B_{primordial} = 10^{-10}$ G			

Table 2.2: Set-up of the different simulations. The table lists the number of gas and dark matter particles, the mass of gas and dark matter particles, the initial SN remnant radius and magnetic seed field strength, and the numerical softening length (where h is the SPMHD smoothing length).

2.4 Simulations

This section presents the results of our cosmological simulations. Contour images of the different physical quantities and the calculation of intrinsic RM values are created by projecting the SPMHD data in a comoving (1 Mpc)^3 cube, centreed on the largest progenitor halo, on to a 512^2 grid using the code P-SMAC2 (Donnert et al., in preparation). The precise details of the projection algorithm can be found in Dolag et al. (2005). In principle, we calculate the overlap of each particle with each line of sight and integrate

$$A_{\rm proj} = \sigma \int \left[\sum \frac{m_j}{\rho_j} A_j W \left[d_j(r)/h_j \right] \right] dr, \tag{2.13}$$

where A is the quantity of interest, σ the integral normalization, m and ρ the particle mass and density, W and h the SPMHD kernel function and smoothing length and $d(r)$ the element of distance with respect to the position r along the line of sight. Table 2.2 shows the performed simulations: initial conditions of different resolution (GA0, GA1 and GA2) are used to study the seeding model and subsequent amplification.

2.4.1 Morphological evolution

Fig. 2.2 shows the projected and weighted gas density of the gas at six different redshifts in the simulation ga2_seed_all, together with the corresponding virial radii of the forming galactic halo. Fig. 2.3 shows the corresponding projected and weighted total magnetic field strength. The different phases during formation of the halo and the magnetic seeding, amplification and transport can be clearly seen. Within the first protohaloes and filaments, we find SF to set in at a redshift z≈20 and at that time the first magnetic seed fields are also created. The magnetic field is seeded at an amplitude of $\approx 10^{-9}$ G, consistent with our expectations from Section 2.3. In the regions without SF no magnetic field is yet present at these high redshifts. As long as stars continue to form magnetic fields are seeded within the simulation; however, given the decrease of the SF rate towards redshift z≈0, correspondingly less magnetic energy is injected. Subsequently, the seed fields are amplified by gravitational compression and turbulent dynamo action within the first structures (for the amplification mechanism, see also Beck et al., 2012). This leads to μG magnetic fields within the first protogalactic objects shortly after they form. Once seeded, the magnetic field is subject to amplification and diffusion and the contributions of additional SN can be neglected. Afterwards, the magnetic field starts to diffuse outwards from the SF regions and towards outer regions of the halo, thereby enriching the IGM with

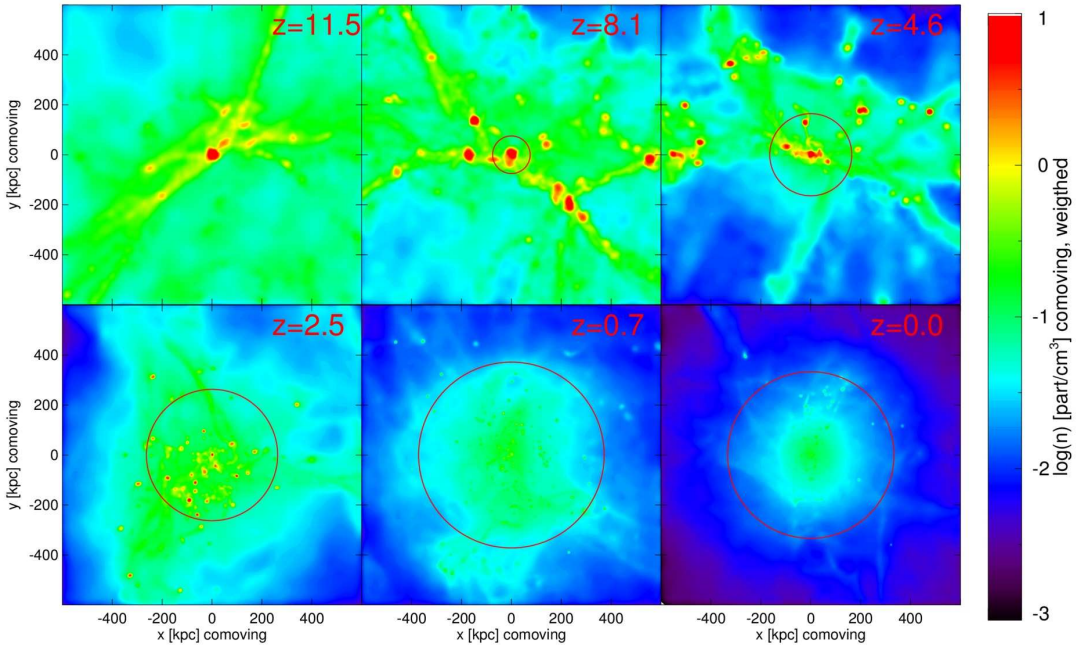

Figure 2.2: Projected and weighted (integrated over 1 Mpc) gas density $n_{\rm gas}$ in comoving units at different redshifts in the simulation ga2_seed_all centreed on the halo centre of mass. The circles indicate the virial radius of the halo. The formation of filaments and protohaloes with subsequent merger events is visible.

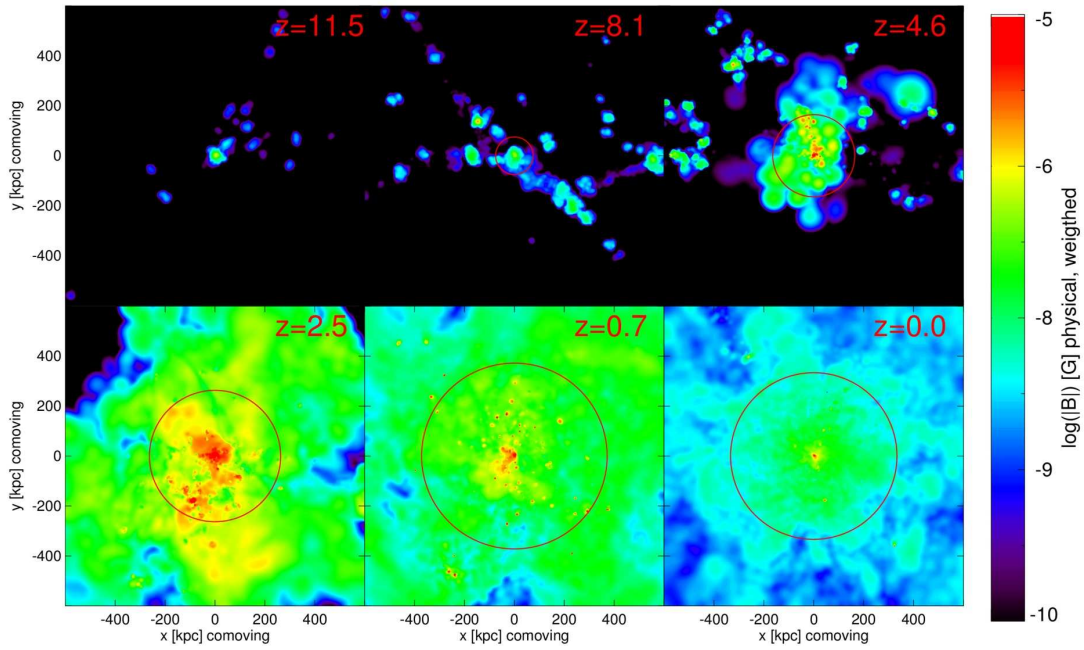

Figure 2.3: Projected and weighted (integrated over 1 Mpc) total magnetic field strength in physical units at different redshifts in the simulation ga2_seed_all centreed on the halo centre of mass. The circles indicate the virial radius of the halo. Seeding and amplification of the magnetic field within SF protohaloes is visible. Furthermore, gas motions and diffusion are carrying magnetic energy towards the halo outskirts.

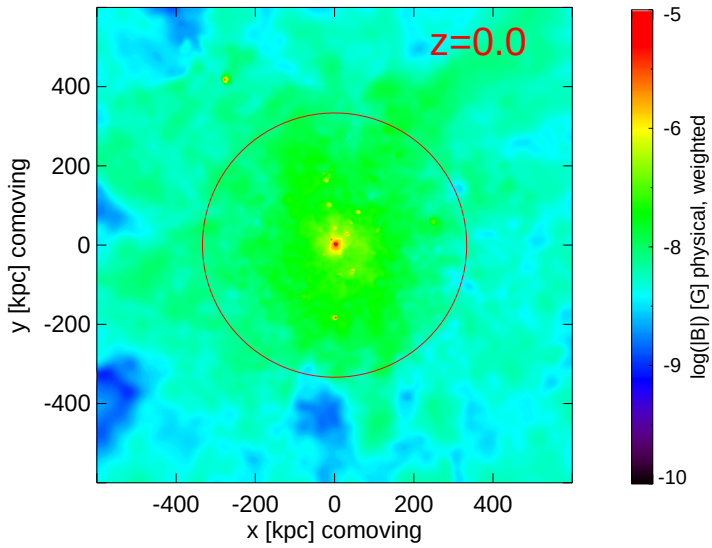

Figure 2.4: Projected and weighted (integrated over 1 Mpc) total magnetic field strength in physical units at redshift z≈0 in the simulation ga2_primordial. The plot corresponds to the bottom right panel of Fig. 2.3, just with a primordial seed field of $B_{\mathrm{primordial}} = 10^{-10}$ G and no SN seeding is applied.

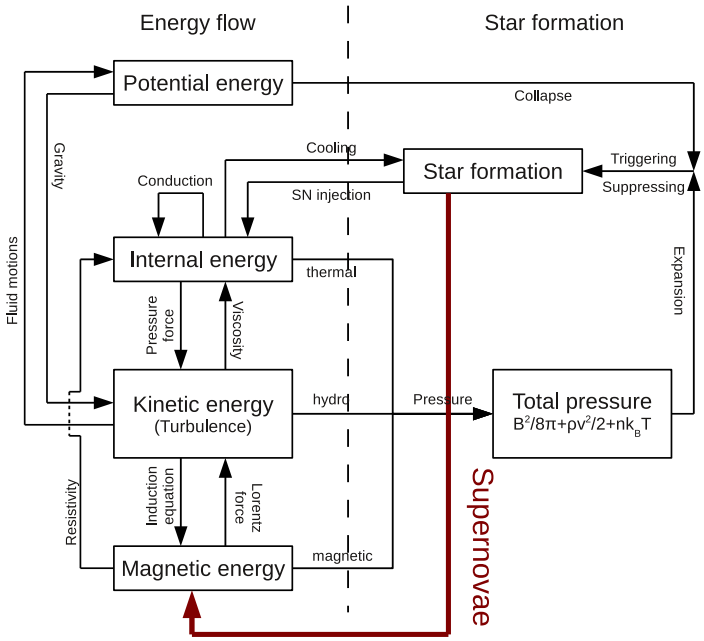

Figure 2.5: Flows of energy within our simulations. The diagram is an adaption of Fig. 7 of Beck et al. (2012) and shows the additional connection between SF and magnetic energy given by our new SN seeding model.

magnetic seed fields. Furthermore, while the assembly of the main galactic halo continues and merger events are taking place, shock waves are propagating outwards from the halo centre. The magnetic fields within the IGM are subsequently amplified by merger-driven shock waves propagating into the IGM. Within each shock wave, the magnetic field can be amplified by compression at the shock front and possible dynamo action behind the shock front (see e.g. Kotarba et al., 2011). Around a redshift of z≈2, the last major merger event takes place and the magnetic field saturates, i.e. it evolves into energy density equipartition. The magnetic field saturates within the innermost regions at a value of a few μG and at the halo outskirts at about $\approx 10^{-9}$ G, both at redshift z≈0.

Fig. 2.4 shows the result of a simulation run with a primordial seed field of $B_{\rm prim} = 10^{-10}$ G but the new diffusion model. The amplitude and distribution of the magnetic field at redshift z≈0 obtained by evolving a primordial seed field or by SN seeding and subsequent evolution are almost indistinguishable within the halo. Outside the halo, the amplitude is slightly higher in the simulation with a primordial seed field than in the simulation with the SN seeding model. For a detailed study of primordial seed fields during galactic halo formation, we refer to our old simulations described in Beck et al. (2012). Fig. 2.5 shows how the simulations have been modified. The most significant differences are the following. In the simulations of Beck et al. (2012), a primordial seed field is already present everywhere at high redshifts and the field is subject to amplification by the very first occurences of compression, random motions and shock waves. By contrast, in our new simulations with SN seeding (this work), the magnetic seed field has to be created first within the SF regions, before it can be subsequently amplified. SF is a new source of magnetic energy in addition to its property as a source and sink of thermal energy. Furthermore, to create an IGM magnetic field, diffusion and gas motions have to transport the magnetic field into the IGM first, before subsequent amplification can take place. Our new simulations do still not form a galactic disc; however, we note that the prior presence of μG magnetic fields at the centre of the halo is sufficient to demonstrate that a disc at the centre could host magnetic fields of similar strength.

2.4.2 Magnetic amplitude and filling factors

Fig. 2.6 shows the magnetic energy density $\varepsilon_{\rm mag} = B^2/8\pi$, the kinetic energy density $\varepsilon_{\rm kin} = \rho v^2/2$, the thermal energy density $\varepsilon_{\rm therm} = (\gamma - 1)\rho u$ and the turbulent energy density $\varepsilon_{\rm turb} = \rho v_{\rm turb}^2/2$ in the simulation ga2_seed_all. The adiabatic index γ is 5/3 and u denotes the internal energy. We estimate the turbulent velocity $v_{\rm turb}$ similarly to Kotarba et al. (2011) and Beck et al. (2012). It is approximated locally by calculating the root-mean-square velocity within the smoothing sphere of each individual SPMHD particle. Kotarba et al. (2011) claim it to be a good approximation of the turbulent velocity, although it might slightly overestimate the turbulence on small scales and it ignores turbulence on scales larger than the smoothing scale. We volume-weight the energy densities among the particles according to

$$\bar{\epsilon} = \sum_j \left(\epsilon_j \frac{m_j}{\rho_j}\right) / \sum_j \left(\frac{m_j}{\rho_j}\right), \tag{2.14}$$

where m and ρ are the local mass and gas density and represent the particle volume. At the beginning of the simulation the magnetic energy density is seeded at values significantly lower than the other energy densities. However, as the halo begins to assemble, the magnetic energy density is amplified to an equipartition value by compression and random motions created by the gravitational collapse. The magnetic energy density remains then within the same order of magnitude as the thermal and turbulent energy densities. After the last merger event, the entire halo virializes and irregularities within the velocity and magnetic fields are dissipated, leading to decaying energy densities.

Fig. 2.7 shows radial profiles of the mass-weighted magnetic field strength inside the galactic halo for two different redshifts. At both times, magnetic field strengths of $\approx 10\mu$G are reached in the

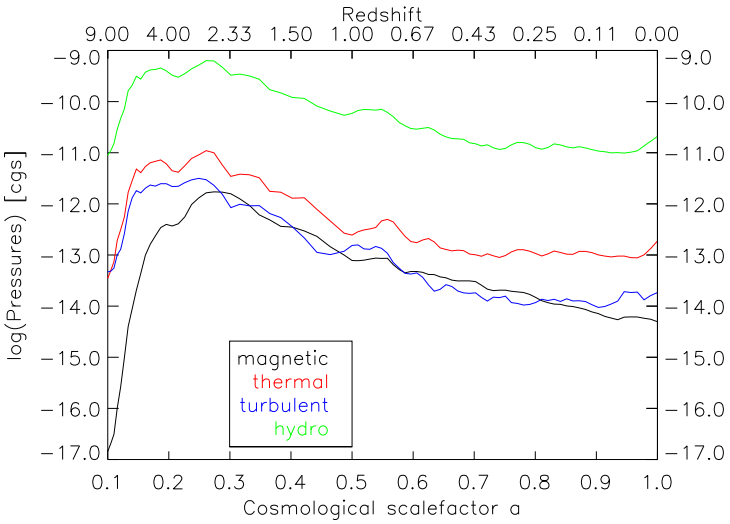

Figure 2.6: Volume-weighted energy densities as a function of redshift in the simulation ga2_seed_all inside the largest progenitor halo. The magnetic energy density gets seeded and amplified during the phase of galactic halo formation until it reaches equipartition with the corresponding energy densities, particularly the turbulent energy density.

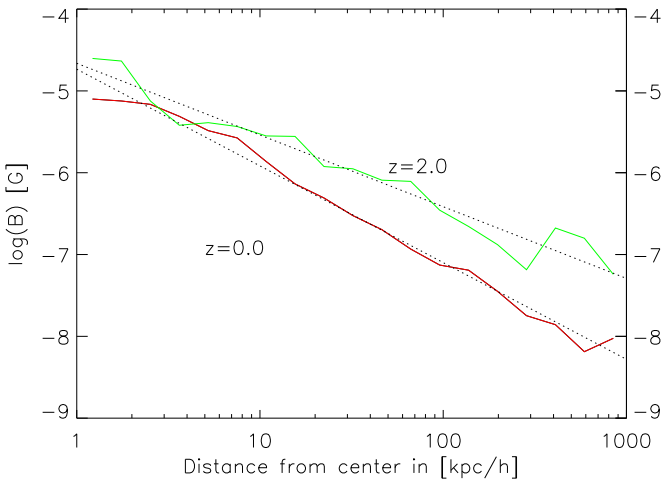

Figure 2.7: Radial profiles of the mass-weighted magnetic field strength inside the largest progenitor halo in the simulation ga2_seed_all for redshifts z≈2 and z≈0, respectively. The slope of the magnetic field at redshift z≈2 is about −0.9 and that at redshift z≈0 about −1.2.

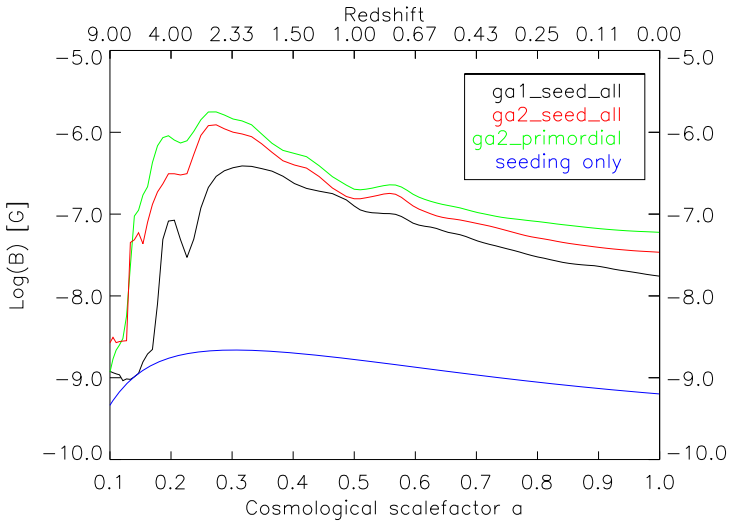

Figure 2.8: Volume-weighted magnetic field strength as a function of redshift in different types of simulations inside the largest progenitor halo. The results from the primordial seed field and from the SN seeded fields agree well. The seeding by SN alone seems not sufficient to generate strong magnetic fields and additional amplification or injection via AGN (see e.g. Daly & Loeb, 1990; Kronberg et al., 2001) is necessary.

innermost parts of the halo; however, at redshift z≈0 the magnetic field strength at the halo outskirts is slightly lower. Outside the halo the magnetic field decreases, because forces maintaining the magnetic field operate efficiently only at the halo centre. Furthermore, after the halo has assembled, the effect of shock waves contributing to the amplification of the IGM magnetic field is significantly reduced.

Fig. 2.8 shows the magnetic field strength within the halo for different types of simulations. In the simulation with the primordial seed field (starting value of 10^{-10} G) the magnetic field is amplified during the formation of the halo until it saturates around a redshift of z≈2 at values of a few μG. Subsequently, the magnetic field is subject to diffusion, which leads to a decay of the amplitude until redshift z≈0 to values of a few 10^{-8} G. In the simulations performed with SN seeding, the magnetic field is first seeded at an amplitude of $\approx 10^{-9}$ G Gyr^{-1} and then behaves qualitatively similar manner to the run with primordial seeding. However, in the simulation with the primordial seed field, the amplification is more efficient and the saturation values at high and at low redshifts are slightly higher. In simulations with higher resolution, the magnetic field is amplified more efficiently and it saturates at a slightly higher amplitude.

Fig. 2.8 also shows a fictive growth curve corresponding to the case where the only source of magnetic energy is SN seeding. We model this case by calculating the cumulative seeding rate over time as approximated by equation 2.9 with the SN rate normalized to the Milky Way and evolving with time as suggested by Hernquist & Springel (2003). Furthermore, we include cosmological dilution as described in Beck et al. (2012) and turbulent diffusion on a time-scale of the Hubble time, but we neglect possible post-amplification processes (see e.g. Ryu et al., 2008). We conclude that the seeding by SN only is unable to build up strong magnetic fields at high redshifts and also leads to a significantly lower amplitude at z≈0. The amplification of magnetic seed fields seems crucial in the build-up of galactic magnetic fields. There can be several contributors to enhancement of the magnetic field: First, compression of the gas can lead to an increase in the magnetic field proportial to ρ^{α}. The case

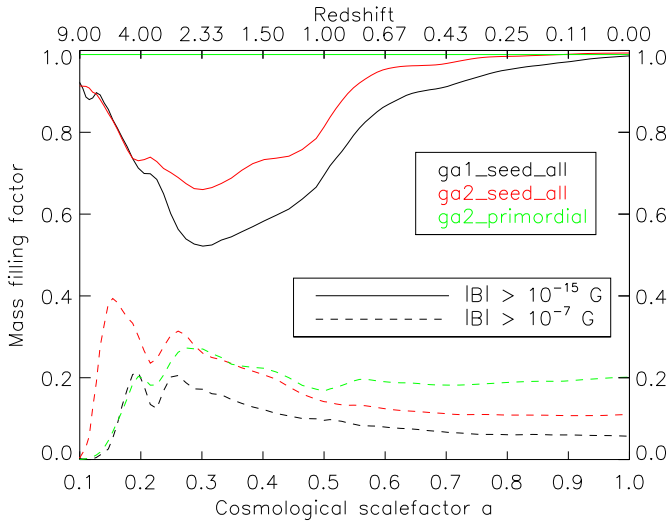

Figure 2.9: Mass fraction of the largest progenitor halo filled with magnetic fields. The dashed lines correspond to strong magnetic fields and the solid lines to weak magnetic fields. Most of the halo mass is filled with weak magnetic fields; however, strong magnetic fields are only contained within the mass at the halo centre.

of isotropic compression would correspond to $\alpha = 2/3$. Secondly, random and turbulent motions can drive a small-scale dynamo within the halo, which leads to an exponential growth of the magnetic field by $e^{\gamma t}$. In the simulations with higher resolution, smaller scales and gas motions are resolved, leading to a faster amplification of the magnetic field. During the assembly of this galactic halo, the magnetic field is amplified on a time-scale $1/\gamma$ of the order of 10^7 yr (see Beck et al., 2012). We refer to the simulations of Beck et al. (2012) for more details about the amplification process.

Fig. 2.9 shows the fraction of magnetized halo mass against redshift in the simulation ga2_seed_all. The size of the halo is determined by its virial radius and is dominated by the dark matter content. At first, the halo is small in size and the majority of the gas content is located at the halo centre and connected to SF regions. Within these SF regions, the magnetic field is seeded and amplified, leading to a high magnetized mass fraction. As the halo continues to grow in size, the mass magnetization fraction drops, presumably because the rate of accretion of unmagnetized gas is higher than the rate of magnetization. Note that the gas mass content also changes as highly magnetized gas particles are converted into stars. Until redshift z≈0, diffusion and gas motions are able to remagnetize the entire galactic halo with magnetic fields stronger than 10^{-15} G. However, magnetic fields stronger than 10^{-7} G are only contained within the innermost SF region of the halo. Within this densest region, seeding is still ongoing and dynamo action is most efficient here in maintaining strong magnetic fields.

Fig. 2.10 shows the fraction of magnetized halo volume against redshift in the simulation ga2_seed_all. At first, most of the gas mass is located at the halo centre, leading to a high magnetized gas fraction, but a low magnetized volume fraction. Throughout the simulation seeding and amplification of the magnetic field up to a few μG occur only in the innermost region of the halo. Thus, magnetic fields stronger than 10^{-7} G are reached only in the innermost parts of the halo volume. However, the total magnetized halo volume increases significantly over time as the magnetic field diffuses towards the halo outskirts.

Independent of resolution, at redshift z≈0 the entire halo mass and volume are magnetized. How-

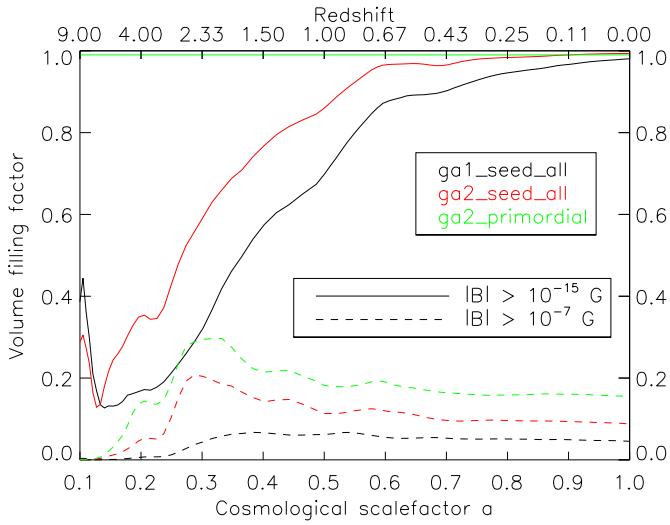

Figure 2.10: Volume fraction of the largest progenitor halo filled with magnetic fields. The dashed lines correspond to strong magnetic fields and the solid lines to weak magnetic fields. At first, only the innermost region of the halo where SF takes place is magnetized. Afterwards, diffusion and gas motions transport weak magnetic fields into the entire halo; however, strong magnetic fields are only contained within the innermost region at the halo centre.

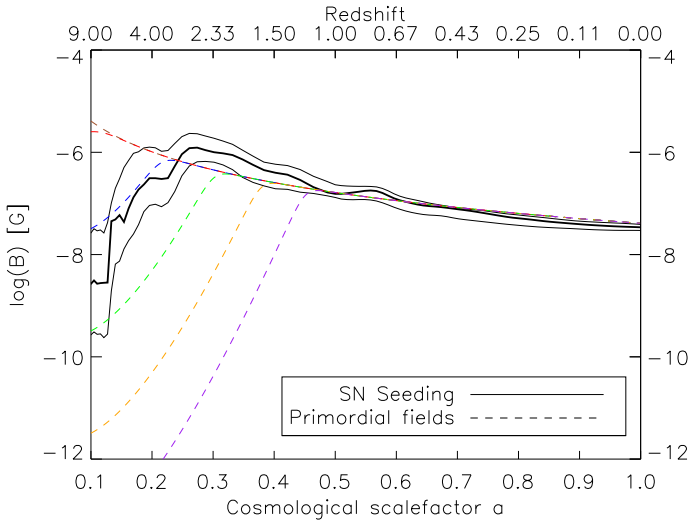

Figure 2.11: Various analytical model growth curves of Beck et al. (2012) adapted for our simulations. The model curves represent the growth of the magnetic field amplitude within the diffuse halo gas for different initial primordial magnetic seed fields. Overlaid (thick black lines) is the time evolution from our simulations with SN seeding for three different amplitudes. The SN seed field is self-consistently created during the simulations. The seed field is hence no longer a free parameter.

ever, in the simulation with higher resolution the magnetization occurs faster. In Fig. 2.8 we showed that in the simulations with higher resolution the magnetic field is amplified faster and it also reaches higher saturation values. Thus, the Alfvén speed reaches higher values earlier in the simulations and also its maximum value is higher. Because the diffusion speed is coupled to the sound and Alfvén speed (see Section 2.2) we expect diffusion to behave differently. Thus, it seems plausible that the magnetization of the halo mass and volume occur faster when increasing the numerical resolution.

We want to note that our simulations do not include cosmic-ray dynamics (see e.g. Hanasz et al., 2009b) or an explicit model for galactic winds (see e.g. Springel & Hernquist, 2003a). Cosmic-ray-driven winds can attain high velocities (see e.g. Breitschwerdt et al., 1991; Reuter et al., 1994; Newman et al., 2012) and could magnetize a galactic halo and the IGM quiet fast (Kronberg et al., 1999) or even the largest voids (Beck et al., 2013b). The addition of an explicit model for galactic winds or a cosmic-ray energy budget and pressure component into our simulations could cause additional gas motions. Then the diffusion of the magnetic field would behave differently and could proceed much faster. In the future, it will be worth pursuing cosmological simulations including cosmic rays and magnetic fields.

Fig. 2.11 shows the redshift evolution of the halo magnetic field of our simulations with SN seeding and model growth curves of primordial fields. The model growth curves reflect the time evolution of magnetic fields for different strengths of primordial seed field, as found in simulations of the formation of a galactic halo (for more details see Beck et al., 2012). Various mechanisms exist for the generation of a primordial magnetic field, leading to a free and ambiguous parameter, with so far only very weak constraints from observations.

In our SN seeding model no free parameter is left, as the seeding of the magnetic field is self-consistently coupled to the underlying SF and the associated magnetic field strength seeded by each SN is taken from the observed value of magnetic fields in SN remnants. The distribution and amplitude of the magnetic seed field are therefore the result of the underlying SF process and the distribution and strength of SF during structure formation. We note that primordial seeding mechanisms may still operate and may also lead to initial magnetic fields outside SF regions or even create magnetic fields before the formation of stars. However, as soon as the first magnetic fields are seeded by SN, the resulting magnetic fields within the associated structures by far exceed the contributions of primordial magnetic fields.

2.4.3 High redshift rotation measures

In this section we discuss the redshift evolution of the intrinsic RM of the forming galactic halo in our simulation. The RM is calculated as the integrated line-of-sight product of the electron density n_e and the magnetic field component $B_\parallel$ parallel to the line of sight l:

$$\mathrm{RM} \sim \int n_e B_\parallel dl. \tag{2.15}$$

Within the simulations the exact length of the integration path does not play an important role, as long as the halo is well inside the integrated line of sight. We use a comoving line of sight of 200 kpc, which covers the virial radius of the forming galactic halo at all redshifts.

The evolution of the magnetic field distribution within the simulated galactic halo will also leave its imprints in the evolution of the RM. Fig. 2.12 shows the maps of the intrinsic RM signal of the halo at six different redshifts in the simulation ga2_seed_all together with a circle, corresponding to the virial radius of the forming galactic halo. In general, within the densest (see Fig. 2.2) and strongest magnetized (see Fig. 2.3) regions we also find the largest intrinsic RM values. Some of the values even exceed 1000 rad m^{-2}. At the halo outskirts we find values of a few 10 rad m^{-2}. Most interestingly, the central protogalactic SF region at redshift z≈12 already hosts intrinsic RM values of several 1000 rad m^{-2}, indicating that strong magnetic fields and large RM must result during the formation of

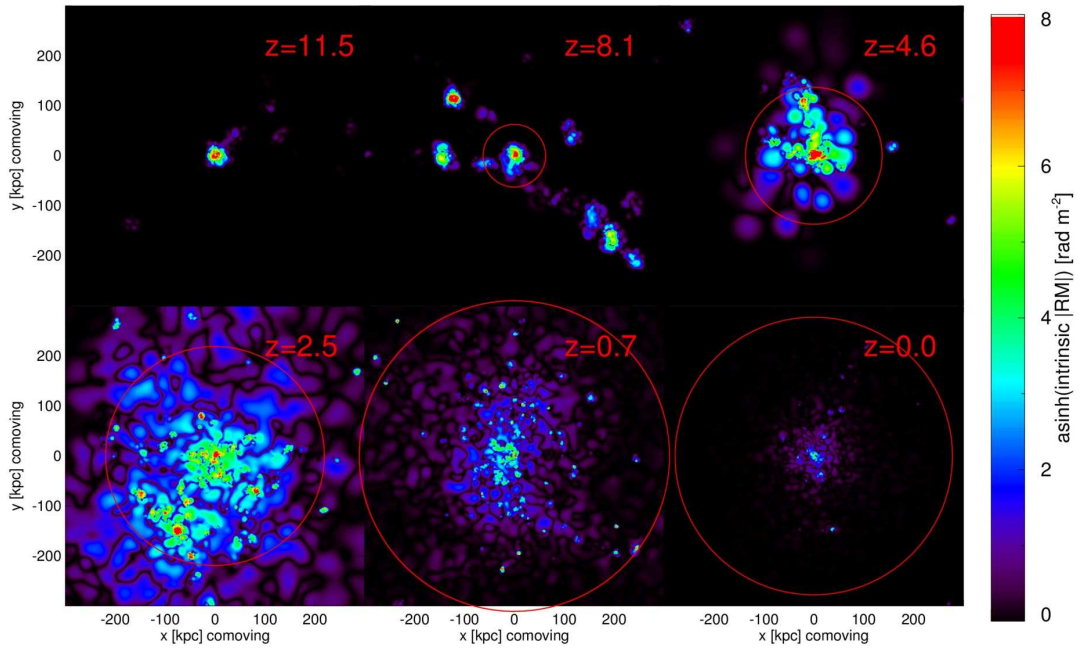

Figure 2.12: Intrinsic RM at different redshifts in the simulation ga2_seed_all of the forming galactic halo on an 'asinh' scale for better visibility. The contour plots can be interpreted in terms of a composition of Figs. 2.2 and 2.3. Intrinsic RM values exceeding 1000 rad m^{-2} can be found in SF, strongly magnetized and dense gas clumps of the assembling halo at high redshift. Towards redshift z≈0 the halo virializes and the intrinsic RM values decline.

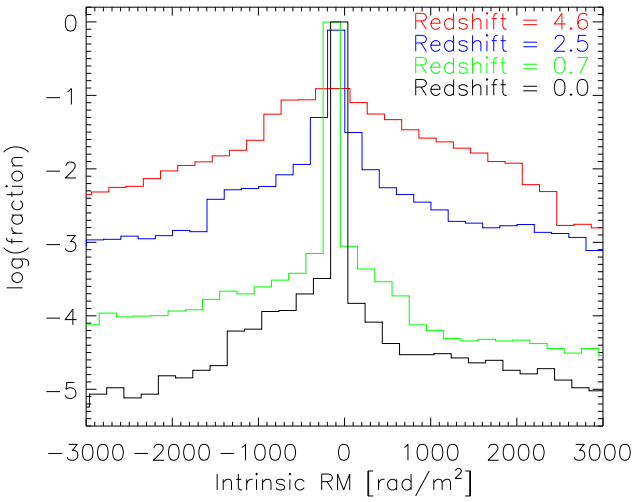

Figure 2.13: Histograms of the halo intrinsic RM in the simulation ga2_seed_all for different redshifts. At high redshift, a large fraction of the halo hosts intrinsic RM exceeding 1000 rad m^{-2}, corresponding to a heterogeneous distribution of strongly magnetized and dense gas. Towards redshift z≈0 the halo virializes, the gas density and the magnetic field decline, substructures have disappeared and the intrinsic RM values decline (corresponding to Fig. 2.12).

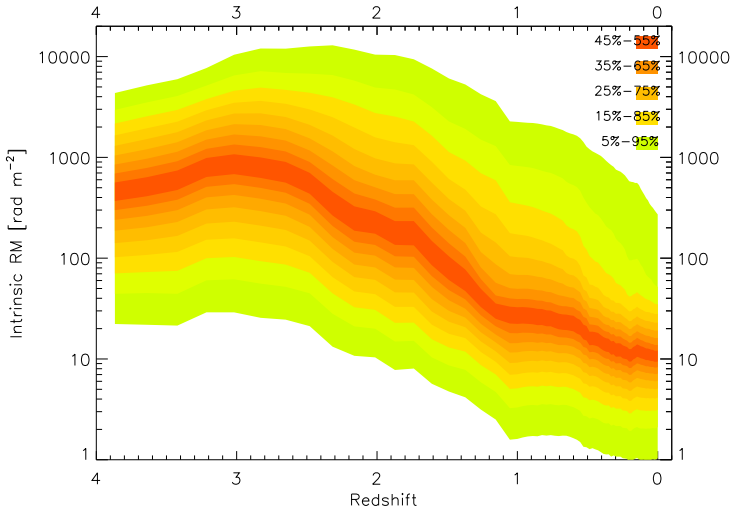

Figure 2.14: Evolution of the mean intrinsic RM in the simulation ga2_seed_all with redshift. We show the mean intrinsic RM (smoothed with a Gaussian beam of 10 kpc) of the innermost 10 per-cent of the halo. The colored region represents, on a per-cent-level spacing, the per-centiles of the intrinsic RM distribution. At redshift z≈3 the RM reaches values of about 1000 rad m^{-2}. Towards redshift z≈0, the mean value declines significantly and becomes as low as 10 rad m^{-2}.

the first protogalaxies. Fig. 2.13 shows the distribution of the intrinsic RM values within the halo for different redshifts. At high redshift, the distribution of the intrinsic RM is widespread, corresponding to a heterogenous distribution of the gas within the halo during its assembly. By virialization towards z≈0, the magnetic field amplitude decreases and thus the intrinsic RM values decrease also. The distributions at high and low redshift differ significantly. We assume this to be caused by the process of halo formation and virialization. At high redshift, the halo is in the process of formation and the distribution of dense and magnetized gas is highly heterogeneous, leaving its imprint in the intrinsic RM signal. Towards redshift z≈0, the halo virializes and the gas density declines as well as the magnetic field strength; the intrinsic RM values also decline.

Fig. 2.14 shows the evolution of the intrinsic RM value in the simulation ga2_seed_all with redshift. We show the mean intrinsic RM value of the innermost 10 per-cent of the largest progenitor halo. The underlying coloured regions mark the per-centiles of the intrinsic RM distribution (per-cent-level spacing) and the outermost contours mark the region of the 0.05-0.95 per-centiles. We smoothed our simulated synthetic intrinsic RM data with a beam size of 10 kpc to produce the mock data. At redshift z≈3, the RM reaches values of about 1000 rad m^{-2}. Towards redshift z≈0, the mean value declines significantly and becomes as low as 10 rad m^{-2}.

Given the extremely complex nature of RM observations, we do not intend to perform a comparison of our simulation with observations. Furthermore, our simulation represents a single isolated evolving galactic halo, while the limited sample of observational data points at high redshift reflects a wide range of gas environments.

2.5 Summary

In this article we present a model for the seeding and evolution of magnetic fields in protogalaxies. We introduce a numerical subgrid model for the self-consistent seeding of galactic magnetic fields by SN explosions. We perform cosmological simulations of Milky Way-like galactic halo formation including MHD, radiative cooling and SF. The main results are summarized as follows.

Within SF regions, magnetic fields are seeded by SN explosions at a rate of about 10^{-9} G Gyr^{-1}. In our simulations the first magnetic seed fields are created when the first stars form within the first protohaloes within the cosmic web. Subsequently, the seeds are amplified by compression and turbulent dynamo action up to equipartition with the corresponding turbulent energy densities during the virialization of these first objects. The random and turbulent motions are created by the gravitational collapse, SN activity and multi-merger events during the assembly of galactic haloes. Within the hierarchical picture of structure formation, large objects form by mergers of multiple smaller objects. As shown in simulations of idealized galactic mergers (see Kotarba et al., 2011; Geng et al., 2012b), each merger event contributes to the amplification of the magnetic field. This magnetic field is then also carried into the IGM by merger-driven gas motions and turbulent diffusion, providing a seed field outside SF regions. Furthermore, the IGM magnetic field is amplified by merger-induced shock waves, as well as possible dynamo action. The final magnetic field strength reaches a few μG in the centre of the halo and $\approx 10^{-9}$ G at the halo outskirts (IGM). The magnetic field distribution within the halo at redshift z≈0 is comparable to the distribution obtained in simulations with primordial seeding (see Beck et al., 2012).

The resulting magnetic field configuration is random and turbulent and additional galactic dynamo processes are necessary to produce a large-scale regular magnetic field topology. In the assembly phase of the galaxy, the magnetic field can be amplified on time-scales of a few tens of millions of years (see Beck et al., 2012). In the case of primordial mechanisms, the amplitudes of the magnetic seed fields are quite weak (order of $\approx 10^{-18}$ G). However, in the case of seeding by SN explosions, seed fields located within the SN remnants or – more precisely – within the resulting superbubbles of SF regions are much stronger, with typical values of $\approx 10^{-9}$ G (see also Rees, 1994). The presence of these

stronger, non-primordial magnetic seed fields, lowers the amount of e-folding required to reach μG amplitudes and hence significantly shortens the time to reach equipartition magnetic fields within virialized haloes. However, the build-up of IGM magnetic fields is more challenging, as the magnetic field first has to be transported from the SF regions into the IGM, before it can subsequently be amplified and distributed further.

At high redshifts, we find that our simulated halo to hosts intrinsic RM values exceeding 1000 rad m^{-2} within dense and highly magnetized regions. The spatial distribution of those very large intrinsic RM is widespread, corresponding to the heterogenous distribution of SF and thus magnetized, gas within the halo during its assembly. While the halo virializes towards redshift $z\approx0$ the gas distribution becomes more homogenous and also the halo magnetic field declines. We find the intrinsic RM of our simulated halo to drop to a mean value below 10 rad m^{-2} at redshift $z\approx0$.

Up to now, models for the evolution of cosmic magnetic fields always faced the problem of having the magnetic seed field as a free and ambiguous input parameter. However, with our SN seeding model, the initial magnetic seed field is no longer a free parameter, but is self-consistently created and described by the SF process during the formation of cosmic structures. Furthermore, the mean magnetic field generated by this mechanism in the protogalaxy by far exceeds the contribution of reasonable, primordial magnetic fields showing that primordial seeding mechanisms are not important in the context of galaxy formation. Thus, our presented seeding model provides a general solution to the seed field problem within the context of galactic and cosmic magnetism. We note that additional magnetic seed fields can still also be provided by AGN or primordial mechanisms.

So far, we only cover the evolution of the magnetic field within a forming galactic halo, as our simulations do not yet form a galactic disc at the halo centre. In the future, we plan to focus on the cosmological formation of disc galaxies within our simulations and study the detailed magnetic field structure within the evolving discs.

We conclude that the seeding of magnetic fields by SN and subsequent amplification during structure formation are able to build up strong magnetic fields of μG strength within very short time-spans. This leads to very strong magnetic fields within the very first collapsing and SF protohaloes at very high redshifts, which are the building blocks for the very first galaxies and could explain the observed, strong magnetic fields in galactic haloes at high redshifts. However, given the complex nature of SF and MHD transport processes, we are still far from understanding the full spectrum of consequences and especially the imprint strong magnetic fields might impose on structure formation.

2.6 Acknowledgments

We thank the anonymous referee for a report that helped to improve the presentation of the paper. We acknowledge additional comments from Uli Klein, Michal Hanasz, Rainer Beck and the members of the DFG Research Unit 1254. We thank Stefan Heigl for proofreading the article. Special thanks go to Felix Stoehr for providing the original initial conditions. KD is supported by the DFG Cluster of Excellence 'Origin and Structure of the Universe'. PPK acknowledges support from an NSERC (Canada) Discovery Grant A5713.

Chapter 3

Paper III: On the magnetic fields in voids

A.M. Beck, M. Hanasz, H. Lesch, R.-S. Remus & F.A. Stasyszyn, 2013,
Monthly Notices of the Royal Astronomical Society, 429, L60

ABSTRACT

We study the possible magnetization of cosmic voids by void galaxies. Recently, observations revealed isolated SF galaxies within the voids. Furthermore, a major fraction of a voids volume is expected to be filled with magnetic fields of a minimum strength of about 10^{-15}G on Mpc scales. We estimate the transport of magnetic energy by CR from the void galaxies into the voids. We assume that CR and winds are able to leave small isolated void galaxies shortly after they assembled and then propagate within the voids. For a typical void, we estimate the magnetic field strength and volume-filling factor depending on its void galaxy population and possible contributions of strong active galactic nuclei (AGN) which border the voids. We argue that the lower limit on the void magnetic field can be recovered, if a small fraction of the magnetic energy contained in the void galaxies or void bordering AGN is distributed within the voids.

Key words: magnetic fields, methods: analytical, cosmic rays, galaxies: magnetic fields, early Universe, large-scale structure of Universe

This chapter is a complete presentation of Beck et al. (2013b).

3.1 Introduction

Recently, high-energy observations revealed a lower limit of about 10^{-15} G on Mpc lengths for cosmic scale magnetic fields. These observations indicate the existence of magnetic fields in voids, with an argumentation as follows. TeV γ-ray photons from distant extragalactic blazars are passing through voids, creating electron/positron pairs when interacting with the extragalactic background light. These pairs would travel in the same direction as the original photon and produce an observable electromagnetic cascade emission. However, in the presence of void magnetic fields, the pairs are deflected and the cascade emission is suppressed. Since the observations of the distant TeV blazars do not detect the full cascade emission, magnetic fields have to be present in at least half of a voids volume (see e.g. Murase et al., 2008; Neronov & Vovk, 2010; Tavecchio et al., 2010; Dermer et al., 2011; Dolag et al., 2011; Essey et al., 2011; Huan et al., 2011; Tavecchio et al., 2011; Taylor et al., 2011; Arlen et al., 2012; Essey & Kusenko, 2012; Kusenko, 2013; Miniati & Elyiv, 2013; Neronov et al., 2012; Takahashi et al., 2012).

Of course, the origin of magnetic fields in the empty voids appears to be enigmatic. We do not intend to discuss the several proposals, but rather point out the new perspectives given by the most recent detections of a galaxy population in the voids themselves. Until recently, voids have been considered as completely empty regions, present in the largest structures known in our Universe in a web-like distribution. This cosmic web is the result of anisotropies during the gravitational collapse within an expanding Universe, when matter gets concentrated within overdense regions, the filaments and sheets (see e.g. Mo et al., 2010).

Recently, first public void catalogues of the local Universe have been constructed (Pan et al., 2012; Sutter et al., 2012). These surveys, performed on the Sloan Digital Sky Survey (SDSS) Data Release 7 (DR 7; Abazajian et al., 2009), show that voids tend to have elliptical shapes and a high-density contrast at the borders. Their effective radii range from a few Mpc up to several hundred Mpc.

However, voids are only less dense regions and still contain matter and structures. Over the past years, several void galaxy surveys have been performed identifying and analysing galaxies within the voids (see e.g. Grogin & Geller, 1999, 2000; Rojas et al., 2004, 2005; Park et al., 2007; Kreckel et al., 2011a,b; Pustilnik & Tepliakova, 2011; Hoyle et al., 2012; Tavasoli et al., 2013). From the SDSS DR 7, Pan et al. (2012) identified a sample of $\approx 10^3$ voids, hosting $\approx 10^4 - 10^5$ galaxies.

Surprisingly, the void galaxies are similar to the corresponding galaxies in the high-density environments (see e.g. Kreckel et al., 2012). They tend to be blue galaxies and exhibit effective radii of a few kpc, but are less massive and lower in luminosity. Also, they are commonly gas-rich, SF and show a regular rotation; however, most have disturbed gas morphologies indicating ongoing accretion or strong turbulence. The galaxies live mainly in isolation and evolve slowly, but a few appear in small groups.

We may summarize that a typical void contains a few 10 SF galaxies. Now, we can design a scenario, which relies on the following line of thoughts derived from the evolution of magnetic fields in well-studied galaxies (see also Kronberg et al., 1999; Samui et al., 2008; Chyży et al., 2011).

Galaxies in the process of assembly are known to build up an equipartition magnetic field (on cosmic magnetism see e.g. Kulsrud & Zweibel, 2008; Vallée, 2011b). It is assumed that first SN explosions deliver interstellar magnetic seed fields of the order of 10^{-9} G (see e.g. Bisnovatyi-Kogan et al., 1973; Rees, 2006). During the galactic halo and galaxy assembly the magnetic field is amplified up to equipartition with the corresponding turbulent energy density by compression and small-scale dynamo action (see e.g. Kulsrud et al., 1997; Beck et al., 2012; Geng et al., 2012a,b). Turbulence yields a total amplification time of a few hundred Myr, leading to a μG magnetic field very shortly after the assembly process started. Even if the galaxies evolve slowly, the existence of equipartition magnetic

fields can be assumed at high redshift (see e.g. Zweibel, 2006; Kronberg et al., 2008; Arshakian et al., 2009; Beck et al., 2012).

The SF within the forming void galaxies also leads to the production of CR within SN and acceleration of CR within SN remnants (see e.g. Longair, 2010). A dynamo driven by these CR contributes to the amplification of the galactic-scale magnetic field (Lesch & Hanasz, 2003; Hanasz et al., 2009b; Siejkowski et al., 2010). Furthermore, CR are driving winds from the galaxies. CR-driven winds can attain high velocities exceeding the escape velocity of galactic haloes and therefore the CR could propagate into the voids (see e.g. Bertone et al., 2006; Breitschwerdt, 2008; Everett et al., 2008; Samui et al., 2010; Enßlin et al., 2011; Uhlig et al., 2012; Dorfi & Breitschwerdt, 2012). Together with the CR escaping from the galaxies, magnetic field lines are carried outwards, resulting in the transport of magnetic energy into the voids (see e.g. Longair, 2010). We note that the electric current carried by the propagating CR may generate magnetic fields at a rate of 10^{-16} G Gyr^{-1} within the voids (Miniati & Bell, 2011, 2012). However, for significantly stronger magnetic fields, different mechanisms or the transport of magnetic energy together with the CR are necessary.

Furthermore, black holes are commonly assumed to reside at the centre of galaxies. These black holes are known to launch jets of charged particles, which can transport magnetic fields far into the IGM, in the case of supermassive black holes within giant radio galaxies even onto scales of several Mpc (see e.g. Willis & Strom, 1978; Strom & Willis, 1980; Kronberg, 1994; Kronberg et al., 2001; Kronberg, 2009; Colgate et al., 2011). However, the small mass of the void galaxies makes a void supermassive black hole population unlikely. Also, Kreckel et al. (2012) did not find evidence for strong AGN activity within their sample of void galaxies. Hence, a magnetization of the voids by an intrinsic population of supermassive black holes seems not plausible. Still, dwarf galaxies can host intermediate-mass black holes (see e.g. Bellovary et al., 2011; Nyland et al., 2012), whose pc- or kpc-scale jets support the outflows and winds. In addition, the highly magnetized Mpc scale jets of strong AGNs at the voids borders can penetrate into the voids and contribute to their magnetization.

In this Letter, we combine the latest observations of void magnetic fields and void galaxies. We discuss the transport of magnetic energy from the void galaxies and bordering AGNs into the voids by CR.

3.2 Estimations

Before starting with the estimations, we will obtain some characteristic values. From a public void catalogue (Pan et al., 2012; Sutter et al., 2012), we find that typical voids have a characteristic radius of $R_{\rm V} \approx 20$ Mpc and contain $N \approx 10$ SF galaxies. Within the voids, magnetic fields of at least $B_{\rm V} \approx 10^{-15}$ G have been detected (see e.g. Neronov & Vovk, 2010). From the void galaxy survey (see e.g. Kreckel et al., 2012), we find a typical void galaxy to have a characteristic radius of $R_{\rm G} \approx 3$ kpc and, if SF was constant, an age of $T_{\rm G} \approx 7.5$ Gyr. The dynamical mass is lower than $M_{\rm G} \approx 10^{11}\ M_\odot$ and the velocity dispersion $\sigma \approx 100$ km s^{-1}, leading to a galactic halo virial radius of $R_{\rm H} = GM/\sigma^2 \approx 50$ kpc. We assume the galactic equipartition magnetic field to be $B_{\rm G} \approx 5\ \mu$G (see e.g. Vallée, 2011b).

First, we can compare the magnetic energies of a typical void and of a typical void galaxy. The magnetic energy within a sphere of radius R and with a magnetic field B is given by

$$E = \frac{R^3 B^2}{6}. \tag{3.1}$$

Thus, the magnetic energy within the galaxy is of the order $E_{\rm G} \approx 10^2 (\mu{\rm G})^2 {\rm kpc}^3$ and of the void at least of the order $E_{\rm V} \approx 10^{-6} (\mu{\rm G})^2 {\rm kpc}^3$. The void contains only a fraction of the magnetic energy produced within a void galaxy. This fraction can also be recovered, when expanding the magnetic energy from the galaxy radius onto the void radius (i.e. $(R_{\rm G}^3/R_{\rm V}^3)^{2/3} \approx 10^{-8}$). Therefore, the magnetic

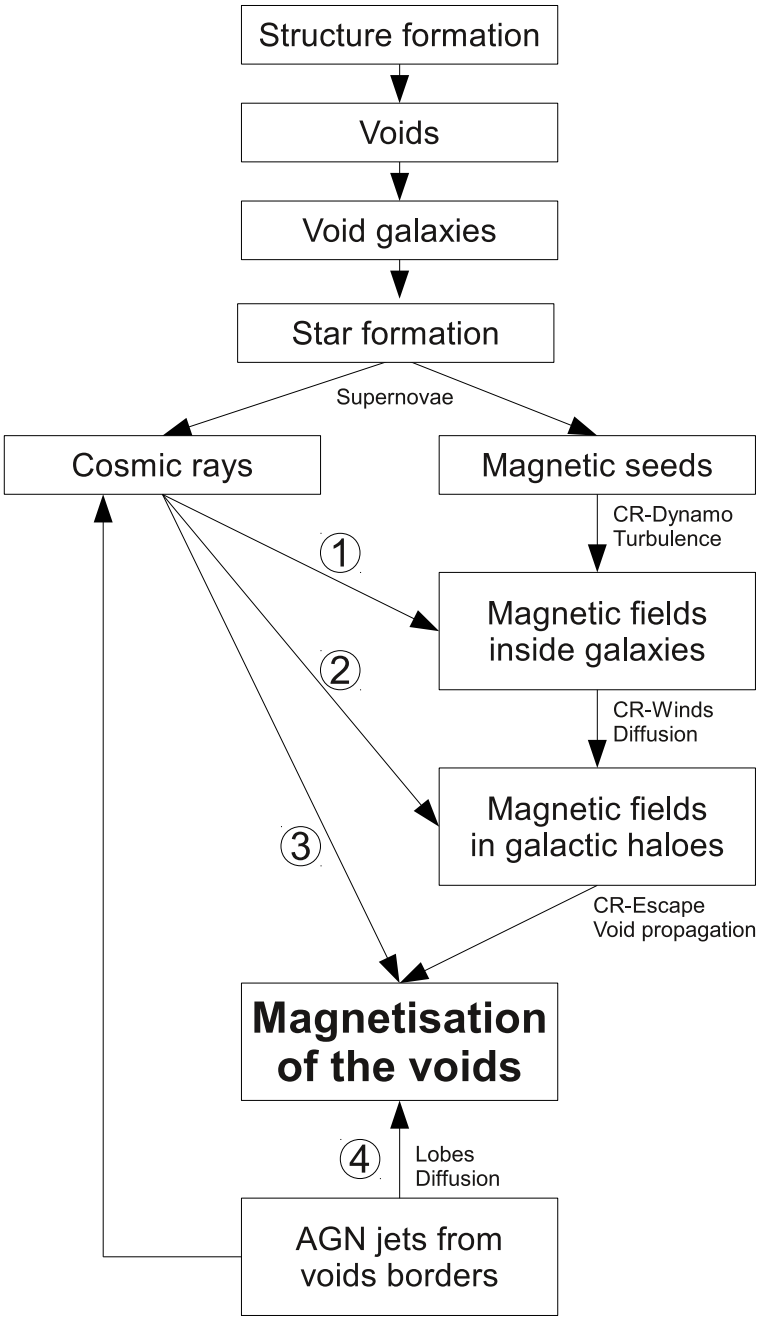

Figure 3.1: Schematic view on the processes and structures involved in the magnetization of cosmic voids. CR lead to the amplification of the void galactic magnetic field (1), as well as winds escaping into the void galactic haloes (2) and the magnetization of the voids themselves (3), supported by AGNs which border the voids (4).

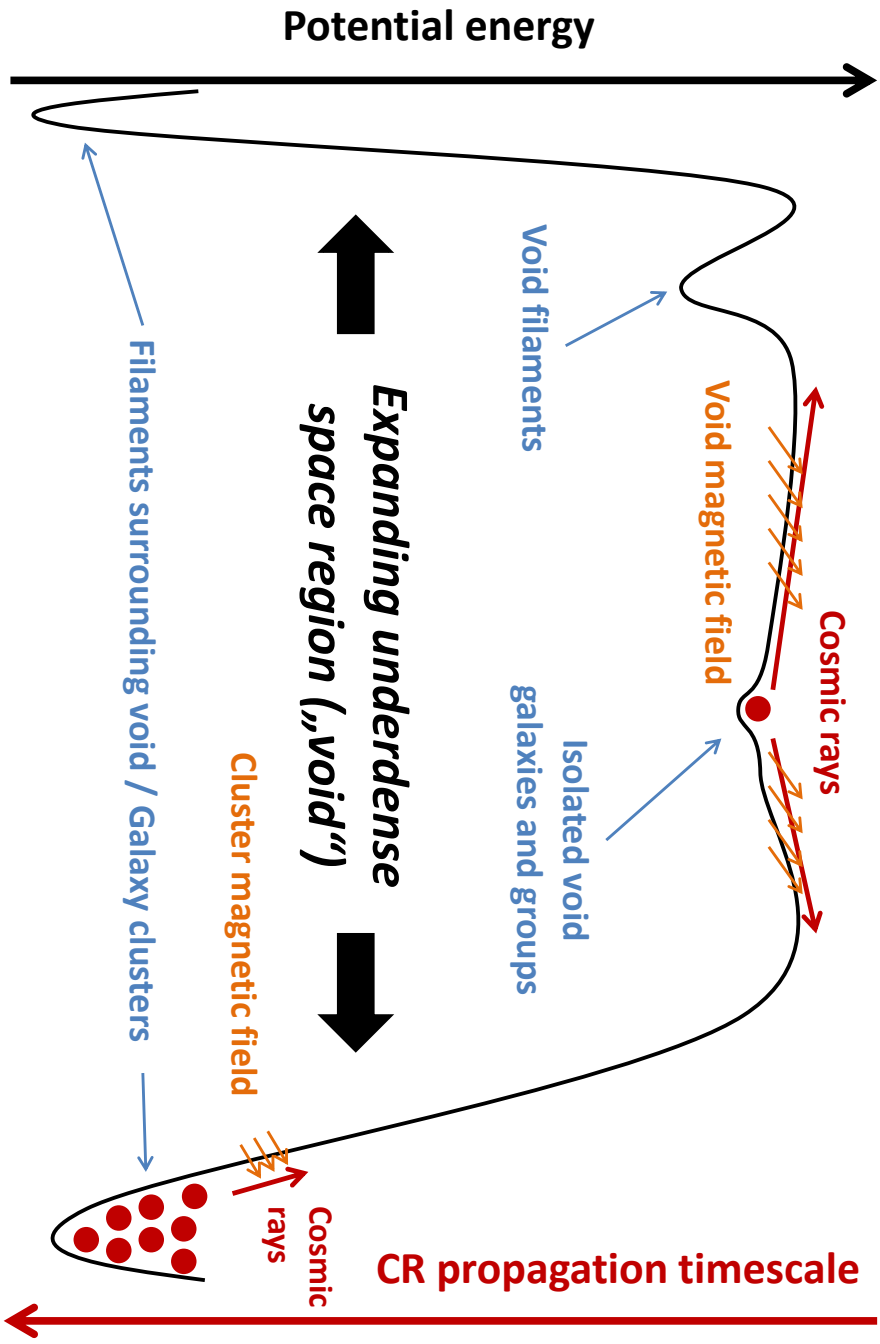

Figure 3.2: Schematic view on a typical void and its galaxies within, as well as the connected CR and magnetic fields. CR are able to propagate more easily into the voids from the void galaxies than from the filament galaxies.

energy contained within a void galaxy is sufficient in magnetizing the void at the observed level, if it can be transported far enough outwards. We will argue that CR are responsible for the magnetization of a fraction of the voids volumes. The propagation of CR carrying an electric current through space can already generate magnetic fields at a rate of 10^{-16} G Gyr^{-1} (Miniati & Bell, 2011). However, in addition to that, we note that magnetic field lines from the void galaxies can be dragged along with the propagating CR into the voids, leading to the transport of magnetic energy.

The CR are mainly produced in SN and accelerated within SN remnants. Intermediate-mass black holes at the centres of the void galaxies can drive supersonic outflows, leading to shocks that subsequently accelerate charged particles. The confinement time of CR within galaxies is known to be of the order of a few 10 Myr (see e.g. Longair, 2010). The escape velocity of a galactic halo depends on its mass and the distance from the centre of mass, at which the particles are launched. For galaxies in the process of assembly with yet small masses, the winds are launched further outside, as the mass is not yet compressed within a central region. Numerical simulations indicate that CR-driven winds exceed the escape speed of dwarf galactic haloes (Samui et al., 2010; Uhlig et al., 2012). These numerical models also show, that the smaller the haloes, the more spherically symmetric the outflows. Recent work by Dorfi & Breitschwerdt (2012) finds that time-dependent effects of winds and shocks within the galactic haloes could reaccelerate the CR, leading to wind speeds exceeding the escape velocity. It is known that CR can be confined within group atmospheres, if the group is large enough and the energy of the CR is too small (see e.g. Berezinsky et al., 1997). However, for the atmospheres of small dwarf galaxy groups, particles with an energy of 1 GeV can still escape. We note that if the void galaxies are grouped into too large structures, the CR and hence also the winds can be confined and not escape into the voids. Summing up, if void galaxies are smaller in mass and reside mainly in isolation, a spherically symmetric galactic wind can escape into the voids and propagate within.

Now, we ask with which velocity the CR are propagating within the voids. We estimate this velocity by considering the lowest possible diffusion coefficient (i.e. Bohm diffusion) for particle propagation along magnetic field lines

$$D_{\mathrm{Bohm}} = \frac{c}{3} r_{\mathrm{Gyro}} = \frac{c}{3} \frac{\gamma m_{\mathrm{p}} c^2}{eB}, \tag{3.2}$$

with the speed of light c, the elementary charge e, the proton mass m_{p} and a Lorentz factor γ. For energies as low as 1 GeV and a length scale of the galactic halo size, the diffusion speed $V_{\mathrm{CR}} = D_{\mathrm{Bohm}}/R_{\mathrm{H}}$ reaches values of $V_{\mathrm{CR}} \approx 1500$ km/s at the galactic peripheries. Because the Bohm diffusion coefficient represents the slowest possible diffusion of charged particles along magnetic field lines, the propagation velocity of the CR can be higher. The CR can propagate far by themselves forming bubbles around the void galaxies, whose expansion, over time, will also be supported by the Hubble flow. However, for simplicity, we assume that CR are propagating at a speed of at least 1500 km s^{-1} or 1.5 Mpc Gyr^{-1} (see also Miniati & Bell, 2011).

Next, we want to estimate how far CR could have propagated since the assembly of the void galaxies started. If, roughly, the build-up of magnetic fields by a turbulent dynamo and the propagation of CR to the galactic periphery took 1 Gyr, CR could have still been propagating within the voids for ≈ 6.5 Gyr. With our assumption of the propagation velocity, this would lead to a travelled distance of the CR of $R_{\mathrm{B}} \approx 10$ Mpc. For simplicity, we assume the expansion to be spherically symmetric. This then allows us to estimate the volume-filling factor of a typical void, which, when assuming a population of N randomly distributed galaxies within, is

$$f = \sqrt{N} \left(\frac{R_{\mathrm{Bubble}}}{R_{\mathrm{Void}}} \right)^3. \tag{3.3}$$

At the start of the galactic assembly process, the voids have a negligible volume-filling factor. However, if a typical present-day void hosts 10 randomly distributed galaxies, the voids volume-filling factor

would be about ≈ 0.4. We note that this estimation is highly speculative, as the alignment of the galaxies within the voids as well as the propagation speed and hence the propagated distances are subject to large uncertanties.

Last, we want to approximate the magnetic field strength within a typical void. By expanding the galactic magnetic field into the bubbles driven by the propagating CR, we estimate

$$B_{\mathrm{Bubble}} = \epsilon\sqrt{N} B_{\mathrm{Galaxy}} \left(\frac{V_{\mathrm{Galaxy}}}{V_{\mathrm{Bubble}}}\right)^{\frac{2}{3}}, \tag{3.4}$$

where ϵ is the fraction of magnetic energy transported from the void galaxies into the voids and N the number of randomly distributed galaxies within a typical void. With our characteristic values and choosing a very low fraction of $\epsilon = 0.001$, we recover the observed lower limit on the void magnetic field of 10^{-15} G. However, numerical simulations performed by Siejkowski et al. (2010) indicate the outflow fraction of magnetic energy to be much higher, which would lead to void magnetic fields significantly stronger than the detected limit.

We note that the above estimations can also be used to approximate the contributions of AGN lobes on the void magnetic fields, if N is assumed to be the number of randomly placed lobes inside a void and B and V the characteristic lobe magnetic field strength and volume. From Kronberg et al. (2001) we take for the lobe of a typical strong AGN a characteristic field strength of the order of $B_{\mathrm{AGN}} \approx 5\mu$G within a volume of about $V_{\mathrm{AGN}} \approx (250\mathrm{kpc})^3$. These values give a magnetic energy of about $E_{\mathrm{AGN}} \approx 10^7(\mu\mathrm{G})^2\mathrm{kpc}^3$ inside a lobe, a value which is many orders of magnitude higher than the lower limit magnetic energy contained within a typical void. We can then approximate the contribution of just one strong AGN lobe, which we assume to have been placed into the void 10 Gyrs ago. With the above Bohm diffusion speed the lobe would contribute to the present-day magnetic filling factor by ≈ 0.4. Choosing a very small fraction of $\epsilon = 10^{-5}$, we again recover the observed lower limit on the void magnetic field of 10^{-15} G. Furthermore, distributing the entire magnetic energy of a strong AGN lobe within a void would also lead to void magnetic fields significantly stronger than the detected limit.

3.3 Summary

Figs 3.1 and 3.2 illustrate our argumentation, summarized as follows. Voids are underdense space regions, growing over cosmic time and surrounded by large filaments. However, within the voids are void galaxies, dwarf-like, mainly isolated and evolving slowly. The galaxies appear to be similar to the corresponding galaxies from high-density environments. They undergo SF, leading to SN and the production of CR and magnetic seed fields. Fast turbulent and CR dynamos are able to build up an equipartition magnetic field during the early stages of the galaxy assembly. The CR are driving high-velocity winds escaping from the galaxies into the voids. The small mass of the void galaxies makes strong AGN activity inside the voids unlikely, but intermediate-mass black holes can support the winds. The CR and the winds are able to leave the atmospheres of the void galactic haloes, in contrast to galactic haloes residing within large filaments or clusters. Over time, the CR can propagate far into the voids, magnetizing a fraction of the voids volumes. The voids are growing by cosmic expansion, but the propagation of the CR also increases the magnetized volume fraction. When assuming expansion of a fraction of the void galactic magnetic fields into bubbles driven by CR, a lower limit for the magnetic field of $> 10^{-15}$ G can be recovered and even stronger magnetic fields are possible.

We have presented and discussed a qualitative scenario for the origin of the magnetic fields in voids. There are two major contributors to the void magnetic fields. First, an intrinsic galaxy population within the voids can produce and spill out magnetic fields. Secondly, highly magnetized jets from

giant radio galaxies bordering the voids can penetrate the voids. Both mechanisms are capable of delivering enough magnetic energy into the voids to yield the observed lower limit of void magnetic fields. However, the high volume-filling factors especially for the largest voids still remain challenging. In the view without primordial magnetic seed fields, a combined contribution of void galaxies and border AGN is probably responsible for the magnetic fields in voids.

3.4 Acknowledgments

AMB is deeply grateful for the hospitality of the University of Konstanz and many discussions with Annette Geng, Marcus Beck and Peter Nielaba. We thank our referee P. P. Kronberg for prompt reviewing and valuable suggestions. FAS is supported by the DFG Research Unit FOR1254. MH acknowledges the generous support of the Alexander von Humboldt foundation during his stay at the University Observatory Munich. R-SR acknowledges a grant from the International Max-Planck Research School of Astrophysics (IMPRS).

Chapter 4

Paper IV: Magnetic field amplification and X-ray emission in galaxy minor mergers

A. Geng, H. Kotarba, F. Bürzle, K. Dolag, F. Stasyszyn, **A. Beck** & P. Nielaba, 2012,
Monthly Notices of the Royal Astronomical Society, 419, 3571

ABSTRACT

We investigate the magnetic field evolution in a series of galaxy minor mergers using the N-body/SPH code GADGET. The simulations include the effects of radiative cooling, SF and SN feedback. MHD is implemented using the SPH method. We present 32 simulations of binary mergers of disc galaxies with mass ratios of 2:1 up to 100:1, whereby we have additionally varied the initial magnetic field strengths, disc orientations and resolutions. We investigate the amplification of a given initial magnetic field within the galaxies and an ambient IGM during the interaction. We find that the magnetic field strengths of merger remnants with mass ratios up to 10:1 saturate at a common value of several μG. For higher mass ratios, the field strength saturates at lower values. The saturation values correspond to the equipartition value of magnetic and turbulent energy density. The initial magnetization, disc orientation and numerical resolution show only minor effects on the saturation value of the magnetic field. We demonstrate that a higher impact energy of the progenitor galaxies leads to a more efficient magnetic field amplification. The magnetic and turbulent energy densities are higher for larger companion galaxies, consistent with the higher impact energy supplied to the system. We present a detailed study of the evolution of the temperature and the bolometric X-ray luminosity within the merging systems. Thereby we find that magnetic fields cause a more efficient increase of the IGM temperature and the corresponding IGM X-ray luminosity after the first encounter. However, the presence of magnetic fields does not enhance the total X-ray luminosity. Generally, the final value of the X-ray luminosity is even clearly lower for higher initial magnetic fields.

Key words: MHD, methods: numerical, galaxies: evolution, galaxies: kinematics and dynamics, galaxies: magnetic fields, galaxies: spiral

This chapter is a presentation of the main results of Geng et al. (2012b). Our full study consists of 19 journal pages, including 6 tables and 12 figures. However, to stay in the scope of this thesis, we picked out the most important and to this thesis connected results. In particular, we present 8 scenarios of how in general minor mergers of galaxies can amplify magnetic seed fields. We do not show a detailed parameter study (additional 24 scenarios) of varied initial conditions as well as an analysis of the temperature evolution and X-ray emission. We refer the reader to our paper (Geng et al., 2012b) for the entire study.

4.1 Introduction

In the framework of hierarchical growth of structure in the Universe, galaxy interactions are believed to be an essential part of galaxy formation and evolution. The Λ cold dark matter (ΛCDM) cosmology predicts the formation of dark matter haloes due to gravitational instabilities in the early Universe which later on form larger haloes by accretion and mergers (White & Rees (1978); White & Frenk (1991)). In the continuing process, baryonic particles get gravitationally bound to the haloes, forming structures which are consistent with the galaxies observed today. The merger rate of dark matter haloes is an increasing function of redshift (Kolatt et al. (1999); Gottlöber et al. (2001)), implying that collisions and mergers were much more frequent in the early Universe. Moreover, simulations of merger history trees (Wechsler et al., 2002) indicate that major merger events were comparatively rare and thus dark matter haloes grow mainly by the accretion of smaller objects. More precisely, minor mergers are expected to be at least one order of magnitude more common than major mergers (Hernquist & Mihos (1995) and references therein). Interactions of galaxies lead to significant changes of the dynamics of the progenitor galaxies due to the alteration of the gravitational potential (e.g. Toomre & Toomre (1972); Naab & Burkert (2003)). Thereby, most of the galaxy collisions result in a merger of the progenitor systems.

So far, simulations of galaxy mergers were predominantly dedicated to studies of SF, stellar dynamics, gas flows, supermassive black holes or feedback from stars and black holes (e.g. Di Matteo et al. (2005); Springel et al. (2005a,b); Robertson et al. (2006); Cox et al. (2008); Johansson et al. (2009)). However, galaxy mergers are also interesting in the context of the amplification and restructuring of small-scale magnetic fields within the scope of the global evolution of cosmic magnetism.

In order to investigate the idea of an interaction-driven amplification of galactic magnetic fields, numerical simulation of a galactic (major) merger of the Antennae Galaxies (Karl et al., 2010), including the evolution of magnetic fields (Kotarba et al., 2010) were performed. They found that the magnetic field within the colliding system gets amplified by compression and shear flows up to a saturation value of $\approx 10\mu$G, independent of the initial magnetic field of the progenitor discs, which was varied between 10^{-9} and 10^{-6} G. Within this work, the saturation level was found to be near equipartition between magnetic and turbulent gas pressure. In a continuative study, Kotarba et al. (2011) considered a major collision of three galaxies. These studies confirmed the saturation of the galactic magnetic field at the equipartition level of several μG independent of the initial magnetic field. Furthermore, an additionally included ambient IGM allowed also for studies of its magnetization, which was shown to saturate at $\approx 10^{-8}$G. However, all of these studies are dedicated to galactic major mergers. As galaxy minor mergers are expected to be far more frequent within the process of structure formation, it is definitely interesting to consider the influence of the mass ratios of the progenitor galaxies on the magnetic field amplification and saturation value. This idea is pursued within the presented work.

Disc parameters		
Concentration	CC	12
Spin parameter	λ	0.1
Disk mass fraction[a]	$m_{\rm d}$	0.05 $M_{\rm tot}$
Bulge mass fraction[a]	$m_{\rm b}$	0.02 $M_{\rm tot}$
Disk spin fraction	$j_{\rm d}$	0.05
Gas fraction	f	0.2
Disk height	z_0	0.2 $l_{\rm d}$
Bulge size	$l_{\rm b}$	0.2 $l_{\rm d}$
Scalelength of extended gas disc	$l_{\rm g}$	6 $l_{\rm d}$
Multi-Phase Model Parameters		
Gas consumption time-scale	$t_{\rm MP}$	8.4 Gyr
Mass fraction of massive stars	$\beta_{\rm MP}$	0.1
Evaporation parameter	A_0	4000
Effective SN temperature	$T_{\rm SN}$	4×10^8 K
Temperature of cold clouds	$T_{\rm CC}$	1000 K

Table 4.1: Parameters of initial set-up common to all galaxy models.

4.2 Method and initial conditions

All galaxy collision simulations have been performed with the standard numerical method. The simulations are performed with the N-body / SPMHD code GADGET (Springel et al., 2001b; Springel, 2005; Dolag & Stasyszyn, 2009), where we applied their standard (direct) SPMHD method (see also Price, 2012), following the induction equation and including Lorentz forces as well as artificial dissipation. Furthermore, we used the Springel & Hernquist (2003a) SF model without the implementation of galactic winds. It describes radiative cooling, UV background heating and SN feedback in a consistent self-regulated two-phase sub-resolution model for the ISM.

In order to perform a series of simulations of unequal mass mergers, we set up structurally similar galaxy models (see Table 4.1) with different total masses. The galaxies are set up using the method described by Springel et al. (2005c). This method allows for a galaxy model consisting of a cold dark matter halo, an exponential stellar disc, a stellar bulge (all of these components being collisionless N-body particles) and an exponential gaseous disc (SPH particles). Both the virial mass M_{200} and the virial radius r_{200} of the galaxy depend on the virial velocity v_{200} (Springel et al., 2005c; Johansson et al., 2009) via

$$r_{200} = \frac{v_{200}}{10 H_0}, \tag{4.1}$$

$$M_{200} = \frac{v_{200}^3}{10 G H_0}, \tag{4.2}$$

with the Hubble constant $H_0{=}h \cdot 100$ km s^{-1} Mpc^{-1} and $h = 0.71$. Thus, we determine the masses of our galaxy models by varying the virial velocity v_{200}. We assume the same halo concentration CC, spin parameter λ, disc and bulge mass fractions $m_{\rm d}, m_{\rm b}$, disc spin fraction $j_{\rm d}$, gas fraction f, disc height z_0, bulge size $l_{\rm b}$ and the scale length of extended gas disc $l_{\rm g}$ for all of the used galaxy models.

Medium resolution							
Galaxy	$M_{\rm tot}$ [$10^{10} M_\odot$]	r_{200} [kpc h^{-1}]	$l_{\rm d}$ [kpc h^{-1}]	$N^a_{\rm halo}$	$N^b_{\rm disc}$	$N^c_{\rm gas}$	$N^d_{\rm bulge}$
M1	134.1	160	7.1	400 000	960 000	240 000	400 000
M2	64.0	125	5.5	200 000	457 764	114 441	190 735
M3	43.6	110	4.9	133 333	311 954	77 988	129 981
M4	32.8	100	4.2	100 000	234 375	58 594	97 656
M5	26.8	94	4.1	80 000	191 579	47 895	79 824

(a) Collisionless particles within dark matter halo. (b) Collisionless particles within disc.

(c) Gas particles within disc. (d) Collisionless particles within bulge.

Table 4.2: Parameters for the galaxy models.

Merger scenarios					
Scenario	Mass ratio	Orbit	Initial $B_{\rm gal,0}$	Initial $B_{\rm IGM,0}$	Resolution
M1M2_G9I9 / I12	2:1	Prograde	10^{-9} G	10^{-9} / 10^{-12}	Medium
M1M3_G9I9 / I12	3:1	Prograde	10^{-9} G	10^{-9} / 10^{-12}	Medium
M1M4_G9I9 / I12	4:1	Prograde	10^{-9} G	10^{-9} / 10^{-12}	Medium
M1M5_G9I9 / I12	5:1	Prograde	10^{-9} G	10^{-9} / 10^{-12}	Medium

Table 4.3: Simulated galaxy merger scenarios.

Model M1 is the most massive galaxy in our sample and the other models are numbered according to their mass with respect to the M1 model, i.e. model M2 is a galaxy with half the mass of model M1, M3 has one third of the mass of M1 and so forth (see Table 4.2).

The initial magnetization of the progenitor discs is given by $B_{\rm x} = B_{\rm gal,0}$ and $B_{\rm y} = B_{\rm z} = 0$ G with the z-axis being the axis of rotation. Thus, the initial field lies always in the plane of the galactic discs. As we are interested in the influence of minor mergers on the galactic magnetic field evolution, particularly its amplification, we mainly focus on a small initial magnetic field strength of $B_{\rm gal,0} = 10^{-9}$ G.

Within all of the presented simulations (see Table 4.3) the largest (i.e. most massive) galaxy model M1 interacts with one of the smaller (i.e. less massive) models M2-5. In order to ensure a collision, the galaxies are set on a parabolic orbit, resulting in a prograde encounter (i.e. the spin direction is the same within both galaxies) in most of the simulations. The initial separation $r_{\rm sep}$ of the galaxies is determined by the sum of their virial radii. The pericenter distance in all simulations is $r_{\rm p} = 5\ h^{-1}$ kpc. The disc orientation (see Toomre & Toomre, 1972) is set to $\iota = 60°$ and $\omega = 60°$ for the largest galaxy M1 and $\iota = 60°$ and $\omega = -60°$ for the companion galaxy, respectively, within all of our merger scenarios.

We include an ambient IGM composed of additional gas particles surrounding the galaxies similar to Kotarba et al. (2011). The IGM particles are arranged in a hexagonal closed-packed lattice. The mass of the IGM gas particles is the same as the mass of the galactic gas particles. The volume filled with the IGM is 700 $\times$700 $\times$700 h^{-3} kpc^3 centered on the common center of mass of the progenitor galaxies at the beginning of the simulation. For simplicity, we assume that the IGM is pervading the

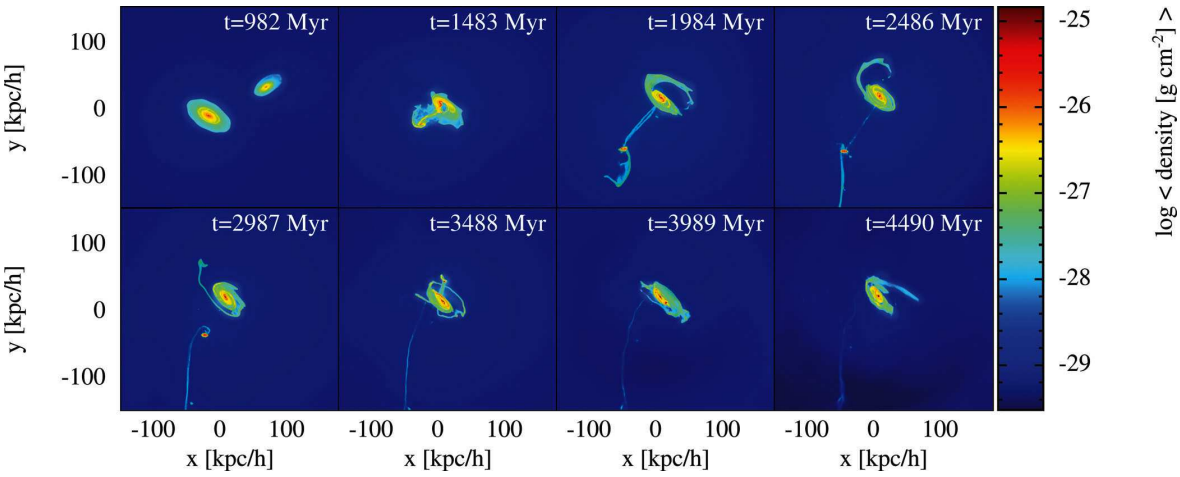

Figure 4.1: Evolution of the projected mean line-of-sight density at eight different times for the minor merger scenario M1M4_G9I9.

galaxies. The density of the IGM is $\rho_{\rm IGM} = 10^{-29}$ g cm^{-3}.

The internal energy of the IGM is calculated via $u_{\rm IGM} = v_{200}^2/2$, using the virial velocity v_{200} of the larger progenitor galaxy M1. This sets the temperature of the IGM to the virial temperature at the virial radius of the galaxy M1:

$$T_{\rm IGM} = \frac{2}{3} u_{\rm IGM} \frac{m_p \mu}{k_B} = \frac{1}{3} \langle v_{200}^2 \rangle \frac{m_p \mu}{k_B} \approx 6 \cdot 10^5 \text{ K}, \tag{4.3}$$

with the mean molecular weight for a fully ionized gas of primordial composition $\mu \approx 0.588$, proton mass m_p and Boltzmann constant k_B.

The initial magnetic field of the IGM is assumed to be homogeneous and directed in x-direction, i.e. $B_{\rm IGM,0} = B_{\rm IGM,x}$, with now the x-y-plane being the orbital plane. Due to our setup, the IGM magnetic field is also pervading the galaxies. $B_{\rm IGM,0}$ is assumed to have values of either 10^{-9} G or 10^{-12} G, depending on the merger scenario.

We let our initial system evolve for 200 Myr to allow possible numerical discontinuities associated with the initial set-up (e.g. effects caused by overlayed magnetic fields of galaxies and IGM) to relax.

4.3 Results from the simulations

4.3.1 Morphological and magnetic evolution

Fig. 4.1 shows the projection of the mean line-of-sight density exemplarily for the present-day scenario M1M4_G6I9. In the beginning of the simulation, the galaxies are moving towards each other due to their mutual gravitational attraction. The first encounter takes place at $t \approx 1.3$ Gyr, whereupon prominent tidal arms are developing. The first encounter is followed by a series of subsequent encounters until the final merger occurs at about $t \approx 4$ Gyr. For smaller progenitor galaxies, subsequent encounters take place at later times (and more of them until the final merger) due to the weaker gravitational attraction. In most of the simulated scenarios, the disc of the larger progenitor galaxy M1 outlasts the interaction. However, in scenarios with the largest companion galaxies M2 and M3, the disc of M1 gets largely disrupted.

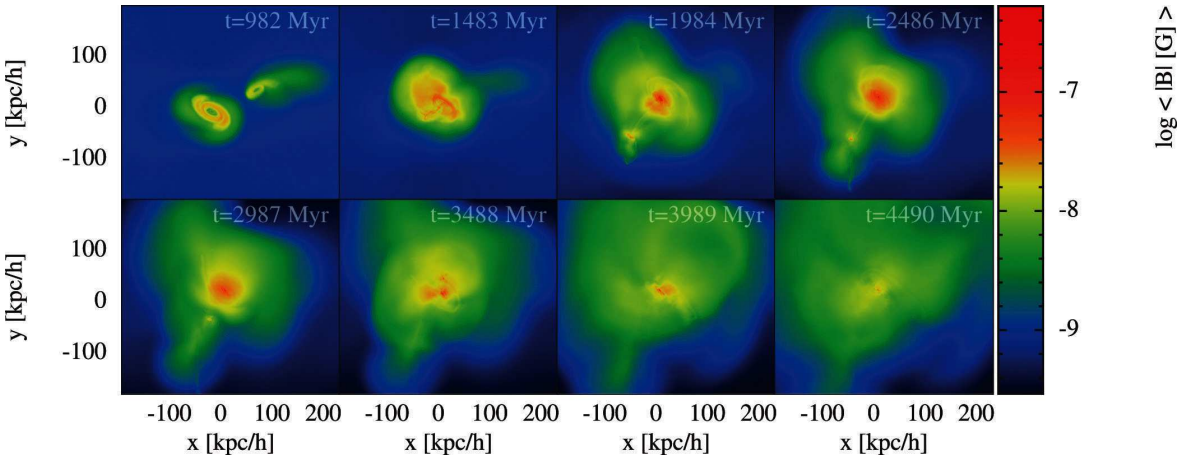

Figure 4.2: Evolution of the projected mean line-of-sight total magnetic field strength at eight different times for the minor merger scenario M1M4_G9I9.

Fig. 4.2 shows the morphological evolution of the projection of the mean line-of-sight total magnetic field strength for the present-day scenario M1M4_G6I9. Before the first encounter, the galactic magnetic field gets wound up by the differential rotation of the discs and gains a non-axisymmetric pattern with two magnetic arms. Shocks and interaction-driven outflows caused by the first encounter are propagating into the IGM, whereby the IGM magnetic field is strengthened within the shocked regions. During the subsequent evolution, further encounters take place, which are also accompanied by shocks and outflows and therefore lead to a further magnetization of the IGM. At the time of the final merger, the magnetic field in the galaxies has approximately retained its initial value of 10^{-6} G, whereas the IGM magnetic field got amplified within an extended region around the galaxies up to a value of several 10^{-9} G.

Fig. 4.3 shows the evolution of the total magnetic field strength as a function of time for four of the standard scenarios ($B_{\mathrm{gal},0} = B_{\mathrm{IGM},0} = 10^{-9}$ G) and for the same scenarios with a lower initial IGM magnetic field of $B_{\mathrm{IGM},0} = 10^{-12}$ G. In all of the presented simulations, a slight amplification of the total galactic magnetic field by approximately a factor of 4 caused by the winding process is visible in the two progenitor discs before the first encounter. All of the presented merger simulations show this initial amplification with the same order of magnitude.

During the first encounter, the galactic magnetic field gets efficiently amplified, whereby the maximum magnetic field strength and the slope of the amplification depend on the mass ratio of the progenitor galaxies. Thereby, lower mass ratios lead to a slightly higher maximum value of the magnetic field and a steeper slope of the amplification, caused by the presumably higher turbulence driven by the first encounter. In case of lower mass ratios, the maximum value of the galactic magnetic field strength is mostly reached after the first encounter. However, the maximum value of the magnetic field in scenarios with higher mass ratios is usually not reached until the time of the second encounter.

The spikes in the galactic magnetic field strength after the maximum value in the simulations with mass ratios of 2:1 up to 5:1 correspond to the second encounters. The second encounter takes place at a later time for smaller companion galaxies. For smaller companion galaxies, the second encounter generally results in a further increase of the galactic magnetic field strength, whereby the maximum value of the magnetic field is reached at the time of the second encounter. The subsequent encounters and the final merger do not lead to any considerable further amplification of the galactic magnetic field. At the end of the simulations, the galactic magnetic field strengths for the presented merger

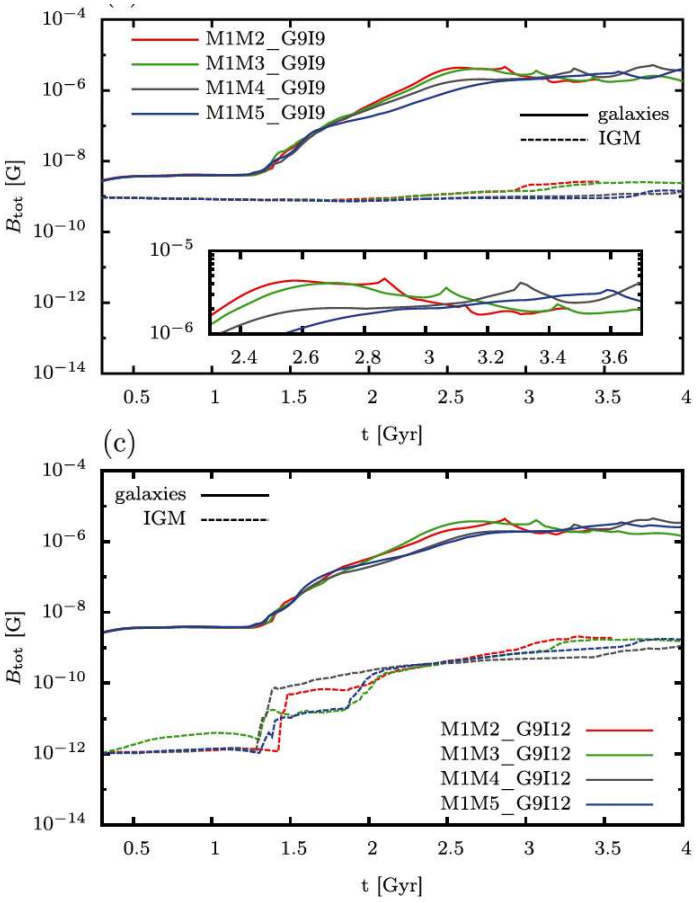

Figure 4.3: Total magnetic field strength as a function of time for various merger scenarios. Galaxies (solid lines) and IGM (dashed lines) are shown separately using a density threshold of 10^{-29} g cm^{-3}.

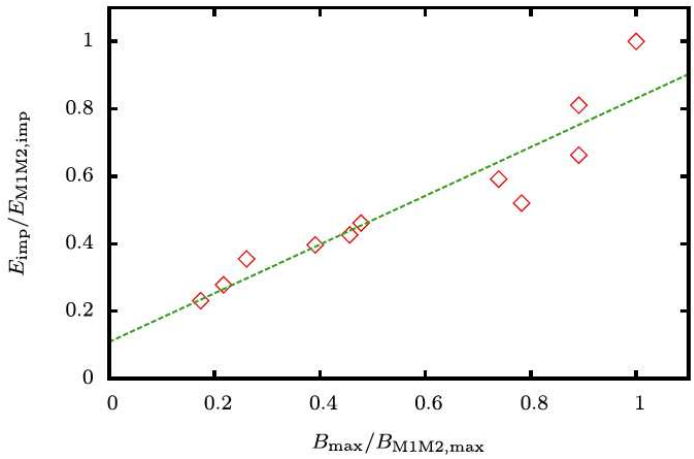

Figure 4.4: Maximum magnetic field strength $B_{\rm max}$ (reached between the first and second encounter within each scenario) as a function of the impact energy $E_{\rm imp}$ for various scenarios. There is a clear correlation between the the maximum magnetic field strength and the impact energy of the progenitor galaxies.

scenarios saturate at a similar value of several μG.

The IGM magnetic field saturates at a value of order nG within most of the scenarios. Thus, an initial magnetic field of $B_{\rm IGM,0} = 10^{-9}$ G does not significantly grow during the interaction, whereas an initial field of $B_{\rm IGM,0} = 10^{-12}$ G is clearly amplified up to the saturation value by three orders of magnitude. Within the simulations with an initial galactic magnetic field of $B_{\rm gal,0} = 10^{-6}$ G, the IGM magnetic field amplification at the time of the first encounter is slightly more efficient because magnetic energy is additionally transported from the galaxies into the IGM. However, at the end of the simulations, we find the same saturation value of the IGM magnetic field as within all other scenarios. Moreover, the saturation value of the IGM magnetic field is on general independent on the masses of the progenitor galaxies.

4.3.2 Impact energy and equipartition

The kinetic energy of the progenitor galaxies, which is released during the interaction, is expected to be partly converted into magnetic energy. Thus, the higher the impact energy, the higher the amount of turbulence and the more efficient the expected field amplification. The impact energy can be estimated on the basis of the masses and the centre-of-mass velocities of the progenitor galaxies just before the first encounter (this velocity is much less than the initial velocity of the galaxies since the galactic haloes already overlap, which causes a slowdown of the galaxies). The impact energy may be approximated by

$$E_{\rm impact} = \frac{1}{2} m_{\rm G1} v_{\rm G1}^2 + \frac{1}{2} m_{\rm G2} v_{\rm G2}^2. \tag{4.4}$$

As we set the galaxies on nearly-parabolic Keplerian two-body orbits, the centre-of-mass velocity of the companion galaxy increases with decreasing mass, whereas the centre-of-mass velocity of the larger galaxy M1 is slightly decreasing with decreasing mass of the companion galaxy. As a result, we find the impact energy of the M1M5 model to be roughly half the energy of the M1M2 model. This is consistent with the trend that scenarios with smaller companion galaxies show lower maximum

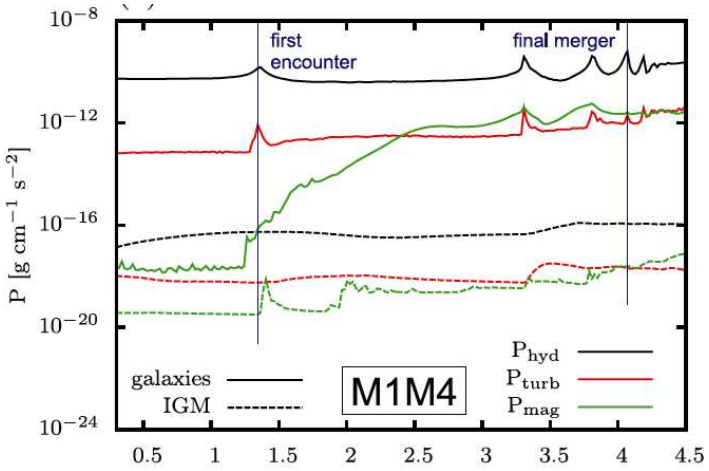

Figure 4.5: Evolution of the pressure components $P_{\rm hyd}$, $P_{\rm turb}$ and $P_{\rm mag}$ as a function of time for the scenario M1M4 with the standard initial magnetization of 10^{-9} G. At the time of the final merger, the magnetic and the turbulent energy densities show approximately the same order of magnitude. Galaxies (solid lines) and IGM (dashed lines) are shown separately using a density threshold of 10^{-29} g cm^{-3}.

values of the galactic magnetic field strength and also flatter slopes of the amplification during the interaction. The reason for this behaviour can most probably be ascribed to the lower impact energy which is available for conversion into magnetic energy. The resulting correlation between the maximum magnetic field strength and the impact energy is shown in Fig. 4.4.

The release of kinetic energy during the interaction drives turbulence, which in turn results in an amplification of the magnetic field by random motions. However, if the magnetic energy density reaches the magnitude of the turbulent energy density, the magnetic field amplification caused by the turbulent motion of the gas is suppressed by the magnetic field itself via the Lorentz force. The system therefore tends to maintain a dynamic equilibrium or equipartition between turbulent and magnetic energy density. In order to study the expected energy equipartition between the magnetic and the turbulent energy density (or, equivalently, magnetic and turbulent pressure) in more detail, we follow Kotarba et al. (2011) and choose $v_{\rm rms}$ (rms velocity around the mean velocity inside the smoothing length h) as an estimator for the local turbulent velocity. The turbulent pressure is then given by $P_{\rm turb} = 1/2\rho v_{\rm rms}^2$.

Fig. 4.5 shows the turbulent pressure, the hydrodynamic pressure $P_{\rm hyd} = 1/2\rho v^2$ (with v the total velocity of each particle) and the magnetic pressure $P_{\rm mag} = B^2/8\pi$ exemplarily for the M1M4 scenario with the standard magnetization of 10^{-9} G. While the hydrodynamic pressure within the galaxies in both scenarios evolves relatively smoothly and stays in the same range of magnitude during the whole interaction (except for the peaks indicating the different encounters of the discs), the turbulent pressure slightly increases after each encounter. During the collision, the galactic turbulent pressure lies below the galactic hydrodynamic pressure by roughly two orders of magnitude. The magnetic pressure gets strongly amplified during the interaction (according to the amplification of the magnetic field itself).

Within the scenario, the system reaches the equipartition level between turbulent and magnetic pressure at about 1 Gyr after the first encounter. In this scenario, the magnetic pressure stays slightly above the turbulent pressure until the final merger, whereupon an approximate equipartition is reached. In the subsequent evolution the magnetic pressure gets amplified again with each further

encounter, whereas each amplification period is followed by a period of decreasing magnetic field until the next encounter takes place. At the time of the final merger, the magnetic and the turbulent energy densities show approximately the same order of magnitude. As the equipartition value within each model depends on the energy supplied to the system (impact energy), we generally find higher equipartition values for lower mass ratios of the galaxies.

The IGM shows a slight increase in the hydrodynamic pressure at the beginning of the simulation, followed by a relatively smooth evolution. The IGM turbulent pressure clearly shows some peaks, corresponding to the encounters. The IGM turbulent pressure lies below the IGM hydrodynamic pressure by roughly two orders of magnitude during the whole simulation, which is a comparable separation as for the corresponding galactic pressure components. The IGM magnetic pressure within each scenario gets amplified during the first encounter. In the subsequent evolution, a loose equipartition between the IGM turbulent and magnetic pressure is maintained until the end of the simulations.

4.4 Conclusions and discussion

Summing up, minor mergers of various mass ratios are able to amplify small magnetic seed fields up to μG order within galaxies and up to $\approx 10^{-9}$ G within the IGM.

Furthermore, the maximum values of the galactic magnetic field reached during the interactions are higher and the slope of the amplification is steeper for lower mass ratios. This is reasonable because the main source for the magnetic field amplification is the impact energy released during the interaction. Moreover, we find that the magnetic pressures associated with the IGM and galactic magnetic fields saturate at the equipartition level between turbulent and magnetic pressure. As the energy equipartition within each scenario depends on the impact energy supplied to the system, the equipartition values are on general higher for larger companion galaxies, i.e. lower mass ratios.

Galactic interactions provide a promising alternative or complement to the standard amplification scenarios for cosmic magnetic fields: As galaxy mergers and especially minor mergers, are believed to have been much more frequent in earlier times of the universe, it is likely that the presented interaction-driven amplification also provided for a significant contribution to the amplification of the galactic and intergalactic magnetic fields on short time-scales. Hence, for future studies it would be interesting to focus on mergers of dwarf galaxies to gain a more complete picture of the evolution of magnetic fields within mergers. Furthermore, studies of the magnetic field evolution in the early Universe in a cosmological context and within the formation of galaxies would be very worthwhile for a better understanding of the overall process of the magnetic field amplification caused by galaxy formation and interaction events in the history of the Universe.

4.5 Acknowledgments

We thank the referee Michal Hanasz for his valuable comments which improved the paper a lot. AG thanks Volker Springel for the programs to set up the initial galaxy models. Rendered plots were made using the SPLASH software written by Daniel Price (see Price, 2007) and with SMAC (see Dolag et al., 2005) with contributions by Julius Donnert. Granting of computing time from John von Neumann-Institute for Computing (NIC), Jülich, Germany is gratefully acknowledged. KD acknowledges the support by the DFG Priority Programme 1177 and additional support by the DFG Cluster of Excellence 'Origin and Structure of the Universe'.

Chapter 5

Paper V: Synthetic X-ray and radio maps for two different models of Stephan's Quintet

A. Geng, **A.M. Beck**, K. Dolag, F. Bürzle, M.C. Beck, H. Kotarba & P. Nielaba, 2012,
Monthly Notices of the Royal Astronomical Society, 426, 3160

ABSTRACT

We present simulations of the compact galaxy group Stephan's Quintet (SQ) including magnetic fields, performed with the N-body/SPH code GADGET. The simulations include radiative cooling, SF and SN feedback. MHD is implemented using the standard SPMHD method. We adapt two different initial models for SQ based on Renaud et al. and Hwang et al., both including four galaxies (NGC 7319, NGC 7320c, NGC 7318a and NGC 7318b). Additionally, the galaxies are embedded in a magnetized, low-density IGM. The ambient IGM has an initial magnetic field of 10^{-9}G and the four progenitor discs have initial magnetic fields of 10^{-9} to 10^{-7} G. We investigate the morphology, regions of SF, temperature, X-ray emission, magnetic field structure and radio emission within the two different SQ models. In general, the enhancement and propagation of the studied gaseous properties (temperature, X-ray emission, magnetic field strength and synchrotron intensity) are more efficient for the SQ model based on Renaud et al., whose galaxies are more massive, whereas the less massive SQ model based on Hwang et al. shows generally similar effects but with smaller efficiency. We show that the large shock found in observations of SQ is most likely the result of a collision of the galaxy NGC 7318b with the IGM. This large group-wide shock is clearly visible in the X-ray emission and synchrotron intensity within the simulations of both SQ models. The order of magnitude of the observed synchrotron emission within the shock front is slightly better reproduced by the SQ model based on Renaud et al., whereas the distribution and structure of the synchrotron emission are better reproduced by the SQ model based on Hwang et al.

Key words: methods: numerical, galaxies: interactions, galaxies: kinematics and dynamics, galaxies: magnetic fields, galaxies: spiral

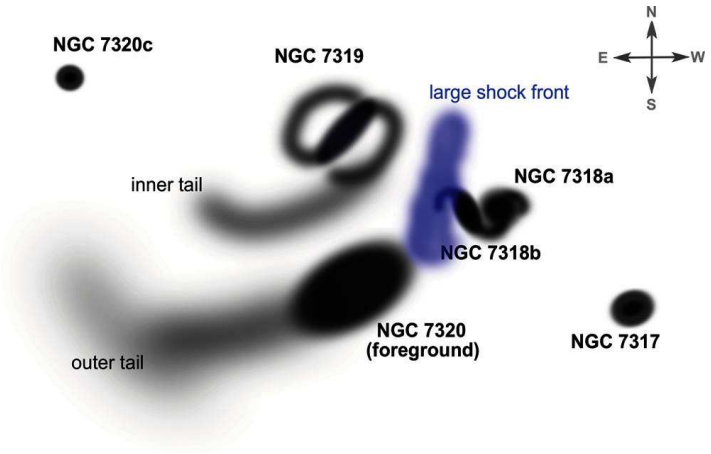

Figure 5.1: Schematic view of the main morphological features of SQ. Historically, SQ consists of the galaxies NGC 7319, NGC 7318a/b, NGC 7320 and NGC 7317. Today, however, only the galaxies NGC 7319, NGC 7318a/b, NGC 7317 and additionally NGC 7320c are observed to form an interdependent galaxy group.

This chapter is a presentation of the main results of Geng et al. (2012a). Our full study consists of 18 journal pages, including 7 tables and 15 figures. However, to stay in the scope of this thesis, we picked out the most important and to this thesis connected results. In particular, we show simulated gaseous properties (X-ray and radio emission) for two different models of Stephan's Quintet. We do not show an in depth comparison with observations on specific features. We refer the reader to our paper (Geng et al., 2012a) for the entire study.

5.1 Introduction

Stephan's Quintet (SQ; Stephan, 1877), also known as Hickson Compact Group 92 (Hickson, 1982), is the first discovered compact galaxy group. SQ consists of five galaxies (NGC 7319, NGC 7318a, NGC 7318b, NGC 7317 and NGC 7320; cf. also Fig. 5.1) with an estimated distance to earth of $\approx$ 94 Mpc (Moles et al., 1998; Appleton et al., 2006). SQ is famous for a physical adjacency between four of the galaxies (NGC 7319, 7318a, 7318b and 7317), whereby strong interactions between three of these members are apparently causing tidal tails, a strong group-wide shock visible in X-ray (Pietsch et al., 1997; Sulentic et al., 2001) and radio emission (Allen & Hartsuiker, 1972; Xu et al., 2003) and a region of active SF northern of the colliding galaxies (Xu et al., 2005). The fifth galaxy, NGC 7320, is observed to be a much closer foreground galaxy and is not part of the interacting group (Shostak, 1974; Allen & Sullivan, 1980; Moles et al., 1997). It has a recessional velocity of $\approx$ 740 km s^{-1} (Falco et al., 1999). Three of the four physically related galaxies, the main galaxy NGC 7319 as well as NGC 7317 and NGC 7318a, have a similar recessional velocity of $\approx$ 6640-6670 km s^{-1} (Fedotov et al., 2011) and represent the core of the compact group (c.f. Fig. 5.1). NGC 7318b is observed to be a high-speed intruder ($\approx$ 5770 km s^{-1}) (Moles et al., 1997; Fedotov et al., 2011). Finally, there is a sixth galaxy, NGC 7320c, which shows a similar recessional velocity ($\approx$ 5990 km s^{-1}) as the core of the compact group (Fedotov et al., 2011) and is therefore suggested to interact with NGC 7319 (Moles et al., 1997), because it reveals connected tidal features in the eastern large tidal tail (cf. the outer tail in Fig. 5.1). Therefore, it is most likely also part of the compact group (Arp, 1973).

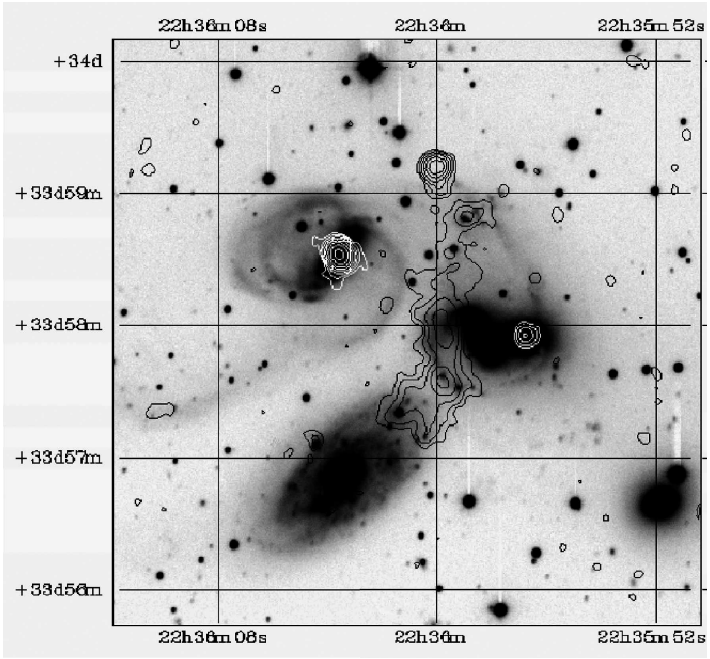

Figure 5.2: *R*-band CCD image overlaid with contours of the radio continuum at 4.86 GHz (total radio emission) observed with the VLA. The lowest contour is 50 μJy beam^{-1} with a further spacing of 2 in ratio. The picture is taken from Xu et al. (2003).

Radio observations reveal the presence of magnetic fields in most late-type galaxies of the local Universe. Galaxy interactions can cause magnetic fields which are much stronger compared to individual galaxies (Beck, 2005; Drzazga et al., 2011). In this context, the SQ is particularly interesting because it shows both galaxy-galaxy and galaxy-IGM interactions. The latter is mainly visible on the basis of the prominent ridge of X-ray and radio emission crossing the system (see Fig. 5.2). Xu et al. (2003) estimate the minimum-energy magnetic field strength within the shock region of SQ to ≈ 10 μG.

Despite an enormous number of observational studies of SQ, revealing different features at different wavelengths, numerical simulations of this system are very rare, due to the difficulties of many free parameters in modelling such a complex interacting system. The simulated models for SQ commonly exclude the foreground galaxy NGC 7320 but include NGC 7320c as a member of the galaxy group. Furthermore, NGC 7317 does not show any visible features of an ongoing or past interaction. Therefore, it is usually not taken into account in the simulations. As a first basis for more detailed studies, Renaud et al. (2010) performed collisionless gravitational N-body simulations proposing a possible formation scenario for SQ. Their simulation is mainly focusing on reproducing the stellar large-scale structure of SQ. Recently, Hwang et al. (2012) presented an extended model including a gaseous component and different galaxy models, suggesting a different formation history. The global morphology of the system is well represented in their simulation, supporting also the idea that the large-scale shock within the system is caused by the interaction of NGC 7318b with the intragroup IGM.

However, until now, detailed numerical studies of the SQ concerning SF, temperature, magnetic fields, X-ray and radio emission are still missing. Therefore, within the presented work, we perform SPMHD studies of SQ on the basis of the two existing models by Renaud et al. (2010) and Hwang et al. (2012). Thereby, we place a particular focus on the properties of the gaseous component, i.e. on the SF rate, the temperature and the magnetic field. We also investigate the presence of the shock front in the X-ray and radio emission.

5.2 Method and initial conditions

All galaxy collision simulations have been performed with the standard numerical method. The simulations are performed with the N-body / SPMHD code GADGET (Springel et al., 2001b; Springel, 2005; Dolag & Stasyszyn, 2009), where we applied their standard (direct) SPMHD method (see also Price, 2012), following the induction equation and including Lorentz forces as well as artificial dissipation. Furthermore, we used the Springel & Hernquist (2003a) SF model without the implementation of galactic winds. It describes radiative cooling, UV background heating and SN feedback in a consistent self-regulated two-phase sub-resolution model for the ISM.

The first attempt towards a morphologically adequate representation of SQ in simulations was made by Renaud et al. (2010). They performed a large number of collisionless N-body simulations to find initial parameters for the four progenitor galaxies, including initial positions and velocities. Starting with these initial parameters, the system undergoes a number of interactions resulting in a morphological structure comparable to observational findings. The large-scale configuration of the tidal features and the galaxies is generally well represented. However, these simulations are purely gravitational and therefore not suitable for more detailed studies of e.g. intergalactic gas properties, shocks, SF activity, magnetic fields, etc. Hence, Renaud et al. (2010) suggest to use their models as a basis for more complex simulations of SQ.

Recently, Hwang et al. (2012) presented a further model, including also a gaseous component. They performed restricted three-body/SPH simulations of the SQ system using different models for the progenitor galaxies and a different formation scenario compared to Renaud et al. (2010). Yet, they were also able to reproduce the main tidal features of the system. Furthermore, they found indications

supporting the hypothesis that the large shock between NGC 7319 and NGC 7318b has been caused by a high-speed collision of NGC 7318b and the IGM. They also studied the behaviour of gas clouds within the shocked region developing after the collision. They found a continuing production of small shocks in this region over a time span of $\approx 10^7$ yrs. However, they were not able to study the SF history and the gas temperature in more detail, because their treatment of heating and cooling was not accurate enough to draw reliable conclusions. Moreover, they did not perform any investigations concerning X-ray emission, magnetic fields and radio emission.

Both of the models include the four strongly interacting galaxies NGC 7319, NGC 7320c, NGC 7318a and NGC 7318b. The galaxies NGC 7317 and NGC 7320 were not considered, as the influence of NGC 7317 on the other group members is negligible at present time (Renaud et al., 2010) and NGC 7320 is observed to be an unrelated foreground galaxy (Shostak, 1974; Allen & Sullivan, 1980; Moles et al., 1997). The sequence of interactions within the model of Renaud et al. (2010) is the following: NGC 7320c undergoes a collision with NGC 7319, then 7318a interacts with the already disturbed galaxy NGC 7319 and finally the high-speed intruder NGC 7318b hits the system. For the model of Hwang et al. (2012), the interaction history is different: NGC 7320c performs a close passage around NGC 7319, then the galaxies NGC 7318a and NGC 7318b undergo a collision behind the orbital plane of the main system followed by a collision of the high-speed intruder NGC 7318b with the IGM material west of NGC 7319.

Modifications of the galaxy models and the initial positions and velocities were required due to the additional inclusion of a gaseous component and an ambient IGM. We note that we did not intend to reproduce the models of Renaud et al. (2010) and Hwang et al. (2012) in detail but rather to use them as basis for our studies of magnetic fields, X-ray and radio emission in SQ.

Renaud et al. (2010) set up their galaxies to be composed of an exponential disc, a bulge and a dark matter halo (all consisting of collisionless gravitational N-body particles) using a method based on Hernquist (1993). As NGC 7320c is assumed to be spherically symmetric it is only made up of a halo and a bulge component.

For our first SQ model, we adopt the total masses as well as the percental masses of bulge, halo and disc (if present). The galaxies are set up using the method described by Springel et al. (2005c), which is also based on the Hernquist method (Hernquist, 1993). This method allows for a galaxy model consisting of a cold dark matter halo, an exponential stellar disc, a stellar bulge (all of these components being collisionless gravitational N-body particles) and an exponential gaseous disc (SPH particles). We included a gaseous disc component using a disc gas fraction of $\mathrm{f} = 0.2$ to all of the galaxy models. The number of particles and thus the resolution were highly increased. The parameters of our galaxy models are given in Table 5.1.

The galaxy models of Hwang et al. (2012) are composed of a dark matter halo and a disc containing star as well as gas particles. NGC 7318a was indeed set up with a disc, but the angular and random velocities are representing an elliptical. Surprisingly, the total masses of the galaxies are roughly a factor of 10 smaller compared to the SQ model of Renaud et al. (2010). Also, the mass ratios of the galaxies among each other differ significantly.

For our second SQ model, we adopt the total masses of Hwang et al. (2012). However, most of the other parameters are chosen in accordance with Renaud et al. (2010). Again, our galaxy models consist of a cold dark matter halo, an exponential stellar disc, a stellar bulge and an exponential gaseous disc. Thus, compared to Hwang et al. (2012), our models additionally contain a bulge. We use a high resolution of the galaxy models. As the true nature of NGC 7318a is still unclear, we have modeled it as a disc galaxy. Thus, the parameters of the galaxy models for our two SQ models differ mainly in the mass (and size) of the galaxies. The parameters common to both of our SQ models are given in Table 5.1.

For simplicity, we refer to the modified galaxy models with 'galaxy model A' and accordingly with 'SQ model A' to the total initial SQ setup including all galaxy models and an ambient IGM for our improvement based on the Renaud model and with 'galaxy model B' and accordingly 'SQ model B'

Galaxy Parameters				
	NGC 7319	NGC 7320c	NGC 7318a	NGC 7318b
Concentration[a] CC	12	20/8	12	12
Spin parameter λ	0.1	0.15	0.1	0.1
Disk mass fraction[b] $m_{\rm d}$	0.125 $M_{\rm tot}$	0.05 $M_{\rm tot}$	0.125 $M_{\rm tot}$	0.125 $M_{\rm tot}$
Bulge mass fraction[b] $m_{\rm b}$	0.0625 $M_{\rm tot}$	0.0214 $M_{\rm tot}$	0.0625 $M_{\rm tot}$	0.0625 $M_{\rm tot}$
Disk spin fraction $j_{\rm d}$	0.125	0.05	0.125	0.125
Gas fraction f	0.2	0.2	0.2	0.2
Disk height[b] z_0	0.2 $l_{\rm d}$	0.2 $l_{\rm d}$	0.2 $l_{\rm d}$	0.2 $l_{\rm d}$
Bulge size[b] $l_{\rm b}$	0.2 $l_{\rm d}$	0.2 $l_{\rm d}$	0.2 $l_{\rm d}$	0.2 $l_{\rm d}$
Scale length of extended gas disc[b] $l_{\rm g}$	6 $l_{\rm d}$	6 $l_{\rm d}$	6 $l_{\rm d}$	6 $l_{\rm d}$
		SQ model A		
Initial coordinates (x,y,z) [kpc h^{-1}]	(0.0, 0.0, 0.0)	(19.92, 10.45, 19.92)	(-83.12, 0.0, 38.70)	(-14.04, 17.64, -217.19)
Initial velocities (v_x,v_y,v_z) [km/s]	(0.0, 0.0, 0.0)	(-620.0, 232.5, -387.5)	(465.0, -46.5, -93.0)	(218.0, 0.0, 1025.0)
Disc orientation (θ, ϕ)	(0, 0)	(0, 0)	(180, 23)	(0, -23)
		SQ model B		
Initial coordinates (x,y,z) [kpc h^{-1}]	(0.0, 0.0, 0.0)	(8.9, -10.9, 10.9)	(-50.0, 7.1, -40.0)	(15.0, 1.4, -241.4)
Initial velocities (v_x,v_y,v_z) [km/s]	(0.0, 0.0, 0.0)	(35.9, 79.5, -77.5)	(100.0, -27.0, -92.5)	(20.0, -7.5, 350.0)
Disc orientation (θ, ϕ)	(0, 0)	(0, 0)	(180, 0)	(180, 0)

(a) Second column: model A / model B.

(b) $M_{\rm tot}$ and $l_{\rm d}$ are given in Table 2.

Table 5.1: Parameters of initial galaxy setup for both models of SQ.

Galaxy	$M_{\rm tot}$ ($\times 10^{10} M_\odot$)	r_{200} (kpc h^{-1})	$l_{\rm d}$ (kpc h^{-1})	$N^a_{\rm halo}$	$N^b_{\rm disc}$	$N^c_{\rm gas}$	$N^d_{\rm bulge}$
			SQ model A				
NGC 7319	258.1	199.0	7.1	706 900	869 600	217 400	544 000
NGC 7320c	44.8	111.0	5.9	141 380	60 952	15 238	32 610
NGC 7318a	88.0	139.0	5.0	240 346	295 660	73 920	184 960
NGC 7318b	46.0	112.0	4.0	127 242	156 530	39 130	97 920
			SQ model B				
NGC 7319	12.5	63.0	2.6	737 456	907 636	226 908	567 272
NGC 7320c	2.5	42.5	3.6	169 780	73 136	18 284	39 128
NGC 7318a	8.2	63.0	2.3	483 364	594 908	148 728	371 820
NGC 7318b	7.1	60.0	2.2	418 008	514 472	128 620	321 544

(a) Collisionless particles within dark matter halo. (b) Collisionless particles within disc.

(c) Gas particles within disc. (d) Collisionless particles within bulge.

Table 5.2: Parameters for the galaxy models.

to our realization of the Hwang model. The total masses, virial radii and stellar disc scale lengths and particle numbers used in our galaxy models are summarized in Table 5.2.

Finally we want to note that our models differ from the correspondent models of Renaud or Hwang in some details. In our representation of the Renaud galaxy models (galaxy models A), the dark matter haloes of the galaxies are more extended and the disc scale lengths differ from the original model. These differences are on the one hand due to the enhancement of the original setup method for the galaxies (Hernquist, 1993) by Springel et al. (2005c) and on the other hand due to the additionally included gaseous component. We feel confident that our new models are appropriate realizations of the SQ galaxies as they now contain gas and show more realistic extensions of the dark matter haloes. In our representation of the Hwang galaxy models (galaxy models B), the galactic disc sizes differ from the original model and we additionally include a bulge component. As in the restricted three-body simulations of Hwang et al. (2012) gas and star disc masses are negligible, we modeled the galaxies for our model B with parameters in analogy to galaxy models A. The parameters which are common to both models are given in Table 5.1.

In addition to the modifications described above, an ambient IGM is included. The IGM is set up to be composed of additional gas particles surrounding the galaxies similar to Kotarba et al. (2011). We arrange the IGM gas particles on a hexagonal closed-packed lattice. The particle masses of the IGM gas particles are adopted from the respective galaxy models. The IGM fills a volume of 1000 $\times 1000 \times 1000\ h^{-3}$ kpc^3 and we assume a density of $\rho_{\rm IGM} = 10^{-29}$ g cm^{-3}. The IGM is assumed to be already virialized, whereby the temperature within each model is set to the virial temperature at the virial radius of the largest galaxy model NGC 7319:

$$T_{\rm IGM} = \frac{2}{3} u_{\rm IGM} \frac{m_p \mu}{k_B} = \frac{1}{3} \langle v^2_{200} \rangle \frac{m_p \mu}{k_B}\ [K]\ , \tag{5.1}$$

with the mean molecular weight for a fully ionized gas of primordial composition $\mu \approx 0.588$, proton mass m_p and Boltzmann constant k_B. This leads to a temperature of the IGM of $T_{\rm IGM} \approx 9.4 \cdot 10^5$ K for the SQ model A and $T_{\rm IGM} \approx 1.2 \cdot 10^5$ K for the SQ model B.

Our models A and B differ in several features (e.g. gaseous component, IGM, dark matter dis-

tribution) from the original models by Renaud et al. (2010) and Hwang et al. (2012), respectively. Therefore, we had to adjust the orbital parameters of the galaxies compared to the original models. We found these new orbital parameters of the galaxies, i.e. new initial velocities in case of SQ model A and initial positions and velocities for SQ model B, by performing more than 100 test simulations. The orbital parameters of the best representation of SQ for each model are found in Table 5.1. The parameters for the disc orientations are the same as in the original models.

The initial magnetization of the galactic discs is set up using $B_{\rm x} = B_{\rm gal,0}$ and $B_{\rm y} = B_{\rm z} = 0$ G with the z-axis being the axis of rotation. This setup ensures that the initial field lies in the plane of the galactic disc. The initial magnetic field strength of the galaxies is assumed to be $B_{\rm gal,0} = 10^{-9}$ G. The initial magnetic field of the IGM is assumed to be uniform in x-direction with an initial value of $B_{\rm IGM,0} = B_{\rm IGM,x} = 10^{-9}$ G and the x-y plane being the orbital plane. In this set-up, the IGM magnetic field is also naturally pervading the magnetic field of the galaxies.

5.3 Results from the simulations

5.3.1 General morphology

In the following, we denote particular evolutionary stages of our simulations with A1 to A3 for the model A and correspondingly B1 to B3 for model B in order to simplify later reference.

For SQ model A, it takes 320 Myr from the initial configuration to reach its best fit with observations. In the course of the evolution, first NGC 7320c undergoes a collision with NGC 7319 (A1: $t_{\rm ot} = t_{\rm A1} = 80$ Myr), producing the outer tail. After $t_{\rm it} = 140$ Myr, NGC 7318a starts interacting with the already disturbed galaxy NGC 7319, resulting in the formation of the inner tail. Afterwards, the final encounter of the discs of NGC 7318a and NGC 7319 takes place at $t_{\rm A2} = 240$ Myr. Subsequently, the high-speed intruder NGC 7318b hits the system, which leads about 40 Myr later to a configuration consistent with the morphology of the observed system (A3 - present day: $t_{\rm pd} = t_{\rm A3} = 320$ Myr) (cf. Fig. 5.1).

Fig. 5.3 (a) shows the gas density overlaid with contours of the stellar surface density for SQ model A at the time $t_{\rm A3} = 320$ Myr. Only NGC 7319 and the galaxy pair NGC 7318a/b are visible. Qualitatively, the model shows a good agreement of the general features with observations, i.e. the morphology of the large galaxy NGC 7319, the inner tail south-east of NGC 7319 and the structure of the western galaxy pair NGC 7318a/b. Some kind of outflow is indicated in the gas density distribution north of NGC 7319 and also north and south-west of the pair NGC 7318a/b. The stellar surface density shows the highest values within the inner disc of NGC 7319 and also within the disc of NGC 7318a. The stellar density in the disc of NGC 7318b is slightly lower. A bridge between NGC 7319 and the colliding pair NGC 7318a/b is clearly visible in the stellar surface density as well as in the gas density. At the left edge of the plot, there is an elongated region with a stellar surface density larger than 0.003 $\rm M_\odot\ pc^{-2}$. This region belongs to the galaxy NGC 7320c which lies outside the plotted region. However, the model does not reproduce the observed position of the galaxy pair NGC 7318a/b correctly and the outer tail is generated in this model but is already too diffuse to be visible at the present-day configuration. These aspects were both already noted for the original model by Renaud et al. (2010). Furthermore, the small-scale details of this galaxy pair, e.g. the structure of the spiral arms of NGC 7318b, are not well reproduced.

For SQ model B it takes 860 Myr from the initial conditions to develop a morphology similar to the observed configuration. However, the interaction history differs significantly from model A: At first, a close passage of NGC 7320c around NGC 7319 (B1: $t_{\rm ot} = t_{\rm it} = t_{\rm B1} = 160$ Myr) simultaneously forms both the inner and outer tails. Subsequently, the galaxies NGC 7318a and NGC 7318b undergo a collision behind the orbital plane of the main system consisting of the galaxies NGC 7319 and NGC 7320c (B2: $t_{\rm B2} = 640$ Myr). Afterwards, the high-speed intruder NGC 7318b is moving towards

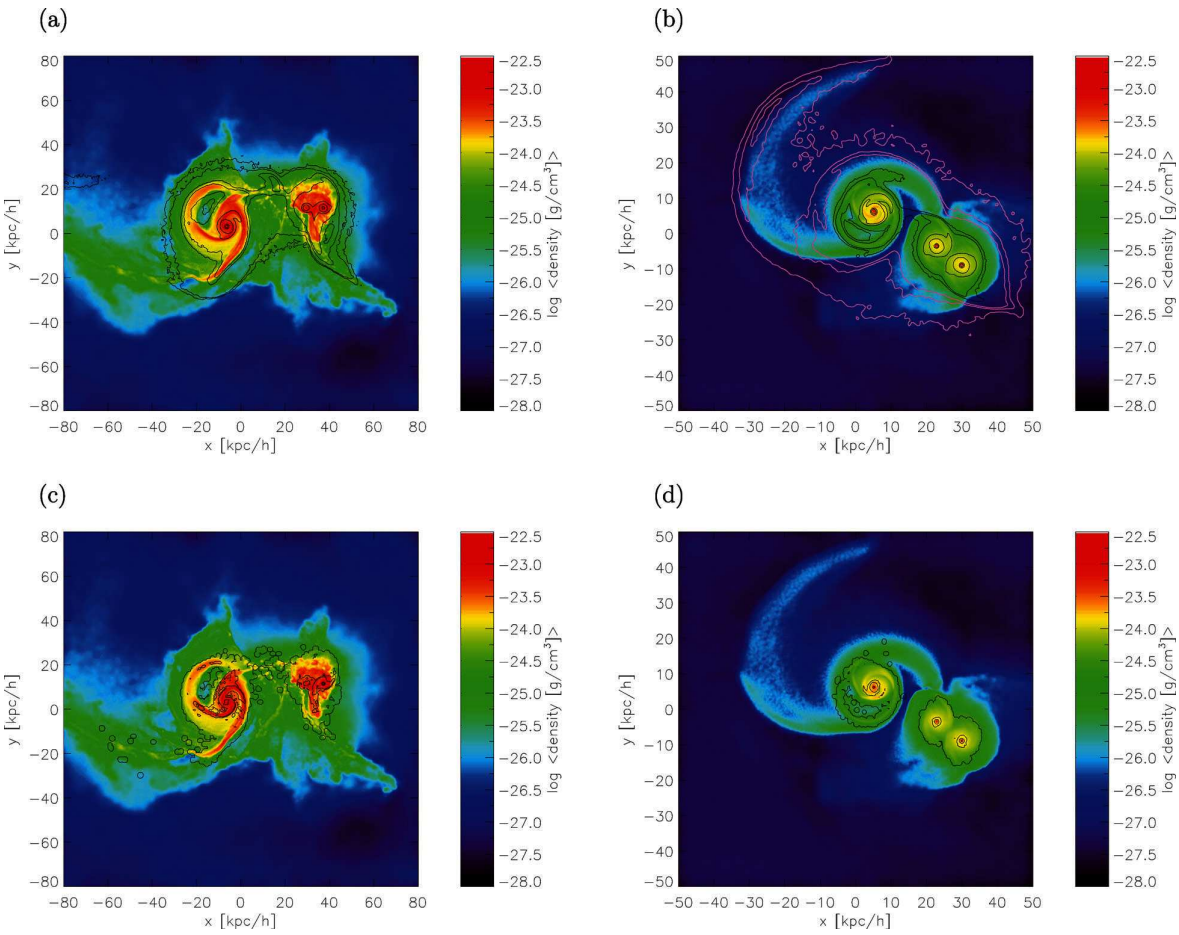

Figure 5.3: (a) Gas density overlaid with contours of the total stellar surface density (contour levels: 0.003, 0.007, 0.03, 0.07, 0.3, 0.7, 3 and 7 $M_\odot$ pc^{-2}) for the present-day configuration of SQ model A (t_{A3} = 320 Myr). (b) Same as (a), but for the present-day configuration of SQ model B (t_{B3} = 860 Myr) with three additional pink contour levels (levels: 0.00007, 0.0003 and 0.0007 $M_\odot$ pc^{-2}), which were smoothed with a circular Gaussian beam with a full width at half-maximum (FWHM) = 3. (c) Gas density overlaid with the stellar surface density of newly formed stars (contour levels: 3 $\times 10^{-7}$, 0.003, 0.007, 0.02 and 0.07 $M_\odot$ pc^{-2}) for SQ model A (t_{A3} = 320 Myr). (d) Same as (c), but for SQ model B (t_{B3} = 860 Myr).

the main system and collides with the IGM material west of NGC 7319. Meanwhile, about 80 h^{-1} kpc behind the plane of the main system, NGC 7318a moves westwards. The evolution results in a configuration similar to observations (B3 - present day: $t_{\rm pd} = t_{\rm B3} = 860$ Myr). Within this model, NGC 7320c is still present in the tail, but however, it is largely disrupted, therefore we had to estimate the coordinates of the center of this galaxy.

Fig. 5.3 (b) shows the same quantities as Fig. 5.3 (a) but for the SQ model B at the time $t_{\rm B3} = 860$ Myr. As for the model A, there is a good qualitative agreement of the general features with observations. Yet, model B reproduces the position of the galaxy pair NGC 7318a/b better than model A (cf. also Fig 1). The stellar surface density shows the highest values in the inner discs of NGC 7319 and NGC 7318a/b. Again, a stellar bridge is visible between NGC 7319 and the galaxy pair NGC 7318a/b. However, the position of NGC 7318a is slightly too much south, which is a feature of our SQ model B, not of the original model by Hwang et al. (2012). SQ model B is also not capable of reproducing small-scale features like the spiral arms of NGC 7318b or the detailed structure of NGC 7319 correctly and the outer tail is shorter compared to observations.

SQ model A and SQ model B differ significantly in the formation scenario of the outer and the inner tails. Whereas in the first case the two tails are evolved in two different interactions of NGC 7319 with NGC 7320c and NGC 7318a, within the SQ model B the tails are created by only one interaction event of NGC 7319 with NGC 7320c. Within SQ model A, the outer tail is formed about $t_{\rm pd} - t_{\rm ot} = 240$ Myr ago and the inner tail about $t_{\rm pd} - t_{\rm it} = 180$ Myr ago, resulting in a formation age difference of ≈ 60 Myr (which is similar to the results of the model of Renaud et al. (2010), who found a formation age difference between the tails of ≈ 70 Myr). In contrast, SQ model B shows an equal formation age of both tails about $t_{\rm pd} - t_{\rm ot} = 700$ Myr ago. However, observations are still suggesting different ages of the tails: Moles et al. (1997) proposed an age of the outer tail of $\geq 500 - 700$ Myr and for the inner tail ≈ 200 Myr by considering the radial velocity difference between NGC 7319 and NGC 7320c. Later, Sulentic et al. (2001) found that this measurement of the radial velocity was highly overestimated and suggested a much slower radial velocity for NGC 7320c (almost identical to that of NGC 7319) resulting in a prediction for the encounter of NGC 7319 with 7320c (causing the inner tail) about ≥ 500 Myr ago, which is similar to the predicted age of the outer tail. Fedotov et al. (2011) suggested an age of ≈ 400 Myr for the outer tail and ≤ 200 Myr for the inner tail. However, Fedotov et al. (2011) also found that the inner tail also contains some old clusters with an age of ≈ 500 Myr, even if it is mainly composed of blue clusters. Hwang et al. (2012) argue that the different formation ages would not have necessarily taken place in order to explain the different SF histories, as the outer tail evolves in a different environment, which may be less dense compared to the environment of the inner tail.

SQ model B clearly supports the idea of a common origin of the both tails caused by only one interaction event about ≈ 700 Myr ago, which agrees well with observational predictions for the formation age of the outer tail (see e.g. Moles et al., 1997). In contrast, SQ model A implies different formation ages of the tails, whereby the finding of a formation age of the inner tail of ≈ 200 Myr corresponds also to observational findings (e.g. Moles et al., 1997; Fedotov et al., 2011), whereas the formation age difference of only ≈ 60 Myr seems to be too small compared to observations. To conclude, we cannot rule out any of the proposed formation scenarios and ages for the two tails, however, the slightly better agreement of the resulting positions of the galaxies (particularly of the galaxy pair NGC 7318a/b) and the larger formation age of the tails may be interpreted as an indication to prefer the formation scenario of SQ model B.

5.3.2 Star formation

SF activity in SQ is believed to be triggered by the interactions (Xu et al., 2005). Fig. 5.3 (c) again shows the gas density for model A at $t_{\rm A3} = 320$ Myr, but this time overlaid with contours of the stellar surface density of the newly formed stars (i.e. stars which were not present in the initial set-

up). Most new formed stars are found within the inner disc regions of NGC 7319 and NGC 7318a. Slightly less SF takes place within NGC 7318b. A low SF activity and thus a low surface density of newly formed stars is found within the spiral arms of NGC 7319, the outer discs of NGC 7318a/b, in the IGM between NGC 7319 and NGC 7318a/b and in the region of the inner tail south-east of NGC 7319. The surface density of newly formed stars within the IGM mainly traces the stellar and gaseous bridge. However, parts of this SF region seem to coincide also with probably the edges of a shock region visible in X-ray and radio emission, which in principle corresponds to the observed SF regions (Xu et al., 2005; Cluver et al., 2010). However, the starburst region north of NGC 7318a/b found in observations is not revealed in the surface density of new formed stars in our SQ model A.

Fig. 5.3 (d) shows the same quantities as Fig. 5.3 (c) but for the present-day configuration of SQ model B. The highest surface density of new formed stars is found within the inner discs of NGC 7319 and NGC 7318a/b. Less SF takes place in the outer discs of the galaxies and within the spiral arm structure of NGC 7319. The lowest SF is found north of NGC 7319. Most of these regions are indeed also observed to form stars (Xu et al., 2005). However, there is no region of noticeable ongoing SF in the IGM between the main galaxy NGC 7319 and the galaxy pair NGC 7318a/b, i.e within or at the edges of the supposed shock region. The starburst region north of the pair NGC 7318a/b found in observations is also not reproduced.

5.3.3 Temperature and X-ray emission

The main source of X-ray emission is hot gas, which is heated by shocks accompanying the interactions. We calculate the bolometric X-ray luminosity following the method of Navarro et al. (1995), which assumes thermal bremsstrahlung to be the main X-ray source in agreement with the applied zero-metallicity cooling function. The bolometric X-ray luminosity is projected along the line of sight according to

$$L_{\rm x} = 1.2 \cdot 10^{-24} \frac{1}{(\mu m_{\rm p})^2} \sum_{i=1}^{N_{\rm gas}} m_{{\rm gas},i}\ \rho_i \left(\frac{k_{\rm B} T_i}{\rm keV}\right)^{1/2} \left({\rm erg\ s^{-1}}\right), \tag{5.2}$$

with mass $m_{{\rm gas},i}$, density ρ_i and temperature T_i of the ith gas particle in CGS units. Only fully ionized particles should be considered when calculating the luminosity. Therefore, we exclude contributions of particles with temperatures lower than $10^{5.2}$ K and densities higher than 0.01 $\rm M_\odot\ pc^{-3}$ (cf. Cox et al., 2006).

Fig. 5.4 (a) shows the temperature overlaid with contours of the X-ray emission for the present-day configuration of SQ model A. The gas within the galaxies is cooler, whereas the IGM gas is heated by shocks and outflows caused by the interactions. The logarithmic contours illustrating the X-ray emission reveal a total X-ray luminosity which is approximately four orders of magnitude lower than the observed X-ray luminosity in SQ ($10^{40} - 10^{41}$ erg $\rm s^{-1}$, Sulentic et al., 2001). This low X-ray luminosity results most probably from the applied zero-metallicity cooling and the lack of black holes in the simulations (cf. Cox et al., 2006; Geng et al., 2012b). Nevertheless, the X-ray luminosity shows the highest values in the IGM region between NGC 7319 and NGC 7318b, indicating a large shock east of NGC 7318b. This shock region fits very well to the observed shock front visible as a ridge in the X-ray and radio emission (cf. Fig. 5.2). However, the morphology of the shock region found in our simulations differs slightly from the observations. This difference might be explained by the more northern position of the galaxy pair NGC 7318a/b compared to the observed position.

Fig. 5.4 (b) shows the same quantities as Fig. 5.4 (a) for the present-day configuration of SQ model B. Again, the IGM surrounding the galaxies is heated by the shocks and outflows caused by the interactions. One large outflow is clearly visible in the temperature in a region south of the galaxy pair NGC 7318a/b and a smaller outflow in the north-west of the pair. The gas within the galaxies is cooler than within the IGM. The overall temperature of this model is significantly lower compared to

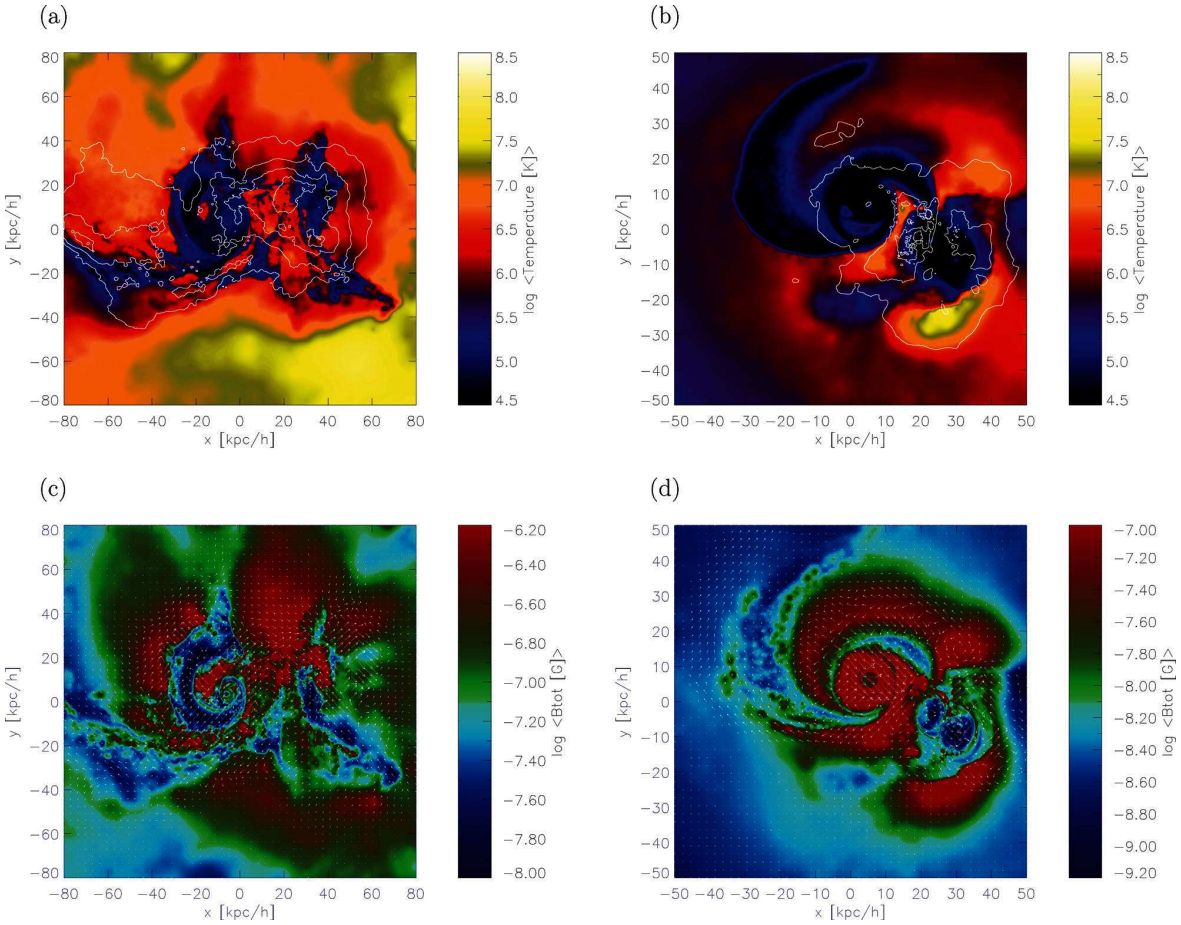

Figure 5.4: (a) Temperature overlaid with X-ray contours (logarithmic contour levels: 36.75, 37.25, 37.75 and 38.25 erg s^{-1}) for the present-day configuration of SQ model A at the time $t_{A3} = 320$ Myr. (b) Same as (a), but for the present-day configuration of SQ model B ($t_{B3} = 860$ Myr) and with lower contour levels (logarithmic contour levels: 35.75, 36.25, 36.75 and 37.25 erg s^{-1}). (c) Magnetic field strength overlaid with arrows showing the direction of the magnetic field (initial magnetic field in x-direction with $B_{gal,0} = B_{IGM} = 10^{-9}$ G) for SQ model A ($t_{A3} = 320$ Myr). (d) Same as (c), but for SQ model B ($t_{B3} = 860$ Myr).

SQ model A (Figs. 5.4 (a) and 5.4 (b) use the same colour bar). This is consistent with the smaller and less massive galaxy models. Consequently, also the X-ray emission is approximately one order of magnitude smaller than for SQ model A. As before, the highest X-ray emission is found within the IGM region between NGC 7319 and NGC 7318b, again indicating a prominent shock. This region of enhanced X-ray emission is more extended compared to SQ model A and agrees in general well with observations (cf. Fig. 5.2).

5.3.4 Magnetic field structure

The magnetic field is expected to get enhanced through random and turbulent motions driven by the interactions of the galaxies (see e.g. Brandenburg & Subramanian, 2005). The compact SQ system has undergone a number of interactions, whereby the magnetic field within the galaxies and within the ambient IGM should have been amplified and distributed significantly.

Fig. 5.4 (c) shows the mean total magnetic field strength overlaid with the magnetic field vectors for the SQ model A. It can be recognized that shocks and interaction-driven outflows are expanding into the IGM, thereby enhancing the magnetic field strength up to values of almost μG order. Some regions, such as the upper galactic arm of NGC 7319, the region around the inner tail and parts within the galaxy pair NGC 7318a/b show lower values of the total magnetic field strength. These regions are most probably not directly affected by the encounters. Hence, the slight enhancement of the magnetic field in these regions might be solely due to the winding process of the galaxies. High values of the magnetic field strength are in particular found within the large outflow in the upper north which seems to originate between NGC 7319 and NGC 7318b, where also the large shock is located. There, we also find high magnetic field strengths. The direction of the magnetic field, which is heading towards NGC 7318b, may indicate that the shock was triggered by a collision between NGC 7318b with the IGM (instead of a collision with NGC 7318a).

Fig. 5.4 (d) shows the same quantities as Fig. 5.4 (c) but for the SQ model B. Note the different colour bar appropriate for the lower magnetic field strengths. As before, shocks and interaction-driven outflows are propagating into the IGM, enhancing the magnetic field strength up to values of order 0.1 μG. Again, regions of lower magnetic field strength are found between the tidal arms of NGC 7319 and within the two galaxies NGC 7318a/b. These regions are probably not directly affected by the interactions (the galaxies NGC 7318a/b are affected by their mutual collision only in the very outer regions of the discs). The highest values of the magnetic field strength are found between the main galaxy and the galaxy pair NGC 7318a/b. Again, this highly magnetized region coincides with the supposed shock region also observed in X-ray. Comparable magnetic field strengths are found within the disc of NGC 7319 and within the outflows north of NGC 7319 and south-west of NGC 7318a/b. The magnetic field vectors within the region of the shock are either directed towards NGC 7318b or along the inner tail. As the collision of NGC 7318b with NGC 7318a happened about 220 Myr before the present-day configuration, the prominent shock found in SQ model B is certainly a result of an interaction of NGC 7318b with the IGM.

5.3.5 Radio emission and polarization maps

We compute synthetic radio emission and polarization maps for our simulations of the two different representations of SQ in an analogous way as presented in Kotarba et al. (2011).

Fig. 5.5 shows synthetic radio maps of model A (a) and model B (b), respectively, at 4.86 GHz for the present-day configuration (A3 and B3). Colours visualize the total intensity $I_{\rm tot}$ and the black contours show the polarized Intensity $I_{\rm p}$ (in μJy/beam). The direction of the magnetic field is indicated by the white lines, whereby the length of these lines is scaled according to the degree of polarization $\Pi_{\rm obs}$ (cf. length scale in lower left corner of the plots). Total as well as polarized synchrotron emission is visible inside but also outside the galactic discs, indicating that the interaction-driven shocks have

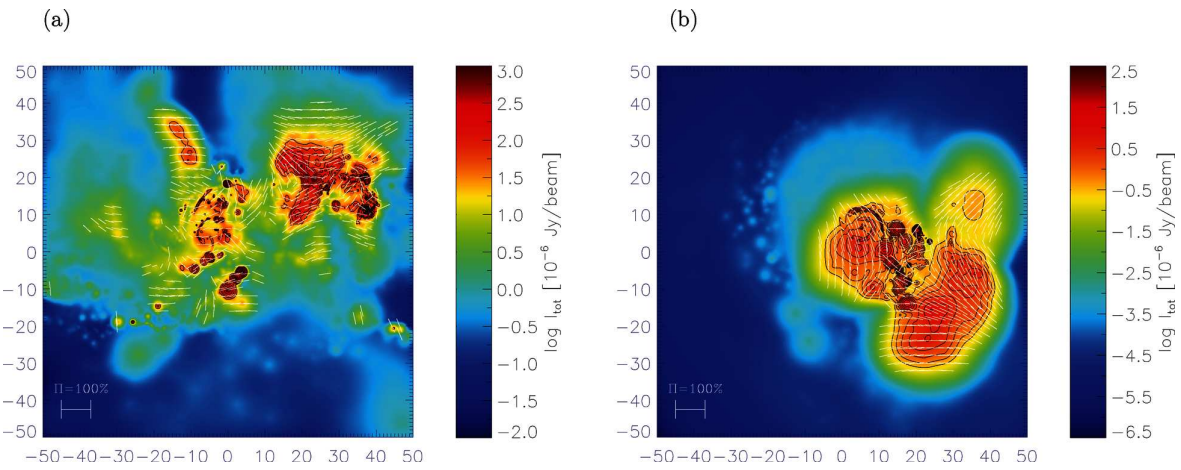

Figure 5.5: Synthetic radio map for model A and model B at 4.86 GHz. Colours visualize the total intensity $I_{\rm tot}$ (in μJy beam^{-1}). Black contours show the polarized Intensity $I_{\rm p}$ and correspond to (a) to 25, 50, 100, 200, 400, 800 and 1600 μJy beam^{-1} and (b) to 0.25, 0.5, 1, 2, 4, 8 and 16 μJy beam^{-1}. Magnetic field lines derived from calculations of polarization are shown in white. Note the different colour coding of the radio maps. Within both models, high total and polarized synchrotron emission is found within the region of the prominent shock between NGC 7319 and NGC 7318a/b.

already magnetized the sourrounding IGM. In both models, high total and polarized synchrotron emission is found within the region of the large shock between NGC 7319 and NGC 7318a/b. The contour levels of the polarized synchrotron emission within SQ model B are approximately a factor of 100 lower compared to SQ model A.

The synthetic radio map of SQ model A (left panel in Fig. 5.5) reveals a high total synchrotron intensity in the central part of NGC 7319, in the disc of NGC 7318a and in the region between NGC 7319 and the galaxy pair NGC 7318a/b. The region of enhanced synchrotron intensity east of NGC 7318b coincides very well with the shock region found in the observed X-ray luminosity. The regions of high synchrotron emission correspond well to observations (cf. Fig. 5.2 and Xu et al., 2003 their Fig. 4). There is a further region of enhanced synchrotron emission north of NGC 7318b, which is presumably due to a strong outflow. The strength of the synchrotron intensity corresponds to the observed order of magnitude.

The synthetic radio map of SQ model B (right panel of Fig. 5.5) reveals a high total synchrotron intensity within the disc of NGC 7319 and a slightly lower synchrotron emission around NGC 7318a. Also, there is a region of high synchrotron emission between NGC 7319 and NGC 7318a/b, which coincides with the shock region found in the X-ray emission. In general, the regions of enhanced synchrotron emission agree well with observations (cf. Fig. 5.2 and Xu et al., 2003 their Fig. 4). However, the strength of the synchrotron emission within this SQ model is approximately a factor of 100 lower compared to SQ model A. There is a region of slightly enhanced synchrotron intensity in the north of the galaxy pair NGC 7318a/b, which may be compared to the observed SF region also showing high radio emission (Xu et al., 2003).

	SQ model by Renaud et al.	SQ model A	SQ model by Hwang et al.	SQ model B
SQ morphology	Qualitative agreement	Qualitative agreement	Qualitative agreement	Qualitative agreement
Large shock	-	Clearly visible in X-ray and radio emission	Indicated by gas distribution and shock-heated gas	Clearly visible in X-ray and radio emission
SF regions	-	General agreement with observations	Hardly comparable (very roughly displayed)	Correspond roughly with observations
SF rates	-	Behaviour in agreement with previous numerical studies	-	Behaviour in agreement with previous numerical studies
Temperature	-	Behaviour in agreement with previous numerical studies	Hardly comparable (very roughly displayed)	Behaviour in agreement with previous numerical studies
X-ray regions	-	Correspond generally with observations	-	Correspond generally well with observations
X-ray strength	-	Too low compared to observations	-	Too low compared to observations
Magnetic field	-	Behaviour in agreement with previous numerical studies	-	Behaviour in agreement with previous numerical studies
Synchrotron regions	-	Good agreement with observations	-	Correspond generally to observations
Synchrotron strength	-	Order of magnitude corresponds to observations	-	Low compared to observations

Table 5.3: Achievement of our SQ simulations compared to previous numerical studies of SQ.

5.4 Conclusions

We have presented simulations of SQ including magnetic fields, radiative cooling, SF and SN feedback. We have investigated different properties of the gaseous component for two different galaxy models: SQ model A, based on Renaud et al. (2010) and SQ model B, based on Hwang et al. (2012). We have set the focus on the general morphology, on the distribution of SF regions and SF rates, on the temperature and the corresponding X-ray emission and finally on magnetic fields and the resulting total and polarized radio emission. A brief listing of the achievement of our simulations in comparison with the previous studies by Renaud et al. (2010) and Hwang et al. (2012) is shown in Table 5.3. The main results of our simulations can be summarized as follows.

- The present-day configuration of SQ model A develops within 320 Myr. The morphology of the system agrees qualitatively well with observations, only the position of the galaxy pair NGC 7318a/b, its small-scale details and the inner and outer tails cannot be reproduced correctly. The outer tail is generated in this model but already too diffuse to be visible at the present-day configuration as already noted for the original model of Renaud et al. (2010).
- The present-day configuration of SQ model B develops within 860 Myr. Again, the morphology of the system agrees qualitatively well with observations; however, the position of NGC 7318a is slightly too southern. Also, the small-scale features such as the arms of NGC 7318b or the smaller-scale structure of NGC 7319 cannot be reproduced correctly and the outer tail is shorter compared to observations.
- Within SQ model A, the total masses of the galaxies are approximately Milky Way-like. In contrast, the galactic masses of SQ model B are roughly a factor of 10 smaller compared to SQ model A. As lower galactic masses imply lower equipartition energies, the enhancement of the gaseous properties is commonly lower for SQ model B.
- The regions of active SF within SQ model A are found mainly in the discs of the galaxies and also within the inner tail and between NGC 7319 and the pair NGC 7318a/b. The latter partly coincides with the region of the large shock. Within SQ model B, the regions of active SF are found within the inner discs of NGC 7319 and the galaxies NGC 7318a/b, but there is no region of active SF between these galaxies.
- In both models, the temperature of the gas within the galaxies is cooler compared to the IGM, which gets heated by shocks and outflows caused by the interactions. The mean temperature in SQ model B is significantly lower compared to SQ model A.
- The X-ray emission shows the highest luminosities in the region of the large shock between NGC 7319 and the pair NGC 7318a/b within both models, in good agreement with observations (Pietsch et al., 1997; Sulentic et al., 2001). The X-ray luminosity in the shock region within SQ model B is about one order of magnitude smaller compared to SQ model A.
- We find high values of the magnetic field strength in the region of the large shock and also within outflow regions in both SQ models. The values of the magnetic field strength within SQ model B are approximately a factor of 3 smaller compared to SQ model A.
- The synthetic radio maps of both models show a high total and polarized synchrotron intensity within the large shock, within NGC 7319 and around and within NGC 7318a. This finding agrees well with observations (cf. Xu et al., 2003).

The large shock revealed by observations of SQ is most likely the result of a collision of NGC 7318b with the IGM. The observed ridge of radio emission can therefore be ascribed to shock activity.

The shock front in our simulations is clearly visible in the X-ray and synchrotron emission within both SQ models. We emphasize the importance of shocks for the magnetic field amplification and the enhancement of the synchrotron emission. Whenever a high amount of synchrotron emission is detected in regions between interacting galaxies, it may be ascribed to shock activity.

For future studies, a further development of the existing SQ models would be essential to draw more detailed conclusions on the extension and strength of the synchrotron emission within SQ. As the SQ model B results in a lower enhancement of the gaseous properties mainly because of the smaller masses, but displays the regions of enhanced X-ray and synchrotron emission quite well, it would be worthwile to use a different scaling of the total masses of SQ model B comparable to the total masses of the SQ model A. This would lead to a better comparability of the strengths of the gaseous properties of the present-day configuration of the two different models of SQ. Another particular focus in further studies should thereby be placed on the position and extension of the galaxy pair NGC 7318a/b, which we found to significantly affect the extension and structure of the large shock in SQ. As in our simulations the used particle masses are of the order of the mass of the largest molecular clouds, small-scale turbulence within the large shock region as recently observed by O'Sullivan et al. (2009) or Guillard et al. (2012) cannot be modeled in our work. Therefore, further numerical simulations focusing on smaller scales would lead to a deeper understanding of the involved processes of shock activity, especially shocks wrapped around clouds and cloud like structures. Furthermore, observations of the radio emission ridge at different frequencies would be of particular interest in order to gain new insights into the shock region. This knowledge could then be used as a basis for further improvements of numerical SQ models.

5.5 Acknowledgments

We thank the referee Jeong-Sun Hwang for very helpful comments which improved the paper significantly. AG is grateful for interesting and helpful discussions with Harald Lesch, Dominik Bomans and Federico Stasyszyn and thanks Volker Springel for the programs to set up the initial galaxy models. Rendered plots were made using P-SMAC2 (Donnert et al., in preparation). Granting of computing time from John von Neumann-Institute for Computing (NIC), Jülich, Germany, is gratefully acknowledged. We acknowledge support through the DFG Research Unit 1254. KD acknowledges the support by the DFG Priority Programme 1177 and additional support by the DFG Cluster of Excellence 'Origin and Structure of the Universe'.

Chapter 6

Paper VI: A divergence-cleaning scheme for cosmological SPMHD simulations

F.A. Stasyszyn, K. Dolag & **A.M. Beck**, 2013,
Monthly Notices of the Royal Astronomical Society, 428, 13

ABSTRACT

In MHD, the magnetic field is evolved by the induction equation and coupled to the gas dynamics by the Lorentz force. We perform numerical SPMHD simulations and study the influence of a numerical magnetic divergence. For instabilities arising from $\nabla \cdot \mathbf{B}$ related errors, we find the hyperbolic/parabolic cleaning scheme suggested by Dedner et al. to give good results and prevent numerical artefacts from growing. Additionally, we demonstrate that certain current SPMHD implementations of magnetic field regularizations give rise to unphysical instabilities in long-time simulations. We also find this effect when employing Euler potentials (divergenceless by definition), which are not able to follow the winding-up process of magnetic field lines properly. Furthermore, we present cosmological simulations of galaxy cluster formation at extremely high resolution including the evolution of magnetic fields. We show synthetic Faraday rotation maps and derive structure functions to compare them with observations. Comparing all the simulations with and without divergence cleaning, we are able to confirm the results of previous simulations performed with the standard implementation of MHD in SPMHD at normal resolution. However, at extremely high resolution, a cleaning scheme is needed to prevent the growth of numerical $\nabla \cdot \mathbf{B}$ errors at small scales.

Key words: magnetic fields, MHD, methods: numerical, galaxies: clusters: general

This chapter is a presentation of the main results of Stasyszyn et al. (2013). Our full study consists of 15 journal pages, including 1 table and 18 figures. However, to stay in the scope of this thesis, we picked out the most important and to this thesis connected results. In particular, we implemented into our SPMHD code a cleaning scheme for numerical non-vanishing $\nabla \cdot \mathbf{B}$ errors. We do not show an application to galaxy cluster formation and the effects on structure functions of synthetic cluster rotation measure maps. We refer the reader to our paper (Stasyszyn et al., 2013) for the entire study.

6.1 Introduction

Within cosmological simulations, many orders of magnitude in dynamical range have to be resolved correctly. Cosmological simulations are usually highly non-linear and also include a wide range of various physical processes. Therefore, it is important to have numerical methods and codes whose results are reliable and can be trusted. The computational challenges range from a proper calculation of the gravitational potential, to capturing shocks correctly within hydrodynamics and to controlling the $\nabla \cdot \mathbf{B} = 0$ constrain within magnetohydrodynamics. Additionally, many sub-grid modules provide further terms within the energy and force equations (i.e. cooling and feedback), which can cause tricky numerical instabilities. In cosmic magnetism, the evolution of any magnetic fields is directly coupled to all of these processes and equations. In particular, within Lagrangian methods such as SPMHD, the constrain $\nabla \cdot \mathbf{B} = 0$ is extremely challenging to maintain. It is usually maintained by regularizing the magnetic field (i.e. dissipating magnetic fluctuations) and transferring the assciated magnetic energy into internal energy, or removing it from the simulations. However, schemes which are over-dissipative or over-regularize the magnetic field can also lead to instabilities, in particular, within long-term simulations. Outstanding progress has been made over the past years in the development of numerical MHD schemes to remove unwanted $\nabla \cdot \mathbf{B}$ errors as well as guarantee numerical stable solutions (e.g. the Dedner divergence cleaning scheme). Concluding, it is important to extensively test our current SPMHD schemes on MHD standard tests and check for their stability and reliability. Within this article, we present an SPMHD implementation of the Dedner divergence cleaning scheme for the GADGET code. We perform the standard MHD test problems and also perform long-time simulations of the Orszag-Tang vortex to check the long-time stability of our schemes.

6.2 Numerical method

We are starting from the SPMHD implementation of Dolag & Stasyszyn (2009) within the cosmological N-Body TreePM/SPMHD code GADGET (Springel et al., 2001b; Springel, 2005). For the details of the implementation we refer to Dolag & Stasyszyn (2009) or to a more general review on SPMHD by Price (2012).

In short, the evolution of the magnetic field is directly followed with the induction equation. The magnetic field acts on the gas via the Lorentz force, written in a symmetric conservative form using the magnetic stress tensor. Also, as originally suggested by Price & Monaghan (2004) the fast magnetosonic wave velocity replaces the sound velocity within the computation of the signal velocity controlling the artificial viscosity and the time step. In the calculation of the gradients and divergence estimators, we follow the standard SPMHD implementation.

6.2.1 Instability correction

To take into account the tensile instability in SPMHD, which occurs when the magnetic pressure exceeds the gas pressure and the force between particles is becoming attractive, a correction term in the force equation is used. This term – introduced by Børve et al. (2001) and further developed in

Børve et al. (2006) – subtracts from the equation of motion any unphysical force resulting from a non-vanishing numerical $\nabla \cdot \mathbf{B}$. Contrary to the original implementation, we restrict the correction to not exceed the Lorentz force, which is necessary at strong shocks. Therefore, we evaluate the correction contribution and if necessary renormalize to be only as much as the Lorentz force.

6.2.2 Time integration

In Dolag & Stasyszyn (2009) the evolution of the magnetic field $\mathbf{B}$ is done in physical units, so that in cosmological simulations the induction equation contained a term of $-2\mathbf{B}$ to capture the cosmological dilution due to the expansion of space. However, defining the magnetic field in comoving units ($\mathbf{B_c} = \mathbf{B}/a^2$), with a the cosmological scale factor allows us to drop the $-2\mathbf{B}$ term and the induction equation becomes

$$\frac{d\mathbf{B_c}}{dt} = (\mathbf{B_c} \cdot \nabla)\mathbf{v} - \mathbf{B_c}(\nabla \cdot \mathbf{v}). \tag{6.1}$$

When reading output data from the simulation the magnetic field is converted back into physical units by multiplying it with $1/a^2$.

To capture in more detail situations where the magnetic field structure is folded on the resolution scale, an additional time-step criterion for every particle i can be constructed as follows:

$$\Delta t_i \approx \frac{h_i}{v_i^{\text{typical}}} \approx h_i \sqrt{\frac{\rho_i}{4\pi(\nabla \cdot \mathbf{B})_i^2}}, \tag{6.2}$$

where h is the SPMHD smoothing length. This criterion allows to capture regions of high numerical divergence, where the magnetic field structures reach the resolution limit and put the particles on lower time-steps ensuring a more detailed evolution of the magnetic field. Although this additional criterion rarely overcomes the standard time-step criterion, there are situations where it seems to be quite helpful to follow the local dynamics with more details.

6.2.3 Divergence Cleaning

It is of fundamental interest in SPMHD simulations to keep the magnetic divergence $\nabla \cdot \mathbf{B}$ arising from the numerical integration schemes to a minimum. We implement into the GADGET code, the divergence-cleaning scheme introduced by Dedner et al. (2002), which evolves an additional scalar potential ψ representing non-vanishing $\nabla \cdot \mathbf{B}$ introduced artefacts. By construction, this potential ψ propagates the numerical errors outwards the simulation, while damping them, by subtracting the gradient of ψ in the induction equation. This method is also widely used in Eulerian codes (i.e. Anderson et al., 2006; Cécere et al., 2008; Keppens et al., 2012) and recently introduced in the moving mesh code AREPO (Springel, 2010a; Pakmor et al., 2011). First attempts to use this technique in SPMHD were made by Price & Monaghan (2005), being not satisfactory. They found only a mild improvement of the numerical $\nabla \cdot \mathbf{B}$ errors and in some test cases the cleaning scheme was even causing instabilities particularly in 3D. Recently, Tricco & Price (2012) also developed a magnetic cleaning scheme conserving energy, which is similar to our considerations. The implementation shown here lowers the $\nabla \cdot \mathbf{B}$ error in general, does not show unwanted effects and additionally leads to a very small numerical diffusion.

Following Dedner et al. (2002), therefore assuming a non-vanishing $\nabla \cdot \mathbf{B}$, an additional term entering the induction equation can be derived as follows:

$$\left.\frac{d\mathbf{B}}{dt}\right|_i^{\text{Ded}} = -(\nabla\psi)_i. \tag{6.3}$$

To be energy conserving, the removed of magnetic energy is transferred into internal energy or entropy A at a rate of

$$\mu_0 \frac{dA}{dt}\bigg|_i^{\mathrm{Ded}} = -\frac{\gamma-1}{\rho_i^{\gamma-1}} \mathbf{B}_i \cdot (\nabla\psi)_i \tag{6.4}$$

where $(\gamma-1)/\rho^{\gamma-1}$ is the conversion factor from internal energy to entropy with the adiabatic index γ.

However, the scalar potential ψ has to be chosen in a way to actually remove numerical errors. Dedner et al. (2002) found that the most effective solution is to construct and evolve ψ propagating the errors away from the source (i.e hyperbolic cleaning) and damping them (i.e parabolic cleaning). This results in the following evolution equation for ψ:

$$\frac{d\psi_i}{dt} = -\left((c_{\mathrm{h}})_i^2 (\nabla \cdot \mathbf{B})_i - \frac{\psi_i}{\tau_i} \right), \tag{6.5}$$

which shows that ψ now satisfies a wave equation propagating the errors outwards the source with a speed of c_{h} (first term of the equation) and decaying them on a timescale of τ (second term in the equation). It is again natural in SPMHD simulations to relate the propagation speed to the fast magnetosonic wave, hence using $c_{\mathrm{h}} = \sigma v^{\mathrm{mhd}}$. Note that this velocity does not have to be related with any special quantity per se, even can be a constant value. Also, the timescale τ can be related to a typical length scale (smoothing length h) and velocity resulting in $h/\lambda v^{\mathrm{mhd}}$, only leaving dimensionless numerical constants λ (parabolic) and σ (hyperbolic) of the order of unity. We choose values of $\lambda = 4$ and $\sigma = 1$ to recover the best solution in Price & Monaghan (2005).

Similar to the tensile instability correction of the Lorentz force (Børve et al., 2001) in the equation of motion, this method can lead to instabilities. In particular, situations where small-scale structures in the magnetic field lead to an imprecise calculation of the $\nabla \cdot \mathbf{B}$ source term. This situation will manifest as an overcorrection of the induction equation. Hence, we use a limiter for the cleaning contribution in a similar form, not allowing the correction in the induction equation to be larger than a given value Q weighted by the local induction value. When the correction exceeds the original term, we renormalize it. To ensure stability, this ratio Q has to be less or at most equal to 1. Testing different parameters we found a value of $Q = 0.5$ to be sufficient in ensuring a proper evolution of the magnetic field while avoiding overcorrections due to the cleaning scheme.

6.3 Standard tests

The problems in structure formation are very complex and astrophysical objects of interest evolve in a strongly, non-linear way from the initial conditions to the final stages during the different cosmological epochs. To be confident about the numerical results, the hydrodynamical solving scheme has to be tested properly and compared with known analytical solutions. Therefore, we tested the new cleaning scheme in an extensive series of shock tubes and planar tests, similar as done in Dolag & Stasyszyn (2009). In the same way as done previously, we performed all the tests by setting up a fully three-dimensional glass like particle distribution, to obtain results under most realistic possible circumstances and compare them with the solution obtained with ATHENA (Stone et al., 2008) (in 1D or 2D, respectively). In the 1D case we use 512 cells for the ATHENA runs and at most 136 particles per cell in the GADGET runs. Note that the GADGET runs are performed with a 3D set-up (in the same way as done in Dolag & Stasyszyn, 2009). To avoid SPH instabilities, all particles have the same mass (which means lowering the particle number to achieve low densities). It is worth to note that the use of glass-like particle distributions ensures that there is no intrinsic scatter due

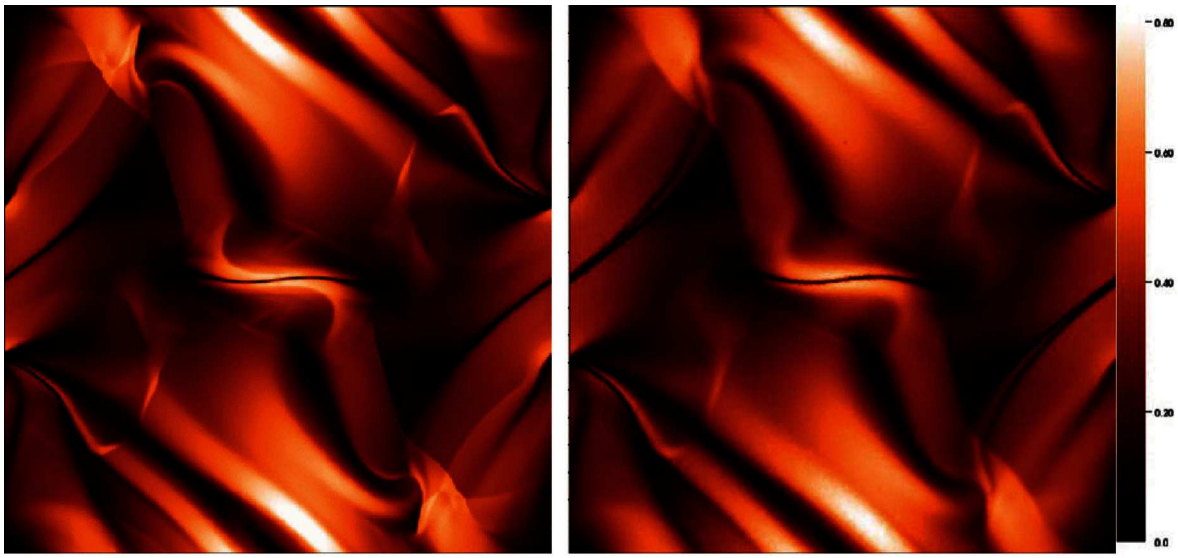

(a) Orszag-Tang Vortex- ATHENA (b) Orszag-Tang Vortex- Dedner

Figure 6.1: The magnetic field strength in the Orszag-Tang Vortex at $T = 0.5$. The left-hand panel shows the ATHENA results, while the right-hand panel shows the SPMHD Dedner scheme. Again, some the sharp features are slightly smoothed in the SPMHD implementations but overall the results compare very well.

particle positions, as they already rest in the lowest energy state (for more details see Price, 2012). Additionally, the $\nabla \cdot \mathbf{B}$ errors are defined by the dimensionless quantity

$$\mathrm{Err}_{\nabla\cdot\mathbf{B}_i} = |\nabla \cdot \mathbf{B}_i| \frac{h_i}{|B_i|} \tag{6.6}$$

which can be calculated for each particle and determines the reliability of the results.

6.3.1 Orszag-Tang vortex

This planar test problem, introduced by Orszag & Tang (1979), is well known for the interaction between several classes of shock waves (at different velocities) and the transition to MHD turbulence. Also, this test is commonly used to validate MHD implementations (for example see Picone & Dahlburg, 1991; Dai & Woodward, 1994; Londrillo & Del Zanna, 2000; Price & Monaghan, 2005; Børve et al., 2006). It consists of ideal gas with $\gamma = 5/3$ within a a box of (e.g. $x = [0, 1], y = [0, 1]$) and periodic boundaries conditions. The velocity field is defined by $v_x = -\sin(2\pi y)$ and $v_y = \sin(2\pi x)$. The initial magnetic field is set to $B_x = B_0 v_x$ and $B_y = B_0 sin(4\pi x)$. The initial density is $\rho = \gamma P$ and the pressure is $P = \gamma B_0^2$. An usual time to evaluate the system $t = 0.5$. Fig. 6.1 shows the final result at that time for the magnetic pressure for the ATHENA run (left-hand panel) and the Dedner scheme (right-hand panel). The results are quite comparable; however, the use of SPMHD method leaves its imprint in a slightly smoothed appearance in the GADGET results. This can also be seen in Fig. 6.2, which shows a cut through the test for different implementations, comparable with other cuts done in the literature (Børve et al., 2006). In general there is reasonable agreement; however, all the SPMHD results clearly show a smoothing of some features. However, the Dedner and standard implementations tend to match better some regions that the dissipative schemes oversmooth

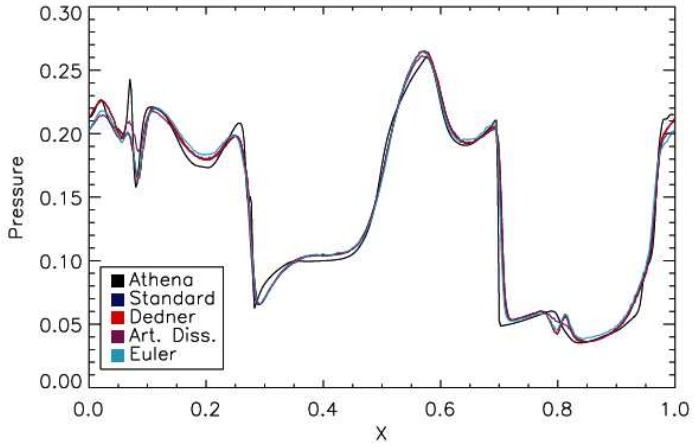

Figure 6.2: A $T = 0.5$ cut of the pressure in the Orszag-Tang Vortex at $y = 0.3125$. The black line reflects the results obtained with ATHENA, while the colours show different MHD schemes. The cut can be compared with existing results (e.g. Børve et al., 2006). Note that the variations in the solution between schemes mainly result from different dissipative characteristics. However, the overall solutions are in good agreement.

(e.g. region near $x \sim 1$ in Fig. 6.2), even better than the Euler scheme. Note that an exact comparison is difficult, mainly because this test includes the propagation of several types of magnetosonic waves, implying that if the correct velocity (i.e. by some dissipative effect) of a particular wave is not achieved, the result will diverge between implementations.

This periodic test in particular is good for checking the SPMHD implementation based on the Euler potentials formalism, finding a very good agreement with other authors (i.e. Rosswog & Price, 2007). As the Euler potentials are be $\nabla \cdot \mathbf{B}$ free by construction, any numerical arising $\nabla \cdot \mathbf{B}$ error can clearly traced back to the numerical inaccuracies in SPMHD formalism itself. Our major interest in this scheme is therefore the possibility to measure the errors that arise from the interpolation.

In Fig. 6.3 we show the calculated $\nabla \cdot \mathbf{B}$ errors as defined by equation 6.6. It can be seen that the numerical errors in the standard SPMHD implementation are only slightly larger than the errors of the implementation based on Euler potential; however, the spatial distribution varies. This is the numerical error limitation, which can be overcome by using higher resolution. Additionally, the numerical $\nabla \cdot \mathbf{B}$ errors we see are caused by the magnetic field structures getting folded below the kernel scales. Then, the basic assumption on which SPMHD works, namely that the values of any quantity of interest are smooth below the kernel scales, starts to get violated. In Eulerian methods such structures are automatically mixed (e.g. dissipated) on the resolution scale. In SPMHD an extra scheme (i.e artificial dissipation) is needed to remove those small-scale structures, acting as regularization of the field below the kernel scale. The Dedner cleaning scheme acts in this way; however, it dissipates mainly the magnetic field structure below the kernel scale and does not lead to strong smoothing of the field on scales larger than the kernel scale. However, it is enough to significantly remove the numerical $\nabla \cdot \mathbf{B}$ errors, as shown in Fig. 6.3. More drastic approaches suffer from the same issue, as can be seen for the artificial dissipation case.

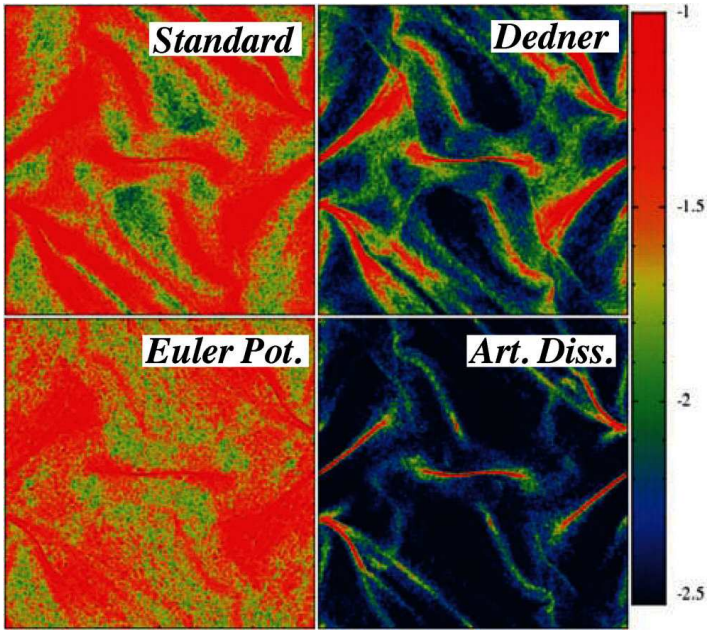

Figure 6.3: $\nabla \cdot \mathbf{B}$ errors as defined by equation 6.6 in the Orszag-Tang Vortex at $T = 0.5$. The upper row shows the standard scheme (left-hand panel) and the Dedner scheme (upper right-hand) panel. The lower row shows the calculated $\nabla \cdot \mathbf{B}$ errors from the Euler potential formulation (left-hand panel) and a run with artificial dissipation (right-hand panel). The Euler potential runs define the real numerical limits of the simulation and confirm the need of a numerical cleaning scheme.

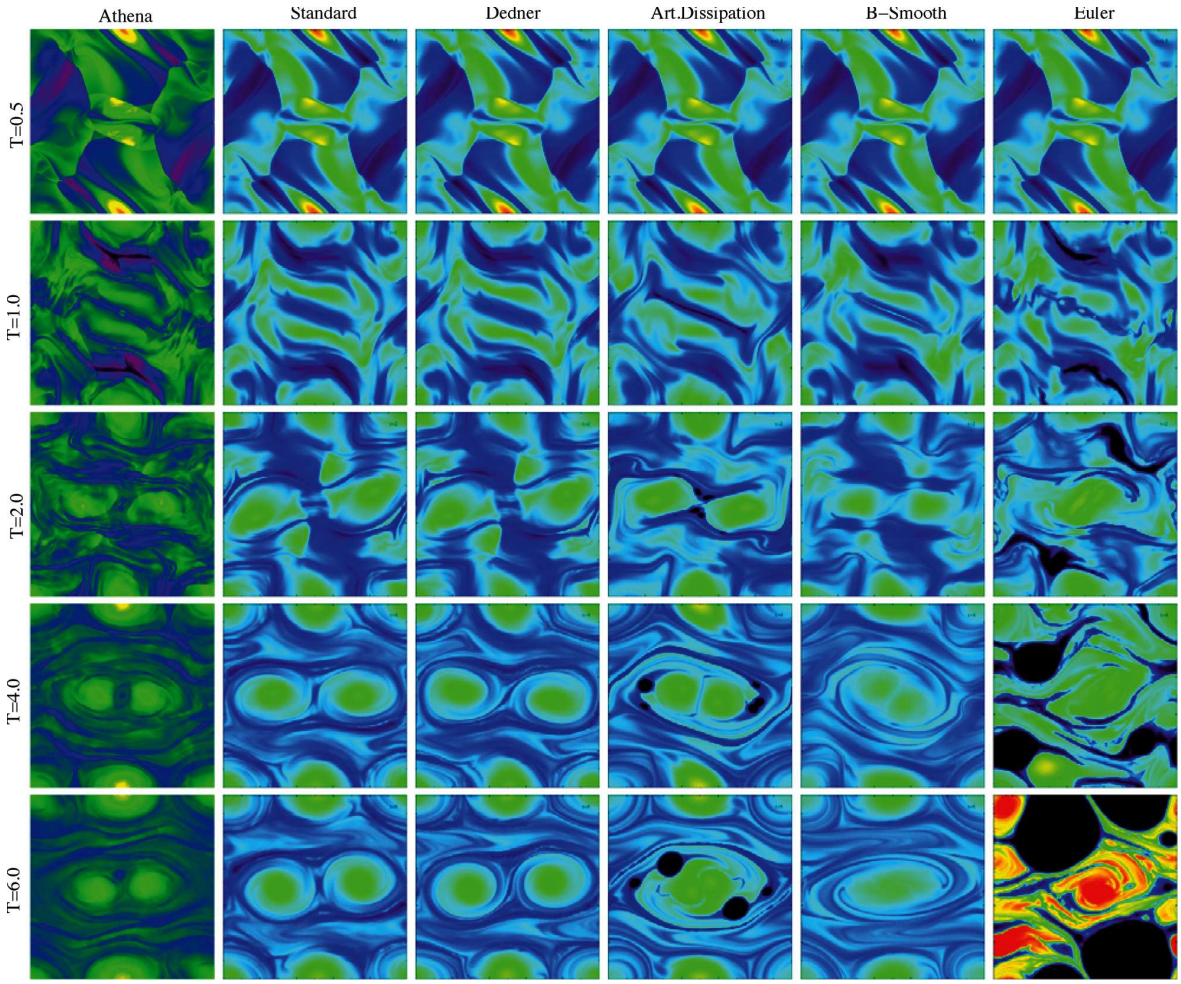

Figure 6.4: Density maps of the Orszag-Tang vortex at various times $T = 0.5, 1, 2, 4$ and 6 using several MHD schemes. There are deviations from the expected solution (ATHENA), even appearing at early times $T = 1.0$ for Euler and later in the more dissipative schemes. There are also problems long-time simulations.

6.3.2 Long-time stability of the Orszag-Tang vortex

The long-time evolution of the Orszag-Tang vortex was first studied by Picone & Dahlburg (1991). They focused on the possible stable solutions of the supersonic flow. Therefore, they studied the long-time evolution varying initial Mach numbers. Interestingly, they always found a quasi-stable configuration in the long time evolution, where they typically evolved the problem until $t = 8$. We run the Orszag-Tang vortex to large times to investigate the stability of the different implementations as well as the influence of the differently strong numerical dissipation. Additionally, we wanted to confirm the limitations of the Euler potential formalism (Brandenburg, 2010). In Fig. 6.4, we show the long-time evolution of the density distribution at various times. As expected, the implementation based on Euler potentials starts to deviate from the expected solution quite early ($t = 1$) and even runs into some severe instability at larger times $t > 4$. The regularization scheme based on artificial dissipation, as well as periodically smoothing the magnetic field, shows some significant effects of the underlying dissipation at times $t > 4$. These deviations even develop an instability within the scheme based on artificial dissipation and even at earlier times $t < 4$ for higher dissipation constants. However, both the standard MHD implementation as well as the one based on the Dedner cleaning scheme show excellent performance in the long-term evolution and stability, well comparing to the results presented in Picone & Dahlburg (1991). It is worth to note that both schemes appear to have less numerical dissipation than ATHENA. In our ATHENA run, the two central density peaks start to approach each other, while they are still stable in both, the standard as well as the Dedner SPMHD implementation.

6.3.3 Discussion

In Fig. 6.5 we show the comparison of the performance of the different SPMHD implementations among several standard tests we performed. We compare the numerical errors obtained by the different implementations against the standard implementation. Additionally, we resize the points, following the quality criterion as defined in Dolag & Stasyszyn (2009). Therefore, we are able to compare the performance between all against the standard runs. For this, we define three different sizes when comparing to the standard quality value, corresponding to different grades in the improvement.

The Dedner cleaning schemes clearly reduced the $\nabla \cdot \mathbf{B}$ error in all the standard tests. Although the dissipative schemes have even lower $\nabla \cdot \mathbf{B}$ errors, the cleaning scheme out stands, as it lowers the $\nabla \cdot \mathbf{B}$ and also is least dissipative. In contrast, there are some tests showing lower $\nabla \cdot \mathbf{B}$ errors, but the regularization schemes over smooth some features, therefore enhancing differences with the correct solution.

Especially regularization schemes like the one based on artificial dissipation can be seen to mimic the Ohmic dissipation and therefore leading away from ideal MHD. To study the structure of the magnetic field as imprinted by the complex, hydro-dynamical flows as imprinted by structure formation, it is quite important to have a scheme which on one hand regularizes the magnetic field below the kernel scale to avoid unwanted numerical artifacts as well as not influences the magnetic field structure at scales larger than the kernel scale (i.e. by artificial dissipation). As shown by the standard tests, the SPMHD implementation based on the Dedner $\nabla \cdot \mathbf{B}$ cleaning scheme seems to fulfill these requirements.

6.4 Conclusions

We continue the development started by Dolag & Stasyszyn (2009) of an SPMHD implementation of MHD in the cosmological simulation code GADGET. We performed various standard test problems and discussed instability corrections, regularization schemes and $\nabla \cdot \mathbf{B}$ cleaning techniques. The main

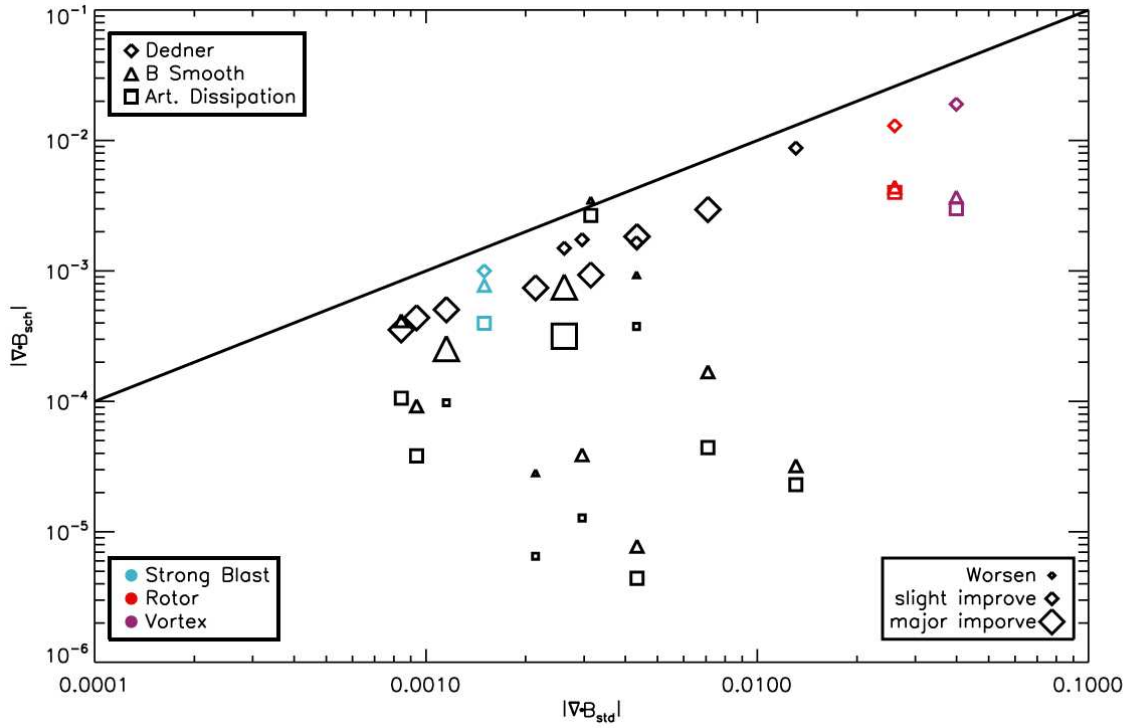

Figure 6.5: Summary plot showing the results of all 1D and 2D tests for the different SPMHD implementations, comparing the average $\nabla \cdot \mathbf{B}$ errors from the different schemes (symbols) and the Dedner $\nabla \cdot \mathbf{B}$ cleaning against the standard SPMHD implementation. In black are the shock-tube tests and in colours are the advanced problems. The point sizes follow a quality criterion defined in Dolag & Stasyszyn (2009), comparing the SPMHD solutions with the Euler ones. We define three different sizes when comparing to the standard quality value, corresponding to worst (small), major (big) or minor (normal) improvement.

focus was set on the role of the $\nabla \cdot \mathbf{B} = 0$ constrain, also comparing with Eulerian solutions. Our main findings can be summarized as follows:

- Correcting the tensile instability by explicitly subtracting the contribution of a numerical non-zero divergence of the magnetic field to the Lorenz force from the Maxwell tensor as suggested by Børve et al. (2001) or Dolag & Stasyszyn (2009) is performing well. To avoid spurious effects due to sampling problems, particularly in the front shocks, a threshold in the correction improves the performance and quality. This feature turns out to be fundamental for simulations with extremely high spatial resolution, where previously the numerical instabilities dominated and the simulations could not have been performed.

- We successfully implemented a multidimensional divergence-cleaning method in SPMHD. The GADGET SPMHD implementation continues to perform very well on our multidimensional shock-tube tests as well as on commonly used planar test problems. We showed that the Dedner cleaning scheme does not affect the shape of shocks, but reduces the $\nabla \cdot \mathbf{B}$ errors. This is important in astrophysical situations. Also, the evolution of the cleaning is completely local and only affected by the SPMHD interpolants.

- Testing our schemes in long-time runs of the Orszag-Tang vortex, we found that regularization schemes which depend on dissipation as well as implementations based on Euler potentials can lead to instabilities, whereas the standard implementation as well as the Dedner cleaning scheme is found to be robust and stable. This is a warning on the limits of possible MHD implementations within astrophysical environments.

We obtained our most important findings by comparing with an Euler (divergence-free by construction) scheme. This shows, that we have already reached the $\nabla \cdot \mathbf{B}$ error levels inherent from the SPMHD scheme itself (see Fig. 6.3) and any further cleaning or regularization will require to numerically dissipate the magnetic field. However, this does not yield an error-free implementation; thus, still some $\nabla \cdot \mathbf{B}$ related instabilities can arise. In the case of the Euler potentials, we stress the fact that this representation lacks important features in the evolution of the magnetic field (Brandenburg, 2010). However, outstanding progress has been made on providing stable MHD and SPMHD implementations, removing unwanted instabilities.

Furthermore, our code has different features with each regularization or cleaning scheme used. The success of the Dedner cleaning brings the simulations closer to the 'ideal' MHD state, by locally calculating and subtracting the error term in the induction equation. In Fig. 6.5 we show a comparison between all the implementations in different tests. The dissipative schemes have lower $\nabla \cdot \mathbf{B}$ errors, however the Dedner cleaning schemes stands out, lowering the $\nabla \cdot \mathbf{B}$ error and can in most cases improve the results. In contrast, there are some tests showing that to lowering $\nabla \cdot \mathbf{B}$ errors can over smooth important features in contrast to a correct solution.

6.5 Acknowledgements

Rendered plots were made using SPLASH (Price, 2007). KD is supported by the DFG Priority Programme 1177 and by the DFG Cluster of Excellence 'Origin and Structure of the Universe'. FAS is supported by the DFG Research Unit 1254. FAS thanks the useful discussions with Axel Brandenburg, Daniel Price and Florian Bürzle, during the development of this project.

Chapter 7

Final remarks

In this chapter, now that this thesis is coming to an end, we want to summarize our main findings and give an outlook. It might seem to the reader that we have completely illuminated the seeding and build-up of magnetic fields within galaxies. However, this thesis should be seen as just another scratch on the surface of a still expanding balloon of science. We have just begun to get a slight understanding of the complex processes and interplays.

Firstly, we have investigated the evolution of primordially seeded magnetic fields during the formation of a Milky Way-like galactic halo. We find that the formation and virialization of the galactic halo from the highest redshifts until today is sufficient to amplify magnetic seed fields of any strength up to μG values. The amplification is the result of a manifold interplay of turbulences, which accompany the very process of structure formation and which can be driven externally (e.g. gravitationally) or internally (e.g. SF). Additionally, the cooling and collapse of the gas leads to amplification by compression of the magnetic field lines. The growth truncates when energy equipartition between the magnetic pressure and the turbulent pressure is reached.

Secondly, we have investigated the evolution of SN seeded magnetic fields. The strength and distribution of the magnetic seed fields is given by the strength and distribution of SF. We find again that on galactic scales μG magnetic fields are reached during the formation and virialization of the galactic halo and conclude that, in a galaxy, the origin of the magnetic seed field seems not to be important. Many different drivers of non-equilibria exist and the system looses its memory of the initial conditions. However, the distribution of the magnetic field within the IGM or large-scale structure can differ significantly. In the case of primordial magnetic seed fields, magnetic fields are already present in all regions of space. In the case of SN seeding, magnetic fields are only present within SF regions and a secondary transport problem into the large-scale structure arises. Furthermore, we analysed the intrinsic RM distribution of our forming galactic halo. We find the halo to host a widespread heterogenous distribution of RM values of several 1000 rad m^{-2} at a peak redshift of z$\approx$3. During the virialization towards redshift z$\approx$0 the RM distribution becomes more homogenous and the RM values decline and become as low as 10 rad m^{-2}.

Thirdly, we have constructed a scenario for the magnetization of the largest cosmological voids by galaxies within the voids. Recently, observations revealed the presence of magnetic fields within the voids as well as the presence of an isolated population of void galaxies. In our scenario, magnetic seed fields may be created and amplified within the void galaxies. Meanwhile, CR driven outflows from the void galaxies could escape into the voids. The propagating CR could transport magnetic energy from the void galaxies into the void medium and magnetize a large volume fraction.

Fourthly, we have studied the magnetic field evolution in galactic minor merger events, which are frequently occuring during structure formation and thus influences the evolution of galactic magnetic fields. In a series of simulated minor merger scenarios we find that each galactic minor merger leads to an amplification of the galactic magnetic fields. Furthermore, merger-driven shockwaves propagate into the IGM potentially amplifying and distributing magnetic energy.

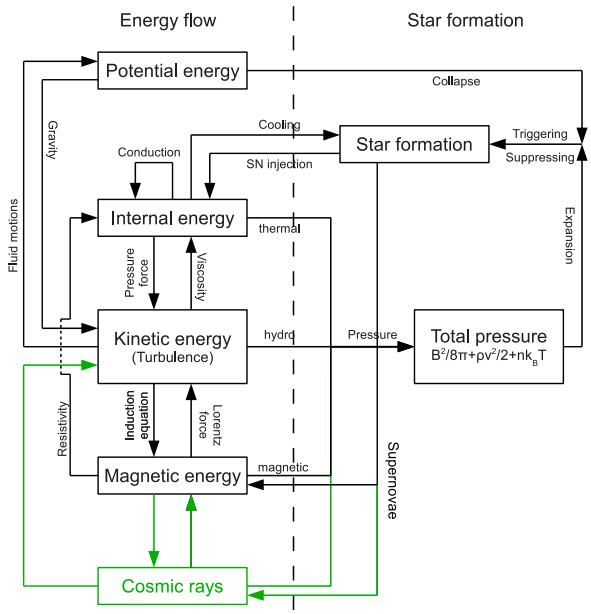

Figure 7.1: Extension of simulation flow as described by Beck et al. (2012) and further developed by Beck et al. (2013a). The diagram shows in black the existing energy connections and sub-grid models within our cosmological simulations and their implications on SF. Additionally, for the future, we plan to add CR dynamics to our simulations.

Finally, we have contributed to the development of the numerical method. All our simulations are performed with the cosmological N-body / SPMHD simulation code GADGET and also include radiative cooling and SF. In particular, we present an SPMHD implementation of the Dedner divergence cleaning scheme. We find the cleaning scheme to slightly reduce the numerical $\nabla \cdot \mathbf{B}$ error within the simulations. Additionally, we are in the process of revamping the entire SPMHD implementation of GADGET. After performing the usual set of MHD standard tests, we find our new numerical scheme to provide significantly more accurate results, giving a good basis for future simulations.

Fig. 7.1 shows a possible extension of the simulation flow (see also Figs. 1.7 and 2.5) by the dynamics of CR (protons and electrons). The presence of a CR energy budget and the resulting CR pressure (mainly protons) can significantly change the dynamics of the simulated systems. In particular, the contribution of the non-cooling and non-thermal CR pressure in the equation of motion can lead to additional gas movements and potentially drive outflows. Furthermore, we can split the CR energy budget (interesting for electrons) into different energy ranges and follow the time evolution of each energy range and thus the complete spectrum. In the past, our synthetic radio maps were created in the post-processing stage and we had to assume a given CR electron energy and spectrum. This new CR evolution model, which will also include reacceleration, diffusion and energy losses, allows to follow the CR energy distribution within the simulations and create realistic synthetic radio maps for high and low frequencies as indicators of the magnetic field evolution.

Fig. 7.2 presents the first simulation of a ΛCDM cosmological box with the new magnetic SN seeding scheme. The upper panel shows a 10 Mpc thick slice through the center of the box and the various elements of the filamentary cosmic structure can clearly be distinguished. In particular, clusters of galaxies (density maxima) and voids (density minima) are visible. The lower panel shows the corresponding total magnetic field strength. The distribution of the magnetic field corresponds

in general well with the distribution of the gas density. Interestingly, some of the voids seem to contain small magnetized regions, which might correspond to regions of SF within the voids (i.e. protogalactic structures). Extending the volume of magnetic SN seeded simulations from galactic to cosmological scales will allow us to follow the seeding of magnetic fields within SF regions and their subsequent amplification and transport into the large-scale structure. In particular, we plan to study the magnetization process of galaxy clusters (Dolag et al., in preparation) and of the voids.

In addition, many more open issues and interesting questions arise. Actually, the combined numerical study of galaxy formation and magnetic fields has just begun. In the following we will give a list of interesting open issues, which could naturally continue this thesis:

- Inevitably, cosmological simulations of galaxy formation should lead to the formation of disc galaxies. In this thesis we performed simulations of galactic halo formation and studied the diffuse halo gas content as well as the SF gas content. In the future, it will be necessary to form realistic disc galaxies within the simulations and study their kinematics as well as magnetic morphologies. What is the structure of the magnetic field in the disc? How do magnetic spiral arms form? Where do the magnetic pitch angles arise from?

- In order to obtain more realistic simulations, we will have to upgrade our numerical routines. On one hand, we have to follow properly the evolution of the magnetic field itself and, in particular, maintain the divergence constrain. This includes continually working on the underlying numerical algorithms of SPMHD as well as potentially compare to solutions obtained with grid codes. On the other hand, we might need to include the magnetic field in subgrid-models describing additional physical processes, leading to the question: How does a present magnetic field change the existing descriptions of e.g. cooling, cold clouds, SN or AGN feedback?

- We did not distinguish between the various independent drivers of the magnetic field amplification. A deeper understanding of the growth is necessary and we can ask: How much of the growth is a result of gravitational compression, of compression by gas cooling, of shocks, of gravitationally driven turbulence or of SN driven turbulence? Furthermore, what are the exact mechanisms transferring magnetic energy from small to large scales? How exactly do the dynamo and dissipation processes operate which give regularity to the magnetic field?

- We have presented the cases of a primordially and a SN seeded magnetic field. However, many more mechanisms of creating magnetic seed fields exist, e.g. the seeding by AGN or ionization processes. What are the contributions of each of these different seed fields to the magnetic fields on various scales (from molecular clouds up to the largest voids)? What fraction of the magnetic field has been seeded and amplified locally and how much has been globally transported?

- The baryonic cycle describes the complex interplay between galaxies and their surrounding gas. It is a model for the inflows and outflows of gas onto galaxies as well as the changes within the galactic gas reservoir. In the light that galactic winds are most likely the result of magnetic field and cosmic ray interplay, what are the possible effects of the magnetic field on the baryonic cyle? Can the magnetic field stop the gas from falling/cooling back onto the galaxy?

- Ultimately, it all comes down to that we need to get a more detailed and deeper understanding on the connections between magnetic fields and the formation and evolution of galaxies and cosmic structure. As structure formation is a highly non-linear and turbulent process, the evolution of the magnetic field can also only be understood by quickly changing potentials and energy budgets. In particular, the formation of cosmic structures and the seeding, amplification and transport of magnetic fields is a combined process. This forces us to parallelize and combine our studies. What is the imprint magnetic fields might have imposed on the statistics of a large galaxy population?

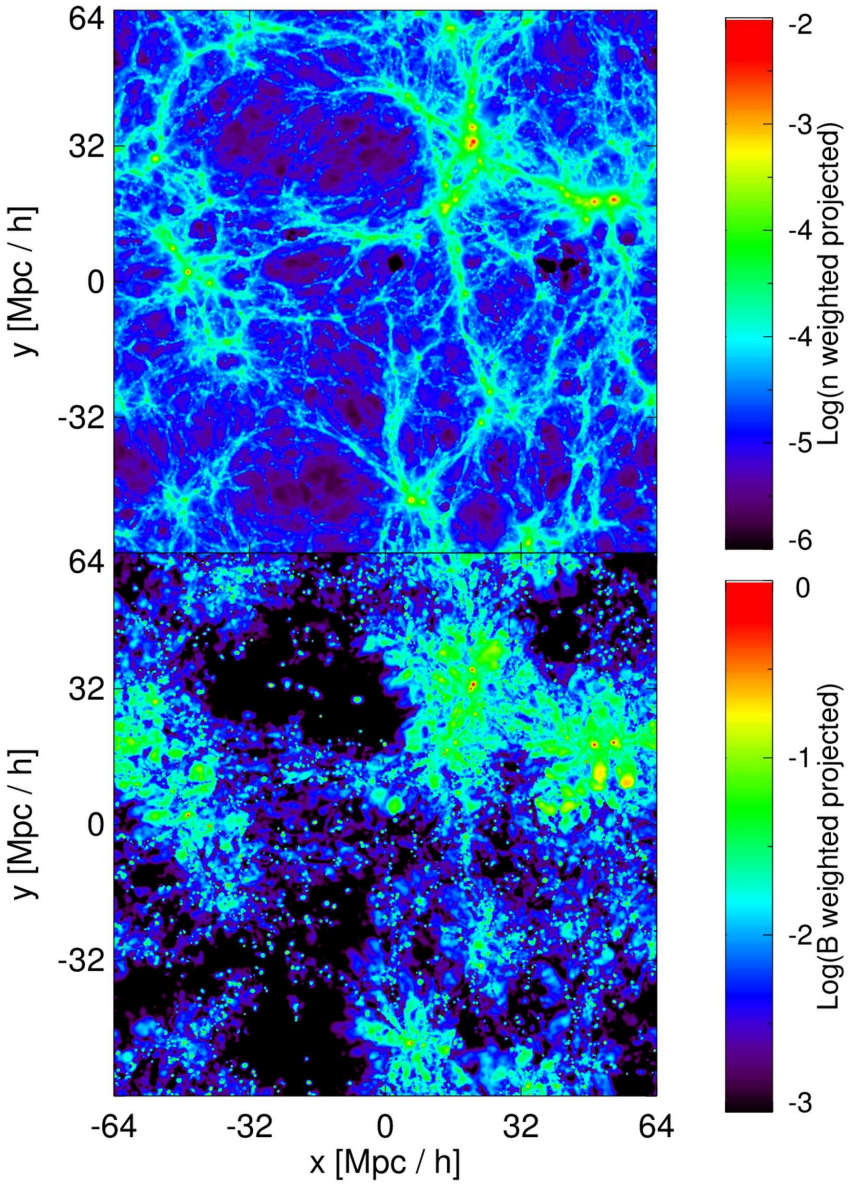

Figure 7.2: Simulation of a ΛCDM cosmological box with the new magnetic SN seeding scheme and without primordial magnetic fields. Shown is the spatial distribution of gas density (top panel) and magnetic field (bottom panel). Such simulations will allow us to follow the seeding and amplification of the magnetic field within SF regions and their subsequent transport into the large-scale structure in great detail. In particular, we plan to numerically study the magnetization process of galaxy clusters (Dolag et al., in preparation) and of the voids.

It will remain a challenge for the future to create joint cosmological simulations including radiative transfer, stellar evolution, black holes, chemical evolution, cosmic rays and magnetic field evolution. Only numerical simulations allow such detailed investigations.

It will also be our task to collect additional observational data, create better numerical models and extend the theoretical descriptions. Additionally, at the end of this decade, a new generation of radio telescopes will become available. The Square Kilometre Array, the Low Frequency Array, the Murchison Widefield Array and many more instruments will allow us to study magnetic fields to higher redshifts and lower amplitudes than ever before. We are about to enter a Golden Age of Radioastronomy. We want to encourage the professionals of today and the students of tomorrow to pick up on the interesting and growing research area of cosmic magnetism.

Bibliography

K. Abazajian, J. K. Adelman-McCarthy, M. A. Agüeros, S. S. Allam, S. F. Anderson, J. Annis, N. A. Bahcall, I. K. Baldry, S. Bastian, and et al. The First Data Release of the Sloan Digital Sky Survey. AJ, 126:2081–2086, October 2003. doi: 10.1086/378165.

K. N. Abazajian, J. K. Adelman-McCarthy, M. A. Agüeros, S. S. Allam, C. Allende Prieto, D. An, K. S. J. Anderson, S. F. Anderson, J. Annis, N. A. Bahcall, and et al. The Seventh Data Release of the Sloan Digital Sky Survey. ApJS, 182:543, June 2009. doi: 10.1088/0067-0049/182/2/543.

T. Abel, G. L. Bryan, and M. L. Norman. The Formation of the First Star in the Universe. Science, 295:93–98, January 2002. doi: 10.1126/science.295.5552.93.

H. Alfven. Cosmical electrodynamics. Coelum Periodico Bimestrale per la Divulgazione dell'Astronomia, 1950.

R. J. Allen and J. W. Hartsuiker. Radio Continuum Emission at 21 cm near Stephan's Quintet. Nature, 239:324–325, October 1972. doi: 10.1038/239324a0.

R. J. Allen and W. T. Sullivan, III. The low and high redshift neutral hydrogen associated with Stephan's Quintet. A&A, 84:181–190, April 1980.

M. Anderson, E. W. Hirschmann, S. L. Liebling, and D. Neilsen. Relativistic MHD with adaptive mesh refinement. Classical and Quantum Gravity, 23:6503–6524, November 2006. doi: 10.1088/0264-9381/23/22/025.

C. Angrick and M. Bartelmann. Triaxial collapse and virialisation of dark-matter haloes. A&A, 518: A38, July 2010. doi: 10.1051/0004-6361/201014147.

P. N. Appleton, K. C. Xu, W. Reach, M. A. Dopita, Y. Gao, N. Lu, C. C. Popescu, J. W. Sulentic, R. J. Tuffs, and M. S. Yun. Powerful High-Velocity Dispersion Molecular Hydrogen Associated with an Intergalactic Shock Wave in Stephan's Quintet. ApJ, 639:L51–L54, March 2006. doi: 10.1086/502646.

T. C. Arlen, V. V. Vassiliev, T. Weisgarber, S. P. Wakely, and S. Yusef Shafi. Intergalactic Magnetic Fields and Gamma Ray Observations of Extreme TeV Blazars. ArXiv e-prints, October 2012.

H. Arp. Neighborhoods of spiral galaxies. I. Multiple interacting galaxies. ApJ, 185:797–808, November 1973. doi: 10.1086/152455.

T. G. Arshakian, R. Beck, M. Krause, and D. Sokoloff. Evolution of magnetic fields in galaxies and future observational tests with the Square Kilometre Array. A&A, 494:21–32, January 2009. doi: 10.1051/0004-6361:200810964.

R. M. Athreya, V. K. Kapahi, P. J. McCarthy, and W. van Breugel. Large rotation measures in radio galaxies at $Z > 2$. A&A, 329:809–820, January 1998.

R. Barkana and A. Loeb. In the beginning: the first sources of light and the reionization of the universe. Phys. Rep., 349:125–238, July 2001. doi: 10.1016/S0370-1573(01)00019-9.

G. K. Batchelor. On the Spontaneous Magnetic Field in a Conducting Liquid in Turbulent Motion. Royal Society of London Proceedings Series A, 201:405–416, April 1950. doi: 10.1098/rspa.1950.0069.

G. K. Batchelor. The Theory of Homogeneous Turbulence. 1953.

A. M. Beck, H. Lesch, K. Dolag, H. Kotarba, A. Geng, and F. A. Stasyszyn. Origin of strong magnetic fields in Milky Way-like galactic haloes. MNRAS, 422:2152–2163, May 2012. doi: 10.1111/j.1365-2966.2012.20759.x.

A. M. Beck, K. Dolag, H. Lesch, and P. P. Kronberg. Strong magnetic fields and large rotation measures in protogalaxies from supernova seeding. MNRAS, 435:3575–3586, November 2013a. doi: 10.1093/mnras/stt1549.

A. M. Beck, M. Hanasz, H. Lesch, R.-S. Remus, and F. A. Stasyszyn. On the magnetic fields in voids. MNRAS, 429:L60–L64, February 2013b. doi: 10.1093/mnrasl/sls026.

R. Beck. Magnetic Fields in Galaxies. In R. Wielebinski and R. Beck, editors, Cosmic Magnetic Fields, volume 664 of Lecture Notes in Physics, Berlin Springer Verlag, page 41, 2005. doi: 10.1007/11369875_3.

R. Beck. Magnetism in the spiral galaxy NGC 6946: magnetic arms, depolarization rings, dynamo modes, and helical fields. A&A, 470:539–556, August 2007. doi: 10.1051/0004-6361:20066988.

R. Beck. Galactic and extragalactic magnetic fields - a concise review. Astrophysics and Space Sciences Transactions, 5:43–47, October 2009. doi: 10.5194/astra-5-43-2009.

R. Beck and R. Wielebinski. Magnetic Fields in Galaxies, page 641. 2013. doi: 10.1007/978-94-007-5612-0-13.

R. Beck, A. Brandenburg, D. Moss, A. Shukurov, and D. Sokoloff. Galactic Magnetism: Recent Developments and Perspectives. ARA&A, 34:155–206, 1996. doi: 10.1146/annurev.astro.34.1.155.

J. Bellovary, M. Volonteri, F. Governato, S. Shen, T. Quinn, and J. Wadsley. The First Massive Black Hole Seeds and Their Hosts. ApJ, 742:13, November 2011. doi: 10.1088/0004-637X/742/1/13.

M. Belyanin, D. Sokoloff, and A. Shukurov. Simple models of nonlinear fluctuation dynamo. Geophysical and Astrophysical Fluid Dynamics, 68:237–261, 1993. doi: 10.1080/03091929308203569.

V. S. Berezinsky, P. Blasi, and V. S. Ptuskin. Clusters of Galaxies as Storage Room for Cosmic Rays. ApJ, 487:529, October 1997. doi: 10.1086/304622.

M. L. Bernet, F. Miniati, S. J. Lilly, P. P. Kronberg, and M. Dessauges-Zavadsky. Strong magnetic fields in normal galaxies at high redshift. Nature, 454:302–304, July 2008. doi: 10.1038/nature07105.

S. Bertone, C. Vogt, and T. Enßlin. Magnetic field seeding by galactic winds. MNRAS, 370:319–330, July 2006. doi: 10.1111/j.1365-2966.2006.10474.x.

L. Biermann. Über den Ursprung der Magnetfelder auf Sternen und im interstellaren Raum (mit einem Anhang von A. Schlüter). Zeitschrift für Naturforschung Teil A, 5:65, 1950.

L. Biermann and A. Schlüter. Cosmic Radiation and Cosmic Magnetic Fields. II. Origin of Cosmic Magnetic Fields. Physical Review, 82:863–868, June 1951. doi: 10.1103/PhysRev.82.863.

J. Binney and S. Tremaine. Galactic Dynamics: Second Edition. Princeton University Press, 2008.

G. S. Bisnovatyi-Kogan, A. A. Ruzmaikin, and R. A. Syunyaev. Star Contraction and Magnetic-Field Generation in Protogalaxies. Soviet Ast., 17:137, August 1973.

A. Bonafede, K. Dolag, F. Stasyszyn, G. Murante, and S. Borgani. A non-ideal magnetohydrodynamic GADGET: simulating massive galaxy clusters. MNRAS, 418:2234–2250, December 2011. doi: 10.1111/j.1365-2966.2011.19523.x.

S. Børve, M. Omang, and J. Trulsen. Regularized Smoothed Particle Hydrodynamics: A New Approach to Simulating Magnetohydrodynamic Shocks. ApJ, 561:82–93, November 2001. doi: 10.1086/323228.

S. Børve, M. Omang, and J. Trulsen. Multidimensional MHD Shock Tests of Regularized Smoothed Particle Hydrodynamics. ApJ, 652:1306–1317, December 2006. doi: 10.1086/508454.

A. Brandenburg. Magnetic field evolution in simulations with Euler potentials. MNRAS, 401:347–354, January 2010. doi: 10.1111/j.1365-2966.2009.15640.x.

A. Brandenburg and K. Subramanian. Astrophysical magnetic fields and nonlinear dynamo theory. Phys. Rep., 417:1–209, October 2005. doi: 10.1016/j.physrep.2005.06.005.

D. Breitschwerdt. Astrophysics: Blown away by cosmic rays. Nature, 452:826–827, April 2008. doi: 10.1038/452826a.

D. Breitschwerdt, J. F. McKenzie, and H. J. Voelk. Galactic winds. I - Cosmic ray and wave-driven winds from the Galaxy. A&A, 245:79–98, May 1991.

J. W. Broderick, C. De Breuck, R. W. Hunstead, and N. Seymour. An extreme rotation measure in the high-redshift radio galaxy PKS B0529-549. MNRAS, 375:1059–1069, March 2007. doi: 10.1111/j.1365-2966.2006.11375.x.

V. Bromm, N. Yoshida, L. Hernquist, and C. F. McKee. The formation of the first stars and galaxies. Nature, 459:49–54, May 2009. doi: 10.1038/nature07990.

F. Bürzle, P. C. Clark, F. Stasyszyn, K. Dolag, and R. S. Klessen. Protostellar outflows with smoothed particle magnetohydrodynamics. MNRAS, 417:L61–L65, October 2011a. doi: 10.1111/j.1745-3933.2011.01120.x.

F. Bürzle, P. C. Clark, F. Stasyszyn, T. Greif, K. Dolag, R. S. Klessen, and P. Nielaba. Protostellar collapse and fragmentation using an MHD GADGET. MNRAS, 412:171–186, March 2011b. doi: 10.1111/j.1365-2966.2010.17896.x.

C. L. Carilli, F. N. Owen, and D. E. Harris. Radio continuum polarimetric imaging of high redshift radio galaxies. AJ, 107:480–493, February 1994. doi: 10.1086/116870.

C. L. Carilli, H. J. A. Roettgering, R. van Ojik, G. K. Miley, and W. J. M. van Breugel. Radio Continuum Imaging of High-Redshift Radio Galaxies. ApJS, 109:1, March 1997. doi: 10.1086/312973.

M. Cécere, L. Lehner, and O. Reula. Constraint preserving boundary conditions for the Ideal Newtonian MHD equations. Computer Physics Communications, 179:545–554, October 2008. doi: 10.1016/j.cpc.2008.04.015.

K. T. Chyży, R. Beck, S. Kohle, U. Klein, and M. Urbanik. Regular magnetic fields in the dwarf irregular galaxy NGC 4449. A&A, 355:128–137, March 2000.

K. T. Chyży, J. Knapik, D. J. Bomans, U. Klein, R. Beck, M. Soida, and M. Urbanik. Magnetic fields and ionized gas in the local group irregular galaxies IC 10 and NGC 6822. A&A, 405:513–524, July 2003. doi: 10.1051/0004-6361:20030628.

K. T. Chyży, D. J. Bomans, M. Krause, R. Beck, M. Soida, and M. Urbanik. Magnetic fields and ionized gas in nearby late type galaxies. A&A, 462:933–941, February 2007. doi: 10.1051/0004-6361:20065932.

K. T. Chyży, M. Weżgowiec, R. Beck, and D. J. Bomans. Magnetic fields in Local Group dwarf irregulars. A&A, 529:A94, May 2011. doi: 10.1051/0004-6361/201015393.

M. E. Cluver, P. N. Appleton, F. Boulanger, P. Guillard, P. Ogle, P.-A. Duc, N. Lu, J. Rasmussen, W. T. Reach, J. D. Smith, R. Tuffs, C. K. Xu, and M. S. Yun. Powerful H_2 Line Cooling in Stephan's Quintet. I. Mapping the Significant Cooling Pathways in Group-wide Shocks. ApJ, 710: 248–264, February 2010. doi: 10.1088/0004-637X/710/1/248.

S. A. Colgate, H. Li, and P. P. Kronberg. The magnetized universe: its origin and dissipation through acceleration and leakage to the voids. In A. Bonanno, E. de Gouveia Dal Pino, and A. G. Kosovichev, editors, IAU Symposium, volume 274 of IAU Symposium, pages 2–9, June 2011. doi: 10.1017/S1743921311006491.

T. J. Cox, T. Di Matteo, L. Hernquist, P. F. Hopkins, B. Robertson, and V. Springel. X-Ray Emission from Hot Gas in Galaxy Mergers. ApJ, 643:692–706, June 2006. doi: 10.1086/503284.

T. J. Cox, P. Jonsson, R. S. Somerville, J. R. Primack, and A. Dekel. The effect of galaxy mass ratio on merger-driven starbursts. MNRAS, 384:386–409, February 2008. doi: 10.1111/j.1365-2966.2007.12730.x.

W. Dai and P. R. Woodward. Extension of the Piecewise Parabolic Method to Multidimensional Ideal Magnetohydrodynamics. Journal of Computational Physics, 115:485–514, December 1994. doi: 10.1006/jcph.1994.1212.

R. A. Daly and A. Loeb. A possible origin of galactic magnetic fields. ApJ, 364:451–455, December 1990. doi: 10.1086/169429.

L. Davis, Jr. and J. L. Greenstein. The Polarization of Starlight by Aligned Dust Grains. ApJ, 114: 206, September 1951. doi: 10.1086/145464.

A. Dedner, F. Kemm, D. Kröner, C.-D. Munz, T. Schnitzer, and M. Wesenberg. Hyperbolic Divergence Cleaning for the MHD Equations. Journal of Computational Physics, 175:645–673, January 2002. doi: 10.1006/jcph.2001.6961.

A. Dekel, Y. Birnboim, G. Engel, J. Freundlich, T. Goerdt, M. Mumcuoglu, E. Neistein, C. Pichon, R. Teyssier, and E. Zinger. Cold streams in early massive hot haloes as the main mode of galaxy formation. Nature, 457:451–454, January 2009. doi: 10.1038/nature07648.

C. D. Dermer, M. Cavadini, S. Razzaque, J. D. Finke, J. Chiang, and B. Lott. Time Delay of Cascade Radiation for TeV Blazars and the Measurement of the Intergalactic Magnetic Field. ApJ, 733:L21, June 2011. doi: 10.1088/2041-8205/733/2/L21.

T. Di Matteo, V. Springel, and L. Hernquist. Energy input from quasars regulates the growth and activity of black holes and their host galaxies. Nature, 433:604–607, February 2005. doi: 10.1038/nature03335.

K. Dolag and F. Stasyszyn. An MHD GADGET for cosmological simulations. MNRAS, 398:1678–1697, October 2009. doi: 10.1111/j.1365-2966.2009.15181.x.

K. Dolag, F. K. Hansen, M. Roncarelli, and L. Moscardini. The imprints of local superclusters on the Sunyaev-Zel'dovich signals and their detectability with Planck. MNRAS, 363:29–39, October 2005. doi: 10.1111/j.1365-2966.2005.09452.x.

K. Dolag, S. Borgani, G. Murante, and V. Springel. Substructures in hydrodynamical cluster simulations. MNRAS, 399:497–514, October 2009. doi: 10.1111/j.1365-2966.2009.15034.x.

K. Dolag, M. Kachelriess, S. Ostapchenko, and R. Tomàs. Lower Limit on the Strength and Filling Factor of Extragalactic Magnetic Fields. ApJ, 727:L4, January 2011. doi: 10.1088/2041-8205/727/1/L4.

J. Donnert, K. Dolag, H. Lesch, and E. Müller. Cluster magnetic fields from galactic outflows. MNRAS, 392:1008–1021, January 2009. doi: 10.1111/j.1365-2966.2008.14132.x.

E. A. Dorfi and D. Breitschwerdt. Time-dependent galactic winds. I. Structure and evolution of galactic outflows accompanied by cosmic ray acceleration. A&A, 540:A77, April 2012. doi: 10.1051/0004-6361/201118082.

R. T. Drzazga, K. T. Chyży, W. Jurusik, and K. Wiórkiewicz. Magnetic field evolution in interacting galaxies. A&A, 533:A22, September 2011. doi: 10.1051/0004-6361/201016092.

Y. Dubois and R. Teyssier. Magnetised winds in dwarf galaxies. A&A, 523:A72, November 2010. doi: 10.1051/0004-6361/200913014.

T. Enßlin, C. Pfrommer, F. Miniati, and K. Subramanian. Cosmic ray transport in galaxy clusters: implications for radio halos, gamma-ray signatures, and cool core heating. A&A, 527:A99, March 2011. doi: 10.1051/0004-6361/201015652.

W. Essey and A. Kusenko. On Weak Redshift Dependence of Gamma-Ray Spectra of Distant Blazars. ApJ, 751:L11, May 2012. doi: 10.1088/2041-8205/751/1/L11.

W. Essey, S. Ando, and A. Kusenko. Determination of intergalactic magnetic fields from gamma ray data. Astroparticle Physics, 35:135–139, October 2011. doi: 10.1016/j.astropartphys.2011.06.010.

J. E. Everett, E. G. Zweibel, R. A. Benjamin, D. McCammon, L. Rocks, and J. S. Gallagher, III. The Milky Way's Kiloparsec-Scale Wind: A Hybrid Cosmic-Ray and Thermally Driven Outflow. ApJ, 674:258–270, February 2008. doi: 10.1086/524766.

E. E. Falco, M. J. Kurtz, M. J. Geller, J. P. Huchra, J. Peters, P. Berlind, D. J. Mink, S. P. Tokarz, and B. Elwell. The Updated Zwicky Catalog (UZC). PASP, 111:438–452, April 1999. doi: 10.1086/316343.

K. Fedotov, S. C. Gallagher, I. S. Konstantopoulos, R. Chandar, N. Bastian, J. C. Charlton, B. Whitmore, and G. Trancho. Star Clusters as Tracers of Interactions in Stephan's Quintet (Hickson Compact Group 92). AJ, 142:42, August 2011. doi: 10.1088/0004-6256/142/2/42.

A. J. Fitt and P. Alexander. Magnetic fields in late-type galaxies. MNRAS, 261:445–452, March 1993.

D.A. Frank-Kamenezki. Vorlesungen über Plasmaphysik. VEB Deutscher Verlag der Wissenschaften, 1967.

S. R. Furlanetto and A. Loeb. Intergalactic Magnetic Fields from Quasar Outflows. ApJ, 556:619–634, August 2001. doi: 10.1086/321630.

A. Geng, A. M. Beck, K. Dolag, F. Bürzle, M. C. Beck, H. Kotarba, and P. Nielaba. Synthetic X-ray and radio maps for two different models of Stephan's Quintet. MNRAS, 426:3160–3177, November 2012a. doi: 10.1111/j.1365-2966.2012.21902.x.

A. Geng, H. Kotarba, F. Bürzle, K. Dolag, F. Stasyszyn, A. Beck, and P. Nielaba. Magnetic field amplification and X-ray emission in galaxy minor mergers. MNRAS, 419:3571–3589, February 2012b. doi: 10.1111/j.1365-2966.2011.20001.x.

W. K. George. The decay of homogeneous isotropic turbulence. Physics of Fluids, 4:1492–1509, July 1992. doi: 10.1063/1.858423.

Gopal-Krishna, M. Mhaskey, and A. Mangalam. On the Injection Spectrum of Relativistic Electrons in High-redshift Radio Galaxies. ApJ, 744:31, January 2012. doi: 10.1088/0004-637X/744/1/31.

S. Gottlöber, A. Klypin, and A. V. Kravtsov. Merging History as a Function of Halo Environment. ApJ, 546:223–233, January 2001. doi: 10.1086/318248.

N. A. Grogin and M. J. Geller. An Imaging and Spectroscopic Survey of Galaxies within Prominent Nearby Voids. I. The Sample and Luminosity Distribution. AJ, 118:2561–2580, December 1999. doi: 10.1086/301126.

N. A. Grogin and M. J. Geller. An Imaging and Spectroscopic Survey of Galaxies within Prominent Nearby Voids. II. Morphologies, Star Formation, and Faint Companions. AJ, 119:32–43, January 2000. doi: 10.1086/301179.

C. Grupen. Astroparticle Physics. Springer, 2005. doi: 10.1007/3-540-27670-X.

P. Guillard, F. Boulanger, G. Pineau des Forêts, E. Falgarone, A. Gusdorf, M. E. Cluver, P. N. Appleton, U. Lisenfeld, P.-A. Duc, P. M. Ogle, and C. K. Xu. Turbulent Molecular Gas and Star Formation in the Shocked Intergalactic Medium of Stephan's Quintet. ApJ, 749:158, April 2012. doi: 10.1088/0004-637X/749/2/158.

A. M. Hammond, T. Robishaw, and B. M. Gaensler. A New Catalog of Faraday Rotation Measures and Redshifts for Extragalactic Radio Sources. ArXiv e-prints, September 2012.

M. Hanasz, K. Otmianowska-Mazur, G. Kowal, and H. Lesch. Cosmic-ray-driven dynamo in galactic disks. A parameter study. A&A, 498:335–346, May 2009a. doi: 10.1051/0004-6361/200810279.

M. Hanasz, D. Wóltański, and K. Kowalik. Global Galactic Dynamo Driven by Cosmic Rays and Exploding Magnetized Stars. ApJ, 706:L155–L159, November 2009b. doi: 10.1088/0004-637X/706/1/L155.

L. Hernquist. N-body realizations of compound galaxies. ApJS, 86:389–400, June 1993. doi: 10.1086/191784.

L. Hernquist and J. C. Mihos. Excitation of Activity in Galaxies by Minor Mergers. ApJ, 448:41, July 1995. doi: 10.1086/175940.

L. Hernquist and V. Springel. An analytical model for the history of cosmic star formation. MNRAS, 341:1253–1267, June 2003. doi: 10.1046/j.1365-8711.2003.06499.x.

P. Hickson. Systematic properties of compact groups of galaxies. ApJ, 255:382–391, April 1982. doi: 10.1086/159838.

C. J. Hogan. Magnetohydrodynamic effects of a first-order cosmological phase transition. Physical Review Letters, 51:1488–1491, October 1983. doi: 10.1103/PhysRevLett.51.1488.

F. Hoyle, M. S. Vogeley, and D. Pan. Photometric properties of void galaxies in the Sloan Digital Sky Survey Data Release 7. MNRAS, 426:3041–3050, November 2012. doi: 10.1111/j.1365-2966.2012.21943.x.

H. Huan, T. Weisgarber, T. Arlen, and S. P. Wakely. A New Model for Gamma-Ray Cascades in Extragalactic Magnetic Fields. ApJ, 735:L28, July 2011. doi: 10.1088/2041-8205/735/2/L28.

J. D. Huba and J. A. Fedder. Self-generation of magnetic fields by sheared flows in weakly ionized plasmas. Physics of Fluids B, 5:3779–3788, October 1993. doi: 10.1063/1.860848.

E. Hummel. The radio continuum-far infrared correlation and magnetic fields in SBC galaxies. A&A, 160:L4–L6, May 1986.

J.-S. Hwang, C. Struck, F. Renaud, and P. N. Appleton. Models of Stephan's Quintet: hydrodynamic constraints on the group's evolution. MNRAS, 419:1780–1794, January 2012. doi: 10.1111/j.1365-2966.2011.19847.x.

J. D. Jackson. Classical electrodynamics. Wiley, 1975.

P. H. Johansson, T. Naab, and A. Burkert. Equal- and Unequal-Mass Mergers of Disk and Elliptical Galaxies with Black Holes. ApJ, 690:802–821, January 2009. doi: 10.1088/0004-637X/690/1/802.

S. J. Karl, T. Naab, P. H. Johansson, H. Kotarba, C. M. Boily, F. Renaud, and C. Theis. One Moment in Time: Modeling Star Formation in the Antennae. ApJ, 715:L88–L93, June 2010. doi: 10.1088/2041-8205/715/2/L88.

N. Katz, D. H. Weinberg, and L. Hernquist. Cosmological Simulations with TreeSPH. ApJS, 105:19, July 1996. doi: 10.1086/192305.

R. C. Kennicutt, Jr. The Global Schmidt Law in Star-forming Galaxies. ApJ, 498:541, May 1998. doi: 10.1086/305588.

R. Keppens, Z. Meliani, A. J. van Marle, P. Delmont, A. Vlasis, and B. van der Holst. Parallel, grid-adaptive approaches for relativistic hydro and magnetohydrodynamics. Journal of Computational Physics, 231:718–744, February 2012. doi: 10.1016/j.jcp.2011.01.020.

R. Kippenhahn and C. Moellenhoff. Elementare Plasmaphysik. Bibliographisches Institut, 1975.

U. Klein, R. Wielebinski, and H. W. Morsi. Radio continuum observations of M82. A&A, 190:41–46, January 1988.

T. S. Kolatt, J. S. Bullock, R. S. Somerville, Y. Sigad, P. Jonsson, A. V. Kravtsov, A. A. Klypin, J. R. Primack, S. M. Faber, and A. Dekel. Young Galaxies: What Turns Them On? ApJ, 523: L109–L112, October 1999. doi: 10.1086/312271.

A. Kolmogorov. The Local Structure of Turbulence in Incompressible Viscous Fluid for Very Large Reynolds' Numbers. Akademiia Nauk SSSR Doklady, 30:301–305, 1941.

E. Komatsu, K. M. Smith, J. Dunkley, C. L. Bennett, B. Gold, G. Hinshaw, N. Jarosik, D. Larson, M. R. Nolta, L. Page, D. N. Spergel, M. Halpern, R. S. Hill, A. Kogut, M. Limon, S. S. Meyer, N. Odegard, G. S. Tucker, J. L. Weiland, E. Wollack, and E. L. Wright. Seven-year Wilkinson Microwave Anisotropy Probe (WMAP) Observations: Cosmological Interpretation. ApJS, 192:18, February 2011. doi: 10.1088/0067-0049/192/2/18.

H. Kotarba, H. Lesch, K. Dolag, T. Naab, P. H. Johansson, and F. A. Stasyszyn. Magnetic field structure due to the global velocity field in spiral galaxies. MNRAS, 397:733–747, August 2009. doi: 10.1111/j.1365-2966.2009.15030.x.

H. Kotarba, S. J. Karl, T. Naab, P. H. Johansson, K. Dolag, H. Lesch, and F. A. Stasyszyn. Simulating Magnetic Fields in the Antennae Galaxies. ApJ, 716:1438–1452, June 2010. doi: 10.1088/0004-637X/716/2/1438.

H. Kotarba, H. Lesch, K. Dolag, T. Naab, P. H. Johansson, J. Donnert, and F. A. Stasyszyn. Galactic ménage à trois: simulating magnetic fields in colliding galaxies. MNRAS, 415:3189–3218, August 2011. doi: 10.1111/j.1365-2966.2011.18932.x.

R. H. Kraichnan. Inertial-Range Spectrum of Hydromagnetic Turbulence. Physics of Fluids, 8:1385–1387, July 1965. doi: 10.1063/1.1761412.

F. Krause and K.-H. Raedler. Mean-field magnetohydrodynamics and dynamo theory. 1980.

M. Krause. Magnetic Fields and Star Formation in Spiral Galaxies. In Revista Mexicana de Astronomia y Astrofisica Conference Series, volume 36 of Revista Mexicana de Astronomia y Astrofisica Conference Series, pages 25–29, August 2009.

K. Kreckel, M. R. Joung, and R. Cen. Simulated Void Galaxies in the Standard Cold Dark Matter Model. ApJ, 735:132, July 2011a. doi: 10.1088/0004-637X/735/2/132.

K. Kreckel, E. Platen, M. A. Aragón-Calvo, J. H. van Gorkom, R. van de Weygaert, J. M. van der Hulst, K. Kovač, C.-W. Yip, and P. J. E. Peebles. Only the Lonely: H I Imaging of Void Galaxies. AJ, 141:4, January 2011b. doi: 10.1088/0004-6256/141/1/4.

K. Kreckel, E. Platen, M. A. Aragón-Calvo, J. H. van Gorkom, R. van de Weygaert, J. M. van der Hulst, and B. Beygu. The Void Galaxy Survey: Optical Properties and H I Morphology and Kinematics. AJ, 144:16, July 2012. doi: 10.1088/0004-6256/144/1/16.

P. P. Kronberg. Extragalactic magnetic fields. Reports on Progress in Physics, 57:325–382, April 1994. doi: 10.1088/0034-4885/57/4/001.

P. P. Kronberg. Magnetic field transport from AGN cores to jets, lobes, and the IGM. In K. G. Strassmeier, A. G. Kosovichev, and J. E. Beckman, editors, IAU Symposium, volume 259 of IAU Symposium, pages 499–508, April 2009. doi: 10.1017/S1743921309031172.

P. P. Kronberg and J. J. Perry. Absorption lines, Faraday rotation, and magnetic field estimates for QSO absorption-line clouds. ApJ, 263:518–532, December 1982. doi: 10.1086/160523.

P. P. Kronberg, H. Lesch, and U. Hopp. Magnetization of the Intergalactic Medium by Primeval Galaxies. ApJ, 511:56–64, January 1999. doi: 10.1086/306662.

P. P. Kronberg, Q. W. Dufton, H. Li, and S. A. Colgate. Magnetic Energy of the Intergalactic Medium from Galactic Black Holes. ApJ, 560:178–186, October 2001. doi: 10.1086/322767.

P. P. Kronberg, M. L. Bernet, F. Miniati, S. J. Lilly, M. B. Short, and D. M. Higdon. A Global Probe of Cosmic Magnetic Fields to High Redshifts. ApJ, 676:70–79, March 2008. doi: 10.1086/527281.

R. M. Kulsrud. Plasma physics for astrophysics. Princeton University Press, 2005.

R. M. Kulsrud and S. W. Anderson. The spectrum of random magnetic fields in the mean field dynamo theory of the Galactic magnetic field. ApJ, 396:606–630, September 1992. doi: 10.1086/171743.

R. M. Kulsrud and E. G. Zweibel. On the origin of cosmic magnetic fields. Reports on Progress in Physics, 71(4):046901, April 2008. doi: 10.1088/0034-4885/71/4/046901.

R. M. Kulsrud, R. Cen, J. P. Ostriker, and D. Ryu. The Protogalactic Origin for Cosmic Magnetic Fields. ApJ, 480:481, May 1997. doi: 10.1086/303987.

A. Kusenko. Cosmic Connections: from Cosmic Rays to Gamma Rays, Cosmic Backgrounds and Magnetic Fields. Modern Physics Letters A, 28:1340001, January 2013. doi: 10.1142/S0217732313400014.

L. D. Landau and E. M. Lifshitz. Fluid mechanics. Pergamon Press, 1959.

M. A. Latif, D. R. G. Schleicher, W. Schmidt, and J. Niemeyer. The small-scale dynamo and the amplification of magnetic fields in massive primordial haloes. MNRAS, 432:668–678, June 2013. doi: 10.1093/mnras/stt503.

H. Lesch and M. Chiba. Protogalactic evolution and magnetic fields. A&A, 297:305, May 1995.

H. Lesch and M. Hanasz. Strong magnetic fields and cosmic rays in very young galaxies. A&A, 401: 809–816, April 2003. doi: 10.1051/0004-6361:20030212.

A. Loeb. How Did the First Stars and Galaxies Form? Princeton University Press, 2010.

A. Loeb and S.R. Furlanetto. The First Galaxies in the Universe. Princeton University Press, 2012.

P. Londrillo and L. Del Zanna. High-Order Upwind Schemes for Multidimensional Magnetohydrodynamics. ApJ, 530:508–524, February 2000. doi: 10.1086/308344.

M. S. Longair. Galaxy Formation. Springer, 2008.

M. S. Longair. High Energy Astrophysics. Cambridge University Press, 2010.

L. Malyshkin and R. M. Kulsrud. Magnetized Turbulent Dynamos in Protogalaxies. ApJ, 571:619–637, June 2002. doi: 10.1086/339985.

S. A. Mao, B. M. Gaensler, M. Haverkorn, E. G. Zweibel, G. J. Madsen, N. M. McClure-Griffiths, A. Shukurov, and P. P. Kronberg. A Survey of Extragalactic Faraday Rotation at High Galactic Latitude: The Vertical Magnetic Field of the Milky Way Toward the Galactic Poles. ApJ, 714: 1170–1186, May 2010. doi: 10.1088/0004-637X/714/2/1170.

S. A. Mao, N. M. McClure-Griffiths, B. M. Gaensler, J. C. Brown, C. L. van Eck, M. Haverkorn, P. P. Kronberg, J. M. Stil, A. Shukurov, and A. R. Taylor. New Constraints on the Galactic Halo Magnetic Field Using Rotation Measures of Extragalactic Sources toward the Outer Galaxy. ApJ, 755:21, August 2012. doi: 10.1088/0004-637X/755/1/21.

W. G. Mathews and F. Brighenti. Self-generated Magnetic Fields in Galactic Cooling Flows. ApJ, 488:595, October 1997. doi: 10.1086/304728.

C. F. McKee and J. P. Ostriker. A theory of the interstellar medium - Three components regulated by supernova explosions in an inhomogeneous substrate. ApJ, 218:148–169, November 1977. doi: 10.1086/155667.

F. Miniati and A. R. Bell. Resistive Magnetic Field Generation at Cosmic Dawn. ApJ, 729:73, March 2011. doi: 10.1088/0004-637X/729/1/73.

F. Miniati and A. R. Bell. Resistive Generation of Intergalactic Magnetic Field at Cosmic Dawn. In N. V. Pogorelov, J. A. Font, E. Audit, and G. P. Zank, editors, Numerical Modeling of Space Plasma Slows (ASTRONUM 2011), volume 459 of Astronomical Society of the Pacific Conference Series, page 125, July 2012.

F. Miniati and A. Elyiv. Relaxation of Blazar-induced Pair Beams in Cosmic Voids. ApJ, 770:54, June 2013. doi: 10.1088/0004-637X/770/1/54.

I. N. Mishustin and A. A. Ruzmaĭkin. Occurrence of 'Priming' Magnetic Fields During the Formation of Protogalaxies. Soviet Journal of Experimental and Theoretical Physics, 34:233, 1972.

H. Mo, F. C. van den Bosch, and S. White. Galaxy Formation and Evolution. Cambridge University Press, May 2010.

M. Moles, J. W. Sulentic, and I. Marquez. The Dynamical Status of Stephan's Quintet. ApJ, 485: L69, August 1997. doi: 10.1086/310817.

M. Moles, I. Marquez, and J. W. Sulentic. The observational status of Stephan's Quintet. A&A, 334: 473–481, June 1998.

K. Murase, K. Takahashi, S. Inoue, K. Ichiki, and S. Nagataki. Probing Intergalactic Magnetic Fields in the GLAST Era through Pair Echo Emission from TeV Blazars. ApJ, 686:L67–L70, October 2008. doi: 10.1086/592997.

T. Naab and A. Burkert. Statistical Properties of Collisionless Equal- and Unequal-Mass Merger Remnants of Disk Galaxies. ApJ, 597:893–906, November 2003. doi: 10.1086/378581.

J. F. Navarro, C. S. Frenk, and S. D. M. White. Simulations of X-ray clusters. MNRAS, 275:720–740, August 1995.

A. Neronov and I. Vovk. Evidence for Strong Extragalactic Magnetic Fields from Fermi Observations of TeV Blazars. Science, 328:73–, April 2010. doi: 10.1126/science.1184192.

A. Neronov, D. Semikoz, and A. M. Taylor. Very hard gamma-ray emission from a flare of Mrk 501. A&A, 541:A31, May 2012. doi: 10.1051/0004-6361/201117083.

S. F. Newman, R. Genzel, N. M. Förster-Schreiber, K. Shapiro Griffin, C. Mancini, S. J. Lilly, A. Renzini, N. Bouché, A. Burkert, P. Buschkamp, C. M. Carollo, G. Cresci, R. Davies, F. Eisenhauer, S. Genel, E. K. S. Hicks, J. Kurk, D. Lutz, T. Naab, Y. Peng, A. Sternberg, L. J. Tacconi, D. Vergani, S. Wuyts, and G. Zamorani. The SINS/zC-SINF Survey of z ≈ 2 Galaxy Kinematics: Outflow Properties. ApJ, 761:43, December 2012. doi: 10.1088/0004-637X/761/1/43.

K. Nyland, J. Marvil, J. M. Wrobel, L. M. Young, and B. A. Zauderer. The Intermediate-mass Black Hole Candidate in the Center of NGC 404: New Evidence from Radio Continuum Observations. ApJ, 753:103, July 2012. doi: 10.1088/0004-637X/753/2/103.

A. L. Oren and A. M. Wolfe. A Faraday rotation search for magnetic fields in quasar damped LY alpha absorption systems. ApJ, 445:624–641, June 1995. doi: 10.1086/175726.

S. A. Orszag and C.-M. Tang. Small-scale structure of two-dimensional magnetohydrodynamic turbulence. Journal of Fluid Mechanics, 90:129–143, January 1979. doi: 10.1017/S002211207900210X.

E. O'Sullivan, S. Giacintucci, J. M. Vrtilek, S. Raychaudhury, and L. P. David. A Chandra X-ray View of Stephan's Quintet: Shocks and Star Formation. ApJ, 701:1560–1568, August 2009. doi: 10.1088/0004-637X/701/2/1560.

R. Pakmor and V. Springel. Simulations of magnetic fields in isolated disc galaxies. MNRAS, 432: 176–193, June 2013. doi: 10.1093/mnras/stt428.

R. Pakmor, A. Bauer, and V. Springel. Magnetohydrodynamics on an unstructured moving grid. MNRAS, 418:1392–1401, December 2011. doi: 10.1111/j.1365-2966.2011.19591.x.

D. C. Pan, M. S. Vogeley, F. Hoyle, Y.-Y. Choi, and C. Park. Cosmic voids in Sloan Digital Sky Survey Data Release 7. MNRAS, 421:926–934, April 2012. doi: 10.1111/j.1365-2966.2011.20197.x.

C. Park, Y.-Y. Choi, M. S. Vogeley, J. R. Gott, III, M. R. Blanton, and SDSS Collaboration. Environmental Dependence of Properties of Galaxies in the Sloan Digital Sky Survey. ApJ, 658:898–916, April 2007. doi: 10.1086/511059.

E. N. Parker. Cosmical magnetic fields: Their origin and their activity. Oxford University Press, 1979.

L. Pentericci, W. Van Reeven, C. L. Carilli, H. J. A. Röttgering, and G. K. Miley. VLA radio continuum observations of a new sample of high redshift radio galaxies. A&AS, 145:121–159, July 2000. doi: 10.1051/aas:2000104.

J. M. Picone and R. B. Dahlburg. Evolution of the Orszag-Tang vortex system in a compressible medium. II - Supersonic flow. Physics of Fluids B, 3:29–44, January 1991. doi: 10.1063/1.859953.

W. Pietsch, G. Trinchieri, H. Arp, and J. W. Sulentic. X-ray emission components from Stephan's Quintet resolved with the ROSAT HRI. A&A, 322:89–97, June 1997.

Planck Collaboration, P. A. R. Ade, N. Aghanim, C. Armitage-Caplan, M. Arnaud, M. Ashdown, F. Atrio-Barandela, J. Aumont, C. Baccigalupi, A. J. Banday, and et al. Planck 2013 results. I. Overview of products and scientific results. ArXiv e-prints, March 2013.

W. H. Press and P. Schechter. Formation of Galaxies and Clusters of Galaxies by Self-Similar Gravitational Condensation. ApJ, 187:425–438, February 1974. doi: 10.1086/152650.

D. J. Price. splash: An Interactive Visualisation Tool for Smoothed Particle Hydrodynamics Simulations. PASA, 24:159–173, October 2007. doi: 10.1071/AS07022.

D. J. Price. Smoothed particle hydrodynamics and magnetohydrodynamics. Journal of Computational Physics, 231:759–794, February 2012. doi: 10.1016/j.jcp.2010.12.011.

D. J. Price and J. J. Monaghan. Smoothed Particle Magnetohydrodynamics - I. Algorithm and tests in one dimension. MNRAS, 348:123–138, February 2004. doi: 10.1111/j.1365-2966.2004.07345.x.

D. J. Price and J. J. Monaghan. Smoothed Particle Magnetohydrodynamics - III. Multidimensional tests and the div(B) = 0 constraint. MNRAS, 364:384–406, December 2005. doi: 10.1111/j.1365-2966.2005.09576.x.

E. Priest and T. Forbes. Magnetic Reconnection. Cambridge University Press, February 2007.

R. E. Pudritz and J. Silk. The origin of magnetic fields and primordial stars in protogalaxies. ApJ, 342:650–659, July 1989. doi: 10.1086/167625.

S. A. Pustilnik and A. L. Tepliakova. Study of galaxies in the Lynx-Cancer void - I. Sample description. MNRAS, 415:1188–1201, August 2011. doi: 10.1111/j.1365-2966.2011.18733.x.

P. Rebusco, E. Churazov, H. Böhringer, and W. Forman. Effect of turbulent diffusion on iron abundance profiles. MNRAS, 372:1840–1850, November 2006. doi: 10.1111/j.1365-2966.2006.10977.x.

M. J. Rees. The origin and cosmogonic implications of seed magnetic fields. QJRAS, 28:197–206, September 1987.

M. J. Rees. Origin of the Seed Magnetic Field for a Galactic Dynamo. In D. Lynden-Bell, editor, NATO ASIC Proc. 422: Cosmical Magnetism, page 155, 1994.

M. J. Rees. Origin of cosmic magnetic fields. Astronomische Nachrichten, 327:395, June 2006. doi: 10.1002/asna.200610540.

F. Renaud, P. N. Appleton, and C. K. Xu. N-body Simulation of the Stephan's Quintet. ApJ, 724: 80–91, November 2010. doi: 10.1088/0004-637X/724/1/80.

H.-P. Reuter, U. Klein, H. Lesch, R. Wielebinski, and P. P. Kronberg. The magnetic field in the halo of M 82. Polarized radio emission at lambda-lambda(6.2) and 3.6 CM. A&A, 282:724–730, February 1994.

O. Reynolds. On the Dynamical Theory of Incompressible Viscous Fluids and the Determination of the Criterion. Royal Society of London Philosophical Transactions Series A, 186:123–164, 1895. doi: 10.1098/rsta.1895.0004.

S. P. Reynolds, B. M. Gaensler, and F. Bocchino. Magnetic Fields in Supernova Remnants and Pulsar-Wind Nebulae. Space Sci. Rev., 166:231–261, May 2012. doi: 10.1007/s11214-011-9775-y.

B. Robertson, J. S. Bullock, T. J. Cox, T. Di Matteo, L. Hernquist, V. Springel, and N. Yoshida. A Merger-driven Scenario for Cosmological Disk Galaxy Formation. ApJ, 645:986–1000, July 2006. doi: 10.1086/504412.

K. Rohlfs and T. L. Wilson. Tools of radio astronomy. Springer, 2004.

R. R. Rojas, M. S. Vogeley, F. Hoyle, and J. Brinkmann. Photometric Properties of Void Galaxies in the Sloan Digital Sky Survey. ApJ, 617:50–63, December 2004. doi: 10.1086/425225.

R. R. Rojas, M. S. Vogeley, F. Hoyle, and J. Brinkmann. Spectroscopic Properties of Void Galaxies in the Sloan Digital Sky Survey. ApJ, 624:571–585, May 2005. doi: 10.1086/428476.

S. Rosswog and D. Price. MAGMA: a three-dimensional, Lagrangian magnetohydrodynamics code for merger applications. MNRAS, 379:915–931, August 2007. doi: 10.1111/j.1365-2966.2007.11984.x.

A. A. Ruzmaikin, V. I. Turchaninov, I. B. Zeldovich, and D. D. Sokoloff. The disk dynamo. Ap&SS, 66:369–384, December 1979. doi: 10.1007/BF00650011.

G. B. Rybicki and A. P. Lightman. Radiative processes in astrophysics. Wiley-Interscience, 1979.

D. Ryu, H. Kang, J. Cho, and S. Das. Turbulence and Magnetic Fields in the Large-Scale Structure of the Universe. Science, 320:909–, May 2008. doi: 10.1126/science.1154923.

S. Samui, K. Subramanian, and R. Srianand. Constrained semi-analytical models of galactic outflows. MNRAS, 385:783–808, April 2008. doi: 10.1111/j.1365-2966.2008.12932.x.

S. Samui, K. Subramanian, and R. Srianand. Cosmic ray driven outflows from high-redshift galaxies. MNRAS, 402:2778–2791, March 2010. doi: 10.1111/j.1365-2966.2009.16099.x.

A. A. Schekochihin, S. C. Cowley, G. W. Hammett, J. L. Maron, and J. C. McWilliams. A model of nonlinear evolution and saturation of the turbulent MHD dynamo. New Journal of Physics, 4:84, October 2002. doi: 10.1088/1367-2630/4/1/384.

A. A. Schekochihin, S. C. Cowley, S. F. Taylor, J. L. Maron, and J. C. McWilliams. Simulations of the Small-Scale Turbulent Dynamo. ApJ, 612:276–307, September 2004. doi: 10.1086/422547.

D. R. G. Schleicher, R. Banerjee, S. Sur, T. G. Arshakian, R. S. Klessen, R. Beck, and M. Spaans. Small-scale dynamo action during the formation of the first stars and galaxies. I. The ideal MHD limit. A&A, 522:A115, November 2010. doi: 10.1051/0004-6361/201015184.

R. Schlickeiser, A. Sievers, and H. Thiemann. The diffuse radio emission from the Coma cluster. A&A, 182:21–35, August 1987.

M. Schmidt. The Rate of Star Formation. ApJ, 129:243, March 1959. doi: 10.1086/146614.

R. K. Sheth and G. Tormen. An excursion set model of hierarchical clustering: ellipsoidal collapse and the moving barrier. MNRAS, 329:61–75, January 2002. doi: 10.1046/j.1365-8711.2002.04950.x.

R. K. Sheth, H. J. Mo, and G. Tormen. Ellipsoidal collapse and an improved model for the number and spatial distribution of dark matter haloes. MNRAS, 323:1–12, May 2001. doi: 10.1046/j.1365-8711.2001.04006.x.

G. S. Shostak. H I emission from Stephan's Quintet. ApJ, 187:19–23, January 1974. doi: 10.1086/152584.

F. H. Shu. The physics of astrophysics. Volume II: Gas dynamics. University Science Books, 1992.

A. Shukurov. Introduction to galactic dynamos. ArXiv Astrophysics e-prints, November 2007.

H. Siejkowski, M. Soida, K. Otmianowska-Mazur, M. Hanasz, and D. J. Bomans. Cosmic-ray driven dynamo in the interstellar medium of irregular galaxies. A&A, 510:A97, February 2010. doi: 10.1051/0004-6361/200912729.

M. Simard-Normandin, P. P. Kronberg, and S. Button. The Faraday rotation measures of extragalactic radio sources. ApJS, 45:97–111, January 1981. doi: 10.1086/190709.

R. S. Somerville, G. Rosenfeld, T. S. Kolatt, A. Dekel, J. C. Mihos, and J. R. Primack. Galaxy Interactions and Starbursts at High Redshift. In F. Combes, G. A. Mamon, and V. Charmandaris, editors, Dynamics of Galaxies: from the Early Universe to the Present, volume 197 of Astronomical Society of the Pacific Conference Series, page 331, 2000.

L. Spitzer. Physics of fully ionized gases. Interscience Publication, 1965.

V. Springel. The cosmological simulation code GADGET-2. MNRAS, 364:1105–1134, December 2005. doi: 10.1111/j.1365-2966.2005.09655.x.

V. Springel. E pur si muove: Galilean-invariant cosmological hydrodynamical simulations on a moving mesh. MNRAS, 401:791–851, January 2010a. doi: 10.1111/j.1365-2966.2009.15715.x.

V. Springel. Smoothed Particle Hydrodynamics in Astrophysics. ARA&A, 48:391–430, September 2010b. doi: 10.1146/annurev-astro-081309-130914.

V. Springel and L. Hernquist. Cosmological smoothed particle hydrodynamics simulations: the entropy equation. MNRAS, 333:649–664, July 2002. doi: 10.1046/j.1365-8711.2002.05445.x.

V. Springel and L. Hernquist. Cosmological smoothed particle hydrodynamics simulations: a hybrid multiphase model for star formation. MNRAS, 339:289–311, February 2003a. doi: 10.1046/j.1365-8711.2003.06206.x.

V. Springel and L. Hernquist. The history of star formation in a Λ cold dark matter universe. MNRAS, 339:312–334, February 2003b. doi: 10.1046/j.1365-8711.2003.06207.x.

V. Springel, S. D. M. White, G. Tormen, and G. Kauffmann. Populating a cluster of galaxies - I. Results at z=0. MNRAS, 328:726–750, December 2001a. doi: 10.1046/j.1365-8711.2001.04912.x.

V. Springel, N. Yoshida, and S. D. M. White. GADGET: a code for collisionless and gasdynamical cosmological simulations. New Astron., 6:79–117, April 2001b. doi: 10.1016/S1384-1076(01)00042-2.

V. Springel, T. Di Matteo, and L. Hernquist. Modelling feedback from stars and black holes in galaxy mergers. MNRAS, 361:776–794, August 2005a. doi: 10.1111/j.1365-2966.2005.09238.x.

V. Springel, T. Di Matteo, and L. Hernquist. Black Holes in Galaxy Mergers: The Formation of Red Elliptical Galaxies. ApJ, 620:L79–L82, February 2005b. doi: 10.1086/428772.

V. Springel, S. D. M. White, A. Jenkins, C. S. Frenk, N. Yoshida, L. Gao, J. Navarro, R. Thacker, D. Croton, J. Helly, J. A. Peacock, S. Cole, P. Thomas, H. Couchman, A. Evrard, J. Colberg, and F. Pearce. Simulations of the formation, evolution and clustering of galaxies and quasars. Nature, 435:629–636, June 2005c. doi: 10.1038/nature03597.

V. Springel, C. S. Frenk, and S. D. M. White. The large-scale structure of the Universe. Nature, 440: 1137–1144, April 2006. doi: 10.1038/nature04805.

F. A. Stasyszyn, K. Dolag, and A. M. Beck. A divergence-cleaning scheme for cosmological SPMHD simulations. MNRAS, 428:13–27, January 2013. doi: 10.1093/mnras/sts018.

M. Stephan. Nebulæ (new) discovered and observed at the observatory of Marseilles, 1876 and 1877, M. Stephan. MNRAS, 37:334, April 1877.

F. Stoehr. Circular velocity profiles of dark matter haloes. MNRAS, 365:147–152, January 2006. doi: 10.1111/j.1365-2966.2005.09676.x.

F. Stoehr, S. D. M. White, G. Tormen, and V. Springel. The satellite population of the Milky Way in a ΛCDM universe. MNRAS, 335:L84–L88, October 2002. doi: 10.1046/j.1365-8711.2002.05891.x.

F. Stoehr, S. D. M. White, V. Springel, G. Tormen, and N. Yoshida. Dark matter annihilation in the halo of the Milky Way. MNRAS, 345:1313–1322, November 2003. doi: 10.1046/j.1365-2966.2003.07052.x.

J. M. Stone, T. A. Gardiner, P. Teuben, J. F. Hawley, and J. B. Simon. Athena: A New Code for Astrophysical MHD. ApJS, 178:137–177, September 2008. doi: 10.1086/588755.

R. G. Strom and A. G. Willis. Multifrequency observations of very large radio galaxies. II - 3C236. A&A, 85:36–54, May 1980.

K. Subramanian, A. Shukurov, and N. E. L. Haugen. Evolving turbulence and magnetic fields in galaxy clusters. MNRAS, 366:1437–1454, March 2006. doi: 10.1111/j.1365-2966.2006.09918.x.

J. W. Sulentic, M. Rosado, D. Dultzin-Hacyan, L. Verdes-Montenegro, G. Trinchieri, C. Xu, and W. Pietsch. A Multiwavelength Study of Stephan's Quintet. AJ, 122:2993–3016, December 2001. doi: 10.1086/324455.

P. M. Sutter, G. Lavaux, B. D. Wandelt, and D. H. Weinberg. A Public Void Catalog from the SDSS DR7 Galaxy Redshift Surveys Based on the Watershed Transform. ApJ, 761:44, December 2012. doi: 10.1088/0004-637X/761/1/44.

K. Takahashi, M. Mori, K. Ichiki, and S. Inoue. Lower Bounds on Intergalactic Magnetic Fields from Simultaneously Observed GeV-TeV Light Curves of the Blazar Mrk 501. ApJ, 744:L7, January 2012. doi: 10.1088/2041-8205/744/1/L7.

S. Tavasoli, K. Vasei, and R. Mohayaee. The challenge of large and empty voids in the SDSS DR7 redshift survey. A&A, 553:A15, May 2013. doi: 10.1051/0004-6361/201220774.

F. Tavecchio, G. Ghisellini, L. Foschini, G. Bonnoli, G. Ghirlanda, and P. Coppi. The intergalactic magnetic field constrained by Fermi/Large Area Telescope observations of the TeV blazar 1ES0229+200. MNRAS, 406:L70–L74, July 2010. doi: 10.1111/j.1745-3933.2010.00884.x.

F. Tavecchio, G. Ghisellini, G. Bonnoli, and L. Foschini. Extreme TeV blazars and the intergalactic magnetic field. MNRAS, 414:3566–3576, July 2011. doi: 10.1111/j.1365-2966.2011.18657.x.

A. M. Taylor, I. Vovk, and A. Neronov. Extragalactic magnetic fields constraints from simultaneous GeV-TeV observations of blazars. A&A, 529:A144, May 2011. doi: 10.1051/0004-6361/201116441.

A. Toomre and J. Toomre. Galactic Bridges and Tails. ApJ, 178:623–666, December 1972. doi: 10.1086/151823.

T. S. Tricco and D. J. Price. Constrained hyperbolic divergence cleaning for smoothed particle magnetohydrodynamics. Journal of Computational Physics, 231:7214–7236, August 2012. doi: 10.1016/j.jcp.2012.06.039.

M. Uhlig, C. Pfrommer, M. Sharma, B. B. Nath, T. A. Enßlin, and V. Springel. Galactic winds driven by cosmic ray streaming. MNRAS, 423:2374–2396, July 2012. doi: 10.1111/j.1365-2966.2012.21045.x.

J. P. Vallée. Magnetic fields in the nearby Universe, as observed in solar and planetary realms, stars, and interstellar starforming nurseries. New Astron. Rev., 55:23–90, May 2011a. doi: 10.1016/j.newar.2011.01.001.

J. P. Vallée. Magnetic fields in the galactic Universe, as observed in supershells, galaxies, intergalactic and cosmic realms. New Astron. Rev., 55:91–154, May 2011b. doi: 10.1016/j.newar.2011.01.002.

P. Wang and T. Abel. Magnetohydrodynamic Simulations of Disk Galaxy Formation: The Magnetization of the Cold and Warm Medium. ApJ, 696:96–109, May 2009. doi: 10.1088/0004-637X/696/1/96.

R. H. Wechsler, J. S. Bullock, J. R. Primack, A. V. Kravtsov, and A. Dekel. Concentrations of Dark Halos from Their Assembly Histories. ApJ, 568:52–70, March 2002. doi: 10.1086/338765.

G. L. Welter, J. J. Perry, and P. P. Kronberg. The rotation measure distribution of QSOs and of intervening clouds - Magnetic fields and column densities. ApJ, 279:19–39, April 1984. doi: 10.1086/161862.

S. D. M. White and C. S. Frenk. Galaxy formation through hierarchical clustering. ApJ, 379:52–79, September 1991. doi: 10.1086/170483.

S. D. M. White and M. J. Rees. Core condensation in heavy halos - A two-stage theory for galaxy formation and clustering. MNRAS, 183:341–358, May 1978.

L. M. Widrow. Origin of galactic and extragalactic magnetic fields. Reviews of Modern Physics, 74: 775–823, 2002. doi: 10.1103/RevModPhys.74.775.

L. M. Widrow, D. Ryu, D. R. G. Schleicher, K. Subramanian, C. G. Tsagas, and R. A. Treumann. The First Magnetic Fields. Space Sci. Rev., 166:37–70, May 2012. doi: 10.1007/s11214-011-9833-5.

H. Wiechen, G. T. Birk, and H. Lesch. Generation of magnetic seed fields in protogalactic clouds due to plasma-neutral gas friction. A&A, 334:388–394, June 1998.

A. G. Willis and R. G. Strom. Multifrequency observations of very large radio galaxies. I - 3C 326. A&A, 62:375–392, January 1978.

J. H. Wise and T. Abel. Resolving the Formation of Protogalaxies. I. Virialization. ApJ, 665:899–910, August 2007. doi: 10.1086/520036.

A. M. Wolfe, E. Gawiser, and J. X. Prochaska. Damped Ly α Systems. ARA&A, 43:861–918, September 2005. doi: 10.1146/annurev.astro.42.053102.133950.

C. K. Xu, N. Lu, J. J. Condon, M. Dopita, and R. J. Tuffs. Physical Conditions and Star Formation Activity in the Intragroup Medium of Stephan's Quintet. ApJ, 595:665–684, October 2003. doi: 10.1086/377445.

C. K. Xu, J. Iglesias-Páramo, D. Burgarella, R. M. Rich, S. G. Neff, S. Lauger, T. A. Barlow, L. Bianchi, Y.-I. Byun, K. Forster, P. G. Friedman, T. M. Heckman, P. N. Jelinsky, Y.-W. Lee, B. F. Madore, R. F. Malina, D. C. Martin, B. Milliard, P. Morrissey, D. Schiminovich, O. H. W. Siegmund, T. Small, A. S. Szalay, B. Y. Welsh, and T. K. Wyder. Ultraviolet Emission and Star Formation in Stephan's Quintet. ApJ, 619:L95–L98, January 2005. doi: 10.1086/425130.

H. Xu, H. Li, D. Collins, S. Li, and M. L. Norman. Formation of X-Ray Cavities by the Magnetically Dominated Jet-Lobe System in a Galaxy Cluster. ApJ, 681:L61–L64, July 2008. doi: 10.1086/590407.

H. Xu, H. Li, D. C. Collins, S. Li, and M. L. Norman. Evolution and Distribution of Magnetic Fields from Active Galactic Nuclei in Galaxy Clusters. I. The Effect of Injection Energy and Redshift. ApJ, 725:2152–2165, December 2010. doi: 10.1088/0004-637X/725/2/2152.

H. Xu, F. Govoni, M. Murgia, H. Li, D. C. Collins, M. L. Norman, R. Cen, L. Feretti, and G. Giovannini. Comparisons of Cosmological Magnetohydrodynamic Galaxy Cluster Simulations to Radio Observations. ApJ, 759:40, November 2012. doi: 10.1088/0004-637X/759/1/40.

I. B. Zel'dovich, A. A. Ruzmaikin, and D. D. Sokolov, editors. Magnetic fields in astrophysics, volume 3 of The Fluid Mechanics of Astrophysics and Geophysics, 1983.

Y. B. Zel'dovich. Gravitational instability: An approximate theory for large density perturbations. A&A, 5:84–89, March 1970.

E. G. Zweibel. Evolution of magnetic fields at high redshift. Astronomische Nachrichten, 327:505, June 2006. doi: 10.1002/asna.200610573.

List of scientific publications

Refereed publications

- **A.M. Beck**, H. Lesch, K. Dolag, H. Kotarba, A. Geng & F.A. Stasyszyn, 'Origin of strong magnetic fields in Milky Way-like galactic haloes', 2012, *MNRAS*, 422, 2152
- **A.M. Beck**, M. Hanasz, H. Lesch, R.S. Remus & F.A. Stasyszyn, 'On the magnetic fields in voids', 2012, *MNRAS*, 429, L60
- **A.M. Beck**, K. Dolag, H. Lesch & P.P. Kronberg, 'Strong magnetic fields and large rotation measures in protogalaxies from supernova seeding', 2013, *MNRAS*, 435, 3575
- A. Geng, H. Kotarba, F. Bürzle, K. Dolag, F. Stasyszyn, **A. Beck** & P. Nielaba, 'Magnetic field amplification and X-ray emission in galaxy minor mergers', 2012, *MNRAS*, 419, 3571
- A. Geng, **A.M. Beck**, K. Dolag, F. Bürzle, M.C. Beck, H. Kotarba & P. Nielaba, 'Synthetic X-ray and radio maps for two different models of Stephan's Quintet', 2012, *MNRAS*, 426, 3160
- F.A. Stasyszyn, K. Dolag, & **A.M. Beck**, 'A divergence-cleaning scheme for cosmological SPMHD simulations', 2013, *MNRAS*, 428, 13

Conference proceedings

- **A.M. Beck**, H. Lesch, K. Dolag & A. Geng, 'Magnetic fields during galactic halo formation', in: Proceedings of Magnetic Fields in the Universe III, edited by M. Soida, K. Otmianowska-Mazur, E.M. de Gouveia Dal Pino & A. Lazarian
- A. Geng, H. Kotarba, F. Bürzle, K. Dolag, F. Stasyszyn, **A. Beck** & P. Nielaba, 'Magnetic fields in galaxy mergers', in: Proceedings of Magnetic Fields in the Universe III, edited by M. Soida, K. Otmianowska-Mazur, E.M. de Gouveia Dal Pino & A. Lazarian

Danksagung

An erster Stelle bedanke ich mich bei den beiden Menschen, die es mir erstens ermöglicht haben, zu promovieren und zweitens erheblich zum Gelingen dieser Arbeit beigetragen haben:

- Lieber Harald, vielen Dank für Dein grenzenloses Vertrauen, die endlose Geduld und die permanente Motivation. Bei Dir werden Menschen gefördert, nicht nur Physiker. Ich wüsste nicht, was ich ohne Dich getan hätte.
- Lieber Klaus, vielen Dank für Deine Unterstützung, auch wenn ich immer meinen eigenen Kopf hatte und nie das gemacht habe, was Du von mir wolltest. Du hast mich jedoch oft in die richtige Richtung geschoben.
- Zusätzlich danke ich meinen Eltern herzlichst für all die Unterstüzung während des Studiums und auch weiterhin in der Promotion.

Desweiteren bedanke ich mich bei allen Menschen, die diese Arbeit begleitet haben:

- Für die Finanzierung meiner Doktorarbeit Ralf Bender und dem Max-Planck-Institut für Extraterrestrische Physik in Garching.
- Für die Übernahme des Zweitgutachtens Jochen Weller, die gute Zusammenarbeit Michal Hanasz und Philipp Kronberg, die fundierte Grundstromlegung Hanna Kotarba, sowie Andreas Burkert und der CAST-Gruppe für die Kooperation.
- Den Mitgliedern der DFG Forschergruppe RU 1254, insbesondere Uli Klein, dass sie es mir ermöglicht haben, meine Arbeit einem größeren Fachpublikum präsentieren zu können.
- Den Konstanzern Annette Geng, Florian Bürzle, Marcus Beck und Peter Nielaba für die vielen schönen Tage am Bodensee und die fruchtbare Kooperation.
- Den Damen im Sekretariat Angelika Rühfeld, Ilse Holzinger, Nicola Auer, Sabine Grötsch und Uta Le Guay, sowie der guten Seele des Hauses Adolf Karasz.
- A big thanks to all my colleagues and in particular: Stefan Heigl, David Schlachtberger, Stephanie Pekruhl, Lisa Bachmann, Natascha Greisel, Anna Schauer, Jiayi Liu, Franco Vazza, Annalisa Bonafede, Veronika Junk, Dominik Bomans, Judith Ngoumou, Alexandro Saro, Alfredo Zenteno, Christina Hennig, Ralf Kosyra and Ulrich Hopp.

Furthermore, many of you are more friends than colleagues to me and I cannot imagine a life without you. For the exceptionally good times I had over the past years at lunch, the millions of coffee breaks and also in the evenings: Anna Monna, Anna Brucalassi, Alexander Arth, Julius Donnert, Maximilian Imgrund, Federico Stasyszyn, Sebastian Bocquet, Rhea Remus, Tadziu Hoffmann and Annalisa Mana. You know very well what you contributed to my mental sanity during the past years, I do not need to go into details. **Thanks!**

In particolare, la vita sarebbe noiosa senza gli italiani. Voi avete il miglior cibo e siete le migliori persone con cui stare. Mi mancherete tutti.

Ciao!